Coatings with tailored electronic and optical properties for advanced glazing

Thèse N° 9199

OLIVIA VALÉRIE CHARLOTTE BOUVARD

EPFL
ÉCOLE POLYTECHNIQUE
FÉDÉRALE DE LAUSANNE

2019

« Not everything that can be counted counts, and not everything that counts can be counted. »

William Bruce Cameron

Résumé

Les vitrages modernes comportent des revêtements nanométriques permettant de modifier leurs caractéristiques. Les revêtements basse émissivité améliorent les performances thermiques d'un vitrage grâce à une fine couche métallique, cependant cette dernière nuit à la transmission des micro-ondes utilisées pour les télécommunications. Les revêtements électrochromes permettent de moduler les gains solaires d'un bâtiment tout en préservant la vue vers l'extérieur. Des produits commerciaux existent mais leur amplitude et vitesse de coloration ainsi que leur durabilité est perfectible.

Cette thèse de doctorat s'intéresse à l'étude des propriétés électroniques et optiques de ces revêtements pour mieux les adapter à leur application.

Une approche innovante afin d'améliorer le passage des micro-ondes à travers un revêtement conducteur transparent est présentée. De premiers tests sont réalisés pour valider le concept et une gamme de motifs réalisés par ablation laser est déterminée. Une transmission des micro-ondes quasiment aussi haute que le verre non revêtu est obtenue tout en préservant les qualités thermiques et visuelles. Des vitrages comprenant ce revêtement sont déjà utilisés par une entreprise ferroviaire suisse pour équiper les fenêtres de ses wagons et ainsi éviter l'usage d'amplificateurs de signal.

Les revêtements conducteurs transparents sont aussi utilisés comme électrode dans les vitrages électrochromes. Afin de ne pas endommager les couches sous-jacentes, un dépôt sans chauffage est préférable. Des paramètres de dépôt donnant des propriétés optiques et électriques convenables sont présentés.

La présence d'un électrolyte polymère ou gel limite la durabilité, justifiant l'étude de dispositifs electrochrome tout-solide et inorganiques. La cinétique et le contraste de coloration de l'oxyde de tungstène (WO_3) peut être améliorée en augmentant la nanoporosité de la couche. Par ailleurs, l'utilisation d'un nanocomposite nickel-tantale-oxygène permet d'obtenir un meilleur rendu de couleur. En combinaison avec un électrolyte solide d'oxyde de tantale, le passage des ions lithium devrait être facilité.

D'autres électrolytes solides tels que l'oxynitrure de phosphate de lithium (LiPON) et l'oxyde de titane lithium lanthane (LLTO) sont envisagés. Il est montré que la stabilité du LiPON dans l'air ambiant peut être améliorée en augmentant la quantité d'argon dans un plasma argon-azote durant le dépôt. De plus, il est montré que le LLTO présente une transmittance solaire élevée.

L'insertion de lithium lors d'un procédé sous vide faciliterait la production des dispositifs électrochromes. Une méthode de lithiation par voie sèche, ne nécessitant pas l'usage d'éléments sensible à l'humidité, est présentée. Utilisée pour la lithiation d'un film de WO_3, elle permet de réduire sa transmittance lumineuse de 83 à 2%.

Des dispositifs électrochromes tout solide, comprenant une étape de lithiation sous vide et un electrolyte inorganique sont produits, principalement avec des cibles métalliques, ce qui permet d'obtenir des vitesses de dépôt plus élevées qu'avec des cibles céramiques.

Par ailleurs, l'étude des interfaces, et des films lithiés, par spectroscopie photoélectronique permet d'obtenir des informations menant à une meilleure compréhension des hétérostructures composant la cellule électrochrome.

Ces connaissances visent à contribuer à l'élaboration de vitrages électrochromes optimisés pour une meilleure gestion des gains solaires et de la lumière du jour.

Mots-clés

Abstract

Modern envelope glazing relies on nanoscale coatings to meet a range of specific needs. Low emissivity coatings can improve the thermal performance of glazing thanks to a thin metallic film. However, the conductive nature of this layer leads to an attenuation of the microwaves used in telecommunications. Electrochromic coatings on the other hand can modulate the solar heat gains of a building while preserving the view toward the exterior. Yet, the switching speed and contrast as well as the durability of commercial products are unsatisfactory.

This thesis focuses on the improvement of the electronic and optical properties of such coatings to address the shortcomings listed above.

A novel approach to increase the transmission of microwaves through transparent conductive coatings is presented. Experiments are performed to validate the proof of concept, a variety of patterns obtained by laser ablation are then determined. These allow a transmission of microwaves close to the one of uncoated glass while preserving the thermal and visual properties of the glass. Glazing with these novel coatings is now used by a Swiss railway company for the windows of its wagons to avoid the use of signal amplifiers.

Transparent conductive coatings are also used as electrode in electrochromic devices; in order not to damage the underlying layers, deposition of this electrode without heating is preferable. Deposition parameters giving suitable optical and electrical properties are presented.

Since gel or polymer electrolytes limit the durability of electrochromic glazing, all-solid state, inorganic devices are considered. The optical contrast and switching dynamics of tungsten trioxide can be improved by increasing the nanoporosity of the layer. Furthermore, the use of a nickel-tantalum oxide nanocomposite for the counter electrode yields a better color rendering. In combination with tantalum pentoxide as a solid electrolyte, the migration of lithium ions should be facilitated.

Other solid electrolytes such as lithium phosphate oxynitride (LiPON) and lanthanum lithium titanium oxide (LLTO) are envisioned. It is shown that the stability of LiPON in ambient air can be enhanced by increasing the amount of argon in an argon-nitrogen plasma during deposition. In addition, it is shown that LLTO films have a high solar transmittance, allowing its use in electrochromic devices.

Lithium insertion during a vacuum process would facilitate the production of electrochromic devices. A dry lithiation method, which does not require the use of elements sensitive to humidity, is presented. Used for the lithiation of a tungsten trioxide, it makes it possible to reduce its light transmittance from 83 to 2%.

All-solid-states devices, lithiated in vacuum and produced using a nanoporous tantalum pentoxide as a lithium ion conductor, exhibit a fast switching time and a good contrast. Except for the top electrode, they are manufactured using metallic sputtering targets, which allow faster deposition rates compared to ceramic targets.

Additionally, the study of lithiated films and interfaces by photoelectron spectroscopy provides information on the modification of the work function and oxidation levels of the host material, leading to a better understanding of the semiconductor heterostructures constituting all-solid-state-devices.

These insights are expected to help to develop optimized electrochromic glazing for a better management of solar heat gains and daylight in buildings.

Keywords

Contents

Nomenclature

Symbol	Name
A	Ampere
K	Kelvin
kg	Kilogram
m	Meter
mol	Mole
s	Second
cd	Candela
°	Degree of arc
°C	Celsius degree
at:%	atomic percent
bar	Bar
C	Coulomb
cc	cubic centimeter
dB	Decibell
h	Hour
Hz	Hertz
J	Joule
l	Litre
min	Minute
Pa	Pascal
rad	Radian
S	Siemens
sccm	Standard cubic centimeters per minute
sr	Steradian
T	Tesla
V	Volt
W	Watt
Ω	Ohm

Constants

Symbol	Name	Value	Unit
c	speed of light	299 792 458	m/s
e	elementary charge	$1.6021 \cdot 10^{-19}$	C
F	Faraday constant	$9.64853399 \cdot 10^4$	$C \cdot mol^{-1}$
$\hbar$	reduced Planck constant	$6.582119514 \cdot 10^{-16}$	eV.s
k_B	Boltzmann constant	$8.6173303 \cdot 10^{-5}$	$eV.K^{-1}$
m_e	rest mass of an electron	$9.11 \cdot 10^{-31}$	kg
R	universal gas constant	8.314472	$J \cdot K^{-1} \cdot mol^{-1}$
π	Pi	3.141 592 653 589 793	-
σ	Stefan-Boltzmann's constant	$5.67\ 10-8$	$W.m^{-2}.K^{-4}$

Variables

Symbol	Name	Unit
e	elementary charge	C
A	area	cm^2
C	electrical capacitance	F
CE	Coloration Efficiency	mC/cm^2
CPE	Constant Phase Element	F
E_a	activation energy	eV
f	frequency	Hz
h	heat transfer coefficient	$W.m^{-2}.K^{-1}$
h_t	total thermal conductance	$W.m^{-2}.K^{-1}$
m^*	effective mass of the carriers	kg or m_e
n	carrier concentration of electrons	cm^{-3}
OD	Optical Density	-
p	carrier concentration of holes	cm^{-3}
Q	charge	mC/cm^2
R	electrical resitance	Ohm
R_a	color rendering index	-
T	temperature	K
t	time	s, min or h
U, U value	thermal transmittance	$W.m^{-2}.K^{-1}$
Z	impedance	Ohm
α	aborptance	
Δ	phase difference (in ellispometry)	rad
ε	emissivity	%
ε_0	vacuum permittivity	$F.m^{-1}$
λ	wavelength	nm or m
$\mu_{n,p}$	electrons, holes carrier mobility	$cm^2 \cdot V^{-1} \cdot s^{-1}$
ρ	reflectance	
σ	electrical conductivity	$S.cm^{-1}$
σ_i	ionic conductivity	$S.cm^{-1}$
τ	transmittance	
Φ	work function	eV
ψ	amplitude component (in ellispometry)	rad
ω_p	plasma frequency	$rad \cdot s^{-1}$

Acronyms and abbreviation

Symbol	Name
©	Copyright
®	Registered trademark
AC	Alternative Current
AM0	Air Mass zero, solar radiation quantities outside the Earth's atmosphere
AM1.5	Air Mass of 1.5 (solar zenith angle of 48.19°)
ASTM	American Society for Testing and Materials
at.	atomic
AZO	Aluminium doped Zinc Oxide
BE	Binding Energy
CA	Chrono-Amperometry
CAE	Constant Analyzer Energy
CBM	Conduction Band Minimum
CIE	International Commission on Illumination
CLC	Cholesteric Liquid Crystals
cos	cosine of an angle
CRI	Color Rendering Index
CRR	Constant Retardation Ratio
CV	Cyclic Voltammetry
D65	Standard Illuminant representative of daylight (temperature of ~ 6500 K)
DC	Direct Current
DC-p	Bipolar-pulsed Direct Current
DFT	Density Functional Theory
e.g	*exempli gratia* in Latin, "for example"
EC	Electrochromic
EC-PC	Ethylene Carbonate - Propylene Carbonate
EDX	Energy-Dispersive X-ray spectroscopy
E_F	Fermi level
EHT	Electron High Tension (SEM)
EIS	Electrochemical Impedance Spectroscopy
EN	European Norm
EPFL	Ecole Polytechnique Fédérale de Lausanne
eq.	equation
ESB	Backscattered electrons
ETHZ	Ecole Polytechnique Fédérale de Zurich
EU	European Union
FSS	Frequency Selective Surface
FTIR	Fourier-Transform InfraRed spectroscopy
FTO	Fluor doped Tin Oxide
FWHM	Full-Width at Half-Maximum
G173	Reference Solar Spectral Irradiance at Air Mass 1.5 (ASTM G-173-03)
GSM	Global System for Mobile communications
i.e.	*id est* in Latin, "that is"

IEA	International Energy Agency
IMFP	Inelastic Mean Free Path
IR	Thermal infrared range of the electromagnetic spectrum (0.8 - 50 µm)
ITO	Indium Tin Oxide
KE	Kinetic Energy
LESO	Laboratoire d'Energie Solaire et Physique du Bâtiment
Li-PC	Propylene Carbonate containing dissolved $LiClO_4$
LiPON	Lithium phosphate oxynitride
LLTO	Lithium lantanum titanium oxide $(Li_{3x}La_{2/3-x})TiO_3$
low-e	Low emissivity
MF	Medium Frequency
MIR	Middle infrared range of the electromagnetic spectrum (2.5 - 20 µm)
MW	Microwaves range of the electromagnetic spectrum (5-50 cm)
NIR	Near infrared range of the electromagnetic spectrum (780-2500 nm)
NIST	National Institute of Standards and Technology
NMR	Nuclear Magnetic Resonance
NW	nanowires
PC	Propylene Carbonate
PDLC	Polymer Dispersed Liquid Crystal
pp	percentage points
RF	Radio-Frequencies
RMSE	Root Mean Square Error
RSF	Relative Sensitivity Factor
SCCER	Swiss Competence Center for Energy Research
FEEB&D	Future Efficient Energy Districts and Buildings
SEA	Spectroscopic Ellipsometry Analyzer software
SEM	Scanning Electron Microscopy
sin	sine of an angle
SPDs	Suspended Particle Devices
SUT	Sample Under Test
SWNT	Single-Walled Nano-Tubes
tan	tangent of an angle
UMTS	Universal Mobile Telecommunications System
UPS	Ultraviolet Photoelectron Spectroscopy
USA	United States of America
UV	Ultraviolet
V(λ)	Spectral luminous efficiency for photopic vision
VBM	Valence Band Minimum
Vis	Visible range of the electromagnetic spectrum (380-780 nm)
VNA	Vector Network Analyzer
vol.	Volume
WD	Working Distance (SEM)
WP	Working Pressure (during sputtering deposition)
wt.	Weight
XPS	X-ray Photoelectron Spectroscopy
XRD	X-ray Diffraction

Elements

Symbol	Name
Ag	Silver
Al	Aluminum
C	Carbon
Co	Cobalt
Cu	Copper
F	Fluor
Ge	Germanium
H	Hydrogen
He	Helium
In	Indium
K	Potassium
Li	Lithium
Mg	Magnesium
Mn	Manganese
Mo	Molybdenum
N	Nitrogen
Na	Sodium
Nb	Nobium
Ni	Nickel
O	Oxygen
Sb	Antimony
Si	Silicon
Sn	Tin
Ta	Tantalum
Ti	Titanium
V	Vanadium
W	Tungsten
Zr	Zirconium

Chapter 1   Introduction and state of the art

This chapter aims to illustrate the context of the research performed within the framework of this thesis on coatings with tailored electronic and optical properties for advanced glazing. This chapter also introduces the working principles and reviews the state of the art of spectrally selective and switchable glazing. First, it unveils how it is possible to achieve high transmittance in the visible range, for low emissivity coatings having a low absorptance in the infrared. The use of these coating as transparent electrodes is described. The idea of a frequency selective surface and its application in the microwave frequency range is described. In a second part, the concept of electrochromism and its use in switchable glazing is presented. The main components contained in an electrochromic device are described and their assembly and deposition methods are exposed.

1.1   Context

1.1.1 Energy consumption in the building sector

In its energy technology perspective report (IEA, 2017), the International Energy Agency states that the building sector is responsible for 30% of the final energy consumption worldwide and more than 55% of the global electricity demand as illustrated in Figure 1:1. In the European Union (EU 27), buildings represent the largest energy consumer with close to 40% of the final energy use in 2010 (IEA,2013). The repartition of energy consumption varies from northern to Mediterranean climates with more or less heating/cooling demand but in average space and water heating constitute about 70 % of the final energy consumption (IEA, 2013).

Global final energy consumption by sector, 2015

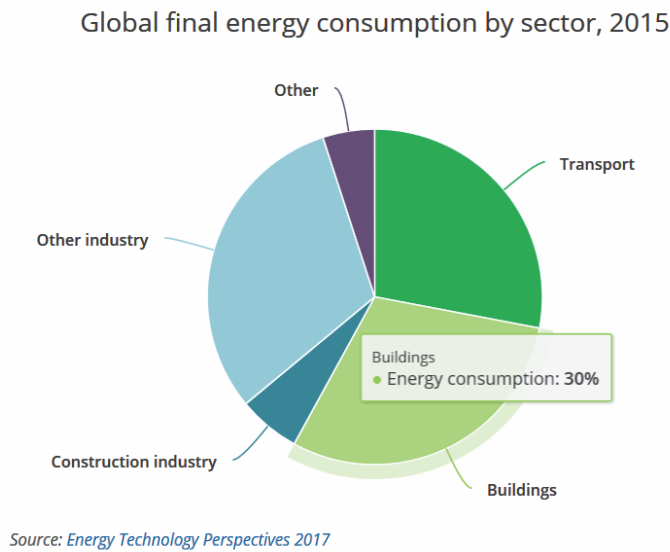Source: *Energy Technology Perspectives 2017*

Figure 1:1   Global final energy consumption by sector worldwide in 2015. The building sector represent 30 % of energy consumption. Reproduced from (IEA, 2017).

In Switzerland, close to 50% of the end energy demand is due to buildings and should be reduced considerably to meet the requirements of the Energy Strategy 2050 (SCCER, 2015). The energy balance of a building is determined by the amount of losses versus the amount of gains. Thermal energy is lost mainly through the opaque envelope of the façade, walls and roof, through ventilation and through the openings, windows and doors. Windows can also provide solar gains, which may reduce the need for space heating in winter or on the contrary, increase the need for cooling in summer.

1.1.2 Glazing in today's architecture

Building envelopes have evolved tremendously in the last centuries giving glass an increasing importance as illusatrated in Figure 1:2. Technological progress in the production of glass panes as well as the use of energy efficient glazing fostered the use of large glass facades since the invention of the float glass process by Pilkington in 1959. Nowadays, some buildings exhibit a window-to-wall ratio of 100 %, as illustrated in Figure 1:2 c). Glazing is one of the most important elements of the façade letting in daylight and playing a main role in the aesthetic of the building. Windows also provide a view towards the outside and can control natural ventilation. However, the increased surface of glazing in building façade can also lead to excessive solar gains during sunny days and excessive heat loss during the heating season. Furthermore, modern telecommunications technologies rely on microwave transmission and modern glazing can be an obstacle to them.

Figure 1:2   Illustration of different types of windows: a small window of an old house, windows in modern flats and the fully glazed façade of a library (images from the public domain).

1.1.3 Transmission of microwaves through modern glazing

Windows are regarded as an important source of sunlight and thermal losses; their properties regarding the transmission of microwaves are generally overlooked. However, it was found that low-emissivity coatings which greatly improve the thermal properties of windows, also reduces their ability to transmit the microwave used by most of today wireless telecommunication technologies. In the context of a project on the energy efficiency of train wagons, it was noticed that railway companies were reluctant to install glazing with better thermal properties due to the limitations it would imply on the availability of the telecommunication network for passengers. A modification of the low-emissivity coatings to reduce the mobility of the electrons and limit their ability to block the electromagnetic waves used for telecommunication was thus investigated.

The aim of this research is to propose a novel type of low-emissivity coatings which combine high thermal efficiency with high microwave transmission without perturbing the view towards outside.

1.1.4 Solar protection in highly-glazed buildings

Heating and cooling buildings represent a large share of the world energy consumption. In order to limit cooling needs, glazing with a low spectral transmittance in the solar range are used in highly glazed buildings; however, they also prevent solar gains in winter when they are desirable. Dynamic shading systems are therefore preferable and could contribute to increase the energy efficiency of buildings. Such dynamic systems could reduce the cooling load as well as the space heating needs. This research was performed in the framework of the Swiss Competence Center for Energy Research on Future Energy Efficient Buildings & Districts (SCCER FEEB&D).

Another important aspect of a window is to provide a view towards the exterior. In highly-glazed buildings, solar protections are needed to avoid overheating. However, these solar protections such as blinds might obstruct the view, especially in west and east orientations where the sun altitude is low. Furthermore, mechanical solutions require regular maintenance, which might necessitate specific equipment as illustrated in Figure 1:3, and are subject to damages due to strong winds.

Figure 1:3   Maintenance of the external venetian blinds on the Rolex Learning Center building, EPFL.

Electrochromic windows can darken on demand to modulate solar gains, a coating or a film is applied to the glass to provide this ability. Since no mechanical parts are involved they are less subject to damages due to strong winds. Commercial products exist but their current cost limit them to a niche market. Furthermore, several challenges in terms of durability, switching time or color properties still limit their implementation. Some electrochromic windows use gel or polymer electrolytes which, as organic materials, degrade with time.

Therefore it was decided to investigate all-solid-state inorganic electrochromic devices. The electronic and optical properties of the electrochromic oxides and inorganic electrolytes are studied to get a better understanding of the mechanisms governing their relation. The influence of the deposition parameters on the morphology, the stoichiometry or the switching behavior on these properties is then investigated to develop optimized coatings. A method to insert lithium in the electrochromic layer is developed and used to produce all-solid-state devices.

1.2   Spectrally selective glazing

Selective surfaces are of special interest because their properties vary according to the part of the spectrum considered. The electromagnetic spectrum is shown in Figure 1:4 and highlights the region of the spectrum corresponding to solar radiation, thermal infrared radiation and the microwaves used for telecommunications. Kirchhoff's Law states that the absorptance and the emittance are equal for each wavelength (Kirchoff, 1860). However, the visible absorption coefficient can be different from the infrared one. One can take advantage of this to develop new materials tailored to their usage. The application of thin film can add new properties to glazing either constant (scratch resistance, low emissivity, electromagnetic…) or dynamic (self-cleaning, electrochromics …)(Casini, 2018). Section 1.4 will deal with the dynamic, or switchable, glazing.
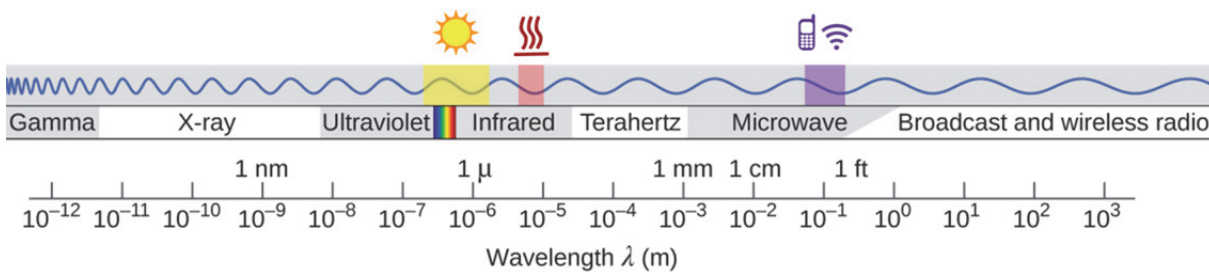
Figure 1:4   The electromagnetic spectrum. Adapted from (OpenStax, 2016).

1.2.1 Low emissivity coatings

In a standard double glazing two third of the heat transfer is due to radiation (Grosse, 1997). Reducing the infrared emissivity of glass would therefore decrease the thermal losses. Low emissivity (low-e) coatings or transparent heat mirrors combine high transparency in visible range (0.4 to 0.8 μm) and high reflectivity in the thermal infrared range (6 to 12 μm). Therefore, these coatings have a low emissivity in the wavelength range where a blackbody at 300 K emits and are able to reduce the thermal losses of a conventional double glazing by almost a factor of two. Figure 1:5 illustrates single, double and triple glazing configurations.
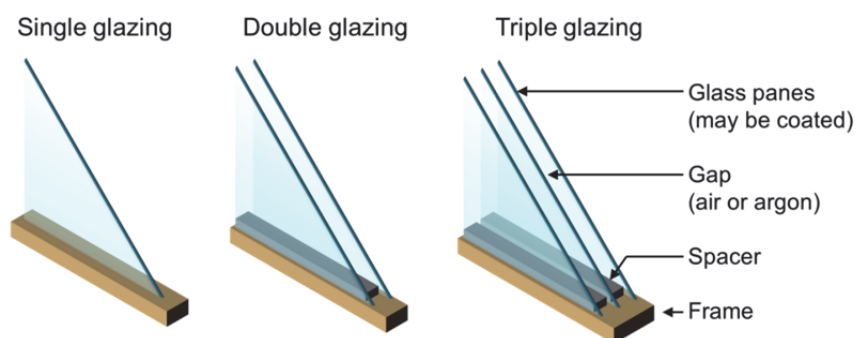

Figure 1:5   Different glazing types. The glass panes may be coated with low-e or solar protection coatings. The gap between the glass panes may be filled with air, argon or other gas.

The variation of emissivity on the thermal performances of a double glazing unit can be evaluated by calculating the U value, or thermal transmittance (in $W.m^{-2}.K^{-1}$) of the center of the glazing, U, according to the standard EN 673 (2011) (eq.(1),(2)):

$$\frac{1}{U} = \frac{1}{h_e} + \frac{1}{h_t} + \frac{1}{h_i} \tag{1}$$

h_e and h_i are the external and internal heat transfer coefficient. h_t is the total conductance of the glazing. The modification of the emissivity of the coated glass ε_2 will impact the radiation conductance h_r which is a contribution to h_t (Bouvard, 2017a). All other parameters were kept constant and as specified in EN 673.

$$h_r = \left(\frac{1}{\varepsilon_1} + \frac{1}{\varepsilon_2} - 1\right)^{-1} \cdot 4 \cdot \sigma \cdot T^3 \tag{2}$$

Figure 1:6 shows the calculated U-value for different configurations of glazing. A double glazing with a low-e coating has a better (lower) U-value than a triple glazing without coating.
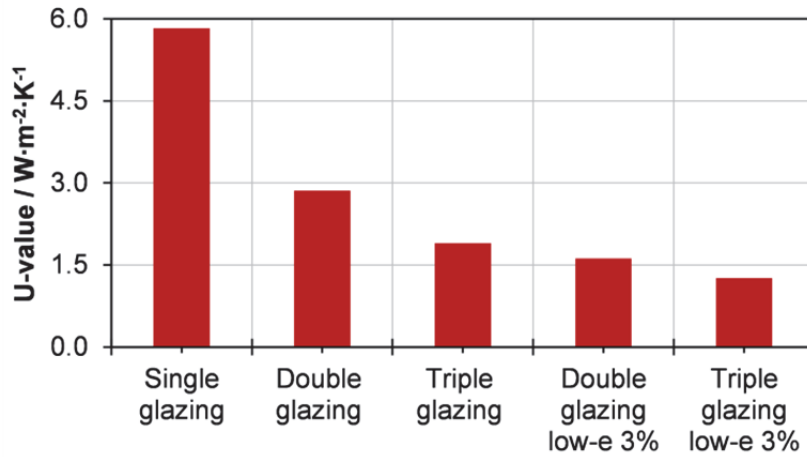
Figure 1:6   U-value calculated according to EN673 for a single glazing, an uncoated double glazing, an uncoated triple glazing, a double glazing with a low-e coating having an emissivity of 3 % and a triple glazing with one low-e coating having an infrared emissivity of 3 %. 3 mm thick clear glass pane(s) and 12 mm air gap(s) were used for all configurations. A double glazing with low-e insulates better than a triple glazing without coating.

In many cases, metals have a low emissivity in the infrared; however their reflectivity in the visible range is too high to be used in architectural glass. Berning and Turner (1957) showed theoretically that a metal film can be induced to transmit a high amount of energy if embedded in carefully selected dielectrics. The thickness and the refractive indices of the non-absorbing dielectrics can be optimized to design an optical band pass filter. Earlier, Gilham (1955) showed that gold films deposited between bismuth oxide films exhibited a high visible transmittance. These coatings were used as a transparent conductor for de-icing windows. Holland (1958) used these bismuth oxide/gold stacks as heat reflective mirror. One of the first industrial applications of transparent conductive oxide was the use of tin or indium oxide on low-pressure sodium discharge lamps to reduce the heat losses (van

Boort, 1968; Köstlin, 1975). In the architectural glass sector, thin-film coatings started to be used to reduce cooling loads. The development and industrial implementation of low emissivity coatings for energy savings windows was boosted by the energy crisis of 1974 (Gläser, 2008). Two types of materials were used for low-emissivity coatings: 1) semiconductors with enough free-carrier concentration to be reflective in the infrared range and a wide band gap to be transparent in the visible range and 2) metal/dielectric stacks. Sn-doped In_2O_3 (ITO) and Sb-doped SnO_2 were investigated (Fraser, 1972; Vossen 1972) and showed very high visible transmission; their reflectivity in the infrared was up to 80-90 %. Silver-based stack were found to have higher infrared reflectivity and therefore lower emissivity in this region compared to semiconductor low-e coating (Fan, 1974). Furthermore, silver-based coatings had better color neutrality compared to gold-based films. The color rendering of the reflected light was and still is an important factor for architectural acceptation of coated glass (Berning, 1983). Building regulations in Europe fostered the demand for low emissivity coatings on architectural glass (Schaefer, 1997; Kugler, 2015).

Nowadays, low-e coatings are commonly deposited by magnetron sputtering. This coating consists of a stack of dielectric and metallic thin films. Generally, there are one to three layers of silver and several layers of non-absorbing dielectrics such as titanium, silicon or tin oxide. The vacuum deposition allows for precise control of the thickness and homogeneity of the coatings. However, these sputtered coatings, also called soft coatings, are easily scratched and must be physically protected (Arbab, 1997): they are used towards the air gap in a multiple glazing unit. Another method to deposit low-e coatings is spray pyrolysis of F-doped SnO_2. It can be installed directly on the production line, the precursors being applied by chemical vapour deposition directly on the hot glass leaving the float line (Aukkaravittayapun, 2006). These pyrolytic coatings, also called hard coatings, are more resistant and the glass can be handled as a regular single glazing. Their solar transmittance and infrared emissivity are higher compared to silver-based coatings.

Since having high reflectivity in the infrared generally imply electrical conductivity, the materials used as transparent heat mirrors can also be used as transparent conductors. ITO is not used anymore for low-e coatings due to the high price of indium (Ellmer, 2012); however, it is still one of the best transparent conductive oxide available today (Ginley, 2010).

1.2.2 Transparent electrodes

Transparent electrodes are required in various fields of application such as flat-panel displays, optoelectronic devices, resistive heating for de-icing, photovoltaics or electrochromic devices (Katayama, 1999; Granqvist, 2007). To exhibit a high electrical conductivity σ (in

S/cm), a material must have a high carrier concentration n (electrons) or p (holes) (in cm^{-3}) and/or a sufficiently high carrier mobility $\mu_{n,p}$ (in cm$^2 \cdot$V$^{-1} \cdot$s^{-1})(Seeger, 1991), eq.(3).

$$\sigma = en\mu_{n,p} \tag{3}$$

where e is the elementary charge in Coulomb (C).

Due to their small effective mass, electrons are considerably more mobile than ions (and also holes), which imply good electrical conductors use electrons as charge carriers (Ellmer, 2012). From eq. (3) both carrier concentration n and mobility μ could in principle be increased to maximize the electrical conductivity σ. However, the absorption of light by free carriers (electrons) limits the carrier concentration in transparent electrodes. In the electrical field of a light wave, the electron cloud forms a collective plasma excitation (a 'plasmon') (Pankove, 1971). The plasma frequency ω_p (in rad$\cdot$s^{-1}) is given by the classical Drude theory as eq. (4).

$$\omega_{p=} \sqrt{\frac{ne^2}{m^* \varepsilon_r \varepsilon_0}} \tag{4}$$

where m^* is the effective mass of the carriers (usually stated in units of the rest mass of an electron, m$_e$ (9.11$\cdot$10^{-31} kg)) and $\varepsilon_r \varepsilon_0$ is the permittivity of the material (in F$\cdot$m^{-1}).

The wavelength of the plasmon and its energy are given by $\lambda_P = 2\pi\hbar/\omega_p$ and $E_P = c\omega_p$, respectively, where c is the speed of light (in m/s) and $\hbar$ the reduced Planck constant (in eV$\cdot$s$\cdot$rad^{-1}) (Ellmer, 2012).

Therefore, the optimization of transparent electrodes should aim to increase the carrier mobility and limit the carrier concentration: the latter is driven by the desired spectral region of transparency. Figure 1:7 a) displays the spectral sensitivity of the human eye for a white illuminant and the solar irradiance from the sun (under AM1.5 conditions). The region of transparency for transparent electrodes will depend on the usage; for display applications, high transmittance in the visible range (400-800 nm) is enough while for photovoltaics or electrochromic electrodes, a high transmittance in the solar range (350-2500 nm) would be preferable.

Various technologies of transparent electrodes exist; Figure 1:7 b) shows the spectral transmittance of some of them, namely: tin-doped indium oxide (ITO), fluorine-doped tin oxide (FTO), single-walled carbon nanotube (SWNT) films, Ag nanowire (Ag NW), aluminum doped zinc oxide (AZO) and a low-e coating $SnO_2/Ag/SnO_2$. Three of these films are single layers oxides: ITO, FTO and AZO, their transmittance decrease around 1200 nm because of the free carrier absorption. The oscillations are due to optical interferences at the substrate/coating interfaces. The spectral transmittance of the Ag nanowires is relatively

flat while the $SnO_2/Ag/SnO_2$ low-e stack has a narrow range with high transmittance. The sheet resistivity and transmittance at 550 nm for the transparent electrodes displayed in Figure 1:7 b) are indicated in Table 1:1.
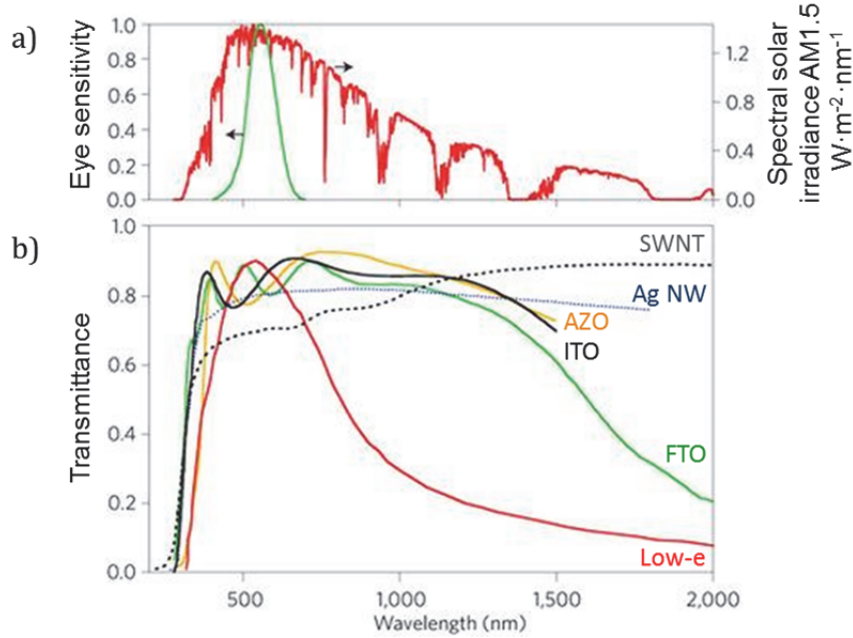

Figure 1:7   a) sensitivity function of the human eye (green) and spectral solar irradiance under the AM1.5 conditions (red). b) Spectral transmittance of different transparent electrodes. Reproduced from (Ellmer, 2012).

		R_s / $\Omega.sq^{-1}$	$\tau(550)$ %
Low-e	$SnO_2/Ag/SnO_2$	7	89.5
ITO	Sn doped In_2O_3	12	82.7
FTO	F doped SnO_2	10	82.7
Ag NW	Ag nanowires	23	79.6
AZO	Al doped ZnO	50	79.6
SWNT	single-walled carbon nanotube	56	69.4

Table 1:1 Sheet resistivities, Rs, and transmittance, τ, at 550 nm of transparent electrodes in Figure 1:7 b). Adapted from (Ellmer, 2012).

For one type of transparent electrode, the transmittance and sheet resistivity can vary; for example, in ITO, the oxygen level can be varied and for metal meshes the thickness can be increased. The carrier concentration will reduce the sheet resistivity at the expense of the transmittance in the visible range. Figure 1:8 b) shows the transmittance of several transparent electrodes against their sheet resistivity. The dashed rectangle indicates the target region of optimal transmittance and sheet resistivity for transparent electrodes.

The transmittance was most often taken at 550 nm; however, this does not provide indication on the width of the transparent region. A better approach would be to use the light and solar transmittance values (see Chapter 3) which are taking into account the full visible range and solar range respectively.
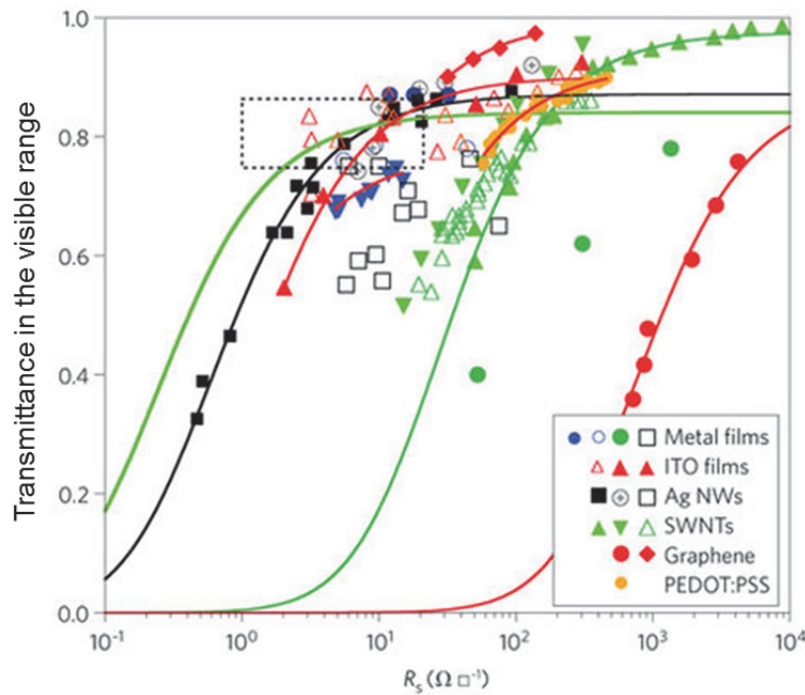
Figure 1:8   Transmittance T in the visible range as a function of the sheet resistance Rs for transparent conductor films. The dotted rectangle marks the T–Rs target region for transparent electrodes. Reproduced from (Ellmer, 2012).

Transparent conductors are a wide area of research fostered by the cost and scarcity of indium. New alternatives such as graphene or nanowires still require attention for industrial implementation.

One side effects of the presence of conductive layers on glass however is that the transmission of the microwaves frequencies used for telecommunications is strongly attenuated. Mobile network reception problems in modern buildings start to arise as metallic frame and reinforced concrete walls also attenuate the frequencies useful for telecommunications (Liikenne-ja, 2013; Asp, 2012; Philippakis, 2004).

1.3   Frequency selective surfaces

The previous section has shown it was possible to achieve visible/infrared selectivity by applying a coating on the glass. Another selectivity step is explored here - infrared/microwave- in order to preserve the thermal properties of metallic surfaces while allowing transmission of the microwaves used for telecommunications.

Frequency Selective Surfaces (FSS) are periodic arrays of elements designed to transmit, reflect or absorb selected electromagnetic fields based on their frequency (Munk, 2000). Typical elements are illustrated in Figure 1:9, they are usually made of a metallic material or cut into a metal sheet. Examples of applications for FSS include the perforated screen on the door of a microwave oven, radomes protecting antennas and selective shielding in military and airport communication.
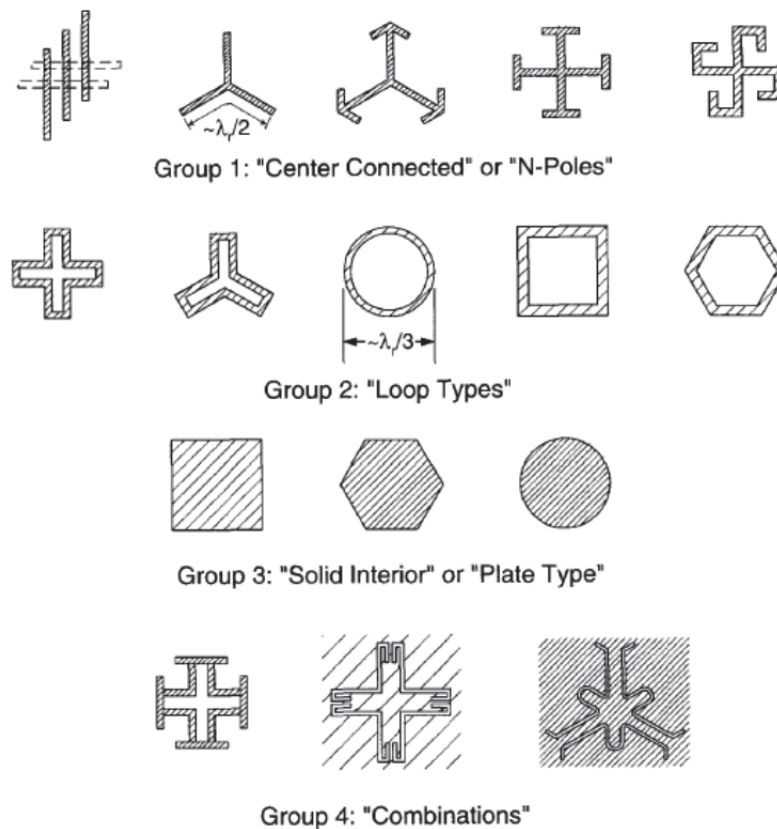
Figure 1:9   Typical elements used in two-dimensional periodic arrays to obtain a frequency selective surface. Reproduced from (Munk, 2000).

Energy saving windows embeds a metallic layer (the low-e coating) and thus strongly attenuates the transmission of microwaves. Table 1:2 gives the shielding efficiency, or attenuation, of common glazing types for three frequencies of interest for the mobile telecommunications: 900 MHz, 1800 MHz and 3 GHz. These results are extracted from the extensive study performed by the National Institute of Standards and Technology (NIST) (Stone, 1997), a study by Asp et al. (2012) and a study from this work (Bouvard, 2017a).

	Material	Source	Shielding effect / dB		
			900 MHz	1800 MHz	3 GHz
Glazing	Glass pane 6 mm	(Stone, 1997)	-0.8	-1.3	-1.9
	Double glazing 4 mm/air 12 mm/5mm	(Bouvard, 2017a)	-0.8	-1.1	-1.2
	Double glazing with commercial low-e 4 mm coated/air 12 mm/5mm	(Bouvard, 2017a)	-30.6	-26.8	-27
	Double glazing with 2 coated glass	(Asp, 2012)	-23	-30	-36

Table 1:2 Comparison of the attenuation of some glazing used in buildings. Adapted from (Bouvard, 2017b).

Widenberg et al. (2002) first proposed a design to improve transmission through the energy saving window pane at defined frequencies (900 MHz and 1600 Mhz). The desired effect was reached by removing narrow slits in a periodic pattern. A patterned conductive coating can be described as a Frequency selective Surface (FSS) (Munk, 2003). Kiani et al. (2009, 2010, 2011) have investigated different patterns and configurations by computer simulations and through experiments. Figure 1:10 a) shows the measurement setup and a glass sample with a FSS. The patterned was performed by milling as depicted in Figure 1:10 b). This 64 mm cross-dipole is highly visible and modifies the aesthetic of the glass. Milling does not remove only the coating but also cut into the glass (Kiani, 2009). This might have an impact on the mechanical properties of the glass. To be accepted in the glazing industry, a FSS glazing should preserve the visual appearance and mechanical properties of the glass pane.

a)   b)
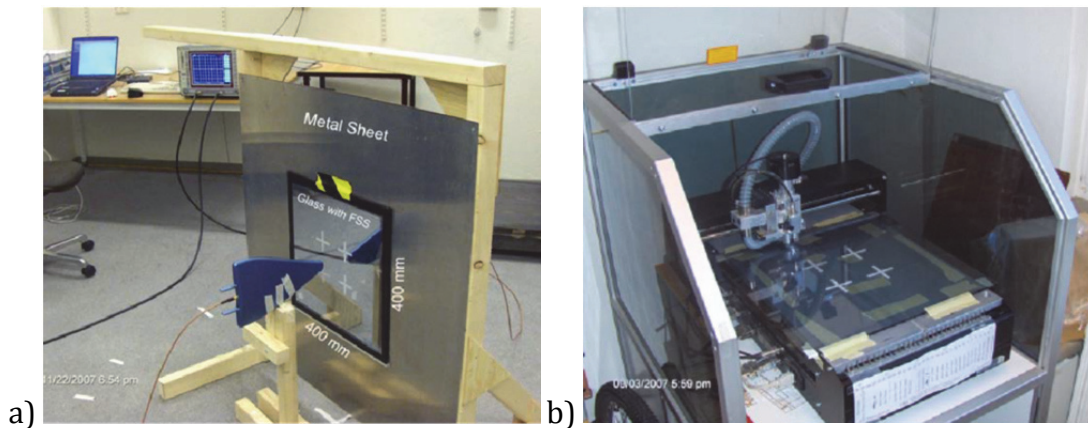
Figure 1:10   a) Measurement setup showing a cross-dipole FSS etched on a glass sample, b) milling machine used to etch the coating. Reproduced from (Kiani, 2009).

Measurements and simulations demonstrated an improvement of the transmission at the desired frequency (Kiani, 2009, 2011). As illustrated in Figure 1:11, the cross-dipole pattern depicted in Figure 1:10 increase the transmission from -27.1 dB to -9.1 dB at normal incidence in TE polarization. It has a width of 8 mm and a length of 64 mm which represent 9.6% of ablated area. Uncoated glass panes have an attenuation of about 1 dB (Stone, 1997) and for a FSS glazing it would be desirable to have the smallest attenuation possible.
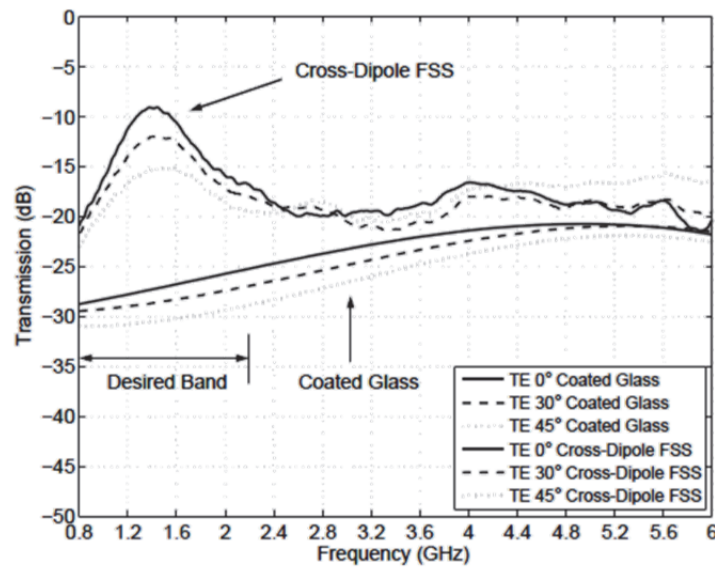
Figure 1:11   a) Measured transmission results of HP Suncool with 2 x 2 cross-dipole etched in the low-e coating by milling. Reproduced from (Kiani, 2009).

The size and shape of the pattern drives its resonance frequency. Another design presented by Ullah et al., which attenuates less than 10 dB, required the ablation of 12.35 % of the coating area (Ullah, 2011a,b). The effect on infrared reflectance and therefore on the thermal emissivity is approximately proportional to the surface of coating removed (Kiani, 2010), which should be minimized.

1.4   Switchable glazing

Low emissivity coatings are now widely used in insulated glazing unit, reducing the thermal losses of windows. Solar protection coatings, specifically designed to reduce the solar heat loads are also used in highly glazed buildings. However, these passive coatings might cut considerable amount of solar gains during the heating season while not providing sufficient reduction during sunny and warm days. To maintain comfortable temperature inside the building, additional blinds or stronger air conditioning are used.

Adaptive facades are able to adapt changing climatic conditions to meet requirements of the occupants' comfort and energy efficiency; they can encompass automated blind, mobile or smart façade elements or switchable glazing.

One approach is to take advantage of the sun altitude depending on the season to redirect the light inside in winter and reject it outside in summer (Kostro, 2015). Another approach is to react to an external stimuli such as UV light for photo-chromic or temperature for thermo-chromic materials (Lampert, 2004). Switchable glazing activated with electricity can be used to complement a building monitoring system in order to actively regulate the indoor temperature and lighting conditions. Technologies of switchable glazing activated by an electrical current includes suspended particle devices (SPDs), polymer dispersed liquid crystal (PDLC), cholesteric liquid crystals (CLC) and electrochromic glazing (Lampert, 2004; Lemarchand, 2018). Technologies based on liquid crystals or suspended particles usually require a voltage to maintain one state (clear or dark) while electrochromic window have an open circuit memory. A current is needed mainly to change state and then only to compensate for self-discharge.

1.4.1 Electrochromic glazing

Electrochromic glazing is able to modulate their optical properties when an electrical potential is applied. Using a control system based, for example, on the indoor temperature, the transmittance of the window can vary to reduce overheating risks leading to energy savings in cooling and an increased thermal comfort. Furthermore, the solar gain is higher in winter for an electrochromic window compared to a glazing with a solar protection coating; additionally, visual comfort can be improved. The advantages compared to blinds are that the view to the exterior is preserved, the switching is silent and less maintenance is needed.

An electrochromic device is generally composed of five layers as depicted in Figure 1:12. A transparent conductive oxide serves as electrode, a cathodic electrochromic oxide acts as the color changing layer, and an electrolyte either liquid, gel or solid, is permeable for the conduction of ions but electrically insulating. A counter electrochromic layer, either not

changing color upon ion insertion or changing complementary to the cathodic electro-chromic layer, and another transparent conductive oxide are completing the device.
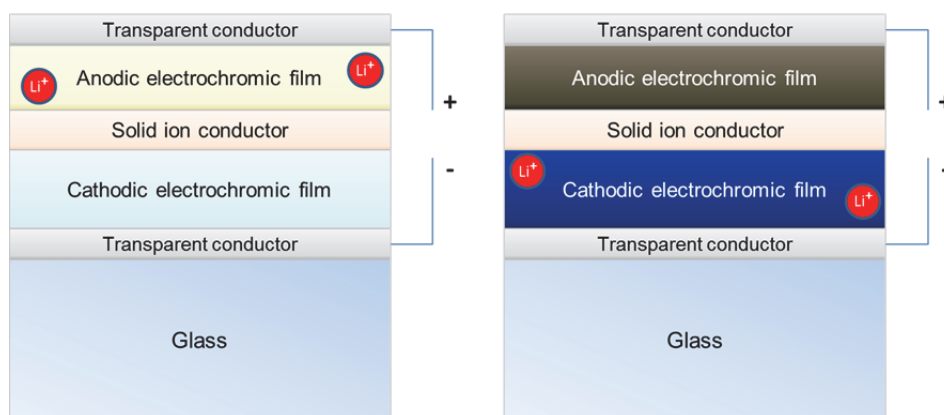

Figure 1:12   Typical five-layer electrochromic device design in bleached and colored state.

Commercial electrochromic glazing is starting to enter the market. The main products are from the following companies: SAGE glass (USA) from the Saint-Gobain group, View Dynam-ic glass (USA), EControl (Germany) and Halioglass/Kinestral Technologies (USA). However, the price of today's electrochromic windows limits their application to prestigious and icon-ic building. Furthermore, existing products still suffer several drawbacks in terms of switch-ing time and contrast, durability or color rendering (Granqvist 2014, Jelle 2012).

1.4.2 Transparent conductors

An essential component of any electrochromic device is the transparent conductor. It should be transparent in a wide range of the solar spectrum while sufficiently conductive to ensure a homogeneous color change. Transparent electrodes were discussed in section 1.2.2. Tin-doped indium oxide (ITO) is still the most common transparent conductive oxide in the industry and was used for the experiments on electrochromic materials of this thesis.

1.4.3 Electrochromic materials

Electrochromism is the alteration of color by passing a current or applying an electrical po-tential; various kinds of materials, called electrochromic materials, exhibit such properties. Frequently, electrochromes are electroactive species which can undergo an electron uptake (reduction) or an electron release (oxidation). For these redox reactions to be possible, a counter electrode with a complementary reaction is needed. The most widely used electro-chromic material is the organic 5,10-dimethyl-5,10-dihydrophenazine used in auto-dimming rear view mirrors developed by the Gentex Corporation (Byker, 2015).

Three types of electrochromes can be described (Monk, 2007 p.7-8). A "type-I" electro-chrome is soluble and remains in solution during electrochromic usage. Aqueous methyl

viologen (1,1'-dimethyl-4,4'-bipyridilium) is one of those. A "type-II" electrochrome is solu-ble in its colorless form but becomes solid on the surface of electrode after the electron transfer. Examples include the cyanophenyl paraquat and heptyl or benzyl viologens. "Type-III" electrochromes stay solid during the reaction. This category includes most of the inorganic electrochromes such as transition-metal oxides.

There are two principle kinds of metal-oxide electrochromes: the one coloring under ion insertion called cathodic and the one coloring under ion extraction, called anodic. Figure 1:13 shows the transition metals whose oxides have well-documented cathodic and anodic electrochromism. Oxides based on vanadium may present anodic or cathodic electrochrom-ism (Granqvist, 1995).

Figure 1:13   The periodic table of elements excepting the lanthanides and actinides. The shaded boxes refer to the transition metals whose oxides have well-documented cathodic (light shade) and anodic (dark shade) electro-chromism. Reproduced from (Granqvist, 1995).

Tungsten trioxide is one of the most widely studied electrochromic (EC) oxide. It can un-dergo a reversible transition from WO_3 to M_xWO_3 tungsten bronzes which display a dark blue color (M can be any atom of the first column of the periodic table: H, Li, Na...) as shown in eq. (5) (Granqvist, 2002).

$$WO_3 + xM^+ + xe^- \rightarrow M_xWO_3$$
transparent   dark blue

(5)

To improve the coloration efficiency, the optically active oxide layer can be modified by doping or substituted by a combination of novel electrochromic oxide materials such as tungsten-containing nickel oxide films (Green, 2014) or nickel containing tungsten films (Valyukh, 2012). Titanium doping was shown to exhibit enhanced durability (Hashimoto, 1991) and to stabilize the highly disorder structure of WO_3 (Ramana, 2013). Mixed oxides of W-D films with D_W being Li, C, N, V, Ni, Nb, Mo, Ru, Sn and Ta have also been studied. Mo-lybdenum oxide has similarities with tungsten oxide. The electrochromic properties of Mo-D films with D_{Mo} being C, Ti, V, Nb and Ce have been investigated (Granqvist, 2015). Work

was also reported on Ti-V and Ti-Zr oxides as well as on Nb-Mo and Nb-Ti oxides (Granqvist, 2015; Ulrich, 2016).

Regarding anodic electrochromic oxides, iridium and nickel were mostly investigated; however, the cost of iridium is too high for most applications (Granqvist, 2014). Mixed binary oxides of Ni-D_{Ni} with D_{Ni} being Li, C, N, F, Al, Ti, V, Mn, Co, Cu and W were studied. One of the reasons to mix Ni oxides with other metals is to improve the visible transmittance in the short wavelengths (Avendeño, 2004), pure nickel oxide being yellowish in the bleached state. Vanadium pentoxide may also be used as an anodic electrochromic layer.

1.4.3.1 Crystalline structures in WO_3

The tungsten trioxide, as many other electrochromic oxides, is commonly arranged in octahedral units. This configuration features spaces between the octahedral units which are large enough to allow the movement of small ions. Figure 1:14 shows possible crystalline structure for WO_3; the dots represent sites where ions can be inserted. It can be observed that the smallest sites are in the cubic structure, then tetragonal structure have an intermediate size, the largest sites being in the hexagonal structure (Granqvist, 1995; Granqvist, 2015). When WO_3 is described as amorphous, it is usually amorphous as seen in X-ray diffraction. Order at smaller dimensions can be present even if the material is not detected as crystalline; nanoporosity and low film density are also beneficial for ion transport (Sun, 2010). The influence of deposition parameters on the nanoporosity will be described in Section 1.4.6.

| Cubic | Tetragonal | Hexagonal |
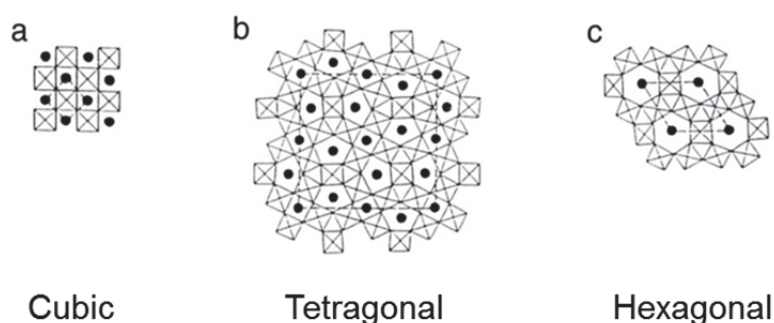
Figure 1:14 W oxide with a) cubic , b) tetragonal and c) hexagonal structure. Dots signify sites for ion insertion in space between the WO6 octahedra. Dashed lines show extents of the unit cell. Adapted from (Granqvist, 1995).

1.4.3.2 Optical absorption in WO_{3-x} and Li_yWO_3

The mechanism responsible for optical absorption of electrochromic oxides is still poorly understood, except maybe for tungsten oxides. It is generally believed to be associated with charge transfer and polaron absorption (Granqvist, 2014). A polaron is a quasi-particle formed by a conduction electron (or hole) with its self-induced polarization in a polar semi-

conductor or in an ionic crystal (Devreese, 1996). The concept of polarons was first pro-
posed by Landau (1933) to describe an electron moving in a dielectric crystal, where the
atoms move from their equilibrium states and screen the charge of an electron, known as a
phonon cloud.

Although defects are present, it is assumed that the main contribution to the optical absorp-
tion is due to the transitions between band states (Berggren, 2007). The intercalation of
ions in tungsten oxide causes the charge-compensating electrons to enter localized states.
The optical absorption can be described as resulting from transitions between occupied and
empty localized conduction band states. The electron localization may be caused by the
electron-phonon interaction (polaronic localization) (Schirmer, 1977) as well as disorder
(Elliott, 1990). Intervalence transfer absorption and small polaron absorption have been
proposed to explain the optical absorption due to localized states (Granqvist, 2015).

Recently, Bondarenko *et al.* (2015) investigated the formation and mobility of polarons in
tungsten oxide in the presence of oxygen vacancies as well as in the presence of intercalated
Li. Figure 1:15 shows the structure of the monoclinic $\gamma-WO_3$ phase without defect (a), with
an oxygen vacancy (b) and with two intercalated Li atoms (c). It illustrates the configuration
where two bound polarons (also called bipolarons) at neighboring sites, $W^{5+} W^{5+}$, can form.
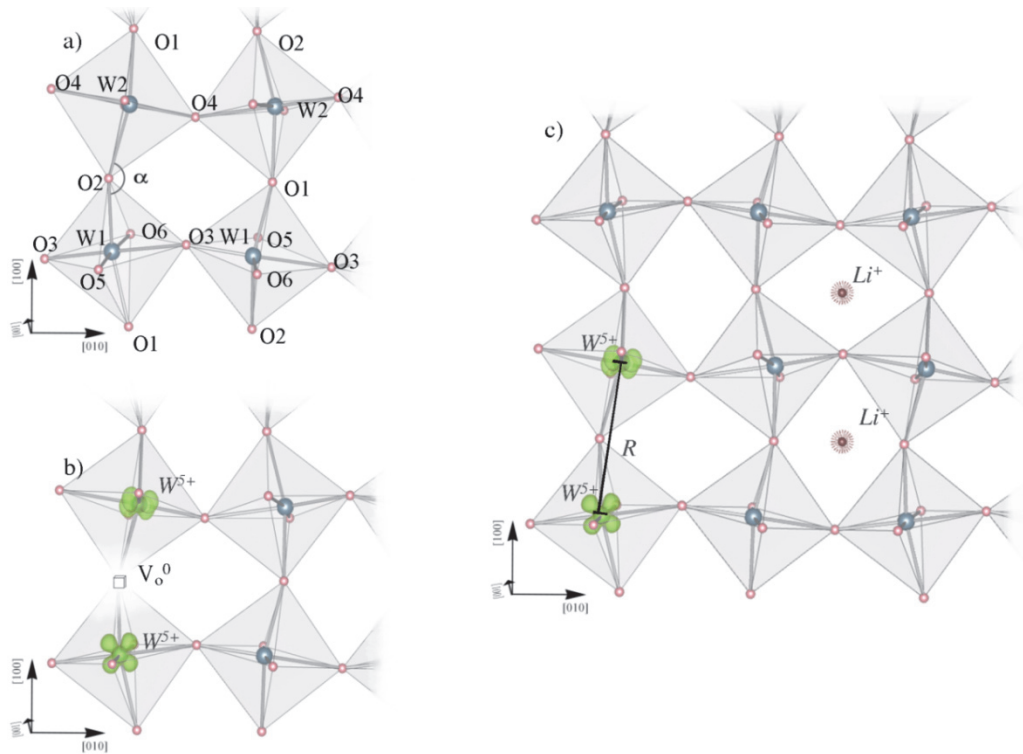
Figure 1:15   The structure of monoclinic $\gamma-WO_3$ phase a) without defect, b) with an oxygen vacancy, and c) with
two Li atoms. Charge distributions are shown for the polaronic W^{5+} states. Reproduced from (Bondarenko, 2015).

They calculated the energy barriers for polaron propagation and studied the relative stability of polarons and bipolarons using a method based on Density Functional Theory (DFT). Their results suggest W^{5+} W^{5+} bipolarons situated along the [001] plane are the most favorable electronic configuration both in the presence of oxygen vacancy or intercalated Li ions. However, in the case of Li intercalation, the energy difference with the case where two separated W^{5+} polarons form is very small. Their results also suggest that the presence of W^{4+} states is unlikely in perfect Li-WO_3 without the presence of structural defects such as vacancies (Bondarenko, 2015).

The polaron absorption is generally the accepted mechanism for optical absorption in crystalline WO_{3-x} and Li_yWO_3. However, it is still debated if this hypothesis can be fully applied to amorphous and highly disordered WO_3. A cluster model based on quantum chemical calculations was proposed to better consider local lattice distortions (Broclawik, 2005; Broclawik, 2006).

1.4.3.3 Electronic structure in WO_3

Crystalline structures of the electrochromic oxides, such as WO_3, can be described by MeO_6 octahedra (where Me denotes metal) with edge-sharing (Granqvist, 1995). In this configuration, the metal d levels are separated from the oxygen $2p$ bands. The octahedral structure leads to a splitting of these d levels into bands usually named e_g and t_{2g}; Figure 1:16 a) depicts the case of a cathodic EC oxide such as H_xWO_3. Pure WO_3 O $2p$ band is full, while d band is empty which makes it transparent. Any similar oxide with a sufficiently large band gap would also be transparent. The insertion of ions and charge balancing electrons would partially fill the d band leading to optical absorption.
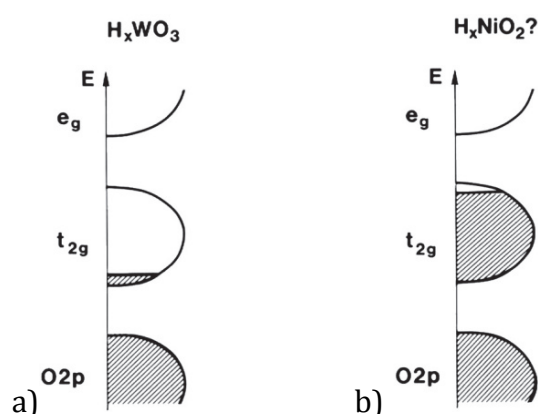
Figure 1:16   Schematic band structures for a) cathodic and b) anodic electrochromic oxides. Shaded regions signify filled states and E denotes energy. Reproduced from (Granqvist, 1995).

1.4.3.4 Electronic structure in anodic electrochromic oxides

For EC devices, it is beneficial to combine an anodic oxide to a cathodic one to achieve better color neutrality and amplitude of modulation. Figure 1:16 b) depict the schematic band structure of an anodic EC oxide, such as H_xNiO_2; anodic EC oxides are characterized by unoccupied t_{2g} states. The insertion of ions would fill these states leading to a band gap between the t_{2g} and e_g levels. The transparency of the material will depend on the width of the band gap.

1.4.4 Electrolytes

Pure ionic conductors, or electrolytes, are needed to separate the two electrochromic layers. Figure 1:17 shows the thermal evolution of ionic conductivity of available lithium solid electrolytes, organic liquid electrolytes, polymer electrolytes, ionic liquids and gel electrolytes for lithium ion batteries. For example, the gel electrolyte 1 M $LiPF_6$/EC–PC (50:50 vol.%) + polyvinylidene difluoride–hexafluoropropylene (10 wt.%) which is used in lithium-ion batteries has an ionic conductivity of 10^{-3} S cm^{-1} at room temperature (Song, 2000; Kamaya, 2011).
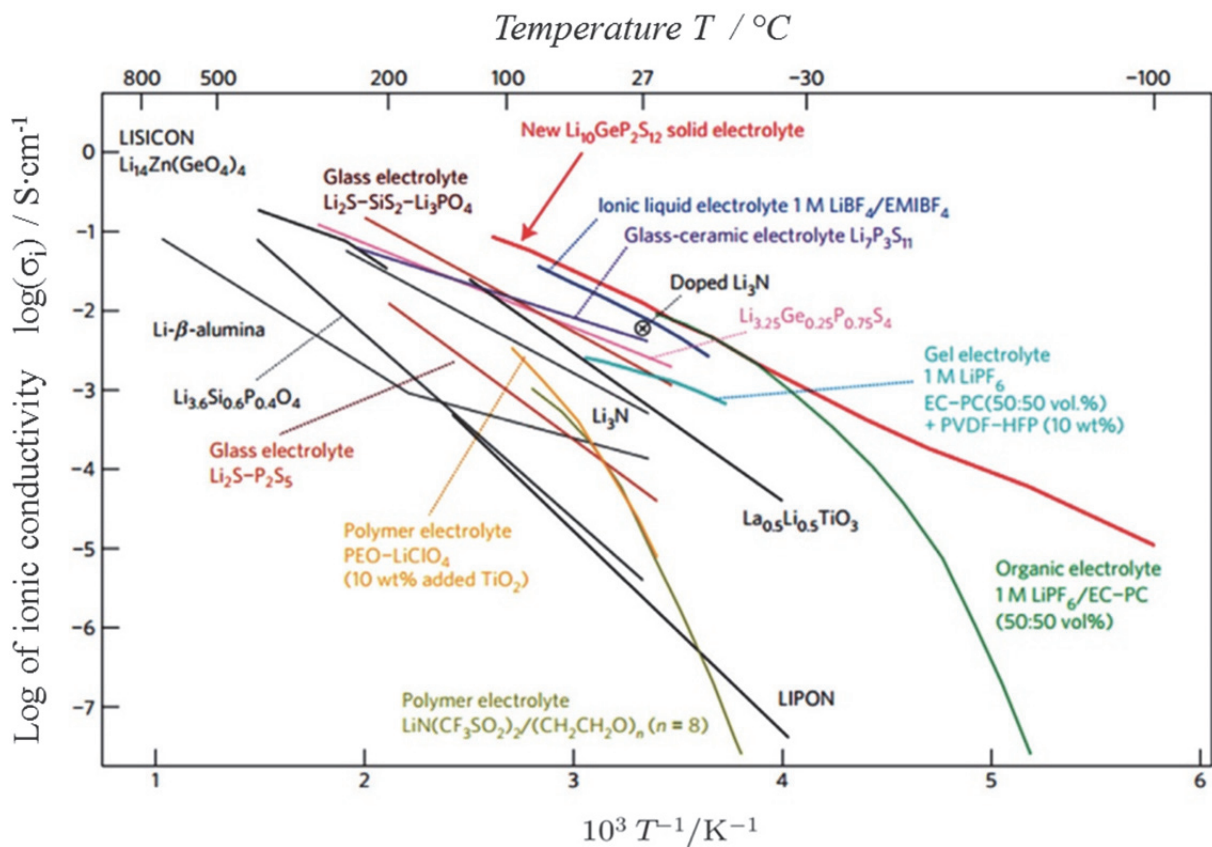
Figure 1:17   Arrhenius plot of available lithium solid electrolytes, organic liquid electrolytes, polymer electrolytes, ionic liquids, and gel electrolytes. Reproduced from (Kamaya, 2011).

The ionic conductivity of lithium phosphate oxynitride (LiPON) at room temperature is lower, in the order of 10^{-5} S.cm^{-1} but it displays an excellent visible transmittance. Another promising solid electrolyte is $(Li_{3x}La_{2/3-x})TiO_3$ (LLTO). It can show Li-ion conductivity as high as 10^{-3} S cm^{-1} at room temperature in single crystals. However, grain boundary resistances often cause a decrease of the ionic conductivity to 10^{-5} S cm^{-1} in sintered LLTO ceramics (Ishikawa, 2018). For solid state lithium batteries, other electrolytes such as $Li_{10}GeP_2S_{12}$ are being developed and aim to compete with liquid electrolytes in terms of ionic conductivity. Experiments on electrochromic materials are often performed using liquid electrolytes: they can be protonic (e.g. KOH) or containing lithium salts (e.g. $LiClO_4$ in propylene carbonate often noted Li-PC). Liquid electrolytes usually have better ionic conductivity than the solid ones; however, their practical use is limited. A window has to endure at the very minimum 20 years and liquid or even gel electrolytes are difficult to maintain in a device for a long time. Figure 1:18 shows an early prototype of electrochromic glazing installed on the LESO experimental building at EPFL. After a few years, the gel electrolyte started to degas creating visible marks on the sides of the glazing.

Figure 1:18   Photograph of an early prototype of electrochromic window using gel electrolyte. This window was installed on the LESO experimental building at EPFL and needed to be replaced after few years of operation. (Photography by A. Schüler)

Solid state electrolytes are attracting increasing interest for electrochemical energy storage technologies (Manthiram, 2017). Polymeric electrolytes are starting to be used in solid-state batteries (Agrawal, 2008) and can also be used in electrochromic devices (Nguyen, 2011). However, the long-term stability of the EC windows is expected to be improved by replacing polymeric electrolytes by inorganic ion conductors (Knauth, 2009). Novel solid-state electrolyte materials with a sufficiently enhanced ionic conductivity can be developed to reduce the switching times of the EC layers (Kamaya, 2011). The requirement for a solid electrolyte is not only a sound ionic conductivity but also a low electronic conductivity.

Table 1:3 shows a selection of inorganic lithium ion conductors used for all solid state batteries. Since electrochromic devices work in a similar manner than all solid state thin film batteries, one can benefit from the expertise and experience from this field.

Short name	Type	Typical composition	RT ionic conductivity S·cm^{-1}	Activation energy eV
Thio-LISICON	Crystalline	$Li_{3.4}Si_{0.4}P_{0.6}S_4$	6.4×10^{-4}	0.5–0.6
LiPON	Amorphous	$Li_{2.88}PO_{3.73}N_{0.14}$	3.3×10^{-6}	0.45–0.55
Garnet	Crystalline	$Li_6La_2BaTa_2O_{12}$	4×10^{-5}	0.4–0.6
Li ion conductor-mesoporous oxide	Composite	$LiI–Al_2O_3$	2.6×10^{-4}	0.4–0.5
NASICON	Crystalline	$Li_{1.3}Al_{0.3}Ti_{1.7}(PO_4)_3$	3×10^{-3}	0.3–0.5
LISICON	Crystalline	$Li_{14}ZnGe_4O_{16}$	10^{-6}	0.4–0.6
LLTO	Crystalline	$Li_{3x}La_{(2/3)-x}\square_{(1/3)-2x}TiO_3$	10^{-3}	0.3–0.4
Sulfide glass	Amorphous	$GeS_2 + Li_2S + LiI + Ga_2S_3$ and La_2S_3	10^{-3}	0.4–0.5

Table 1:3 Summary of inorganic solid Li ion conductor glasses. Reproduced from (Knauth, 2009).

The lithium lanthanum titanates such as LLTO ($Li_{3x}La_{2/3-x}TiO_3$) has also attracted much attention because of its high ionic conductivity (Bohnke, 2008) which is comparable to polymer electrolytes. However, high temperature is necessary to obtain the perovskite crystalline structure. Lithium phosphate oxy-nitride (LIPON) is interesting for electrochromic devices because of its transparency in the solar range (Su, 2016). In addition, it is an amorphous material and can be deposited at low temperature via sputtering. Kovalenko *et al.* (2014) have deposited LIPON by RF magnetron sputtering and studied the effects of deposition parameters on the microstructure.

Recently, Dong et al. (2018) showed that tantalum pentoxide (Ta_2O_5) can operate as a Li^+ ion conductor in an all-solid-state device. Using a metal oxide electrolyte is advantageous because of the low cost and higher deposition rate of metal targets compared to lithium containing targets.

1.4.4.1 Ion conductivity in ceramic electrolyte

In most ionic conductors, the density of mobile ions is substantial and the effect of the ion-ion interactions on the ion dynamics is non-negligible. Disorder and randomness in glassy ionic conductors also complicate the dynamics (Habasaki, 2016). Brownian diffusion does not apply to most ionic conductors of interest and a theory describing the many-ion motion in statistical mechanics is not yet available. Different pathways exist for the ions to diffuse in a crystal. In the vacancy mechanism, ions jump to unoccupied lattice sites; in the interstitial mechanism, ions move from and to a neighboring interstitial site. Usually, this requires a large distortion of the lattice (Habasaki, 2016). Other mechanisms have been proposed

where the diffusion coefficient is proportional to the concentration of ions. In polycrystalline materials, other pathways can be found around grain boundaries or dislocations. Amorphous or glassy materials are usually highly disordered and a wide range of energy barriers may exist.

Regardless of the mechanism involved in the diffusion of ions in the material, the mobile ions have to overcome a potential (or energy) barrier to jump from site to site in the structure (Habasaki, 2016). Therefore the diffusion will be thermally activated and the energy barrier represents the activation energy for ion hopping.

Ionic conductivity can thus be described by an Arrhenius equation as (6) (Arrhenius, 1889).

$$\sigma_i = \frac{\sigma_0}{T} \exp\left(\frac{-E_a}{k_B T}\right) \tag{6}$$

where σ_i is the average ionic conductivity (in S.cm^{-1}), σ_0 a pre-exponential factor, T the temperature (in K), k_B the Boltzmann constant in (eV.K^{-1}) and E_a activation energy (in eV).

The most common method to determine σ_i and E_a experimentally is to perform electrochemical impedance spectroscopy, described in Chapter 3, at various temperatures.

Time-domain nuclear magnetic resonance (NMR) in combination with computational chemistry allow for the characterization of elementary steps of ion hopping and gain a better understanding of ions diffusion pathway through the crystal lattice (Uitz, 2017).

1.4.4.2 Ion transport in a crystalline LiPON

Examples of calculations of energy of migration of lithium ions in solid ions conductors can be found in the scientific literature: Senevirathne et al. (2013), for example, synthetized and studied a crystalline lithium phosphate oxy-nitride compound (Li_2PO_2N). A computational first-principle study by Du and Holzwarth (2010) predicted this stoichiometry to be stable. Its crystal structure has been determined *ab initio* from powder X-ray diffraction data. Senevirathne et al. (2013) computationally studied vacancies and interstitial Li$^+$ defects and their migration energies. On the basis of Nudged Elastic Band calculations they could estimate the activation energy of migration for vacancy to be $0.4 \leq E_m \leq 0.6$ eV for hops to near neighbor vacancy sites and to be $0.8 \leq E_m \leq 0.9$ eV for migration between neighboring interstitial sites. The crystal structure using view of crystal along the chains' direction along with the vacancy and interstitial migration path are depicted in Figure 1:19 a) and c). The migration energy diagram for vacancy are depicted in Figure 1:19 b) and for interstitial in Figure 1:19 d). In this study, the vacancy migration path was energetically more favorable compare to the interstitial one.

Li ion vacancy migration path

Li ion interstitial migration path

grey: Li   black: P   blue: O   green: N
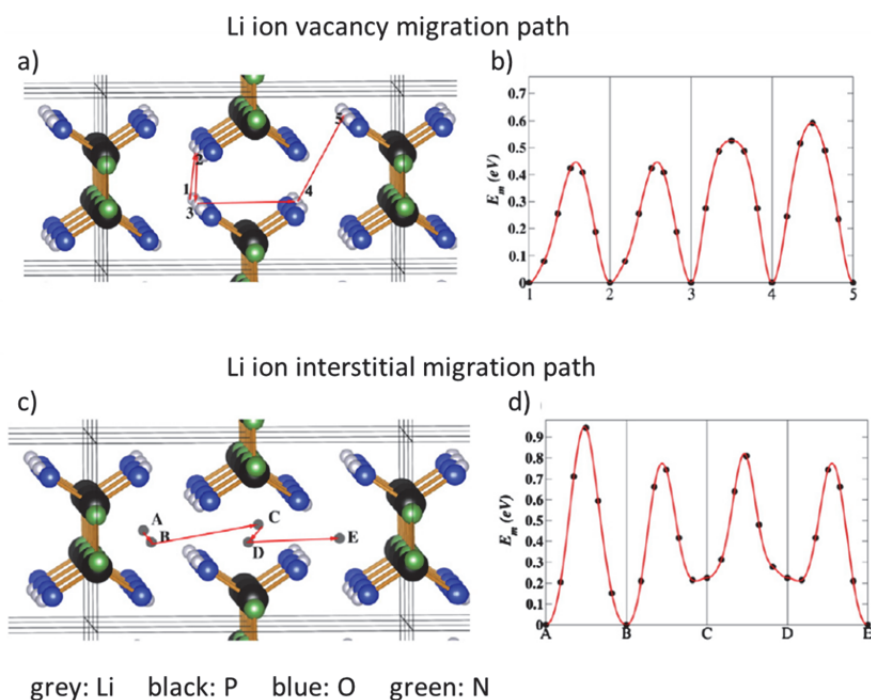
Figure 1:19   Ball and stick diagram using view of crystal along the chains direction of a) possible Li ion vacancy migration path in Li_2PO_2N and c) possible Li ion interstitial migration path in Li_2PO_2N. Migration energy diagram obtained from the Nudged Elastic Band method for b) the vacancy mechanism and d) the interstitial mechanism. Reproduced from (Senevirathne, 2013)

1.4.5 All-solid-state devices

There are various ways to build an electrochromic device: the layers can be organic or inorganic, the electrolyte can be a liquid, a gel, a solid polymer or a ceramic. Figure 1:20 illustrates two different set-up, one polymer-based on a flexible substrate (a) and one based on solid inorganic materials deposited on glass (b).
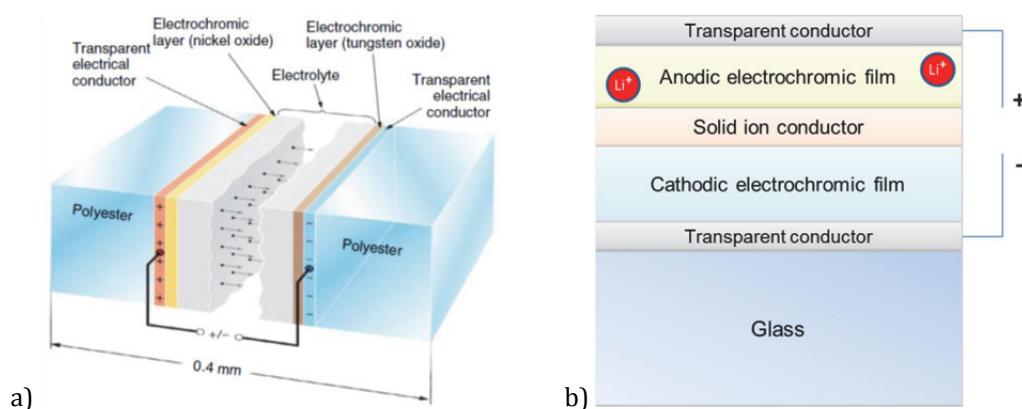
Figure 1:20   a) Principle construction of a foil-based EC device. The tiny arrows indicate ion movement when a voltage is applied between the transparent electrical conductors. The entire foil can be used to laminate glass panes. Reproduced from (Pehlivan, 2014). b) Principle construction of a monolithic EC device on glass substrate.

As seen in section 1.4.4, solid state electrochromic devices are preferable in terms of durability. The monolithic design can be fabricated entirely by magnetron sputtering using ade-

quate targets. This method requires expensive equipment but is already wide-spread in the glass industry (Gläser, 2008); it allows for the use of inorganic materials for each layer including the electrolyte.

Some examples of all solid state inorganic devices can be found in the scientific literature. Oukassi *et al.* (2016) presented results of an electrochromic device using LiPON as an electrolyte. The electrochromic layers were made of WO_3 and V_2O_5 and the contacts made of ITO and AZO/Ag/AZO stacks. They observed that LiPON deposition by sputtering was inserting some Li^+ in the electrochromic oxide. Dong *et al.* (2018) fabricated a full inorganic device: ITO/NiO:(Li, Mg)/Ta_2O_5/WO_3/ITO and succeeded to improve the transmittance in the short wavelength and to avoid the need of a further lithiation step.

The deposition of all solid state devices leads to the question of the interfaces between the thin films. Heterogeneous interfaces are formed between the electrodes and the electrolyte with large charge transfer resistances and may contribute significantly to the resistance of a battery-like device (Song, 2011). The interface between two electronic or ionic conductors typically presents an electric contact potential owing to the equilibration of the electrochemical potential of the mobile charge carrier species at the interfaces (Sze, 1981; Maier, 2004; Weppner, 1999). The alignment of energy levels at the interface will depend on the position of the chemical potential, the initial positions of the energy levels within the two materials and on the formation of an interfacial dipole layer. The alignment of energy levels and the shape of inner electric potential gradient influence the rate of charge transfer at the interface because discontinuities and band bending constitute barriers for charge carriers (Song, 2011).
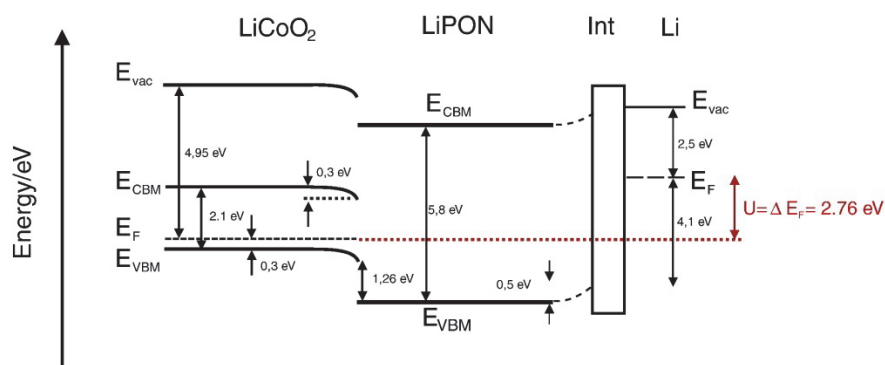
Figure 1:21   Complete energy band diagram of the $LiCoO_2$/LiPON/Li battery stack. Reproduced from (Schwöbel, 2016).

Semiconductor/metal or semiconductor/semiconductor interfaces have been widely studied compared to semiconductor/solid electrolyte interfaces. These interfaces are complex since the chemical potential of the lithium atoms vary during the intercalation process (Laubach, 2009). Schwöbel *et al.* (2016) studied the energy level alignment of a

LiCoO2/LiPON and LiPON/Li interfaces. They could reconstruct the energy band diagram of a LiCoO2/LiPON/Li cell as illustrated in Figure 1:21 using photoelectron spectroscopy and band gap values from the scientific literature.

1.4.6 Deposition methods

1.4.6.1 Thin film deposition

Electrochromic metals oxides can be deposited using a vast number of methods, including chemical and physical vapor deposition and chemical or electrochemical methods; a survey of thin film deposition methods can be found in abundant references such as (Granqvist, 2012) or (Gläser, 2000). As discussed in section 1.2.1, the two methods currently widespread in the glass industry are spray pyrolysis and magnetron sputtering. Spray pyrolysis has to be performed while the glass is still hot, which make it tedious to deposit the three to five layers needed for an electrochromic device. Magnetron sputtering, despite the fact it needs vacuum and therefore expensive equipment, allows for precise control of deposition parameters and reproducibility and is therefore suitable for industrial implementation.

The electrochromic properties of thin films deposited by magnetron sputtering can be extremely various depending on the deposition parameters (Sorar, 2013). Many primary parameters affect the film growth such as target current, voltage, power, substrate distance from target, substrate temperature, working pressure or pulse duration (if pulsed). Structure zone diagrams were proposed to illustrate the common features of films deposited by magnetron sputtering as a function of the deposition parameters. The pressure during sputtering provides an indication on the kinetic energy of the particle colliding on the substrate. At low pressure, the mean free path of atoms ejected from the target is longer as the chances of collisions with another atom are lower. The energy of sputtered atoms is typically in the range of several eV of kinetic energy, which can promote adsorbed atom rearrangement on the surface (Anders, 2010). At high pressure, atoms undergo more collisions with process or reactive gas atoms and have a lower kinetic energy when they reach the substrate.

The Thornton diagram (Thornton, 1974) shows that the film structure is determined mainly by homologous temperature and pressure during deposition. The homologous temperature is defined as the ratio of the film growth temperature on the melting temperature of the material deposited (both temperatures being in Kelvin) (Movchan, 1969). More recently, Anders (2010) proposed an extended zone diagram, illustrated on Figure 1:22, including plasma and ion effects on film growth.
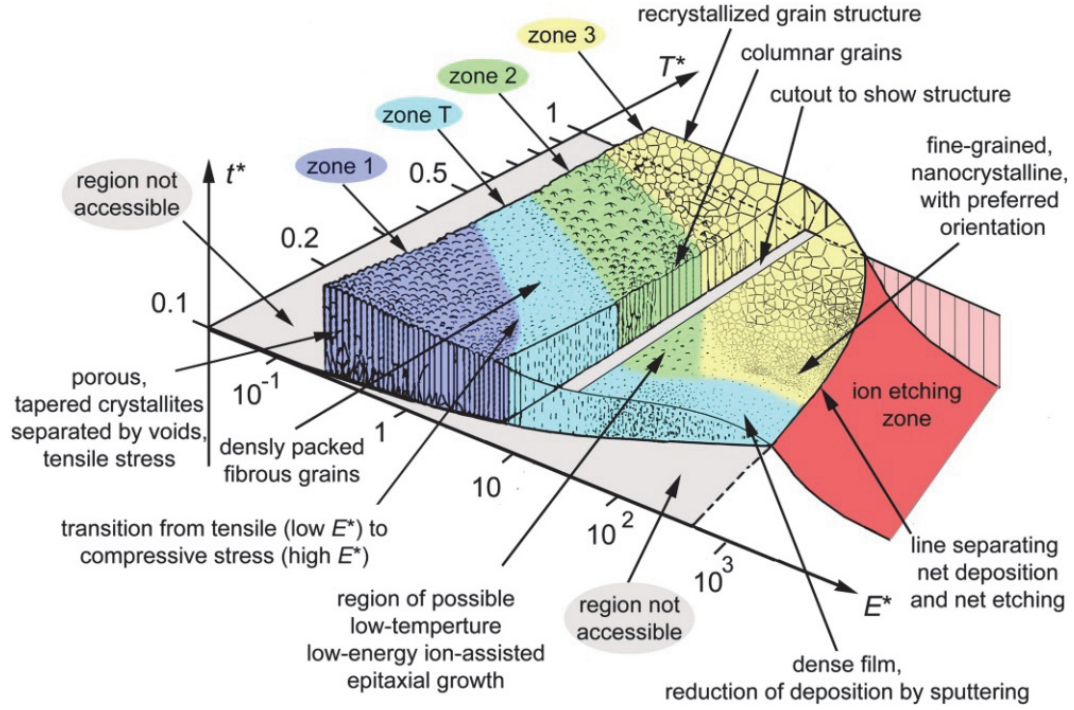
Figure 1:22 Structure zone diagram applicable to energetic deposition. The boundaries between zones are gradual and for illustration only. The numbers on the axes are for orientation only — the actual values depend on the material and many other conditions and therefore the reader should avoid reading specific values or predictions. Reproduced from (Anders, 2010)

The axes of the structure zone diagram proposed by Anders (2010) are:

- The generalized temperature *T** includes the homologous temperature and a temperature increase due to the potential energy of the particle arriving on the surface and can be described by eq. (7).

$$T^* = \frac{T}{T_m} + \frac{1}{k} \sum_\alpha \left(\frac{E_{pot,\alpha} J_\alpha}{N_{moved,\alpha}} \right) / \sum_\alpha J_\alpha \tag{7}$$

where the α subscript represent one of the species arriving, T and T_m are both in Kelvin, k is the Boltzmann constant, E_{pot} is the potential energy in eV, N_{moved} is the number of atoms rearranged and J_α is the energetic ion flux.

- The normalized energy *E** is represented on a logarithmic axis and describes displacement and heating effect due to the kinetic energy of the bombarding particles and can be described by eq. (8).

$$E^* = \sum_\alpha \left(\frac{E_{kin,\alpha}}{E_c} \frac{m_\alpha}{m_s} J_\alpha \right) / \sum_\alpha J_\alpha \tag{8}$$

where the α subscript represent one of the species arriving, E_{kin} is the kinetic energy and E_c is a characteristic energy of the material (e. g. the cohesive energy) both in eV, m_α/m_s is the mass ratio of arriving ions α and atoms on the surface and J_α is the energetic ion flux.

- The net film thickness t* which serve both as a qualitative illustration of the film structure and to indicate the thickness diminution by densification or ion etching. It is usually in nanometers.

From this diagram, we observe that to obtain a porous film, the thermal and kinetic energies should be low (Zone 1). Therefore, high pressure, no substrate bias and low temperatures are preferable for deposition of electrochromic thin films.

1.4.6.2 Lithiation

The color change in an inorganic electrochromic device is caused by Li^+ ions which are intercalated in electrochromic oxides: if these oxides are deposited by magnetron sputtering, lithium has to be added to the device. In research papers, lithiation is often performed in liquid medium, mostly using electrochemical methods in an organic electrolyte containing lithium salts. This wet lithiation process does not permit to deposit all the layers under vacuum in one run, limiting the up-scalability of the method. Furthermore, thorough cleaning has to be performed to ensure no carbon-based material is present in the next steps.

Lithium can be inserted in the electrochromic devices through other means. Lin *et al.* (2013) obtained $Li_{2.34}NiZr_{0.28}O_x$ films by co-sputtering of Ni–Zr alloy (80–20 at.%) and Li_2O. Recently, sputtering of targets alloyed with lithium was proposed by Dong et al (2018). They used Ni and Li:Mg target in co-sputtering to deposit a lithiated Ni:Mg oxide. This method has the advantage to avoid Li-containing ceramic target, which are known for slow deposition rates. However, Li_2O and Li:Mg targets are corrosive and highly sensitive to moisture; they have to be handled under dry protective gas. Therefore, it requires the sputtering machine to be equipped with a glove box with inert atmosphere. The use of a dry lithiation method permits to investigate lithiated compound without the inconveniences of a controlled atmosphere.

Previously, Ashrit (1993) suggested the use of $LiNbO_3$ powder to perform dry lithiation. In his publications (Ashrit, 2001; Beydaghyan, 2008), $LiNbO_3$ powder was heat treated in a tungsten boat under vacuum and gave off lithium atoms which could diffuse in the bulk of the electrochromic oxides. Colorations similar to those obtained by wet lithiation were obtained.

Some industrial applications use vapor of cesium, potassium, sodium, rubidium, and lithium. SAES Getters developed and patented alkali metal dispensers capable of producing lithium vapors some decades ago (Paolo, 1972). Nowadays, these dispensers are used, among other, in the Organic Light Emitting Diode (OLED) industry. These dispensers should be stored in dry air but can be manipulated in ambient air with for short period of time. Fur-

thermore, the powder being enclosed in the dispenser, only limited and usual precautions are necessary to work safely with this material. In this work, such lithium dispenser from SAES Getters were used, more details are given in Chapter 3 and 7.

1.4.7 Nanostructured coatings

The electrochromic coloration involves charge transfer and intercalation of ions. Therefore, the performance of an electrochromic device is commonly limited by the rate of electron conduction, as well as the ion transport in the electrolyte, the EC materials and at their interfaces (Xiong, 2015). The kinetics of charge transfer is therefore an essential aspect of the performance of the electrochromic device. Nanostructured materials have a large specific surface area and limit the charge transport distance in at least one dimension. The nanostructure of electrochromic materials or devices may facilitate ion transport through nanoporosity or even shift the optical band gap of the material to improve the color neutrality.

Numerous examples of nanostructured electrochromic materials can be found as recently surveyed in (Xiong, 2015); they mainly encompass organic electrochromes such as nanopatterned polymer layers or Prussian blue nanoparticles. Studies on nanostructured transition metal oxides are less abundant, especially when looking at materials deposited by magneton sputtering.

A nanocomposite of Ta_2O_5:WO_3 was fabricated by co-sputtering by Shim *et al.* (2006). They evaluated the performance in acidic conditions with liquid electrolyte where H^+ was the intercalating ion. Proton conduction property was improved and the roughness induced by cycling was reduced. Gillaspie *et al.* (2010) studied nanocomposites of tungsten doped nickel oxide with lithium oxide. Their $Li_{1.2}NiW_{0.1}O_x$ film exhibits a slight spectral shift and is significantly more transparent in the bleached state relative to tungsten-free film. Lin *et al.* (2013) also studied tungsten-doped nickel oxide. Furthermore, they investigated nanocomposite of nickel oxide containing Zr and Li. Transparency, especially in the short wavelengths, was improved compared to tungsten-doped films of the same study. Furthermore, the stoichiometry could be varied to obtain a better understanding of the electrochromic effect in those nanocomposites.

Chapter 2   Thesis   structure   and hypotheses

The topic of glazing can be approached by various disciplines such as architecture, civil engineering or materials sciences. In this doctoral thesis, the possibility to modify the features of glazing using coatings with electronic and optical properties tailored to the application is investigated.

2.1   Thesis statements

2.1.1 Study the interplay of electronic and optical properties

The aim of this work is to tailor the properties of coatings in order to adapt them to the required needs. The latter can be modified during their deposition by varying the process parameters such as the total working pressure to change the morphology and the process gas or target materials to adjust the chemical composition. Coatings can also be modified after their manufacturing; it can be by evaporating lithium onto them to adapt their stoichiometry and by laser ablation to alter their electrical conductivity.

Numerous methods can be used in order to investigate how the modification of the deposition process or the post-treatment of the coatings vary their properties. The electronic structure is studied by photoelectron spectroscopy; X-ray photoelectron spectroscopy provides indications on the chemical environment of the atoms by studying the chemical shift of their core-level spectra. UV photoelectron spectroscopy provides information on the valence band edge of the material and its work function, which can be related to the electron flow and the optical properties of the device. The electrical properties of semiconductors influence the optical and thermal properties; sheet resistivity is determined using four-point probe measurements. The optical properties are investigated using spectrophotometry and ellipsometry to determine the solar direct transmittance, the light transmittance, the color coordinates and the refractive indices of materials. Thermal properties, such as emissivity, are determined using Fourier-transform infrared spectroscopy. The switching behavior of the electrochromic material and devices is studied using electrochemical meth-

ods. Electrochemical impedance spectroscopy and chrono-amperometry associated with spectrophotometry can be used to evaluate the coloration efficiency and the switching time. The morphology and the structure of the films can have an impact on the electrochromic properties and are investigated by X-ray diffraction and scanning electron microscopy.
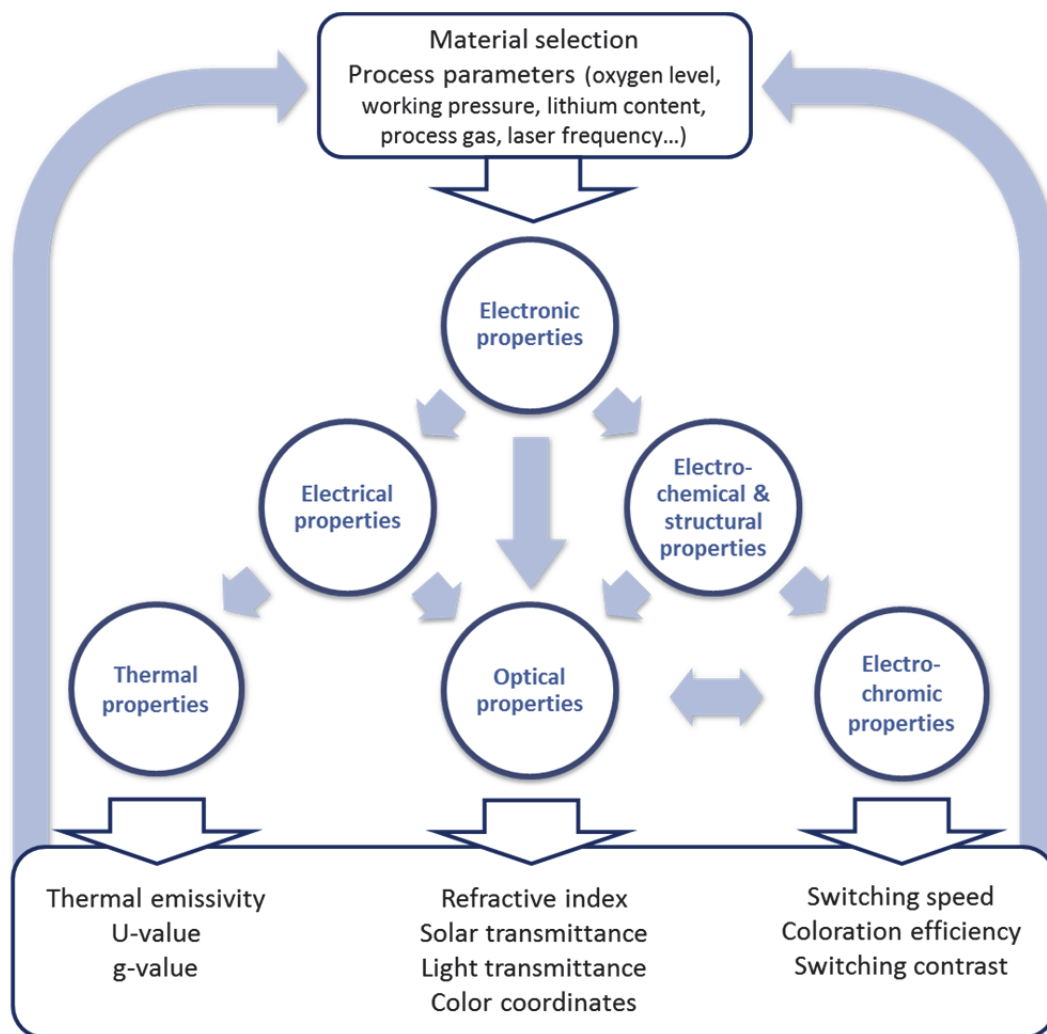
Figure 2:1   Schematic representation of the interplay between the various properties of a material.

Figure 2:1 shows the numerous interrelated properties of materials. The optical spectra of materials can be interpreted in terms of electronic transitions between energy levels, where the width of the bandgap can reveal the color of a semi-conductor (Cohen, 2012). Similarly, the band structure can explain a high electrical conductivity by the presence of delocalized electrons. These electrons are also the origin of the high reflectance of metals in the infrared range leading to a low surface emissivity. The electrochemical properties of ionic conductors are often due to the presence of defects and are constrained by the electronic and crystal structure (Nakamura, 2017). In electrochromic metal oxides, intervalence transfer absorption and small polaron absorption have been suggested to explain the optical absorption due to localized states (Granqvist, 2015; Bondarenko, 2015).

Therefore, understanding how the properties of a material are altered, when the process parameters are varied, permits to adapt those properties in order to obtain the most appropriate coatings for a specific application.

2.1.2 Glazing with double selectivity

On one hand, low-e coatings are spectrally selective, because they have high transmittance in the visible and high reflectance in the mid-infrared range. This reflectance in the mid-infrared (IR), responsible for a low IR emissivity and improved thermal performances, also lead to a strong attenuation of the microwaves used for telecommunications. On the other hand, frequency selective surfaces can be designed so that a metallic sheet becomes transparent to selected wavelengths. One of the investigations of this thesis is to develop a new coating that would combine both benefits: it would be transparent in the visible range, have a low emissivity and a high transmittance for microwaves. The principle of this new coating is described in Figure 2:2.
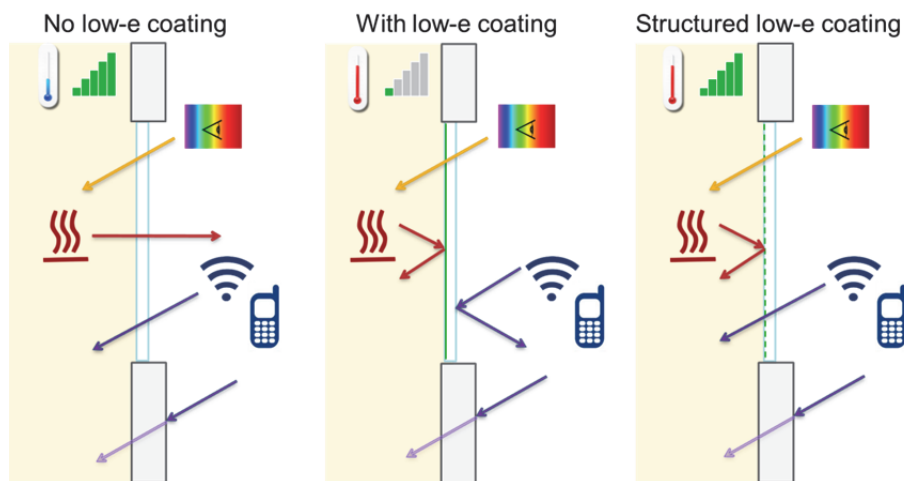
Figure 2:2   From left to right: double glazing without low emissivity coating, Double glazing with a low emissivity coating (low-e) applied on one glass pane, double glazing with double selectivity.

On the left, a first case with an uncoated double glazing is depicted: the average U-value is 2.9 $W.m^{-2}.K^{-1}$. The window is not well insulated, the inside pane is cold in winter and can generate discomfort. Radiofrequencies waves are almost not attenuated through the windows. The second case is a double glazing with a low-e coating applied on one glass pane: the average U-value is 1.6 $W.m^{-2}.K^{-1}$. The losses by infrared radiation of the glass pane are reduced; the thermal comfort is improved and large energy savings are obtained. However, the metallic coatings strongly attenuate the radiofrequency wavelengths used for communications. Building materials can also attenuate radiofrequency depending on their composition and thickness. The third case displays the desired coating having a low IR emissivity and a high transmittance for microwaves.
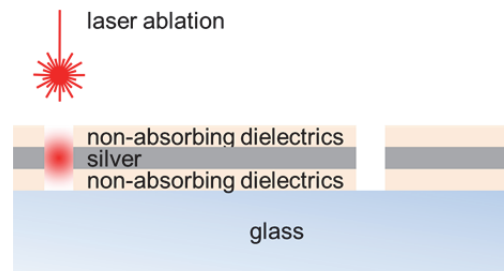
Figure 2:3   Horizontal and vertical structuration of the coating (not to scale).

As described in Chapter 1, the selectivity in the visible/infrared range is usually obtained by depositing a stack of non-absorbing dielectrics and silver layers on the glass surface; besides, it is possible to pattern a metallic coating to modify its transmission to microwaves. Therefore, one of the research questions of this thesis is:

- Is it possible to create a coating having a high transmittance in the visible range, a high reflectance in the infrared range and a high transmittance in the microwave range while preserving the visual aspect?

The hypothesis of this work was that the double selectivity could be achieved by combining a horizontal and vertical structuration of the coating, as illustrated in Figure 2:3. Laser ablation was chosen to modify the low emissivity coatings by producing very fine ablated lines. The parameters of the pattern are optimized to obtain the lowest attenuation of microwaves while preserving the thermal and visual properties of the glazing.

2.1.3 Novel materials for electrochromics

Electrochromic windows can modulate the solar gain passing through the glazing according to the need of the building. Commercial products are reaching the markets, but some drawbacks still need to be tackled. Most electrochromic windows produced in Europe contain a gel electrolyte. Gels are organic materials and are difficult to seal in a glazing for the lifetime of a building, as illustrated in Figure 1:18. Inorganic electrolytes offer a more durable alternative. However, inorganic electrolytes have usually a lower ionic conductivity than liquid or gel counterparts, therefore new materials and methods must be investigated to improve the switching speed of all-solid-state inorganic devices. The effect of nanoporosity is investigated to reproduce the porosity existing in liquid devices. Furthermore, current electrochromic windows have usually a lower solar transmittance and color neutrality in the bleached state than common low-e coatings. Higher solar transmittance in the bleach state could increase the solar gains in winter, when they are needed. Besides, color neutrality is important for the acceptation of the system by the building occupants. Nanocomposite materials using alloy targets or co-sputtering are envisaged to improve these aspects.
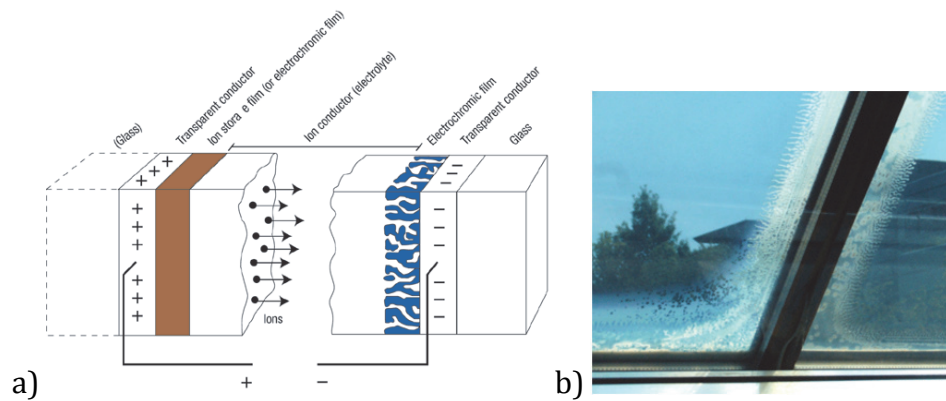
Figure 2:4   a) Schematic illustration of an electrochromic device with a liquid electrolyte. Reproduced from (Granqvist, 2006). b) Photograph of an early prototype of electrochromic window using gel electrolyte. This window was installed on the LESO experimental building at EPFL and needed to be replaced after few years of operation (Photography by A. Schüler). In this study, inorganic solid electrolytes are envisaged to overcome this problem.

This thesis aims to answer the following research questions:

- Is it possible to deposit a top transparent conductive electrode without damaging the underlying layers, having low sheet resistivity and high solar transmittance?

- Is it possible to create nanocomposite layers to improve the color properties and switching dynamics of an electrochromic device ?

- Is it possible to deposit a LiPON electrolyte with sufficient chemical stability in air by magnetron sputtering?

- What are the optical properties of LLTO and is it sufficiently transparent for electro-chromic devices?

- Can a porous metal oxide be a suitable lithium ion conductor in an all-solid state de-vice?

- Is it possible to lithiate an all-solid state device without using a liquid bath, or mate-rials highly sensitive to humidity, with the sample remaining in vacuum?

- Is it possible to produce an all-solid-state device entirely in vacuum mainly from me-tallic sputtering targets to facilitate manufacture?

Novels materials and methods are investigated in order to develop electrochromic devices with an inorganic and solid electrolyte, with better color neutrality in the bleached state and suitable switching dynamics. Experiments are performed in order to determine if na-noporosity have a positive impact on the switching dynamics and contrast and to see if dop-ing and nanocomposite layers can improve the optical properties of the film and the ease of

manufacturing. Additionally, this should provide a better understanding of the limiting factor in the switching dynamics.

Since electrochromic devices have numerous similarities with thin film batteries, electrolytes which are of special interest in the context of batteries are studied e.g. lithium phosphate oxy-nitride films (LiPON) and lithium lanthanum titanium oxide (LLTO) compounds. The motivation is to determine if these electrolytes would be suitable for electrochromic glazing. Furthermore, tantalum pentoxide coatings are studied with the aim to understand if a porous metal oxide can be used as a solid electrolyte.

In a solid-state electrochromic device, one challenge is to incorporate lithium without the need for a liquid bath or the use of lithium compounds highly sensitive to humidity. Intercalation of lithium from the evaporation of lithium dispensers is investigated; this would allow the deposition of the multilayers coating for the preparation of the electrochromic device entirely in vacuum.

Furthermore, the ease of manufacture, which has a great impact on the cost of electrochromic windows, is considered. Deposition of the coatings without substrate heating is easier in large scale coaters and reduces the energy needed to manufature the device. Additionally, the use of metallic targets allows faster deposition rates compared to ceramic target and especially lithium containing ceramic target. Non-magnetic targets are also preferred for a better control of the magnetron sputtering process.

2.2   Stucture of the thesis

This thesis explore the field of advanced glazing regarding questions relative to the transmission of the microwaves used for telecommunications and to new electrochromic materials for the control of solar heat gains. The following structure was adopted:

- Chapter 1: A state of the art explaining the basic principles of spectrally selective glazing, frequency selective surfaces and switchable glazing is presented. It describes the key materials needed to produce an electrochromic glazing and present the current challenges.

- Chapter 2: The hypothesis of the thesis regarding the interplay of the electronic and optical properties are explained and the envisaged approach to improve the transmission of microwave through coated glazing and to improve electrochromic materials and devices are presented.

- Chapter 3: The experimental methods used for the samples preparation, such as magnetron sputtering deposition and laser ablation, are described. The characterization and analysis methods used to determine the electromagnetic, optical, electrochemical and electronic properties of the studied materials are presented for a better interpretation of the results.

- Chapter 4: The transmission of low-emissivity coatings to microwaves is studied and a method to improve it is investigated. Results in terms of microwaves attenuation, as well as thermal and optical properties, are presented. The possible applications of this new technology are discussed. Then, in order to produce all-solid-state devices, transparent coatings are studied to serve as a top electrode. Suitable parameters for deposition at room temperature are determined.

- Chapter 5: The influence of the process parameters on morphology, optical and electronic properties of cathodic and anodic electrochromic oxides is investigated. The determined parameters are used to deposit electrochromic oxides to be assembled in a liquid electrochromic device with the aim to study its switching dynamics and contrast.

- Chapter 6: Materials that could be used as solid electrolytes, such as lithium phosphate oxy-nitride films and lithium lanthanum titanium oxide compounds and a porous metal oxide, are investigated. From this study, a solid ion conductor is chosen to produce all-solid-state devices.

- Chapter 7: A method was developed to introduce lithium in the electrochromic device in vacuum. This method and its impact on the electrochromic coatings are described and used to produce all-solid-state devices along with the previous results. The switching dynamics and contrast are evaluated along with the color rendering of the transmitted light.

- Chapter 8: The achievements and challenges of this work will be discussed opening the way to future research.

Chapter 3   Experimental methods and numerical analysis

This chapter describes the methods used in this work for thin film preparation and to characterization. A wide variety of characterization techniques were employed in order to determine the electromagnetic, optical, thermal, electrochemical, electronic as well as structural properties of the thin films. Numerical methods used to analyse the data and assess relevant factors are described.

3.1   Sample preparation

3.1.1 Magnetron sputtering

In the basic direct current (DC) sputtering process, a voltage is applied between the cathode, carrying a target, and the anode, carrying a substrate. A flow of gas, such as argon, is ionized generating glow discharge plasma. The energetic ions impact the target and remove atoms from it which may condense on the substrate. This process also emits secondary electrons which are playing an important role by maintaining the plasma (Rossnagel, 1995).

Magnetron sputtering was developed to improve the basic DC sputtering process. The magnets placed below the target helps to trap the electrons. It results in an increase of the probability of an ionising electron–atom collision, thus, the plasma is denser and the sputtering rates are higher. If an additional gas is added in the deposition chamber in order to react with the atoms ejected from the target, the process is called magnetron reactive sputtering. In some conditions, the surface of the target will start to oxidised and causing electrical arcs and defects in the film. In order to avoid the surface charging due to this insulating layer, pulsed deposition with a medium-range frequency (10-250 kHz) is used. Figure 3:1 illustrate the principle of DC bipolar-pulsed sputtering: τ_{ON} is the time fraction during which the sputter deposition takes place and τ_{OFF} is the time during when the voltage is reversed to remove the accumulated charges (usually in nanoseconds).
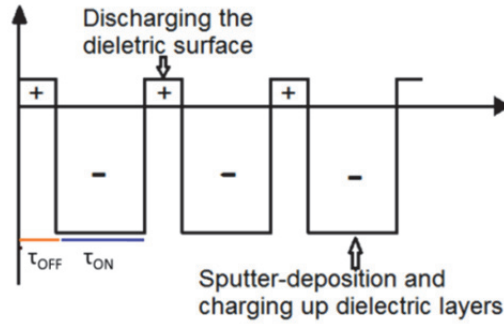
Figure 3:1   DC-bipolar pulsed duty cycle (adapted from Belkind, 2000).

The duty cycle, defined as eq. (9) (Belkind, 2000), can be modified by varying the frequency for a fixed τ_{OFF} or by varying the ratio τ_{ON}/τ_{OFF} for a given frequency. Unless otherwise stated, the frequency used for DC-bipolar pulsed (DC-p) sputtering was 250 kHz with τ_{OFF} = 496 ns which means a duty cycle = 87.6 %. Alternative current with a medium frequency (MF) power supply can also be used.

$$Duty\ cycle = \frac{\tau_{ON}}{\tau_{ON} + \tau_{OFF}} \tag{9}$$

DC, MF and DC-p sputtering are generally controlled for a given power. The repartition of the voltage and the current provides information on the state of the target in reactive sputtering. This variation in voltage is accompanied by a change in deposition rate which can be monitored using a quartz balance. The oscillation frequency of a crystal placed in a vacuum chamber will vary as its mass increases during deposition. An instrument can monitor this frequency change and convert it to deposition rate given a density and some calibration parameters. Figure 3:2 illustrates variation of the discharge voltage and of the deposition rate as the oxygen partial pressure increases for the case of Zr sputtering in O_2-Ar (Venkataraj, 2002). When oxygen flow increases, the coating deposited goes from metallic to oxidized; however, if a thick layer of oxide forms onto the target, then the deposition rate drops. The occurrence of arcs results in poor process stability and lowers the quality of films due to target poisoning. Process parameters should be chosen in the transition zone.
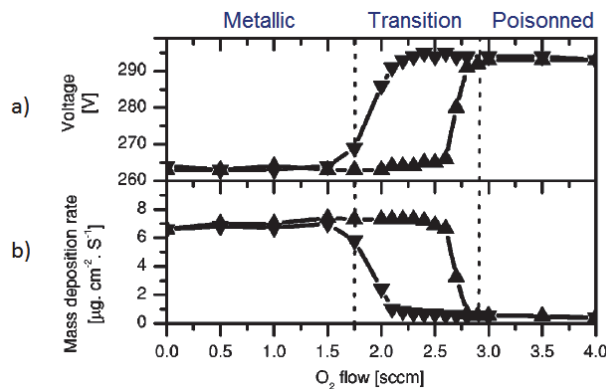
Figure 3:2   Effect of oxygen flow on the a) target voltage and on b) deposition rate during the reactive magnetron sputtering of Zr-O2/Ar (Venkataraj, 2002).

For electrically insulating materials, such as ceramic targets, AC modulation of the power at radio-frequencies (RF 13.56 MHz) is used. RF sputtering usually yields high quality films but with a very low deposition rate. Furthermore, the scale up of RF systems is more complex than DC, DC-p or MF sputtering (Kelly, 2000).

Figure 3:3 a) shows the interior of the deposition chamber used for this work. It comprises five magnetrons in a sputter-up configuration which can be used simultaneously. Argon gas is fed next to the target and the reactive gas (oxygen or nitrogen) are fed next to the sample. In order to obtain good homogeneity (e.g. better than five nanometers on a sample with a diameter of ten centimeters), the sample rotates during deposition and its height can be adjusted. DC, pulsed-DC (MF) and RF power supplies are available for each target. The transfer chamber was equipped with a laminar flow hood (Figure 3:3 b)) to reduce the amount of dust particles on the substrates. It is similar to systems used in clean rooms and allows a net reduction of pinholes in solid state devices.

a)   b)
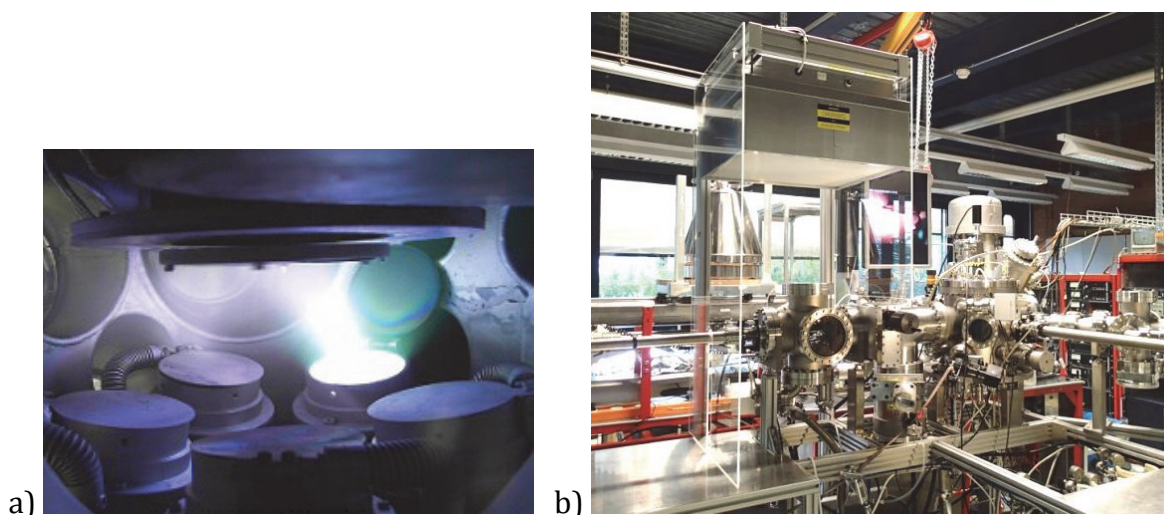
Figure 3:3   Photograph of a) the interior and b) the exterior of the sputtering chamber. A laminar flow hood is installed above the transfer chamber to avoid dust particles on the substrates.

Cylindrical targets with a diameter of 50.8 mm are used in this chamber. This size is common for laboratory scale equipment. In the glazing industry, the glass substrate are usually 3,21 m wide - 6,0 m long and large cylindrical cathodes are then used.

The following targets were used in this study:

- ITO (Kurt J Lesker 99.99%)
- W (Kurt J Lesker 99.95%)
- Ni-V   93-7 wt% (Testbourne 99.95%)
- Ni (AJA, 99.99%)
- Ni-Ta   91-9 at% (AJA, 99.9%)
- Li_3PO_4 density 2.35g/cc (Kurt J Lesker 99.95%)

- LLTO $Li_{0.5}La_{0.5}TiO_3$ (IZTech university)
- Ta (Testbourne 99.99%)
- Al (AJA 99.999%)

The targets were pre-sputtered in order to remove traces of surface oxidation for at least 5 minutes; meanwhile, the sample was protected by a shutter. Then a conditioning step was performed with desired process parameters for at least 10 min with the sample still behind the shutter. Argon, oxygen and nitrogen with a purity of 99.999 % were used as process and reactive gas. The gas lines were purged at least two times before deposition.

Silicon wafers, ITO glass or glass slides were used as substrate. Pieces of silicon wafers were used "as received" while ITO and regular soda lime glass slides were cleaned in isopropanol in ultrasonic bath and dried with nitrogen. Metallic masks and kapton® tape were used to maintain the substrates on the substrate holder and delimitate the area to be coated.

As illustrated in Figure 3:4, the sputtering chamber is connected to a transfer chamber in which a lithium dispenser was installed. The chamber is also connected to the XPS/UPS chamber (more details in section 3.5) via an intermediate chamber. Samples can be measured in-situ, as-deposited or lithiated, as well as ex-situ following a cleaning with the argon ion sputter gun. The sample can be transferred in vacuum from one chamber to the other using magnetic rods.
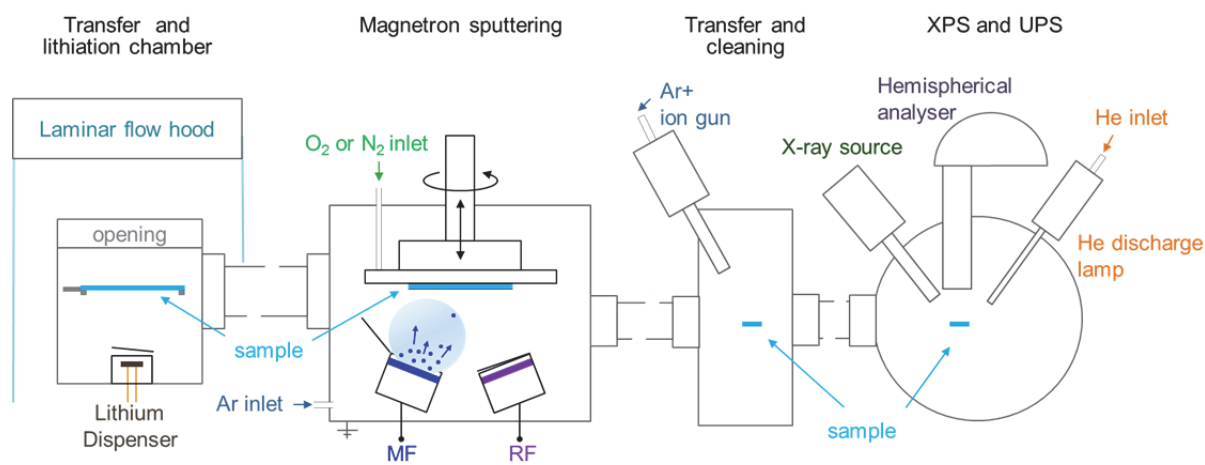
Figure 3:4   Schematic of the installation for transfer, sputter deposition, lithiation and in-situ analysis of the samples.

3.1.2 Lithiation

Lithiation of the samples was performed via wet and dry methods. The wet method consists of dipping the sample in a lithium-salt containing electrolyte, namely $LiClO_4$ in propylene carbonate and to apply an electrical potential step.

In order to manufacture clean samples for photoelectron spectroscopy or to produce all solid state devices in vacuum, a dry lithiation method was developed. Lithium dispensers bought from SAES Getters, Italy were installed in the transfer chamber using an electrical feedthrough and adapted flange as illustrated in Figure 3:5. The lithium dispenser is connected to the electrical feedthrough and heated via resistive heating using a DC power supply. A shutter is used to protect the sample during the conditioning step.

a)   b)
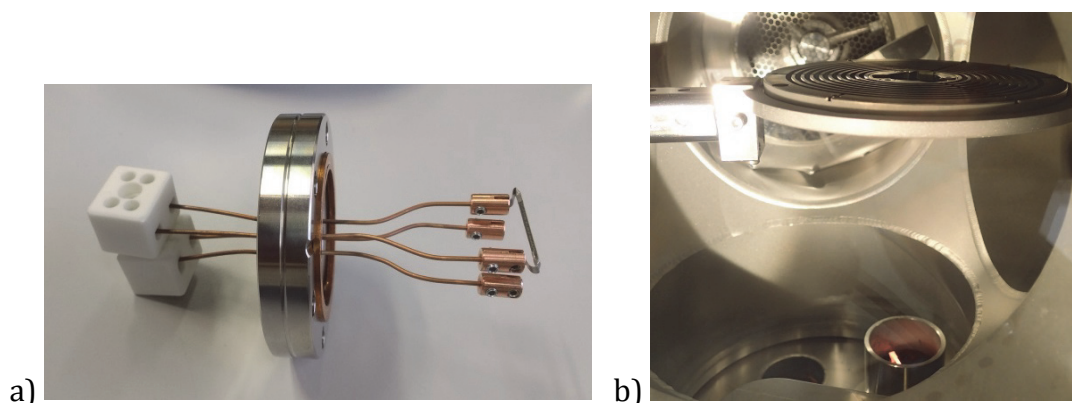
Figure 3:5   a) Electrical feedthrough with its lithium dispenser and b) installation in the vacuum chamber. The sample is translated in vacuum from the deposition chamber. A shutter protects the sample during the conditioning of the lithium dispenser.

3.1.3 Laser ablation

Some parts of the text below is reproduced from: Bouvard O, Lanini M, Burnier L, Witte R, Cuttat B, Salvadè A, Schüler A. Structured transparent low emissivity coatings with high microwave transmission. Applied Physics A. 2017 Jan;123-1. Available from: http://link.springer.com/10.1007/s00339-016-0701-8

Laser ablation was used to remove chosen patterns on low emissivity coatings in order to modify their properties towards the microwaves used for mobile communications. A 1064 nm nanosecond fiber laser was chosen because glass is transparent and silver absorbs in this wavelength range. Patterns (lines or grid) were defined to control the movement of the laser head, the sample staying motionless (Figure 3:6 a)). Lines were ablated by pulses of laser at a frequency of 10 kHz with a speed of 6 m/min and a power of 10.5 W. Samples were processed with the laser beam incident from the back-side to improve the precision of the ablation (Witte, 2013). Focus and power were adjusted in order to obtain an ablation width appropriate for interrupting the electrical conductivity, the latter being measured using a high voltage multimeter. Different laser parameters (power, pulse duration, focus) have been tested in order to obtain the thinnest line while still providing electrical insulation. Figure 3:6 b) shows the laser scribing equipment used to produce the samples.
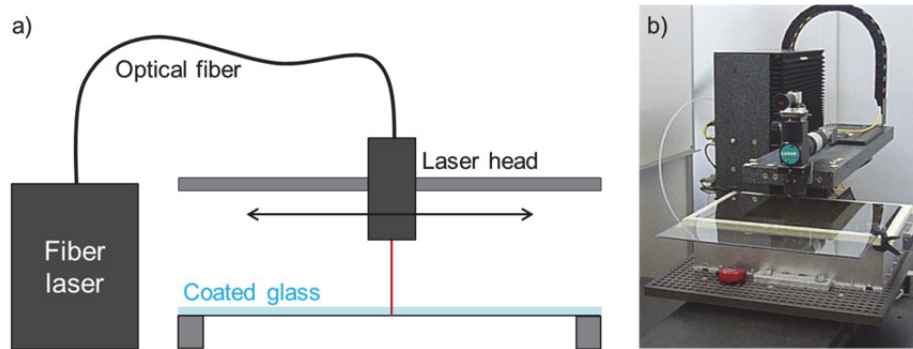
Figure 3:6 a) Diagram of the laser scribing equipment. The sample is on a X-Y table, the laser head is motionless. b) Photograph of the device used to make the first prototypes.

3.2   Electromagnetic properties

3.2.1 Measurement of microwaves transmission

Some parts of the text and figures below are reproduced from : Bouvard O., Lanini M., Burnier L., Witte R., Cuttat B., Salvadè A., Schüler A. Structured transparent low emissivity coatings with high microwave transmission.   Applied   Physics   A.   2017   Jan;   123(1).   Available   from: http://link.springer.com/10.1007/s00339-016-0701-8 (part mostly written by M. Lanini, SUPSI).

Different approaches exist to determine the microwave attenuation or radio frequency (RF) insertion loss of a material (Rahman, 1992). In this work, a free-space approach was adopted (see Figure 3:7 a) and b)) that is recognized to be a good trade-off in of terms of measurement accuracy in a dynamic range of 50-60 dB, repeatability, simplicity of the test fixture and fast measurement time (Wilson, 1988; Grosvenor, 2002). The measured sample dimensions were 50 cm x 50 cm. To achieve the necessary accuracy, the setup includes a large metallic shield to minimize the edge effect at the panel borders (see Figure 3:7 c) and d)) and the measurement is performed with a 2-port Vector Network Analyzer (VNA) with time gating capability (Agilent, 2007). The setup is composed of:

- A sample holder with an additional metallic shield and EMI gaskets for samples under test (SUT) smaller than 60 cm x 60 cm.
- A Vector Network Analyzer Agilent PNA E8364B 10 MHz to 50 GHz, with time domain (Option 010);
- 2 x R&S®HL050 Antenna, High Gain Log-Periodic Antenna 850 MHz to 26.5 GHz;
- 4 x Emerson & Cuming, ECCOSORB® AN 79 broadband absorbers;
- 2 x 2m High performance microwave coaxial cables, Huber + Suhner, Sucoflex® 100;
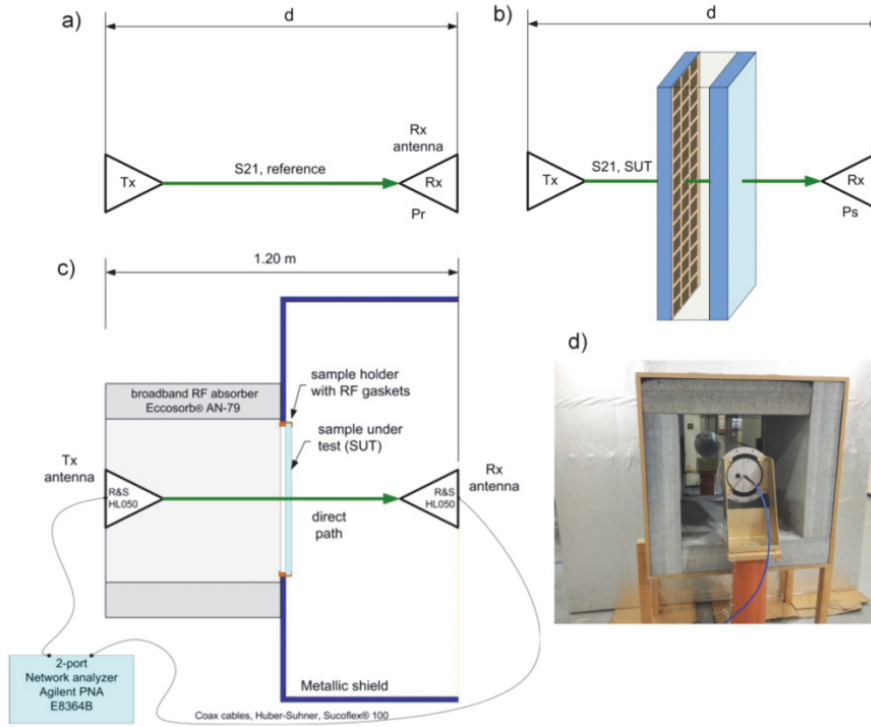
Figure 3:7   The free space method consists of a) a reference measurement of the free space loss and b) the measurement with the SUT. c) To deal with reflections / diffractions the experimental setup was modified with a metallic shield and a time-gated vector network analyzer (VNA). d) Picture of the test fixture and a glazing (SUT) (Bouvard, 2017a).

The time-gated measurement results allow the cancellation of multipath effects of the room (walls, roof floor), but not of the edge effect (scattering on SUT edge). In fact, fading signal (Rician like) can be observed on the envelope of the measured data. This effect is present only on samples smaller than 100 cm by 100 cm as the longest path cannot be discriminated in the time domain and the metallic screen introduces standing waves. Standing waves can be measured by averaging several measurements taken in different positions (IEEE Std, 1969) or by averaging the results in the frequency domain. In the present work, the antennas were fixed in one position (to keep a constant zero reference), thus a post-treatment using a cubic smoothing spline was applied to minimize the ripple on the measured shielding effectiveness (SE) (Unser, 2005).

3.2.1 Computer simulation

The patterned coatings were simulated with the 2.5D EM simulator Ansys® Designer™ (version 15.0.0), a commercial tool that allows the analysis of infinite structures acting as frequency selective surfaces (FSS) with fast and accurate simulations over an extremely wide bandwidth. The solver is based on the solution of mixed potential equations (Multilayered media Green's functions) by means of the method of moments (Gibson, 2008; Michalski, 1997). The following properties were used (Kiani, 2008) : $\varepsilon_{r\ glass}$ = 7.0, coating sheet resistance: 4.0 Ω/sq.

3.3   Optical and thermal properties

3.3.1 Visible/NIR spectrophotometry with integrating sphere

Spectrophotometry is a quantitative measurement of the reflectance $\rho(\lambda)$ and transmittance $\tau(\lambda)$ of a material as a function of the wavelength. The equipment used in this work is composed of a light source, an integrating sphere and a spectrometer. The light source is an incandescent lamp emitting an isotropic radiation with a distribution of intensities close to that of a black body. The integrating sphere (LOT, RT-060-SF) allow the determination of the total reflectance and transmittance as well as their diffuse component. The spectrometer Oriel MultiSpec 125TM 1/8m is equipped with an Instaspec IITM Photodiode Array Detector for the visible range (400 to 800 nm) and an Optronic Laboratories Monochromator OL 750-M-S coupled to a NIR-sensitive PbS detector (OL 730) for the near-infrared range (NIR 800 to 2500 nm).

The spectral properties of materials or devices are used to determine the coefficients of solar direct transmittance τ_e and visible light (or luminous) transmittance τ_v according to equation (10) and (11) respectively (EN410, 2011) (the calculation can be made using the Matlab routine presented in Annex A.1)

$$\tau_e = \frac{\sum\limits_{\lambda=350nm}^{2100nm} S_\lambda \tau(\lambda)\Delta\lambda}{\sum\limits_{\lambda=350nm}^{2100nm} S_\lambda \Delta\lambda} \tag{10}$$

where S_λ is the relative spectral distribution of the solar radiation, $\tau(\lambda)$ is the spectral transmittance of the glazing and $\Delta\lambda$ is the wavelength interval (in nm).

$$\tau_v = \frac{\sum\limits_{\lambda=380nm}^{780nm} D_\lambda \tau(\lambda)V(\lambda)\Delta\lambda}{\sum\limits_{\lambda=380nm}^{780nm} D_\lambda V(\lambda)\Delta\lambda} \tag{11}$$

where D_λ is the relative spectral distribution of illuminant D65, $\tau(\lambda)$ is the spectral transmittance of the glazing, $V(\lambda)$ is the spectral luminous efficiency for photopic vision defining the standard observer for photometry and $\Delta\lambda$ is the wavelength interval (in nm).

The solar direct reflectance ρ_e and the visible reflectance ρ_v can be determined in a similar manner, using eq. (10) and (11), by replacing the spectral transmittance $\tau(\lambda)$ with the spectral reflectance $\rho(\lambda)$. The solar direct absorptance, α_e, can be found using the eq. (12).

$$\tau_e + \rho_e + \alpha_e = 1 \tag{12}$$

3.3.2 Angular dependent optical properties

Optical properties of coated glass vary with the angle of incidence of the light beam. A window test bench, originally developed at University of Basel (Steiner, 2005) and now installed at EPFL/LESO-PB in Lausanne, was used to measure transmittance and reflectance at angles of incidence from 0° to 75°. This experimental set-up is composed of a light source, a support able to carry and rotate an up-to-scale double glazing, a receiver collimator and a Zeiss diode array spectrometer as depicted in Figure 3:8.
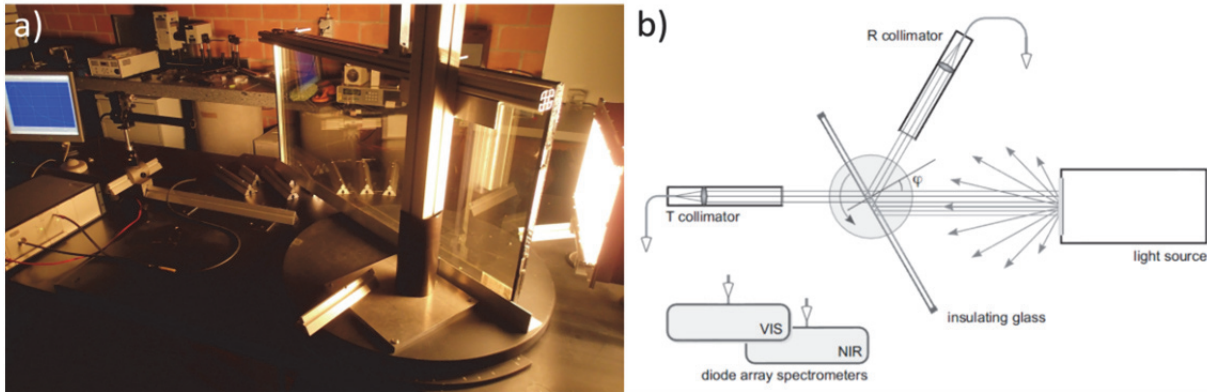
Figure 3:8 Windows test bench used to measure the spectral reflectance and transmittance as a function of the angle of incidence of light. a) Photograph showing the setup. Windows are carried by a rotating holder allowing to vary the angle of incidence of the light. The collimator is connected to an optical fiber and can be positioned at different angles; the optical path is constant regardless of the angle of measurement. b) Diagram depicting the setup (reproduced from Steiner, 2005).

The front diffusor plate of the light source provides a rectangular area (25 cm x 38 cm) of homogeneous diffuse radiation in the near UV, visible and near infrared wavelength range. A homogeneous intensity distribution over the front diffusor plate is required in order to account for the radiation passing through the double glazing indirectly by one or several internal reflections between the glass panes. Furthermore, a high temporal stability of the radiation intensity is obtained by making use of stabilized DC power supplies. The receiver collimator consists of a quartz lens with an aperture of 28 mm and a focal length of 76 mm. The wavelength accuracy of the spectrophotometer is 0.5 nm for $\lambda<500$ nm and 1 nm for $\lambda>500$ nm and the wavelength reproducibility is 0.1 nm. A transmittance measurement performed every 10 s for 20 min showed a deviation from the average line of 0.02% at 550 nm, and smaller than 0.3% in average in the range 350-2150 nm, confirming the stability of the light source and detector. For transmittance, the collimator is placed in line with the light

source. For reflectance measurements, the collimator can be moved to have the same light path length for each angle. Spectral intensities are measured for wavelengths ranging from 350 nm to 2150 nm (UV-Vis-NIR). These measurements can be used to determine the color rendering index (CRI) and the color coordinates of the samples (the calculation can be made using the Matlab routine presented in Annex A.2). Unless otherwise indicated the transmittance measurements are showing specular transmittance and were performed at normal incidence on non-diffusing samples.

3.3.3 Angular-dependent solar gain factor

To assess the solar heat gains through windows in a building, the solar factor, g is necessary: it is defined by eq. (13).

$$g\,(\varphi) = \tau_e\,(\varphi) + q_i \tag{13}$$

where $\tau_e(\varphi)$ is the coefficient of solar direct energy transmission for an angle φ and q_i is the secondary internal heat transfer factor. q_i represents the part of energy absorbed by the glass and reemitted as heat on the interior side.

In the steady state, the solar direct energy absorption (eq. (14) is divided into the secondary internal and external heat transfer factors q_i and q_e.

$$\alpha_e = q_i + q_e \tag{14}$$

Angular dependent solar gain was determined using the method developed by Reber et al. (Reber, 2005). This method is based on the measurement of the external and internal surface temperature of the double glazing while lit by a beam of a solar simulator. The light source of the solar simulator is a water-cooled xenon arc lamp (1000 W). A spectral distribution similar to that of the solar radiation is achieved by the means of filters. The elevation of the surface temperature of the glazing are related to the heat flows from the surfaces towards the ambient according to heat transport theory for free convection. The secondary internal heat transfer factor q_i depends on the external and internal heat transfer coefficients h_e and h_i, respectively that are fixed in standards such as EN 410 (EN410, 2011) to h_e = 23 W/(m^2K) and h_i = 8 W/(m^2K). Since we are not performing the experiment under these conditions (that would require a forced convection of the order of 4 m/s at the outer surface and an internal surface temperature increment of 12 K with respect to ambient), q_i is computed for standard ambient conditions. To determine the g-value, a calculated U-value is used as an input. The thermal performances of a double glazing can be estimated using the standards developed for the buildings such as the EN 673 for the calculation of the U-value (or thermal transmittance) (EN673, 2011). The latter takes into account the conduction through the glass and the air gap, the convection by calculating a Nusselt number and the radiation considering the emissivity of each surface (see Chapter 1, eq. 1 and 2). Glazing

manufacturers are usually using the same standard to determine the U-value of the glazing, this calculation can be used in the absence of data from the manufacturer or to confirm the value indicated in the datasheet. An example of the study of angular dependent properties of new glazing can be found in Annex A.3.

3.3.4 Fourier-transform infrared spectroscopy and emissivity

Fourier-Transform InfraRed spectroscopy (FTIR) is a method used to determine the spectral reflectance of a sample in the infrared range. First, an interferogram of a sample is collected using an interferometer, then a Fourier Transform is performed. In this work, a FTIR spectrometer from Bio-Rad Digilab Division was used to investigate the optical properties of thin films in the middle infrared range, from 2.5 μm to 16.7 μm. It uses a Globar lamp (silicon carbide rod emitting radiations in the middle infrared range, MIR), a beamsplitter made of an MIR transparent crystal and a room temperature deuterated triglycine sulfate (DTGS) detector. The measure is performed in two steps; first a gold standard is measured and corresponds to 100 % reflectivity. Then the sample is measured and the intensity of reflection relative to the former is obtained for each wavelength.

Applying Kirchoff's law, which states that the spectral emissivity, $\varepsilon(\lambda)$ of a body equals its spectral absorptance $\alpha(\lambda)$ at thermal equilibrium, the spectral emissivity of a material opaque in the infrared can be obtained by eq. (15).

$$\alpha(\lambda) = \varepsilon(\lambda) = 1 - \rho(\lambda) = 1 - \frac{I_{reflected}(\lambda)}{I_{incident}(\lambda)} \tag{15}$$

The emissivity ε is then the integral of the spectral absorptance weighted by the spectral emission of a black body at 283 K.

3.3.5 Ellipsometry

Ellipsometry is an optical technique used to determine the optical constants and/or the thickness of thin films. When polarized light reaches a surface, the reflected light is elliptically polarized. The parameters describing the ellipticity of the light (Ψ and Δ), shown in Figure 3:9, are recorded for each wavelength. The shape of the ellipse depends on the optical properties of the investigated samples as well as on the angle of incidence. Roughness tends to depolarize light, therefore the samples should be as flat as possible.
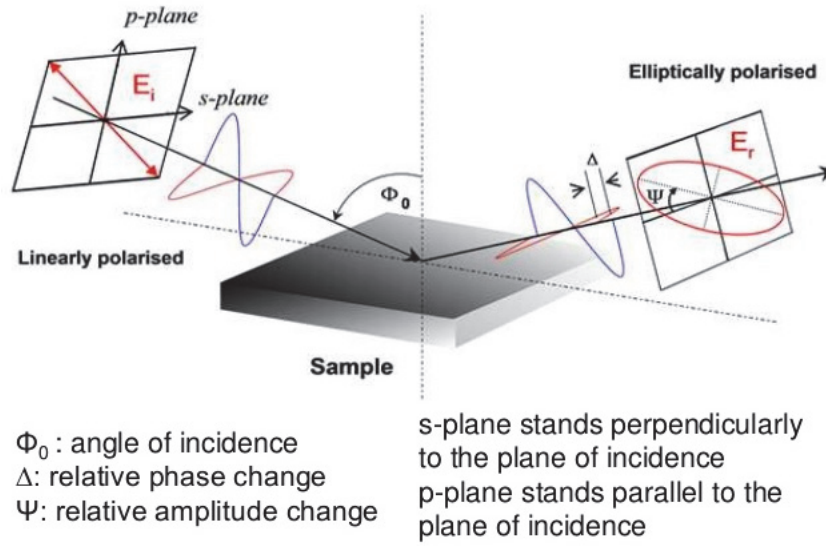
Figure 3:9   Principle of Ellipsometry Φ$_0$: angle of incidence Δ: relative phase change Ψ: relative amplitude change s-plane stands perpendicularly to the plane of incidence p-plane stands parallel to the plane of incidence. Reproduced from (Vijitha, 2014).

For this reason, the samples studied by spectroscopic ellipsometry were deposited on silicon wafer unless otherwise noted. Furthermore, the measurements were performed usually at four angles of incidence (60°, 65°, 70° and 75°) to gain additional information. This is particularly useful when both the optical constants and the thickness are unknown; in this case, a model is necessary to interpret the data.

Cauchy dispersion law was used in the non-absorbing region of the studied thin films (Cauchy, 1836). It can be written in the form of a limited development of the refractive index as a function of the wavelength (eq. (16)).

$$\mathrm{n}(\lambda) = \mathrm{A} + \frac{B}{\lambda^2} + \frac{C}{\lambda^4}$$
(16)

Where A, B and C are positive numbers characterizing the studied medium, respectively without dimension, in m^2 and in m^4.

In this work, a variable-angle spectroscopic ellipsometer SE-2000 from Semilab was used in the visible range (400-800 nm): the softwares Winelli and SEA were used for analysis. The initial guesses of thicknesses were made according to the profilometry or quartz balance results. Ellipsometry was also used to monitor the homogeneity of the thickness on a 10 cm diameter sample. A mapping was performed to monitor the thicknesses relative to the center of the sample.

3.4 Electrochemical properties

A potentiostat Bio-Logic SP200 equipped with a frequency response analyzer was used for the electrochemical measurements. The EC-lab software was used to control the potentiostat and analyze the results. The accuracy of the potentiostat is ±0.03% of the setting for the voltage/current control and 0.03% of the reading for voltage/current measurements.

3.4.1 Chronoamperometry

In chronoamperometry, a chosen voltage (in V) is applied to the electrodes and the resulting current (in A) is measured as a function of time. A potentiostat is used in order to keep the voltage constant between the reference electrode and the working electrode. The potentiostat is an active element which delivers the amount of current required to keep the voltage constant. The current is dependent on the chemical reaction and is recorded as a function of time. Since the amount of charge passing to the system is the integral of the current versus time (Bard, 2001 p.159), this technique is also called chronocoulometry. Figure 3:10 illustrates the excitation waveform of a potential step (a) and the resulting response in current (b). In an electrochromic device under test, the potential would be used to color or discolor the device depending on the chosen voltage.
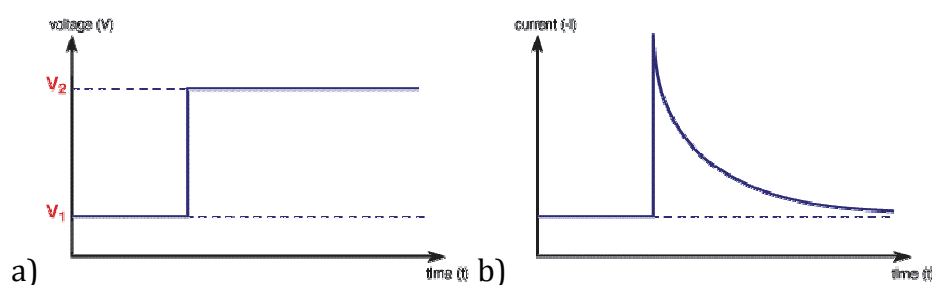
Figure 3:10   Potential step chronoamperometry a) excitation potential waveform b) current response, the part under the curve and above the dotted line represents the amount of charge passed. Reproduced from (Fisher, 2010).

In this work, a potentiostat Bio-Logic SP200 was used for most of the electrochemical measurements. First measurements on a half-cell (WO_3 in Li-PC with graphite as counter electrode) were performed using a power supply unit and a digital multimeter to record currents.

3.4.2 Cyclic voltammetry

In linear sweep voltammetry, a varying potential step is applied to the working electrode from a lower limit to an upper limit. In cyclic voltammetry, the potential is swept in the opposite direction as depicted in Figure 3:11 a), and repeated. Generally the measured current is displayed as a function of voltage as shown in Figure 3:11 b): oxidation and reduction peaks can be observed. By convention, the negative current is associated to the reduction

and the positive current to the oxidation reaction. The current varies as the voltage increase due to the influence of voltage on the equilibrium established at the electrode surface (Fisher, 2010). If the reaction rate is fast compared to the scan rate, the equilibrium can be predicted by thermodynamics. The Nernst equation (eq (17)) is derived from the standard changes in the Gibbs free energy associated with an oxidation-reduction reaction. For an electrochemical half-cell, the Nernst equation is given by (17).

$$\mathrm{E}_{red} = E^0_{red} - \frac{RT}{z\mathcal{F}} lnQ \tag{17}$$

where E_{red} is the half-cell reduction potential at the temperature of interest, R is the universal gas constant (in J·K^{-1}·mol^{-1}), T is the temperature (in K), F is the Faraday constant (in C·mol^{-1}), z is the number of electrons transferred in the cell reaction or half-reaction, Q is the reaction quotient of the half-cell reaction.

When the voltage varies from V$_1$ to V$_2$ the equilibrium position shifts from no conversion at V$_1$ to full conversion at V$_2$ of the reactant at the electrode surface.
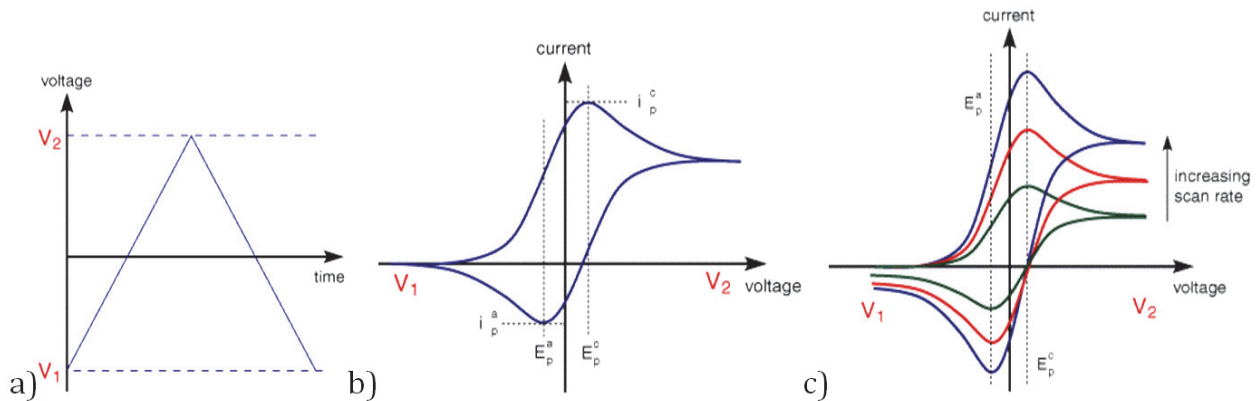
Figure 3:11   Cyclic voltammetry a) excitation waveform b) typical voltammogram for a reversible single electrode transfer reaction c) typical current response of a fast and reversible system with increasing scan rate. Reproduced from (Fisher, 2010).

Further information on the system can be gained by varying the scan rate. Figure 3:11 c) illustrates the typical voltammogram obtained for a fast and reversible system when the scan rate is increased. The current increases but the value of the peak potential stays constant. The diffusion layer above the electrode surface will grow much further from the electrode in a slow voltage scan rate. The flux to the electrode surface, and therefore the current, will be smaller for slower scan rates.

For slow and quasi-reversible systems, the equilibria cannot be reached rapidly (relative to the scan rate). The position of the current maximum will shift depending on the rate constant of chemical reduction and the scan rate. Reactions of intercalation such as in batteries or electrochromic materials are usually slow. The current takes more time to respond to the

applied voltage and the Nernst equation cannot predict the concentrations of reactants at the electrode surface. However, the analysis of the variation of the peak position with the scan rate can be used to estimate the electron transfer rate constants.

3.4.3 Electrochemical impedance spectroscopy

Electrochemical impedance spectroscopy is a non-steady state method used to investigate electrochemical systems. It consists into applying a sinusoidal voltage (or current) varying in frequency and to measure the resulting current (or voltage). The amplitude of the sinusoid should be small enough to be able to consider that the system is linear. When a sinusoidal voltage is applied to a system containing components such as inductors and capacitors, the current response is also sinusoidal but a phase shift occurs. To quantify signal magnitude and phase shift, the concept of impedance (Z) is used, and given by eq. (18).

$$Z(f) = \frac{\mathcal{L}\{E(t)\}}{\mathcal{L}\{i(t)\}} \tag{18}$$

where $\mathcal{L}$ is the Laplace transform, E is the potential and I the current.

The Laplace transform is an integral transform in which a function of time is transformed into a new function of a parameter: here frequency f (Hz)(Lasia, 1999). The response of the system is expressed as the real and imaginary part of the impedance in the Nyquist diagram representation, eq. (19),

$$Z = a + j\,b = \mathcal{R}e(Z) + j\,\mathcal{I}m(Z) \tag{19}$$

with $j^2 = -1$.

or as the modulus and phase shift in the Bode plot representation, eq. (20).

$$Z = \rho(\cos\varphi + j\sin\varphi) \tag{20}$$

where ρ is the modulus and φ the phase shift.

Figure 3:12 shows the typical response in impedance of an ideal resistor, an ideal capacitor, a constant phase element (used for non-ideal capacitors), a resistor and capacitor in series, a resistor and capacitor in parallel and a resistor and constant phase element in parallel. These elements are used to fit the data obtained by electrochemical impedance spectroscopy: they can be related to the nature of the sample. For example, an insulating layer located between two conductive layers will respond as a capacitor and the ionic conduction process respond like a resistor and capacitor in parallel.

a)		d)	
R1 $$Z(f) = R_1$$		R1 C1 $$Z(f) = R_1 + \frac{1}{j2\pi f C_1}$$	$f_c = \frac{1}{2\pi C_1}$
b)		e)	
C1 $$Z(f) = \frac{1}{j2\pi f C_1}$$		C1 R1 $$Z(f) = \frac{R_1}{1 + j2\pi f\, R_1 C_1}$$	$f_c = \frac{1}{2\pi R_1 C_1}$
c)		f)	
Q1 $$Z(f) = \frac{1}{Q_1(j2\pi f)^{\alpha_1}}$$	$-\alpha_1 \frac{\pi}{2}$	Q1 R1 $$Z(f) = \frac{R_1}{1 + R_1 Q_1(j2\pi f)^{\alpha_1}}$$	$\frac{1}{2\pi (R_1 Q_1)^{1/\alpha_1}}$
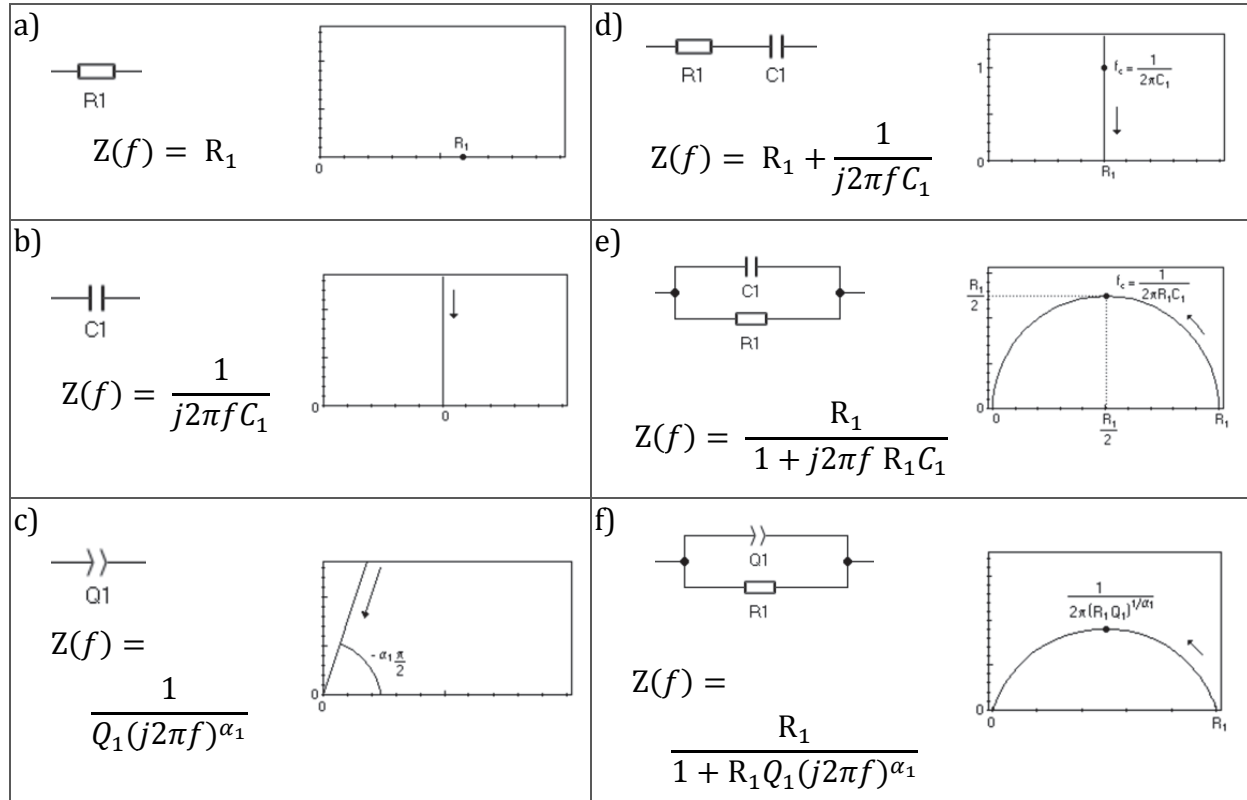
Figure 3:12   Typical elements used for equivalent electrical circuits with their impedance function and representation in Nyquist diagram where the vertical and horizontal axis are respectively minus the imaginary and real part of the impedance (-Im(Z) vs Re(Z)). a) Ideal resistor b) ideal capacitor c) constant phase element, used for non-ideal capacitors d) resistor and capacitor in series e) resistor and capacitor in parallel f) resistor and constant phase element in parallel. Images from (EC-Lab, 2016).

The potentiostat VP-200 from Bio-Logic was equipped with a frequency response analyser with a frequency range of 10 μHz up to 7 MHz. In this work, Electrochemical Impedance Spectroscopy (EIS) was mainly used to determinate the ionic conductivity of the solid state ionic conductors. They were deposited on Indium Tin Oxide (ITO). A shadow mask was used to deposit the metallic contacts (aluminium or tungsten), as depicted in Figure 3:13.
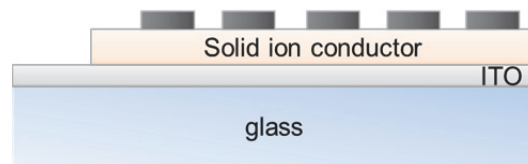
Figure 3:13 Sample for determination of ionic conductivity by EIS.

3.4.4 Spectroelectrochemical experiments

In order to study the optical response of the electrochromic devices, optical measurements were performed while the sample was cycled by chronoamperometry or cyclic voltamme-try. The Zweiss spectrophotometer described in Section 3.3.2 was used. The acquisition time is short and allows a scan in the visible and near infrared (350-2100 nm) every 0.5 seconds: Figure 3:14 a) is a schematic representation of the measurement setup. The elec-

trochromic half device in a liquid bath or the full-device with solid or liquid electrolyte is placed in front of the collimator. A diaphragm is used to limit the light beam only to the switching part of the sample. The potentiostat is connected to the ITO layers (and graphite rod in case of half-cell device) and is used to control the voltage: the current is recorded while the spectral transmittance is measured. Figure 3:14 b) details the four-point connection used between the potentiostat and a solid state sample.
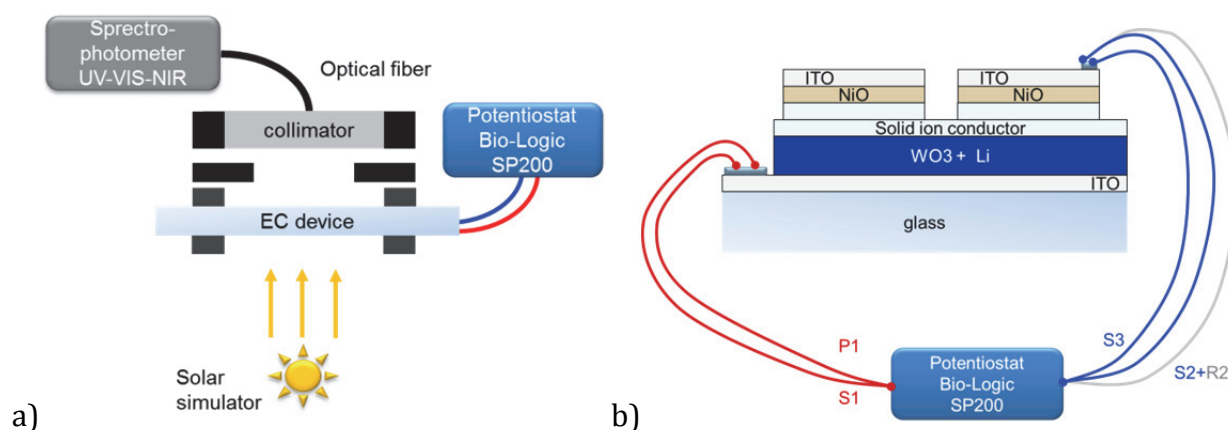
Figure 3:14   a) Setup for spectroelectrochemical experiments. b) Detailed connection between the potentiostat and a solid-state sample. Unless otherwise indicated, the spectral transmittance is the specular transmittance recorded at normal incidence.

3.5   Electronic properties

3.5.1 X-ray Photoelectron spectroscopy

X-ray Photoelectron spectroscopy (XPS) takes advantage of the external photoelectric effect to understand the chemical environment and state of the analyzed sample. The depth of the response will depend on the energy of the incident photon. XPS, alternatively named electron spectroscopy for chemical analysis (ESCA), is commonly performed using soft X-rays provided from Mg Kα or Al Kα at energies of 1253.6 eV and 1486.6 eV respectively.

As illustrated in Figure 3:15, the emitted photoelectrons have to pass through a hemispherical analyzer. Electrostatic fields are established to detect only the electrons of a given energy to arrive on the multichannel plate detector, this is the pass energy. The hemispherical analyzer and the transfer lenses can be operated in two modes, the Constant Analyzer Energy (CAE) and the Constant Retard Ratio (CRR). XPS are usually acquired in CAE mode.
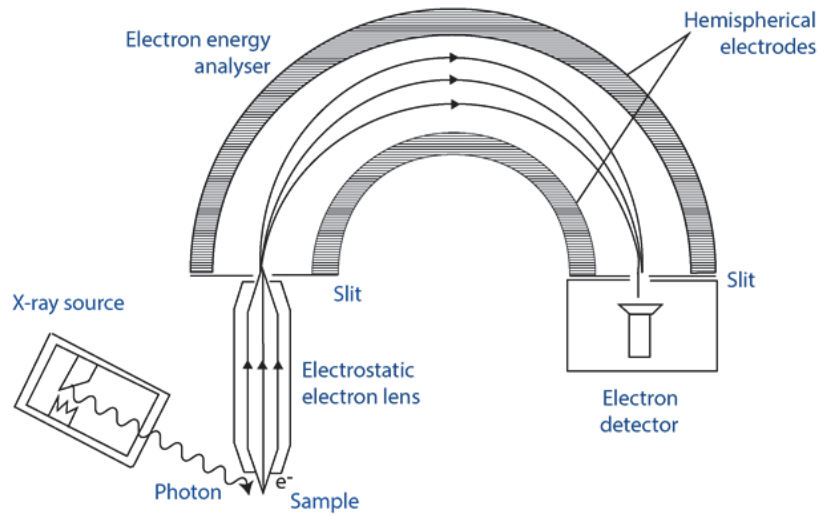
Figure 3:15   Schematic of an X-ray photoelectron spectrometer. Reproduced from (Perumal, 2016).

The photoemission process in XPS can be divided into three processes if a decoupling of intrinsic, extrinsic, surface effects and excitations when the electron moves in the vacuum is assumed (Tougaard, 2010). This is called the three-step model and is illustrated in Figure 3:16. In a first step, the emitted photon is absorbed and e core-electron is excited. In a second step, the electron migrates to the surface and in a third step, the electron escapes to vacuum and travel to the energy analyzer (Dowell, 2009).
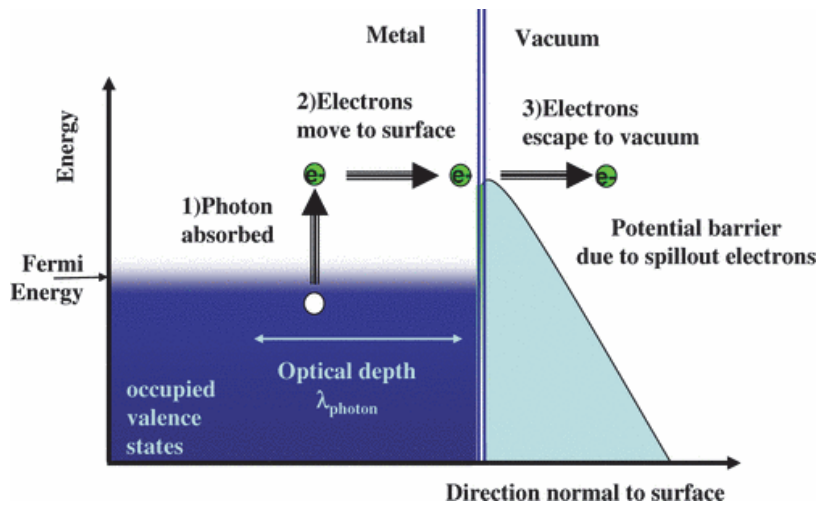
Figure 3:16   Spicer's three-step model for photoemission. Reproduced from (Dowell, 2009).

The core level binding energy (BE) can be determined using eq. (21).

$$BE = h\nu - KE \tag{21}$$

The kinetic energy (KE) is independent of the x-ray photon energy, however as observed from eq. (21), in the binding energy scale, Auger peak positions depends on the X-ray source.

The resulting XPS spectrum represents the intensities of photoelectrons, as a function of the binding or kinetic energy. The peak identification can be performed using reference database such as the NIST X-ray Photoelectron Spectroscopy Database (Naumkin, 2012) or scientific literature on similar elements. For p, d and f peaks, two peaks are observed: the separation between the two peaks, or spin orbital splitting, of a core level of an element in different compounds is nearly the same. Therefore, the spin orbital splitting can assist in peak identification of different oxidation levels. Furthermore, the area ratios between two peaks of a spin split orbital are specific to the core-level. The ratio of the $p_{1/2}$ peak area over the $p_{3/2}$ is 1:2, $d_{3/2}$:$d_{5/2}$, is 2:3 and is 3:4 for $f_{5/2}$:$f_{7/2}$. These values can be used as constraints to perform accurate peak deconvolution.

In this study, XPS measurements were performed with an EA11 energy analyzer from SPECS using a photon energy of 1253.6 eV (Mg K_α). The survey scans were measured at a pass energy of 50.4 eV at the energy analyzer. The high-resolution scans of the elements were measured at a pass energy of 29.9 eV. The spectrometer energy scale was calibrated with Au $4f_{7/2}$ core level signal from a gold bulk element (99.99% purity) at 83.8 eV. The concentrations of elements were obtained by integrating over the core level signal after subtracting a Shirley background and using the Scofield derived relative sensitivity factors (RSF). These theoretical factors were determined for isolated atoms and show a good agreement with experimental data on single element (within 5%, excluding elements with high atomic numbers) (Scofield, 1976). For compounds, the absolute error is usually considered to be about 10%. The relative error between two measurements performed on the same equipment and the same type of sample is small and depends on the level of noise which can be reduced by increasing the acquisition time (CasaXPS, 2011). Deconvolution of spectra was performed using Gaussian-Lorentzian functions in the CasaXPS software.

3.5.2 UV Photoelectron spectroscopy

Ultraviolet photoelectron spectroscopy (UPS) operates on the same principles as XPS, except that the photons energy in the range of tens of eV are used. Since the photons energy is smaller, UPS is sensitive only to the first mono-layers. Information on the sample will originate mainly from the valence band. UPS spectra can also provide information on the work function of the sample.

In this work, a helium discharge lamp is used as photon source for UPS measurement. The He I line has an energy of hv = 21.22 eV and He II of hv = 40.82 eV. Scans were recorded at a constant retardation ratio of 4. The chamber used for the deposition of sample and for the UPS and XPS analysis is depicted in Figure 3:17.
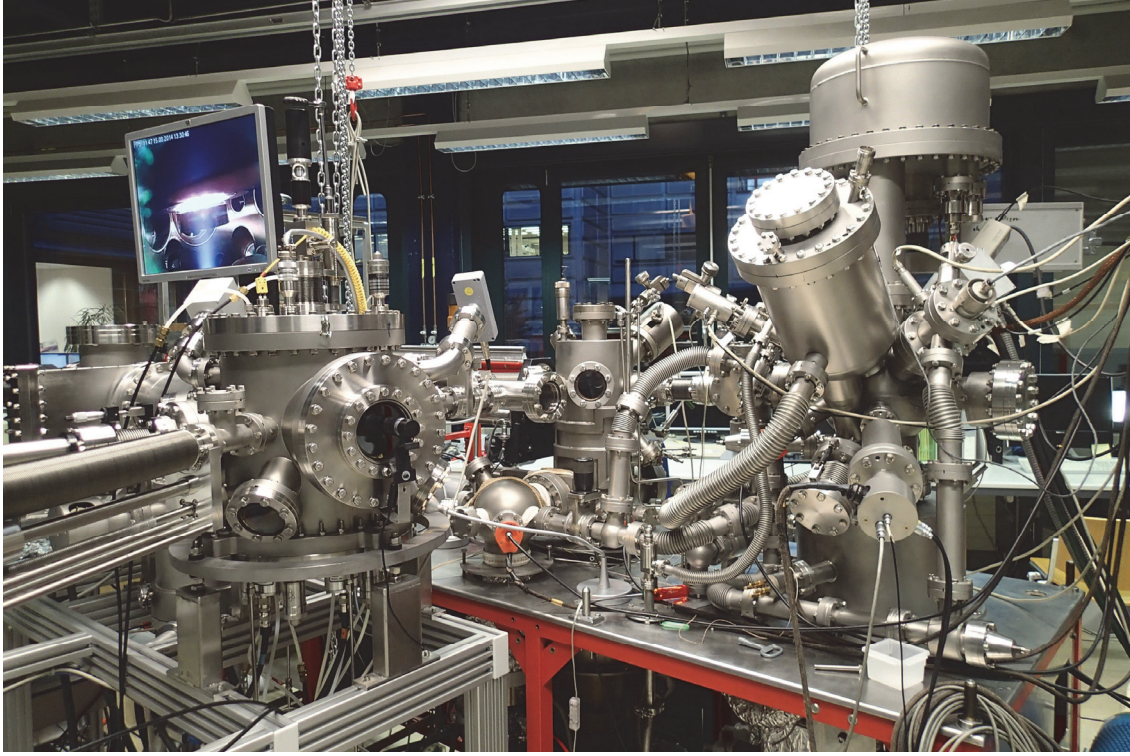
Figure 3:17   Photograph of the laboratory with magnetron sputtering deposition chamber on the left hand side and the XPS/UPS chamber with the hemispherical analyzer on the right hand side.

3.5.3 Resistivity measurements

The resistivity of any conducting sample can be measured using a four-point probe method in the van der Pauw Configuration (Van Der Pauw, 1958). The current is applied on two contacts while the voltage is measured on the two others. The film resistivity is then given by eq. (22):

$$\rho_{DC} = \frac{\pi\,d}{2\,ln2}(R_{12} + R_{23})f\left(\frac{R_{12}}{R_{23}}\right) \tag{22}$$

where d is the film thickness (in nm), R_{ij} the resistance between the point i and j (in Ω) (see Figure 3:18) and f is a tabulated function of geometrical correction. In this work, the samples were nearly square shaped and thus R_{12} and R_{23} were almost equal giving f=1.
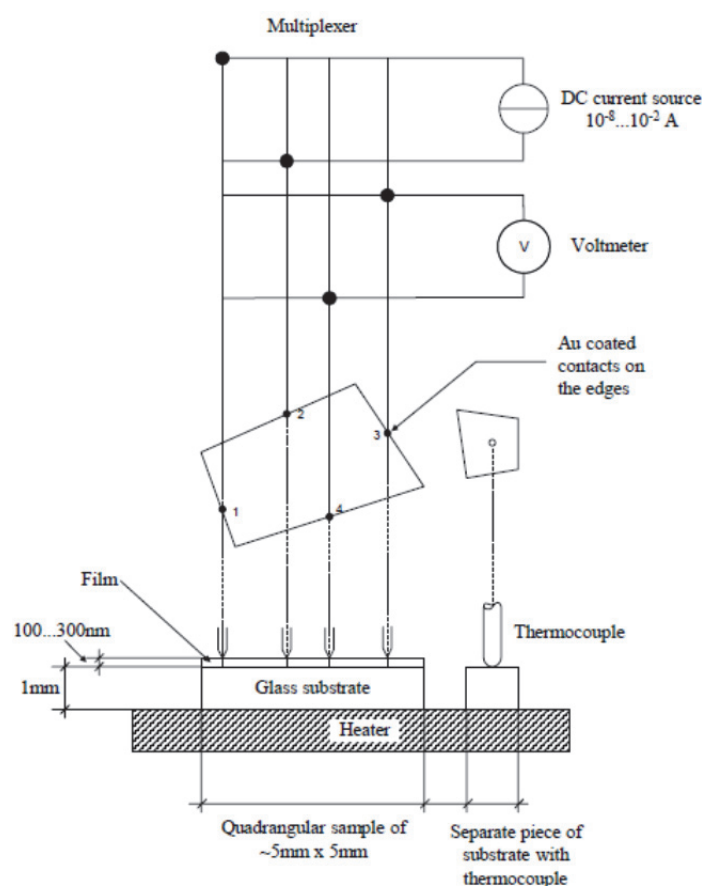
Figure 3:18   Setup for the electrical resistivity measurement. Reproduced from (Springer, 2004).

Temperature influences the electronic conductivity of materials. In metals phonon scattering reduces the electrical conductivity as temperature increase, whereas in semiconductors electrical conductivity increases thanks to thermal activation: therefore, the temperature of the sample was recorded during the measurement. Unless otherwise stated, the value of the resistivity was taken at 25°C. A heating stage was used to increase the temperature if necessary.

3.5.4 Electronic leakage

For electronically insulating samples, such as solid ion conductors, an estimation of the electronic leakage can be determined by apply successively potentials steps for long period of times (Su, 2015). DC current decay curves were measured for 16 to 24h applying a voltage drop of 1, 2 and 3 V. The current decrease and reach a steady current due to the electronic leakage current. The electronic resistance can be obtained from the slope of potential-current curve. This measurement provides an upper limit value of the electronic partial conductivity.

3.6   Morphology and structure

3.6.1 Electron microscopy and X-ray dispersive spectroscopy

A scanning electron microscope (SEM) probes the samples with a focused electron beam to produce the image. The electron beam interacting with the sample is converted into low-energy secondary electrons, high-energy back-scattered electrons, light emission or X-ray emission. The image coming from the secondary electrons reveals mainly the topography, while the back-scattered electrons give information on the relative density of the observed materials. As the energy of X-rays are characteristic of the atomic structure of the element and the energy difference between shells, an elemental analysis can be performed.

In this work, the following SEM were used:

- an FEI XLF30-FEG (Everhart-Thornley secondary-electron detector and Schottky FEG electron gun) with an energy-Dispersive X-ray spectrometer (EDX)
- a Zeiss GEMINI 300 (Thermal field emission, Everhart Thornley Secondary Electron detector, Inlens Secondary Electron detector, Angular selective backscattered detector)

The samples to be observed by SEM were usually deposited on silicon wafer substrates. A thin carbon coating (less than 5 nm) was applied on charging samples.

3.6.2 X-Ray Diffraction

The interaction of X-ray with crystalline matter produces constructive interference. The atomic planes act as three-dimensional gratings for X-rays wavelength in the order of magnitude of the spacing between planes of a crystal lattice (Friedrich, 1912). By scanning at multiple angles, a diffractogram is obtained. The comparison with standard patterns allows for crystal phase identification. This method was also used to confirm that the samples deposited were amorphous. A Empyrean system (Theta-Theta, 240mm) equipped with a PIXcel-1D detector, Bragg-Brentano beam optics and parallel beam optics was used. The Scherrer formula eq. (23) can be used to determine the crystallite size.

$$B(2\theta) = \frac{K\,\lambda}{L\cos\theta} \tag{23}$$

with K the constant of proportionality (usually taken to 0.9), λ the wavelength of the X-ray radiation of the source (0.154056 nm for Cu Kα), L the crystallite size, θ the Bragg angle and B, the line broadening at half the maximum intensity.

3.6.3 Profilometry

A mechanical profilometer has a tip, which scans the sample surface while the variation of its height is measured. This can be used to observe topological change or roughness. In this work, a Bruker Dektak XT surface profiler was used in order to get an estimation of the coatings thickness. Before deposition of the coating, a Kapton tape was placed on the substrate to create a step. A line of few millimetres was then scanned by the tip and the difference between the substrate height and the sample height gives the thickness of the film (in nm). The vertical resolution of the DektakXT stylus profilometer is 0.4 nm; however in practice, the quality of the step and the homogeneity of the sample limit the accuracy of the thickness measured. To reduce the uncertainty, the sample is usually measured in three different positions and the resulting thickness averaged, the deviation is usually about ±10 nm. For transparent samples, the thickness measured is used as an initial value to perform a fit on experimental ellipsometry data.

Chapter 4   Conductive coatings

This chapter first describes the results obtained during the development of a low-e coating with high microwave transmission. The optical and thermal properties of this new glazing are evaluated along with the attenuation of microwaves. The visual appearance and mechanical properties are also considered. Finally, applications for this new type of low-e coating are discussed. In a second part, the conductive coatings used as transparent electrodes for electrochromic devices are investigated. Commercial indium tin oxide coatings as well as coatings deposited in the laboratory with no substrate heating are studied. Their electrical, optical and structural properties are measured and compared.

4.1   Low-e coating with high microwave transmission

Some parts of this text and images are reproduced from: Bouvard O, Lanini M, Burnier L, Witte R, Cuttat B, Salvadè A, et al. Structured transparent low emissivity coatings with high microwave transmission. Applied Physics A. 2017 Jan; 123(1). Available from: http://link.springer.com/10.1007/s00339-016-0701-8

and from: Bouvard O, Lanini M, Burnier L, Witte R, Cuttat B, Salvadè A, et al. Mobile communication through insulating windows: a new type of low emissivity coating. Energy Procedia. 2017 Sep;122:781–6. Available from: https://doi.org/10.1016/j.egypro.2017.07.396

Low-e coatings, due to their electrical conductivity, attenuate the transmission of the microwaves used for mobile communications compared to uncoated glass. If such coatings are used in a train whose envelope is made of metal, the electromagnetic waves used for telecommunications are strongly attenuated as in a Faraday cage. When the attenuation is too strong, repeaters are used to amplify the signal; these need to be replaced whenever communication standards change and their cost is non-negligible. The currently used communication standards include GSM (Global System for Mobile communications, 880–960 MHz) and UMTS (Universal Mobile Telecommunications System, 1920–2170 MHz).

Therefore, there is a need for a new material that could reflect the infrared range and transmit a large band of microwaves while conserving transparency in the visible range: a low emissivity coating with high microwave transmission.

77

4.1.1 Square patch pattern FSS

A large band pass is necessary for a passive system in order to be independent of communication technology modifications. A square patch pattern on a conductive coating is a low pass filter; it is not limited to one specific wavelength and can be optimized for a large range of wavelengths: therefore, it should be suitable to create a low-e coating with a double selectivity. Various techniques exist for analysing frequency selective surfaces (Mittra, 1988); the analytical averaged approach presented by Costa et al. (2014) can be used to analyze the frequency response of the FSS. A square patch pattern can be considered as a non-resonant structure with capacitive behaviour. The system can be modelled using an electrical circuit equivalence, where a resistor ($R_{coating}$) simulates a conventional low-e coating (see Figure 4:1 a)) and a capacitor (C_{fss}) in series with a resistor (R_{fss}) represents a coating patterned in square patches (see Figure 4:1 b)). Z_0 represents the impedance of air and $Z_{0,in}$ = $Z_{0,out}$ = 377 Ω. The pattern can be described by the geometrical parameters linewidth w and periodicity D (see Figure 4:1 c)).
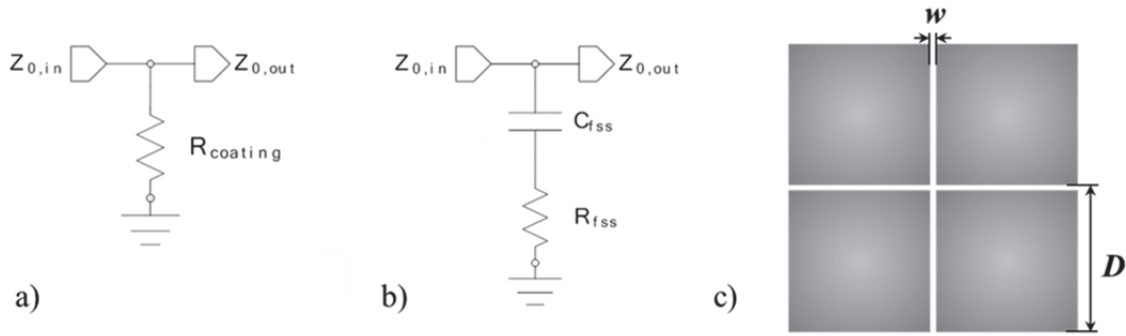
Figure 4:1   a) Equivalent circuit of an electrically conductive coating; b) Equivalent circuit of a capacitive square patch pattern with resistive elements; c) geometrical parameters of a square patch pattern.

For the considered electrical circuit with a resistor and a capacitor in series, the cut-off frequency f_{-3dB} corresponding to an attenuation of 3 dB is given by eq. (24).

$$f_{-3dB} = \frac{1}{2\pi \cdot \left(R_{fss} + \dfrac{Z_0}{2} \right) \cdot C_{fss}} \tag{24}$$

where f_{-3dB} is the cut-off frequency (in Hz), R and Z are resistance and impedance (in Ohm) and C, capacitance (in F).

In the case of a capacitive square patch and at normal incidence, C_{fss} is calculated by eq. (25) (Costa, 2014).

$$C_{fss} = \frac{D\varepsilon_0(\varepsilon_{r1} + \varepsilon_{r2})}{\pi} \ln\left(\frac{1}{\sin\left(\frac{\pi w}{2D}\right)}\right) \tag{25}$$

where D is the FSS periodicity (in mm); w is the linewidth between the conductive patches (in mm); ε_0 is the vacuum permittivity (in F.m^{-1}) and ε_{r1}, ε_{r2} are the relative dielectric permittivities of the surrounding mediums (i.e. air and glass).

If the ratio w/D is maintained constant, C_{fss} becomes independent of w, and is proportional to D.

The surface resistance R_{fss} is given by eq. (26) (Costa, 2010).

$$R_{fss} \approx R_{coating}\frac{D^2}{(D-w)^2} \tag{26}$$

where $R_{coating}$ is the sheet resistance of the patches of the conductive coating. Therefore, if the width w is very small as compared to the distance D, the surface resistance R_{ffs} will be similar to the resistance of the patches of the conductive coating $R_{coating}$, eq. (27).

$$for\ w << D: \quad R_{fss} \approx R_{coating} \tag{27}$$

For patterned conductive low emissivity coatings on glass substrates, and for frequencies clearly below the plasma frequency of the free charge carriers, the following properties are typical (Kiani, 2008): $\varepsilon_{r\ glass}$ = 7.0, coating sheet resistance: 4.0 Ω/sq. Using these values, the cut-off frequency f_{-3dB} can be calculated as a function of w and D.

Figure 4:2 a) shows the behaviour of f_{-3dB} when w is kept constant at a value of 35 μm and D is varied from 0.5 mm to 40 mm. For a decreasing D, f_{-3dB} is monotonously increasing and at D = 2 mm, a cut-off frequency of 5.1 GHz is obtained. Figure 4:2 b) shows the behaviour of the cut-off frequency f_{-3dB} when D is kept constant at a value of 4 mm, and w is varied from 1μm to 100 μm. For small w, f_{-3dB} goes approximately with ln(D/w) (compare with eq. (25)). For increasing w, f_{-3dB} is monotonously increasing, with decreasing slope. For $w \geq 60$ μm, cut-off frequencies f_{-3dB} above 2.5 GHz are obtained.
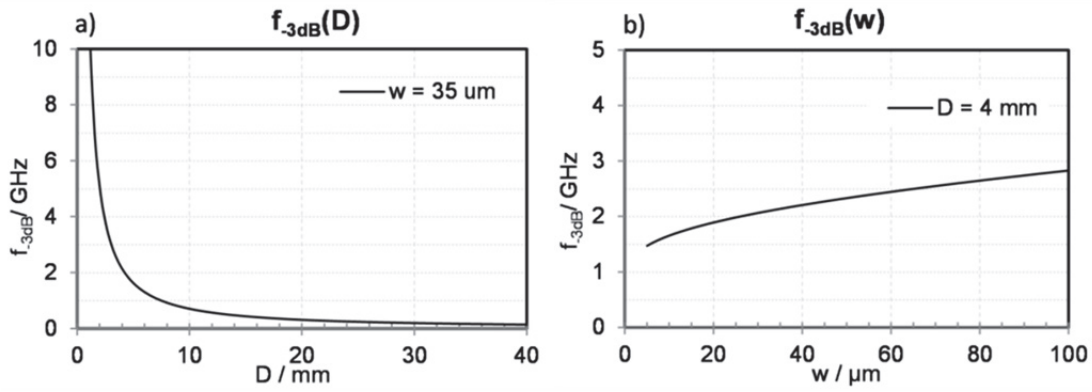
Figure 4:2   a) Cut-off frequency f-3dB as a function of D for w = 35 µm, b) Cut-off frequency f-3dB as a function of w
for D = 4 mm

The following sections presents the experimental results obtained with the square patch pattern.

4.1.2 Characterization of the ablated area

Laser ablation was used to create a non-conductive pattern on a low-e coating. Commercial glass for energy saving windows from AGC Verres Industriels Moutiers was processed. Glass samples with a thickness of 4 mm and a size of 500 mm x 500 mm were used. They were coated with a "Low-e Top N+T" low-emissivity coating. After laser scribing, the glass panes were assembled into double glazing: they are composed of a first glass pane of grey glass 4 mm thick, a 12 mm air gap and the coated glass pane. Large samples (min. 500 mm x 500 mm) are necessary to measure the attenuation of microwaves; in smaller samples edge effects may disturb the measurement.

The total ablated area was kept small thanks to very narrow lines. A nanosecond fiber laser (1064 nm) was used to scribe fine lines on a low-e coating. The pulse frequency was 10 kHz and the displacement speed was 6 m/min (more details can be found in Chapter 3). Figure 4:3 displays images that were obtained by a) scanning electron microscopy (SEM), b) confocal laser microscopy and c) Energy-dispersive X-ray spectroscopy (EDX).
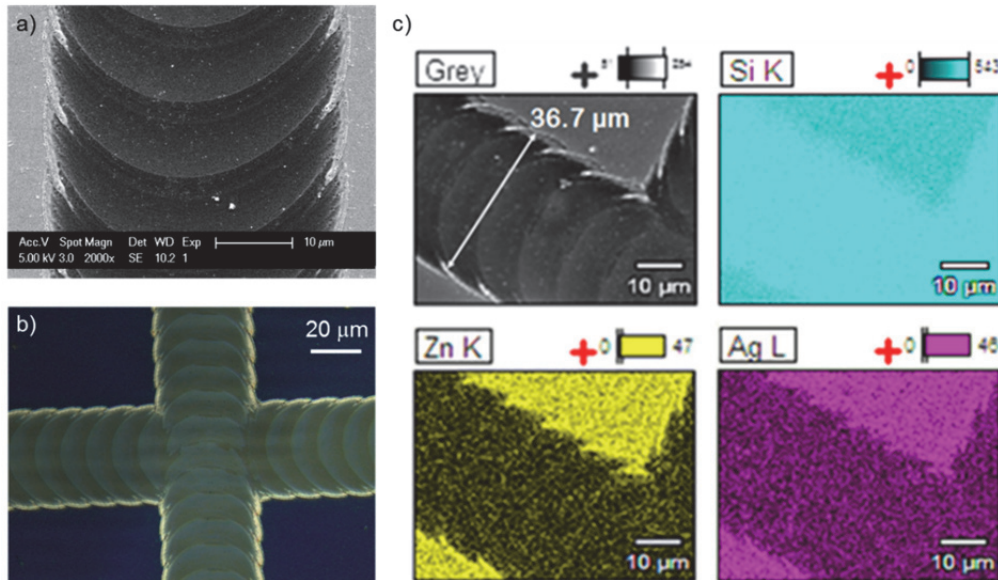
Figure 4:3 a) Observation by scanning electron microscopy (SEM) of the linewidth. On the side of the ablated area, some accumulation of material can be seen. b) image of an intersection of lines ablated by laser pulses with confocal laser microscopy. The dark area represents the coating. On the light part, the superimposition of the pulses can be observed. c) SEM image and EDX element mapping of silicon, zinc and silver at a perpendicular intersection of ablated lines. Adapted from (Bouvard, 2017a) and (Bouvard, 2017b).

Figure 4:3 a) shows the detail of an ablated line; the light grey area corresponds to the low-e coating. Due to the use of a nanosecond pulsed laser, the lines consist of a succession of overlapping disks corresponding to the focal spot of the laser: the overlap is in the order of 70% - 75% of the disc surface. On the edge of the ablated line, an accumulation of material is observed. The material of the low-e coating is ejected to the side of the laser spot. The width of the resulting line is approximately 40 microns. Figure 4:3 b) presents an enlarged view with the intersection of two perpendicular lines. It can be observed that there is no material deposition on the lines around the intersection point. Figure 4:3 c) shows an SEM image of the ablated line along with an EDX element mapping of silicon, zinc and silver. The glass substrate contains Si; it can be seen on the entire image of the element mapping. The low emissivity coating contains ZnO and metallic Ag. The element mapping clearly indicates that the low-e coating was ablated on the dark line visible in the SEM image. An accumulation of materials is observed at the edges of the ablated line but no deposition is observed around the intersection point. The pattern is expected to improve the transmission of microwaves because it interrupts the electric conductivity; therefore, defects in the ablated lines should be avoided.

After ablation, it was verified that the electrical conductivity between two adjacent zones was effectively interrupted using an isolation tester for a representative number of zones. The width of 35-40 microns was selected because it proves sufficient to electrically insulate two adjacent zones. Therefore, patches of conductive coatings could be formed. To create a square patch pattern, an array of parallel lines is first ablated, then an array of parallel lines

perpendicular to the first ones are ablated. The interspacing between parallel lines was varied between 2 and 40 mm. For a linewidth of 40 microns and a spacing of 40 mm, the corresponding ablated area is only 0.2 %. For the same linewidth and a spacing of 2 mm, the ablated area represents 4 % of the coating. To create a pattern with equilateral triangles, parallel lines are first ablated and two series of parallel lines at 60° and -60° from the first ones are ablated.

4.1.3 Thermal properties

The ablated area should be kept as small as possible to preserve the low emissivity and therefore the insulating performances of the window. The reflectance in the mid-infrared region (2.5 µm to 16.7 µm) can be used to determine the emissivity of a coating. It was measured using an FTIR spectrophotometer and is displayed in Figure 4:4. The solid line in Figure 4:4 represents the commercial coating; its reflectance varies from 94 % at 3 µm to 97 % between 10 and 16 µm. The dashed line shows the values measured after the laser engraving. The reflectance is slightly lower with values ranging from 91 % at 3 µm to 95 % around 9 µm. The feature observable around 4.4 µm is due to the absorption of water and was not taken into consideration for the assessment of emissivity.
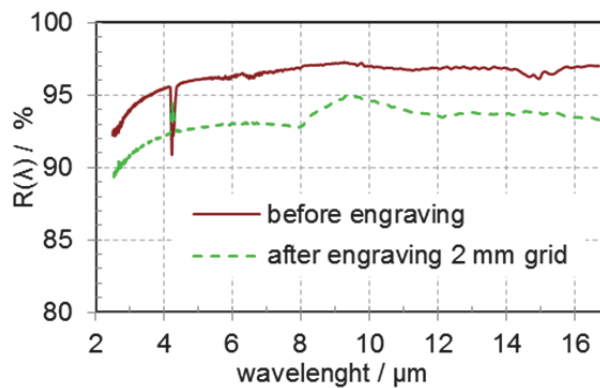
Figure 4:4   Spectral reflectance of the coated glass in the mid-infrared region before and after laser engraving (ablated lines width of w = 37 ± 2 µm, spacing D = 2 mm in grid pattern). The feature at approximately 4 µm is due to the absorption of water. Reproduced from (Bouvard, 2017a).

Table 4:1 displays the emissivity determined from the FTIR measurement and the corresponding thermal transmittance, or U value, calculated according to EN 673 (see Chapter 2). For this calculation, a double glazing composed of two glass panes (one grey uncoated glass, d_1 = 5 mm, and one coated clear glass, d_2 = 4 mm), an air gap of s = 10 mm, and a mean temperature of T = 283 K were used. The laser treatment increases the emissivity of the coating of 3.2 percentage point: it corresponds to an increase of 0.05 W·m^{-2}·K^{-1} for the calculated U value, which is below the uncertainty of the calculation. Hence, we could expect a minor difference between the conventional glazing and the one with a structured glazing in terms of overall thermal performances.

	$\varepsilon_{exp.}$ / %	$U_{calc.}$ ±0.1 / $W \cdot m^{-2} \cdot K^{-1}$	$U_{meas.}$ ±0.04 / $W \cdot m^{-2} \cdot K^{-1}$
Before engraving	3.3	1.81	1.86
After engraving	6.5	1.86	1.87

Table 4:1 Results of emissivity determined form the FTIR measurements performed before and after engraving on the same coated glass. The calculated U value was calculated taking into account the measured emissivity for the full low-e coating and the engraved one. The measured U-value was for a double glazing with 10 mm air gap and an ablated linewidth of 25 µm (these samples were produced in a cleaner atmosphere and thinner lines could be obtained). The measurement uncertainty is ±0.04 $W \cdot m^{-2} \cdot K^{-1}$. Adapted from (Bouvard, 2017a) and (Burnier, 2017).

Table 4:1 also indicates the U-value of selected samples measured by the Fraunhofer Institute for Solar Energy Systems (Burnier, 2017). The measurement was performed on a double glazing similar to the one previously described with a size of 800 × 800 mm² to reduce possible edge effects. The average width of the ablated line was 25 µm. The ablated pattern was a grid with 2 mm spacing which correspond to an ablated area of 2.5 %. The difference between the two measured values is below the uncertainty of the measurement. It can be concluded that the ablation of a small area of the low-e coating (< 2.5%) has a negligible impact on the thermal properties of the window.

4.1.4 Optical properties and visual appearance

After engraving, the glass panes were assembled into double glazing (with an air gap of 12 mm) to resemble a common window; optical measurements were performed on the obtained samples. Figure 4:5 displays the direct transmittance in the solar spectral range (UV, visible, NIR) of the double glazing composed of the conventional low-e coating and the one with a structured coating (2 mm spacing square grid pattern).
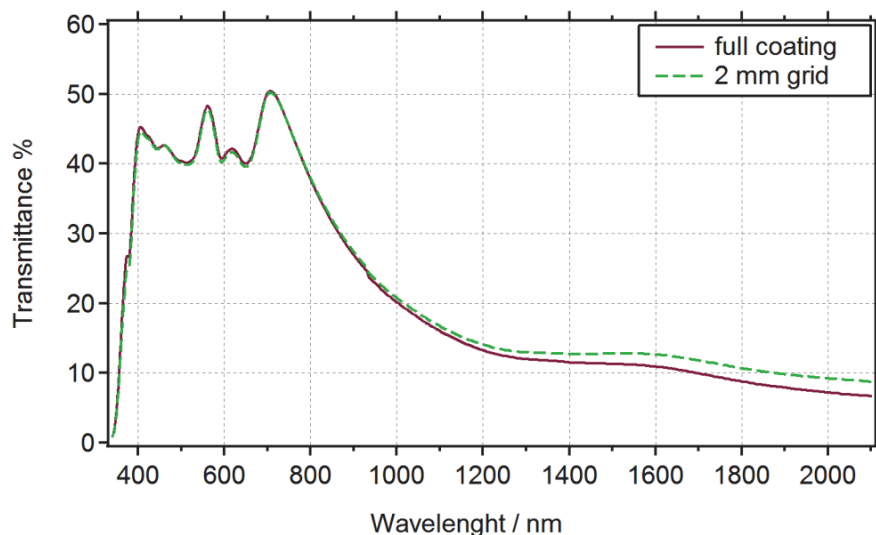
Figure 4:5   Optical transmittance in the solar spectrum range of the double glazing with full low-e coating (full coating) and with laser structured low-e coating (ablated lines width of w = 37 ± 2 µm, spacing D = 2 mm in square grid pattern). Reproduced from (Bouvard, 2017a).

The two spectra are similar; the three peaks visible around 400, 600 and 800 nm are due to spectral features from the grey glass used as second glass pane. A difference can be observed from 1200 nm to 2100 nm where the structured coating is slightly more transparent. This can be explained since a part of the low-e coating which also acts as a solar protection is removed. The solar protection aims at reducing the amount of invisible solar energy (mainly the near infrared) entering the room to prevent overheating. From 400 nm to 800 nm, the measured values are comparable: it shows that the laser treatment does not alter the direct transmittance in the visible range. It was observed that the pattern is not visible in most lighting situations. Figure 4:6 displays photographs of the sample with a 2 mm line spacing.
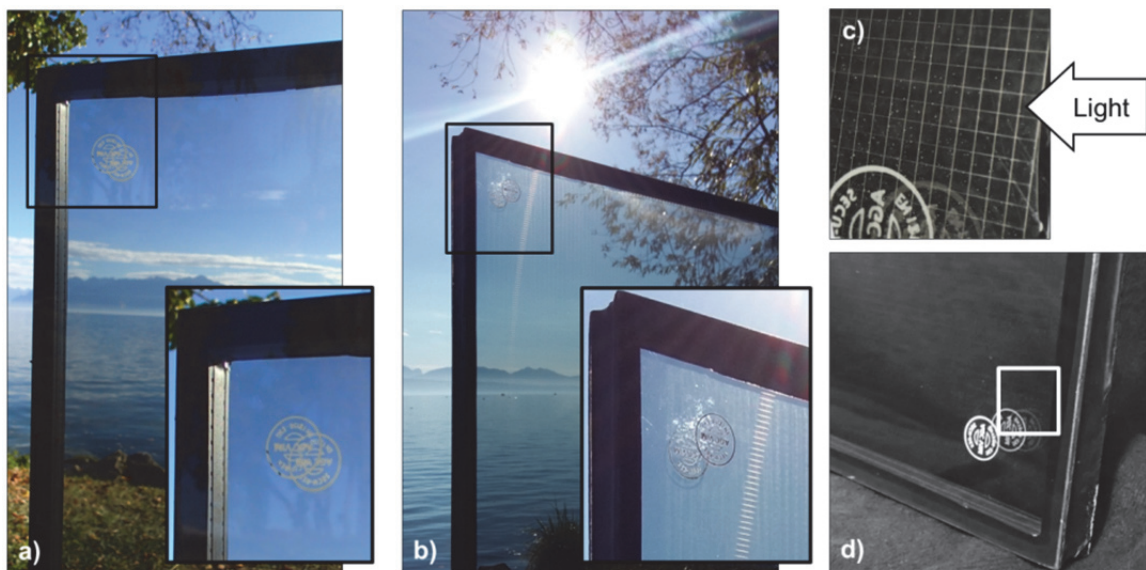
Figure 4:6   Photograph of a double glazing window with laser structured low-e coating (pattern with a line spacing of 2 mm). a) Photograph of the sample in common outdoor conditions. The focus is on the frame, the background is blurry and the pattern is indiscernible. A zoom on the top left corner of the glass is presented in the inset. b) Contre-jour photograph of the sample, in these backlit conditions the pattern can only be distinguished in reflection. The inset shows a zoom of this reflection. c) The pattern is revealed in extreme conditions, here by directing a strong illumination on the sample at grazing incidence. d) Photograph of the sample in indoor conditions with artificial light and a dark background. Reproduced from (Bouvard, 2017a).

In Figure 4:6 a), representing a common situation, the pattern is not visible even though the focus was on the window. Figure 4:6 b) exhibits the specific case with strong backlighting. The pattern appears in the reflection of the sun beam; the other parts of the window remain clear. In Figure 4:6 c) and d), a dark environment was set up in the laboratory. For the image in Figure 4:6 c), a strong illumination was directed towards the sample at a grazing incidence to reveal the pattern, while in Figure 4:6 d), in ambient light, the pattern is not visible. Along with a high transmission of microwaves, the low visibility of this laser pattern is a key element for user acceptance.

4.1.5 Measured attenuation of the microwaves

4.1.5.1 Square grid pattern

The interruption of the electrical conductivity at a scale much smaller than the considered wavelength is expected to enhance microwave transmission. As presented in section 4.1.1, the size of the pattern (D) modifies the capacitive behavior of the coating. Figure 4:7 a) illustrates the measured microwave attenuation of the studied double glazing, composed of a first glass pane of grey glass with a thickness of 5 mm, a 12 mm air gap, and a second glass pane, 4 mm thick, either coated with a commercial low-e coating, uncoated (float glass) or with a laser structured coating. The pattern obtained by laser ablation is composed of parallel and perpendicular straight lines forming a grid, thus resulting in square patches of low-e coating. The spacing D between the lines in horizontal and vertical directions is identical and is varied from 2 mm to 40 mm.
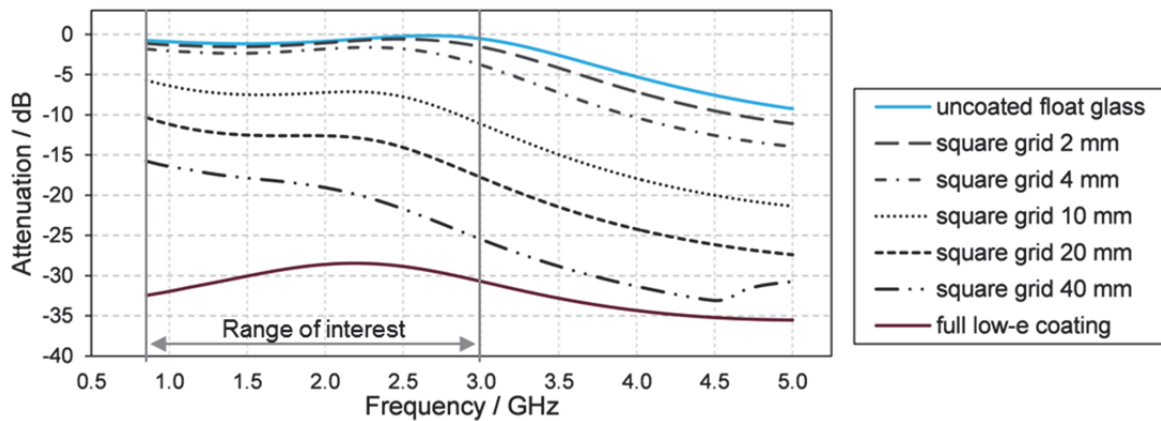
Figure 4:7   Measured attenuation in the mobile communication range (0.850-5 GHz) for the double glazing without coating (uncoated float glass), with full low-e coating and with laser structured low-e coatings in square grid patterns (ablated lines width of w=37 ± 2 µm, spacing D from 2 mm to 40 mm, respectively 4 % to 0.2 % of ablated area). Reproduced from (Bouvard, 2017a).

The window with a full low-e coating exhibits a strong attenuation of the microwaves (-25 dB to -32 dB) in the range of interest (850 MHz – 3 GHz). In contrast, the attenuation of microwaves is very low for a double glazing composed of uncoated glass: less than -1.3 dB for frequencies below 3 GHz. For the laser-structured coatings, the microwave attenuation varies dramatically with the size of the pattern D. Nevertheless, the pattern with D = 40 mm, which represents a surface of ablated coating as small as 0.2 % already reduces the attenuation from -30 dB to -12 dB at 850 MHz. As the line spacing is decreased, the microwave attenuation is decreased: for the pattern with D = 4 mm, the attenuation is less than 5 dB between 850 MHz and 3 GHz. The values obtained for the smallest spacing studied (D = 2 mm) are extremely close to the one of the substrate. The difference between the two samples is ranging from 0.2 dB to 0.6 dB below 3 GHz. By removing less than 4% of the coating, a transparency to microwaves close to that of uncoated glass is achieved. Furthermore, it is

important that the microwave attenuation remains low for a wide range of angles of inci-
dence. Numerical simulations were performed at SUPSI in order to forecast the behavior of
the double glazing window with and without the structured coating. It was shown that the
angular dependent response is dominated by the behavior of the uncoated glass (Bouvard,
2017a). Therefore, the proposed window with structured coating is expected to perform
nearly like an uncoated glazing for a large range of frequencies and even at high angles of
incidence.

4.1.5.2 Alternative pattern

The pattern made by laser ablation is barely visible when looking through the windows.
However, in some cases such as strong reflection or strong backlighting, the pattern may
appear. An interesting alternative to the square patch pattern might be the hexagonal patch
pattern due to its advantageous perimeter to area ratio (Hales, 2001). However, this pattern
does not feature uninterrupted straight lines, and would therefore imply a longer pro-
cessing time and would require a higher precision level in high-speed and large-scale pro-
duction.

Another alternative pattern which could be easier to fabricate compared to the hexagonal
pattern is a pattern made of equilateral triangle patches. A triangle pattern was obtained by
engraving lines with an angle of 60° resulting in patches of equilateral triangles with a
height of 6 mm: the ablated area is about 2 %. Figure 4:8 displays the attenuation as a func-
tion of the frequency of a triangle pattern. Uncoated glass and low-e coated glass as well as
the grid pattern with 4 mm (corresponding to 2% ablated area) are reproduced for compar-
ison.
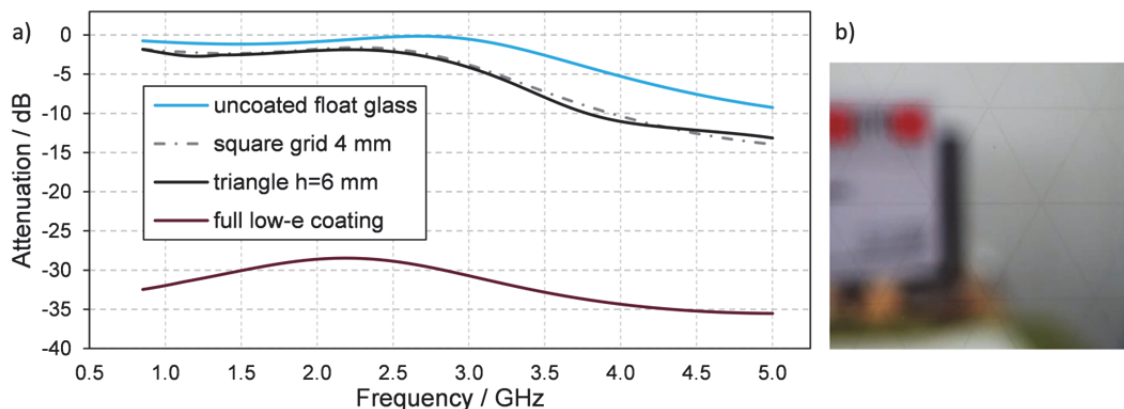
Figure 4:8   a) Measured attenuation in the mobile communication range (0.850-5 GHz) for the double glazing with-
out coating (uncoated float glass), with full low-e coating and with laser structured low-e coatings in equilateral
triangle patterns (ablated lines width of w=37 $\pm$ 2 µm, height of the triangle h= 6 mm, 2 % of ablated area) and
square grid pattern (2 % of ablated area) b) photograph of the coating with the triangle pattern, even with a focus
on the glass pane, the pattern can hardly be observed. Adapted from (Bouvard, 2017b).

Figure 4:8 a) shows that an attenuation lower than 3 dB between 0.85 and 3 GHz can be achieved with the 6 mm height triangle pattern. Expressed in relative terms, it means that 60% up to 85% of the signal is now transmitted by the low-e glass, whereas the fully coated glass (standard low-e), which presents a shielding effect larger than 30 dB, transmits only 0.1% of the signal. This result indicates that not only squares but also triangle patterns can be used. Figure 4:8 b) shows a photograph of the coated glass with a triangle pattern. This photograph was taken with a focus on the pattern, still not very visible. Thanks to the narrow width of the ablated lines, the patterns are barely visible when looking through the window. The fabricated patterns (square and triangles) were simulated at SUPSI (Lanini, 2015). The simulated and experimentally determined attenuation showed good agreement. Other patterns were simulated and provided a similar band pass effect (Lanini, 2015). Therefore, custom patterns with conductive patches of different shapes could be envisaged. Numerical simulations should be used beforehand in order to assess their viability.

4.1.6 Discussion and perspectives

A wide band pass is desired for compatibility with the future evolution of frequencies used for telecommunications; furthermore, the angular dependent transmittance is less critical for a wide band pass: the used grid and triangle patterns fulfil these conditions. The cut-off frequency f_{-3dB} shall be high enough for todays' and future mobile communication; this can be assured by making D sufficiently small. An upper limit for w can then be defined taking into account the desired ratio w/D: too small w can result in a decrease of f_{-3dB}, which is not desired. When w becomes comparable to the thickness of the conductive coating, an additional capacitive effect can be expected, since the structure can then no longer be considered as two-dimensional. Furthermore, the requirement of a low thermal emissivity implies that the surface of ablated coating shall be relatively small, and it defines an upper limit for w/D. Further practical limitations for w are given by the quality of the environment of the laser engraving setup (dust particles), and available lasers and optics. The range of linewidths from 10 μm to 50 μm, in combination with millimetric line-to-line distances D, turned out to represent a reasonable compromise being compatible with all theoretical and practical boundary conditions.

The mechanical properties of the windows are designed to resist mechanical shocks and pressure variations and a treatment should not modify the durability of the substrate. Mechanical resistance was tested by Burnier et al. (2017) using a coaxial double ring test setup. Calculations were performed according to the Roark formula (Young, 2012). Tempered glass with full low-e coating was used as reference. It was shown that the mechanical properties of the glass pane where the pattern was scribe before tempering were not modified. A small reduction of the maximum constrain was observed for the glass panes where the coat-

ing was scribed after tempering. This suggests that the laser treatment has an effect on the mechanical properties when performed after tempering. Laser ablation produces a heat affected zone which might induce thermal stress in the glass. During tempering, compressive and tensile stresses are used to toughen the glass and make it crumble when it breaks which reduces the risk of injuries. This operation might release the stress due to a laser ablation performed with excessive power. The line width of ablated coating for the samples used for the mechanical test was 25 μm. This was obtained thanks to a better focus and a clean environment during laser ablation; however, the power was similar to the one used for the 40 μm line. Laser power and focus could then be adjusted to limit the extent of this heat affected zone. Therefore, we consider that with carefully chosen parameters, laser processing would not impact the mechanical properties of the glazing.

The selected grid pattern with a linewidth of 10-40 microns has a negligible impact on the direct optical transmittance, thermal properties and the visual appearance of the glazing. This is a key parameter for this new structured coating to be used in replacement of a conventional window. As buildings and trains have a long lifetime, the materials used in their construction should withstand at least 25 years. Compared to these time scales, communication technology evolves very rapidly. Repeaters used in trains and buildings consume energy. The typical power consumption of one repeater is in the order of several tens of kWh per day. In addition to that, they need to be replaced when the frequencies used for telecommunications change. A system to improve the propagation of microwaves which does not require electricity to operate is desirable.

4.1.6.1 Application in Swiss regional trains

The patterned low-e coating was developed for regional Swiss trains in order to improve the thermal properties of the wagon without the need to install repeaters. Following this study, large scale prototypes were fabricated by the industrials partners AGC Verres Industriels Moutiers and Class4Laser to be installed in regional trains from the railway company BLS. A first train was equipped with the prototype windows and tested by SUPSI and Swisscom in real conditions (Burnier, 2017). The study revealed that the transmission of microwaves in the prototype train was similar to the one with uncoated windows. Figure 4:9 shows the BLS train equipped with the prototype windows. Looking through the windows, the pattern is indiscernible.

Figure 4:9   Train from the BLS equipped with the newly developed coating. The pattern can only be seen with a strong lighting and focusing on the glazing.

It can be observed only under strong lighting and focusing on the glazing. Incidentally, the operators who installed the prototype windows did not notice a difference compared to the usual uncoated windows and no remarks were received from the customers. This low-e coating with high microwave transmission is a promising alternative to repeaters and has already been installed in 10 trains RABe 525 NINA from the BLS as of November 2017.

4.1.6.2 Towards application in the building sector

This technology could be interesting for the building sector although a better understanding of wave penetration in large structures would be needed (Burnier, 2017; ITU-RM, 2015). Table 4:2 gives the shielding efficiency, or attenuation, of common building materials for three frequencies of interest for the mobile telecommunications: 900 MHz, 1800 MHz and 3 GHz. These results are extracted from the extensive study performed by the National Institute of Standards and Technology (NIST) (Stone, 1997), a study by Asp *et al.* (2012) and published results from this work (Bouvard, 2017a; Bouvard, 2017b). The results displayed in Table 4:2 indicate that most non-metallic materials have a low attenuation (or shielding effect) to the transmission of the microwaves. Concrete alone presents a strong attenuation even when it is not reinforced with a metallic grid: this can be explained by its high density. For comparison, a masonry block of the same thickness (with hollow compartments) shows a 3 times lower attenuation. A comparison of a polyurethane insulation board with and without aluminum foil was performed by Asp et al. (2012): it clearly highlights the influence of the metallic foil on the shielding effect. The insulation board alone is almost transparent to microwaves while one with an aluminum foil shows attenuation levels close to those of 200 mm of concrete. The effect is comparable for uncoated glass compared to glass coated with a low emissivity -hence conductive- coating. Results from this work and from Asp et al. (2012) show that coated glass (one or two coated panes) has a strong attenuation, of the same order of magnitude as reinforced concrete or insulation board with a metallic foil.

It can be observed that the thickness of the air gap in the windows has an influence on the attenuation of a double glazing due to the formation of constructive or destructive interferences (Bouvard, 2017b). It can also explain the fact that double glazing can have a lower attenuation than single glazing.

	Material	Source	Shielding effect / dB		
			900 MHz	1800 MHz	3 GHz
Construction material	Plywood (dry) 19 mm	(Stone, 1997)	-0.7	-1.2	-0.9
	Lumber (dry) 114 mm	(Stone, 1997)	-2.8	-6.4	-13
	Brick 178 mm	(Stone, 1997)	-5	-7	-16
	Masonry block 203 mm	(Stone, 1997)	-8	-11	-15
	Concrete 203 mm	(Stone, 1997)	-23	-28	-47
	Reinforced concrete 203 mm + metallic grid 70 mm	(Stone, 1997)	-30	-35	-53
Insulation Material	Glass wool 100 mm	(Asp, 2012)	~0	~0	~0
	Polyurethane insulation board 100 mm	(Asp, 2012)	~0	~0	~0
	Polyurethane insulation board with aluminium 100 mm	(Asp, 2012)	-23	-34	-35
Glazing	Glass pane 6 mm	(Stone, 1997)	-0.8	-1.3	-1.9
	Double glazing 4 mm/air 12 mm/5mm	(Bouvard, 2017a)	-0.8	-1.1	-1.2
	Double glazing with commercial low-e 4 mm coated/air 12 mm/5mm	(Bouvard, 2017a)	-30.6	-26.8	-27
	Double glazing with 2 coated glass	(Asp, 2012)	-23	-30	-36
Glazing with patterned low-e	Double glazing with square pattern (4 %) low-e coating 4 mm coated/air 12 mm/5mm (measured)	(Bouvard, 2017a)	-1.3	-1.3	-1.9
	Double glazing with triangle pattern (2 %) low-e coating 4 mm coated/air 12 mm/5mm (measured/*simulated*)	(Bouvard, 2017b)	-2.0/*-2.0*	-2.3/*-2.2*	-4.0/*-3.9*
	Double glazing with triangle pattern (2 %) low-e coating 4 mm coated/air 8 mm/5mm (*simulated*)	(Bouvard, 2017b)	*-2.1*	*-3.2*	*-1.5*
	Double glazing with triangle pattern (2 %) low-e coating 4 mm coated/air 16 mm/5mm (*simulated*)	(Bouvard, 2017b)	*-1.8*	*-1.4*	*-7.1*

Table 4:2 Comparison of the attenuation of common building materials and patterned low-e coating. Reproduced from (Bouvard, 2017b).

Figure 4:10 presents some of the data given in Table 4:2 in a graphical way. Modern buildings, especially in the service sector, are often highly glazed and with a structure in reinforced concrete. Furthermore, in order to increase the thermal energy efficiency, insulation board often contain a metallic foil and the thermal transmittance required for glazing implies the use of low-e coatings. As highlighted in Figure 4:10 and Table 4:2, these construction materials attenuate strongly the transmission of microwaves. The microwave propagation is not a factor taken into account in the design of a building and poor network reception can occur. It might be difficult for the inhabitants or the users of a building to know why network quality is so low in the new building, the only solution available today being to install an amplifier inside. We hope that this newly developed coating can provide an alternative to repeaters for future buildings.
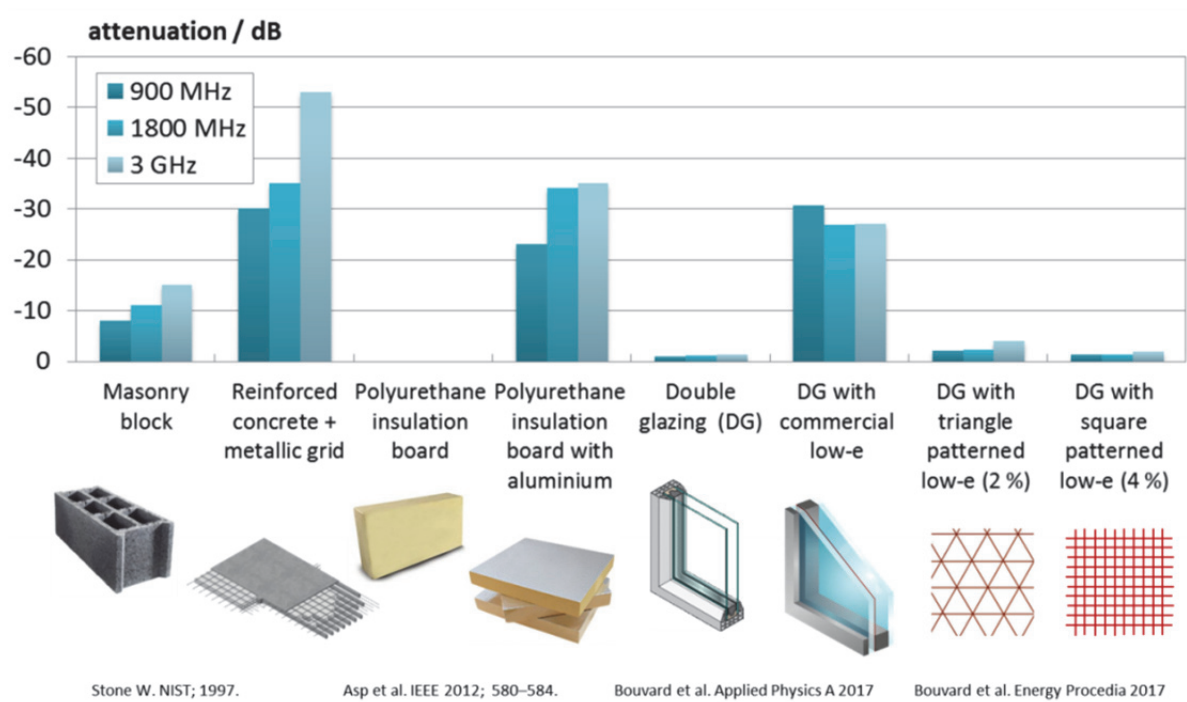
Figure 4:10   Illustration of the attenuation of some common building materials and patterned low-e coating presented in Table 4:2. For patterned low-e, the indicated percentage corresponds to the ablated area. Metallic layers greatly increase the attenuation to microwaves. Patterned coating can reach levels of attenuation nearly as low as uncoated glass.

4.2   Indium tin oxide electrodes for electrochromic devices

Transparent electrodes are required to transport charges in order to modulate the optical properties of electrochromic materials. Despite the price and scarcity of indium, indium tin oxide (ITO) is still commonly used as it presents the best compromise of high optical transparency and high electrical conductivity (Zhang, 2016). Alternatives to ITO are being developed in numerous research department and industries worldwide (Ghaffarzadeh, 2018; Cao, 2014; Ellmer, 2012; Granqvist, 2007). Since the main focus of this work was on the solid state device more than on the transparent electrode itself, ITO was used as a transparent electrode for the electrochromic devices of this study. Glass slides pre-coated with ITO of different sheet resistivities were studied and used as substrate. A second ITO coating made by sputtering was needed for the top layer of the solid state electrochromic devices. Usually, ITO is deposited at high temperature (e.g. above 200°C). However, in the case were ITO has to be deposited on a multilayer stack, heating might cause unwanted diffusion or crystallinity modifications in the stack materials. Furthermore, in a large-scale coater, it is difficult to obtain a homogeneous distribution of the temperature on the glass pane.

Therefore, it is important to achieve good electrical and optical properties without using substrate heating: sputtering targets of In_2O_3/SnO_2 ceramic alloy (90/10 wt%) were used. ITO coatings were deposited by magnetron sputtering and their optical and electrical properties were evaluated.

4.2.1 Characterization of commercial ITO substrates

ITO substrates from Delta Technologies were used as substrates for depositions of electrochromic oxides; their optical and electrical properties were characterized. Figure 4:11 displays the spectral transmittance of four commercial ITO in the solar spectrum range; they all exhibit a large transmission in the visible range. The transmission in the near infrared range is related to their sheet resistivity. The sample with the lowest sheet resistivity (9-15 Ω/sq) has the lowest transmittance in the near infrared. When the carrier concentration increases (e.g. the resistivity decreases) the plasmon frequency increases and therefore its cut-off wavelength decreases (Brewer, 2002). The solar transmittance is therefore limited by the carrier concentration of the ITO (see Chapter 2).
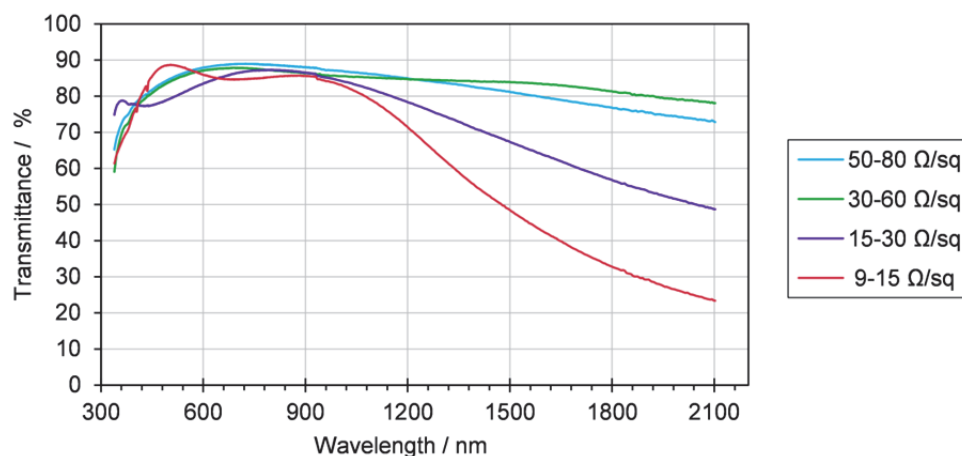
Figure 4:11   Spectral transmittance of commercial ITO with various sheet resistivities. When the sheet resistance decreases e.g. the carrier concentration and mobility increases, the cut-off frequency and thus the transmittance in the near-infrared decreases.

Table 4:3 indicates the labelled and measured sheet resistivity along with the solar and visible transmittance. The sheet resistivity was measured in a square configuration according to the van der Paw method (see Chapter 3).

Sample	Labelled sheet resistivity Rs_l / Ω/sq	Measured sheet resistivity Rs_m / Ω/sq	Solar transmittance τ_e / %	Visible transmittance τ_v / %
X174	9-15	10.8	80	87
X190	15-30	20.8	81	82
X307	30-60	48.2	85	87
X306	50-80	62.0	84	86

Table 4:3 Optical and electrical properties of various commercial ITO.

The measured values are in agreement with the range indicated by the manufacturer. The solar and visible transmittances were calculated from the transmittance spectra as described in Chapter 3: they are ranging from 80 to 85 % and from 82 to 87 % respectively. Such high values are desirable for applications in glazing.

4.2.2 Study of ITO coatings deposited at room temperature

4.2.2.1 Deposition of ITO coatings by bipolar-pulse magnetron sputtering

In order to obtain the deposition parameters for the ITO layer needed on top of the electrochromic device, ITO coatings were first deposited on glass slides from In_2O_3/SnO_2 targets. The deposition parameters were varied until their optical and electrical properties were suitable; all depositions were performed at room temperature. As a starting point, parameters based on those of Hwang *et al.* (2003) were employed; they used bipolar-pulsed magnetron sputtering at relatively low temperatures. For these depositions, the frequency used was 50 kHz with τ_{OFF} = 2016 ns which gives a duty cycle of 90 %. Figure 4:12 shows the

spectral transmittance in the solar range of three samples deposited by bipolar-pulsed sputtering. The corresponding solar and visible transmittances are reported in Table 4:4 along with their resistivity.
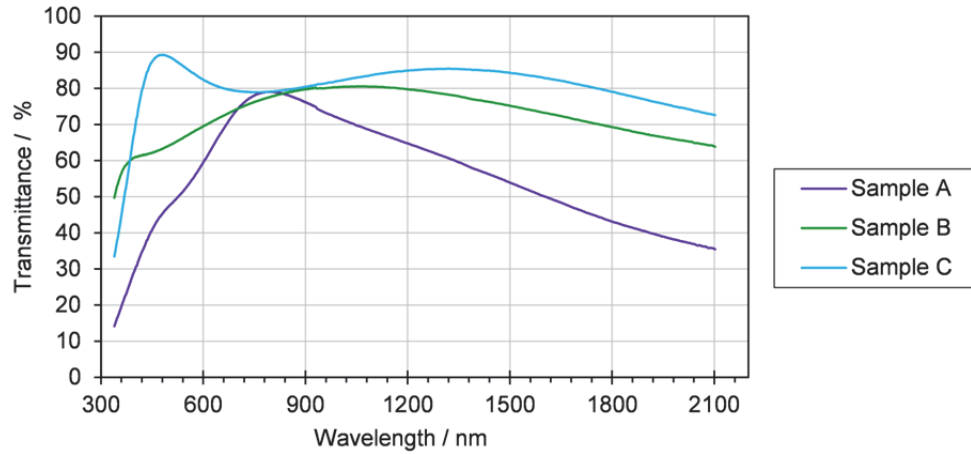
Figure 4:12   Spectral transmittance of ITO coatings deposited by bipolar-pulsed magnetron sputtering. Sample C exhibits a high transmittance in the visible and near-infrared ranges.

As suggested by the low transmittance in the blue part of the spectrum, the sample A has a brown color and was therefore not suited for the application. The sample B has a better visible transmittance however the sheet resistivity is too high. The sample C has a reasonable sheet resistivity of about 76 Ω/sq and excellent optical properties (τ_e=80.8 and τ_v= 85.0 %). The deposition parameters of this sample are an argon to oxygen ratio of 6.35 %, an applied power of 3.2 W/cm^2, a pressure during deposition of 2.4·10^{-3} mbar and a deposition time of 20 min: they were then used for some of the first solid state EC devices.

Sample	Thickness d / nm	Measured resistivity R_m / Ω.cm	Measured sheet resistivity Rs_m / Ω/sq	Solar transmittance τ_e / %	Visible transmittance τ_v / %
A - O80323	230	3.2·10^{-3}	138.7	59.7	54.1
B - O80326-1	60	3.5·10^{-3}	582.0	71.8	67.3
C - O80326-2	120	9.1·10^{-4}	76.1	80.8	85.0

Table 4:4 Optical and electrical properties of ITO deposited by MF magnetron sputtering. *Thicknesses were determined by ellipsometry except for O80326-2 which was calculated according to the deposition rate.

However, after few depositions, frequent arcing occurred: this may be due to an oxidation of the target or the formation of an insulating oxide due to the different sputter yields of In and Sn. Many flakes were present on the ITO sputtering target preventing to start the plasma. Further investigations on ITO were performed using radiofrequency (RF) power supply to reduce the thermal stress in the target.

4.2.2.2 Deposition of ITO coatings by radio-frequency magnetron sputtering

RF sputtering is commonly used for insulating or ceramic targets and was used in this study to deposit ITO films: the sputtering target has the stoichiometry of the desired ITO (In_2O_3 90 wt.%:SnO_2 10 wt.%). However, if no oxygen is added to the plasma, there is an oxygen deficiency in the final film leading to poor optical properties. Depositions were performed varying the oxygen ratio until sound optical and electrical properties were achieved. The deposition parameters are described in Table 4:5.

Sample	RF Power / W	Working pressure / mbar	Deposition time / min	O_2/Ar ratio
D - O80405	75	$3.6 \cdot 10^{-3}$	60	4.0 %
E - O80411	75	$3.6 \cdot 10^{-3}$	45	2.4 %
F - O80417	75	$3.6 \cdot 10^{-3}$	45	1.6 %

Table 4:5 Main deposition parameters of three samples deposited by RF sputtering.

Figure 4:13 shows the spectral transmittance in the solar range of three samples deposited by RF sputtering. The corresponding solar and visible transmittances are reported in Table 4:6 along with their resistivity.
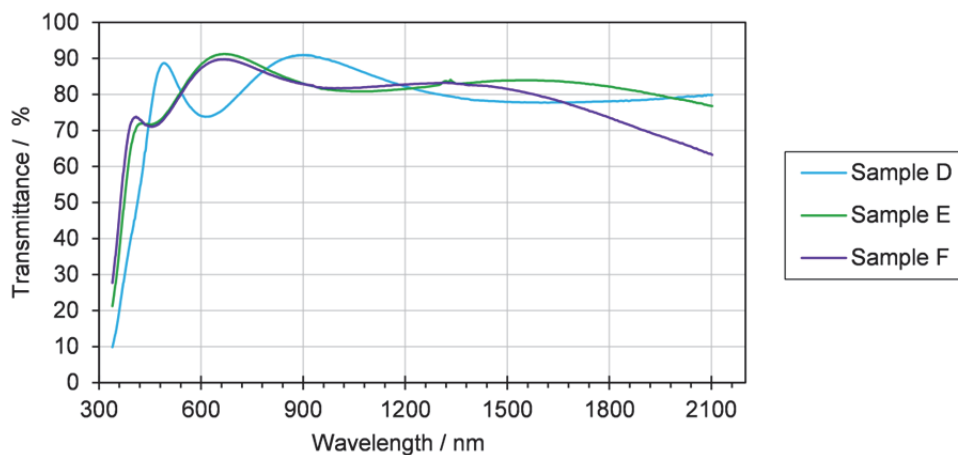
Figure 4:13   Spectral transmittance of ITO coatings deposited by RF magnetron sputtering.

The thickness of the samples was determined by ellipsometry using a Cauchy dispersion law in the transparent region (450-900 nm) and is shown in Table 4:6. The deposition rate is about 3.6 nm/min for the three samples. Sample D is thicker due to a longer deposition time. The resistivity in Ω.cm is independent of the thickness. Sample D was deposited with an oxygen to argon ratio of 4 % and exhibits a much higher resistivity compared to samples E and F which were deposited with an oxygen to argon ratio of 2.4 and 1.6 %, respectively.

Sample	Thickness d / nm	Measured resistivity R_m / Ω.cm	Measured sheet resistivity Rs_m / Ω/sq	Solar transmittance τ_e / %	Visible transmittance τ_v / %
D - O80405	220	$1.4 \cdot 10^{-2}$	647.5	78	78
E - O80411	160	$7.1 \cdot 10^{-4}$	43.8	81	83
F - O80417	160	$5.1 \cdot 10^{-4}$	31.9	81	82

Table 4:6 Optical and electrical properties of ITO deposited by MF magnetron sputtering.

Sample C, deposited by DC bipolar-pulse magnetron sputtering, exhibit similar transmittance than sample E and F, however, the resistivity of this sample is lower. RF magnetron sputtering usually gives rise to ITO thin films with better electrooptical properties; however, the deposition rate of RF is considerably lower than for DC (Lippens, 2012). Commercial ITO used as substrates for electrochromic devices exhibit a sheet resistivity ranging from 20 to 50 Ω/sq. Samples deposited in the laboratory without substrate heating should be in this range too. Sample F has a sheet resistivity of about 32 Ω/sq and is therefore suitable to be used as a top electrode. State of the art commercial ITO coatings show a resistivity in the order of $1–2 \cdot 10^{-4}$ Ω.cm (Ellmer, 2012) but these coatings are usually deposited at high temperatures (above 200°C). Hence, the resistivity of $5.1 \cdot 10^{-4}$ Ω.cm obtained for a sample deposited at room temperature (Sample F) is satisfactory. For comparison, David et al. (2017) obtained resistivities of 8 to $11 \cdot 10^{-4}$ Ω.cm for ITO coating deposited at room temperature by DC pulsed magnetron sputtering.

4.2.3 Structural properties of ITO coatings

In order to compare the ITO coatings bought from an industrial supplier and the one made in our laboratory, X-ray diffraction measurements were performed. Figure 4:14 shows the XRD patterns of two commercial ITO coatings and two samples deposited by magnetron sputtering in our laboratory. The commercial ITO coatings exhibit diffraction peaks at around 2θ = 21.2°, 30.3°, 35.2°, 50.7°, and 60.3°; they were assigned to the (211), (222), (400), (444), and (622) planes respectively, which are typical of a ITO cubic structure. For the sample X174 which has a labelled sheet resistance of 9-15 Ω/sq, the two main orientation are (222) and (400), with similar count intensity. For the sample X307, labelled 30-60 Ω/sq, the main orientation is (222) with an intensity around 2.5 times larger than the (400) peak. High temperature deposition is known to enhance crystallinity; therefore the diffraction patterns of the commercial ITO coatings confirm the assumption of a deposition at high temperature.

The samples made in the laboratory were deposited with no substrate heating. Their diffraction patterns do not display sharp peaks: this suggests an amorphous or nanocrystalline structure. The large bump situated around 32° is about 3.7° wide at half intensity for sam-

ple F. According to the Scherrer formula (see Chapter 3), it means that the majority of the crystalline grains are smaller than 2.2 nm.
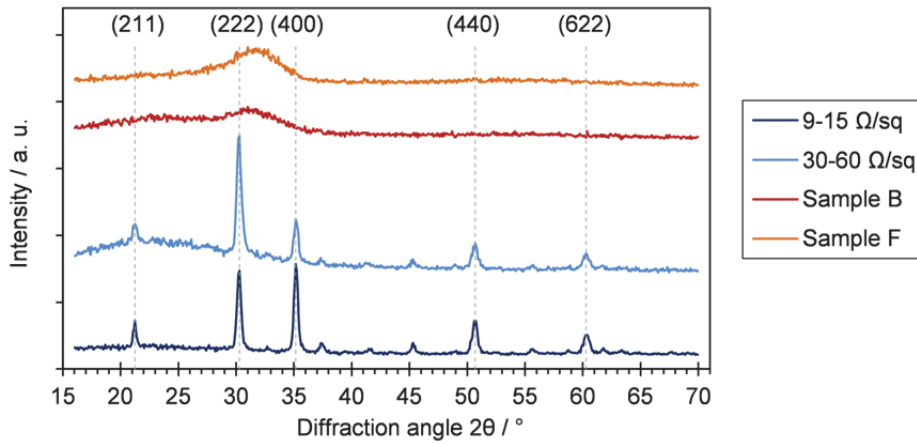
Figure 4:14   XRD patterns of commercial ITO coatings and sample deposited by MF and RF magnetron sputtering. Commercial coatings are crystalline while samples deposited at room temperature are amorphous.

Table 4:7 displays the measured sheet resistivity Rs_m, the energetic transmittance τ_e and the visible transmittance τ_v of five samples, whose XRD pattern are shown in Figure 4:14, including an additional commercial sample (X190) also used in some electrochromic devices. The sample F made by RF sputtering at room temperature, despite not being crystalline, exhibit a sheet resistivity in the same range than the commercial samples (X190 and X307) and high visible and energetic transmittance (similar to X190).

Sample	Rs_m / Ω/sq	τ_e / %	τ_v / %
X174 - 9-15 Ω/sq	10.8	80	87
X190 - 15-30 Ω/sq	20.8	81	82
X307 - 30-60 Ω/sq	48.2	85	87
B - O80326-1	582.0	72	67
F - O80417	31.9	81	82

Table 4:7 Optical and electrical properties of commercial ITO coatings and sample deposited by MF and RF magnetron sputtering.

4.2.4 Discussion and perspectives

ITO coatings are usually deposited at elevated temperature to obtain a better crystallization. Commercial ITO coated glass substrates were most probably deposited at temperature above 200°C or were annealed. This kind of ITO coating was used mostly as a bottom electrode, except in liquid state device were the anodic and cathodic electrochromic layers were each deposited on a commercial ITO coated glass. The effect of the sheet resistivity of the ITO layer on the switching properties of electrochromic devices was investigated and is detailed in Chapter 5 and 7.

In this study, the use of high temperature was not adequate for the top electrode because the ITO films are to be deposited on top of four other layers: heating could damage and/or modify the crystallinity of the underlying layers. Furthermore, coaters used in the glazing industry are large (up 3 m x 6 m), heating the glass homogeneously is challenging and energy intensive. Therefore, deposition parameters to obtain an ITO with satisfactory properties without heating the substrate are needed: bipolar-pulse and radio-frequency sputtering were used for that purpose. It was found that bipolar-pulse was causing arcing on the ITO target, resulting in short circuit which prevents starting the plasma. The pulse frequency, the off time and the duty cycle could maybe be adapted to prevent this. Another option generally used for non-conductive target was the use of a 13.56 MHz RF power supply. Depositions parameters appropriate to obtain an appropriate sheet resistivity were found. A resistivity $5.1 \cdot 10^{-4}$ Ω.cm was obtained which is comparable to state-of-the-art ZnO films and not far from the performances of commercial ITO films (Ellmer, 2012). For the thickness used in this study, it represents a sheet resistivity of 32 Ω/sq which is comparable to the commercial ITO coatings used as substrates.

Argon to oxygen ratio in the plasma proved to be of importance to obtain an ITO coating with high optical transmittance and low resistivity. Even if the target has the optimum stoichiometry (In_2O_3/SnO_2 90/10 wt%), if no oxygen is added to the argon plasma, the resulting film is too dark and display a brownish color. An optimum ratio of 1.6 % of oxygen versus argon was found to provide the required optical and electrical properties. This ratio depends on the pressure during the deposition ($3.6 \cdot 10^{-3}$ mbar) and the power applied to the target (3.7 W/cm^2). If these parameters were to be varied, the oxygen ratio should be adapted.

These experiments show that it is possible to obtain ITO coatings with satisfactory electrical and optical properties without heating the substrate or proceed to an annealing. These coatings are well appropriate for use as a top electrode and were used for solid-state electrochromic devices.

As detailed in Chapter 1, research on transparent conductors is an active field and many indium-free alternatives are investigated. Indium-free electrochromic devices were fabricated e.g. by Li et al. and Koubli et al. (Li, 2015; Koubli, 2015) using $WO_3/Ag/WO_3$ stacks where the WO_3 layers serve both as an electrochromic material and electrode. One could imagine using pyrolytic FTO coated glass as a substrate and a dielectric/Ag/dielectric stack, as a top electrode, to use materials which are well known in the glass industry.

Chapter 5   Electrochromic oxides

In this chapter, the two main layers of an electrochromic device are studied, e.g. the cathodic and anodic electrochromic oxides. Tungsten trioxide was considered first to be used as the cathodic oxide. More specifically, the influence of the deposition parameters, such as the oxygen to argon mass flow ratio and the working pressure, on the stoichiometry and the morphology was studied. The effect on the electronic and optical properties was investigated. The motivation was to determine if nanoporosity have a positive impact on the switching dynamics and contrast of the electrochromic film. Nickel oxide compounds were studied to be used as an anodic electrochromic oxide. The aim was to see if doping can improve the optical properties of the film as well as the ease of manufacturing. Finally, the two layers were assembled with a liquid electrolyte to form a device. This initial test with a liquid electrolyte serves as a preliminary experiment before testing solid-state devices. The optical properties were recorded while the device was colored and bleached upon intercalation and de-intercalation of lithium ions initially contained in the liquid electrolyte. These experiments were conducted to get a better understanding of the limiting factor in the switching dynamics.

5.1   Cathodic electrochromic oxides based on tungsten trioxide

In sputtering deposition, the working pressure is known to have a strong influence on the morphology. Its effects on the optical and electronic as well as the switching behavior of tungsten trioxide were analyzed and are presented in the following sections.

5.1.1 Influence of the chemical composition on the electronic properties

Some parts of the text and images below are reproduced from : Bouvard, O., Krammer, A., Schüler, A., 2016. In situ core-level and valence-band photoelectron spectroscopy of reactively sputtered tungsten oxide films: In situ XPS and UPS study of reactively sputtered tungsten oxide films. Surface and Interface Analysis. https://doi.org/10.1002/sia.5927

The effect of modifying the total working pressure on the chemical composition and the electronic properties of the film were studied. XPS is used to determine the stoichiometry of

the films and to detect the oxidation state of tungsten. Furthermore, we use UV photoelectron spectroscopy to observe the influence of the oxidation state of tungsten on the density of state of the valence band below the Fermi edge, where contribution of tungsten in a reduced oxidation state is expected.

During deposition, the O_2/Ar mass flow ratio was kept at $O_2/Ar = 0.48$, while the total pressure of the chamber was varied. Three samples were deposited, the total working pressure used was: $2.4 \cdot 10^{-2}$ mbar for sample 1, $3.1 \cdot 10^{-3}$ mbar for sample 2 and $2.4 \cdot 10^{-3}$ mbar for sample 3. The deposited tungsten oxide samples were studied by XPS, the corresponding spectra being shown in Figure 5:1.
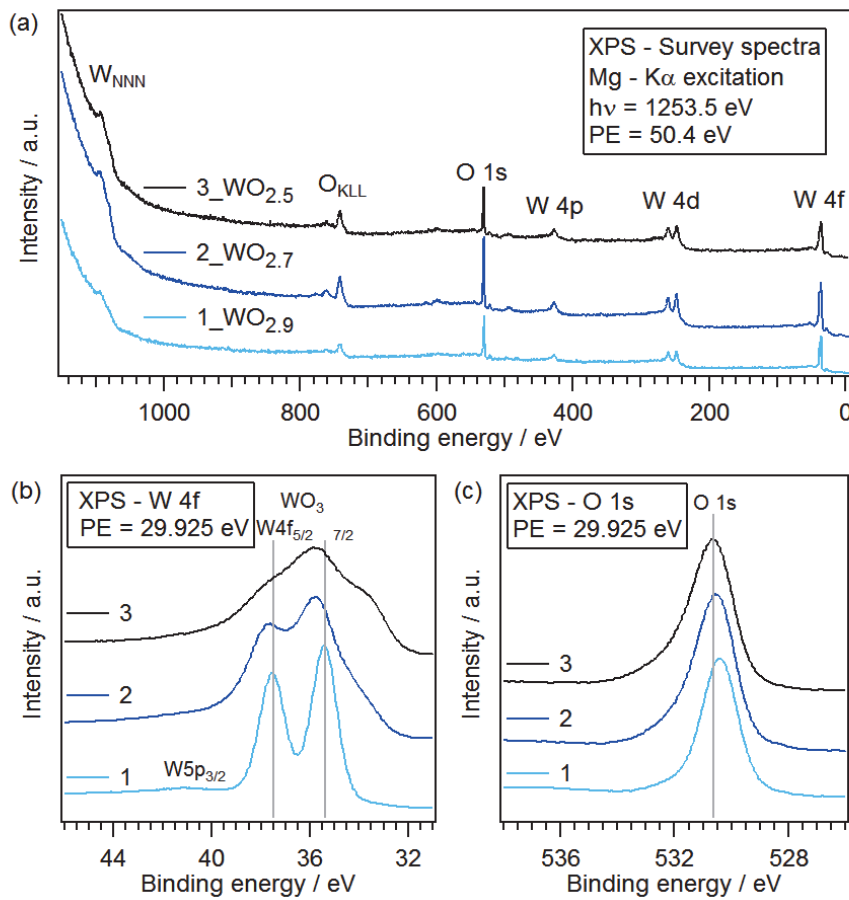
Figure 5:1 a) XPS survey spectra of the three samples b) Core level spectra of W 4f doublet. c) Core level spectra of O 1s peak. The peak position of W $4f_{7/2}$, W $4f_{5/2}$ and O 1s are from Ho (1987) and Naumkin (2012).

The survey spectra are shown in Figure 5:1 a), the legend refering to the stoichiometry of the samples given in Table 5:1. The Auger peaks of W_{NNN} and O_{KLL} and the core-level peaks of O 1s, W 4p, W 4d and W 4f can be observed. Thanks to the in situ transfer, external contamination is very limited, the carbon peak C 1s is not observed. Sputtering by argon ion is therefore not necessary and the surface can be observed as deposited. This is advantageous

because it was shown that argon ion sputtering can lead to a reduction of tungsten and would modify the obtained spectra (Xie, 2012).

Figure 5:1 b) shows the core level spectrum of W 4f: it can be observed that the three samples exhibit spectra of the W 4f peak with different shapes. For the three spectra, the small and broad feature visible at 41 eV is attributed to the contribution of W $5p_{3/2}$ (Bussolotti, 2003). Sample 1, deposited at high working pressure, shows a well-resolved doublet peak due to W $4f_{7/2}$ and $4f_{5/2}$ orbitals. The position of the peak W $4f_{7/2}$ is positioned at approximatively 35.4 eV and the doublet separation is ΔE_B= 2.1 eV, which is in agreement with the literature (Ho, 1987; Naumkin, 2012). Sample 2, deposited at a lower working pressure, presents a broad shape for the W 4f doublet. The two peaks W $4f_{5/2}$ and W $4f_{7/2}$ are positioned at approximatively 37.8 eV and 35.8 eV respectively. At approximately 34 eV, a small shoulder can be seen. Sample 3, deposited at the lowest working pressure of this study, displays a complex shape of the W 4f peak. The position of the maximum of this broad peak, which seems to be a superposition of different features, is located at 35.8 eV. The shoulder around 34 eV is more marked than in sample 2.

Figure 5:1 c) shows the spectrum of the O 1s peak: the line indicates the position 530.5 eV (Naumkin, 2012). A very slight shift towards higher binding energy can be observed from sample 1 to sample 3. In addition, the O 1s peak of sample 2 and 3 is slightly asymmetric with a tail towards higher energy.

Furthermore, XPS provides information on the chemical composition of the studied films. The element concentrations are determined by integration over the W 4f and O 1s core-level signals after subtraction of a Shirley background (Shirley, 1972). The obtained atomic concentrations are displayed in Table 5:1. Sample 1, deposited at a higher working pressure, contains more oxygen than the other samples. Thus, it can be observed that the oxygen content of the films is strongly affected by changing the total working pressure of the chamber.

Sample	Working pressure	O / at. %	W / at. %	O:W at. ratio
1	$2,4.10^{-2}$ mbar	74.1	25.9	2.9
2	$3,1.10^{-3}$ mbar	72.9	27.1	2.7
3	$2,4.10^{-3}$ mbar	71.8	28.2	2.5

Table 5:1 Chemical composition obtained from integration of O 1s and W 4f core level peaks.

It was observed that only sample 1 is transparent; the samples 2 and 3 show a dark blue coloration. Similarly to the samples in section 5.1.2, the measurement of the optical trans-

mittance reveals that this dark blue coloration is similar to the one obtained upon insertion of lithium.

For a better understanding of the complex shapes of the W4f peaks, a deconvolution based on a Shirley background and void profiles with Gaussian and Laurentzian contributions was performed using CasaXPS software. The contributions from the three oxidation states are illustrated in Figure 5:2. The relative intensity used for the peak area ratios of the spin-orbit doublets was set to 3:4 for the $W4f_{5/2}$:$W4f_{7/2}$ ratio (Ho, 1987). In the spectrum of each sample, three peak components have been identified for each oxidation state of W, these components correspond to the two peaks of the doublet W4f and the peak from $W5p_{3/2}$.
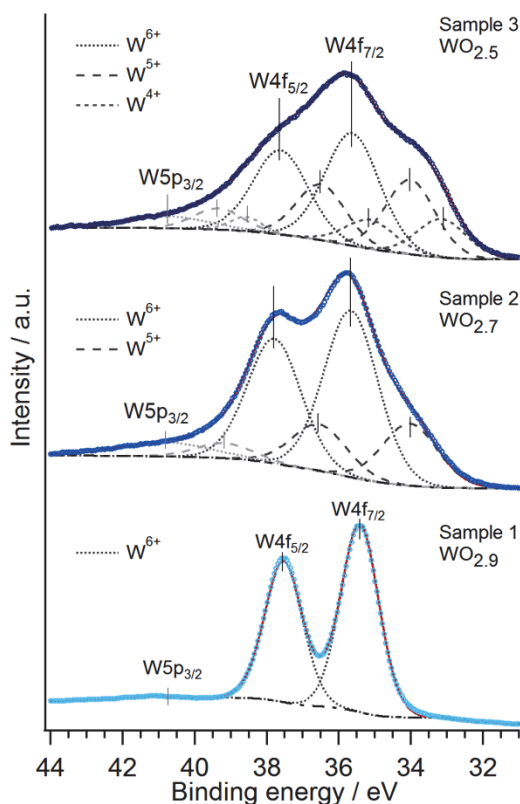
Figure 5:2 Deconvolution of the W4f doublet. Experimental data is shown with open circle. A Shirley background has been used and is represented by the dash-dot line. Contributions of the $Wf_{7/2}$ and $W4f_{5/2}$ peaks are shown in dark grey. Contributions of the $W5p_{3/2}$ peaks are displayed in light grey. Oxygen vacancies induce a reduction of the oxidation state of the tungsten atoms.

In sample 1, the shape of the spectrum reveals a well resolved doublet of the W 4f peak, it is attributed to the doublet W4f of stoichiometric WO_3 (W^{6+}). The small feature around 41 eV is attributed to the $W5p_{3/2}$ core level. The peak position of the $W4f_{7/2}$ core level peak was found at 34.4 eV and the W4f doublet separation is 2.1 eV which is in accordance with the literature (Ho, 1987). For sample 1, the Full Width at Half Maximum (FWHM) of the $W4f_{5/2}$ and the $W4f_{7/2}$ peak was found to be similar. It was fixed as a constraint for sample 2 and 3 to have identical FWHM for the two peaks of a same doublet.

For sample 2, the measured data presents a broader spectrum. The peak fitting shows the contribution of the doublet and $W5p_{3/2}$ for two oxidation state of tungsten: W^{6+} and W^{5+}. The $W4f_{7/2}{}^{5+}$ peak is located at approximately 34.1 eV which is close to values found in literature (Romanyuk, 2006).

The core level spectrum obtained from sample 3 has a broad and complex shape in which the W4f doublet cannot be distinguished. This feature can be explained by the superposition of the W4f doublets and the $W5p_{3/2}$ peak of three oxidation states of tungsten: W^{6+} and W^{5+} and a small contribution of W^{4+}. The peak positions of the three $W4f_{7/2}$ peaks are found to be 35.7 eV for W^{6+}, 34.1 eV for W^{5+} and 33.1 eV for W^{4+}. The $W 4f_{7/2}$ peak of the W^{4+} oxidation state is usually positioned at 32.9 eV (Naumkin, 2012). Studies suggest that the W^{4+} oxidation state can only be found in tungsten oxides films with an O:W ratio smaller than 2.6 (Niklasson, 2004; Stolze, 2002). In our case, sample 3 has an O:W ratio of 2.5 and therefore the presence of the W^{4+} oxidation state can be envisaged.

The O 1s peak is symmetric for sample 1 (near-stoichiometric tungsten trioxide), which is expected for dielectric films. However, sample 2 and sample 3 show a slight asymmetry with a tail towards the higher binding energies. This feature was already observed in other studies (Romanyuk, 2006) and might be due to oxygen atoms in a not fully oxidized local environment due to the sub-stoichiometric tungsten oxide.

From XPS measurements, it was possible to determine the stoichiometry of the samples directly after sputter deposition. The O:W ratio of the three samples was found to be approximately 2.9, 2.7 and 2.5 for sample 1, 2 and 3 respectively. The first sample is therefore a near-stoichiometric tungsten trioxide and sample 2 and 3 are oxygen poor WO_{3-x} with $0.3 \leq x \leq 0.5$. From a visual appearance, sample 1 is clear transparent, while sample 2 and 3 are dark blue. Bondarenko (2015) showed that defects such as oxygen vacancies can give rise to coloration in tungsten oxide.

UV photoelectron spectroscopy provides further information on the density of states of the valence band of the materials. Figure 5:3 shows the valence band spectra of the investigated tungsten oxides obtained by UV photoelectron spectroscopy (Helium discharge lamp, $h\nu$ = 21.22 eV).
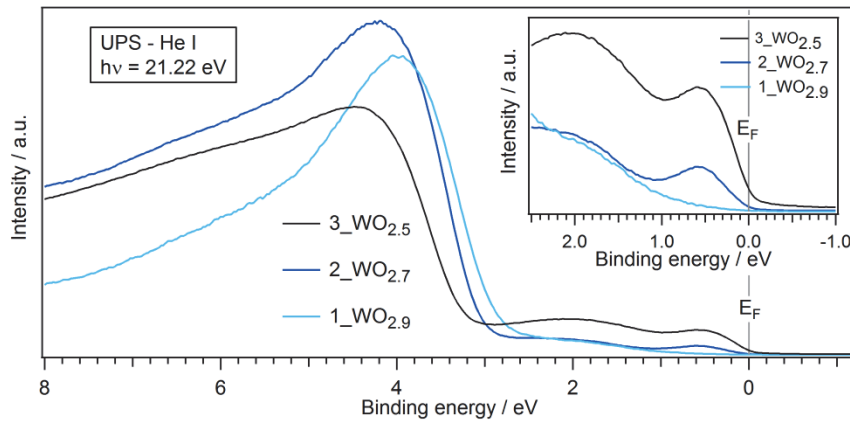
Figure 5:3   He I valence-band spectra obtained from the $WO_{2.5}$, $WO_{2.7}$ and $WO_{2.9}$ films. Inset, zoom into the region of the Fermi level. States in the vicinity of the Fermi level appear when tungsten is reduced.

For the three samples, a broad maximum can be observed at approximately 4 eV. In addition, a slight feature can be observed at 6 eV and a smaller broad feature around 2 eV. The feature at approximately 6 eV is assigned to a hybridized W 5d-O 2p band (Höchst, 1982; Du, 2014) and the main feature at 4 eV is assigned to the O 2p derived band (Höchst, 1982; Du, 2014). The small feature at 2 eV can be attributed to an adsorbed oxygen layer on the top of the sample (Höchst, 1982; Bringans, 1981).

The inset details the part of the spectra close to the Fermi edge. It can be observed that sample 2 and 3 ($WO_{2.7}$ and $WO_{2.5}$), deposited at low pressure, present a peak at around 0.5 eV which is not present in sample 1, containing more oxygen. The broad peak around 2 eV increases also for sample 3: these features are indicative of new occupied states forming inside the band gap (Vasilopoulou, 2014). These bands are attributed to the occupation of W 5d orbitals with t_{2g} symmetry in the reduced tungsten oxides (Goodenough, 1960; 1971). In the oxygen-deficient tungsten oxide (WO_{3-x}), a portion of the electrons coming from the oxygen vacancies (maximum two electrons per oxygen vacancy) is transferred to this initially empty $5d_{t2g}$ (π^* in the Goodenough's model) metallic orbitals, which are located partially at the edge of the conduction band and partially within the band gap, near the Fermi level (Vasilopoulou, 2014; Goodenough, 1971).

The results obtained by XPS and UPS are in agreement with the color of the films deposited on glass. Their dark blue color is an additional evidence of the presence of W^{5+}. Therefore, the total working pressure in the deposition chamber has a strong influence on the sample stoichiometry. This is explained by the fact that a sputtered atom of tungsten has more probability to enter in contact with an oxygen atom, the mean free path of the sputtered W atom in the plasma being shorter.

In situ XPS allows for a quick feedback loop on the deposition parameters and helps to define the ones suitable to reach the desired stoichiometry. In addition, it outlines the differ-

ent oxidation states existing in the samples. UPS yields additional information on the density of states of the studied materials and can therefore provide evidence of the presence of an oxidation state. Here, the valence band spectra near the Fermi edge confirm the presence of W^{5+} as observed by XPS. visual aspect, UPS and XPS are thus in agreement. More details on the optical properties are given in the following section.

5.1.2 Influence of the chemical composition on optical properties

Some parts of the text and images below are reproduced from : Bouvard, O., Gonzalez Lazo M.A., Krammer, A., Schüler, A., 2015. In situ photoelectron spectroscopy: a powerful tool to develop electrochromic materials. EPFL (Lausanne). https://doi.org/10.5075/epfl-cisbat2015-33-38

Tungsten oxide coatings were deposited by reactive magnetron sputtering varying different process parameters. The effect of the total working pressure on the oxygen content was investigated and the oxygen/argon mass flow ratio was adjusted to obtain tungsten trioxide. The modifications' consequences of the total pressure and oxygen to argon mass flow ratio (O_2/Ar) were investigated. Table 5:2 shows the process parameters used for the deposition of the tungsten oxide films.

	Sample A'	Sample B'	Sample C'
Applied power	DC-p 150 W	DC-p 150 W	DC-p 150 W
Substrate	glass	glass	glass
Ratio O_2/Ar	0.48	0.48	0.61
Working pressure	$3{,}1.10^{-3}$ mbar (low working pressure)	$2{,}4.10^{-2}$ mbar (high working pressure)	$2{,}8.10^{-2}$ mbar (high working pressure)

Table 5:2 Deposition parameters

The oxygen to argon mass flow ratio, as well as the power applied on the target, were maintained constant for sample A' and B'. Subsequently, a sample with higher O_2/Ar ratio was deposited (sample C') to observe the impact on the transmittance.
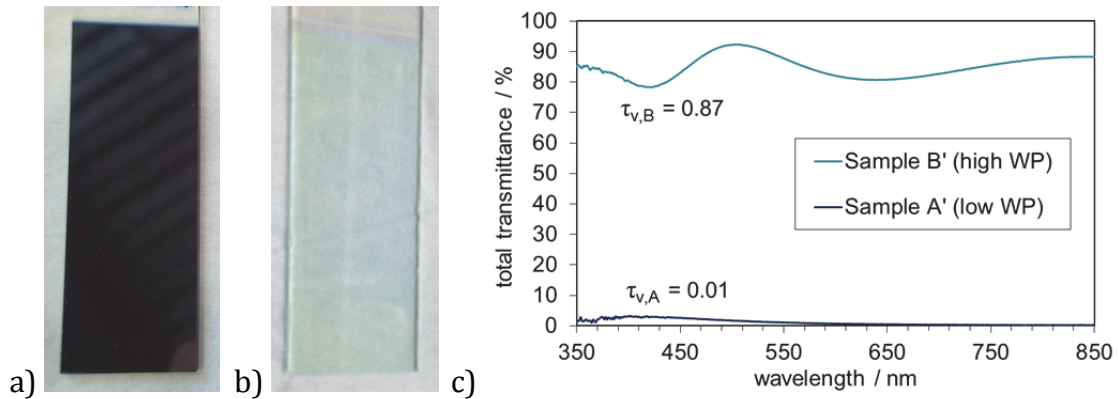
Figure 5:4   a) and b) Pictures of samples A' and B' WO$_3$/glass as deposited. c) Measured total transmittance of the two samples in the visible range. Light transmittance τ$_v$ determined according to EN410 is also indicated. The sample deposited at low working pressure is under-stoichiometric and has a dark blue color.

It can be observed in Figure 5:4 a) and c) that the sample deposited at low working pressure (sample A') shows a very dark blue tint and a visible transmittance of only 1 %. With the same mass flow of reactive gas, sample B' is transparent and its visible transmittance reaches 87 % as illustrated in Figure 5:4 b) and c); for comparison, the ITO-coated glass substrate alone has a visible transmittance of 88 %.

Sample C was deposited with a higher O$_2$/Ar ratio as well as at a high working pressure. Figure 5:5 a) displays the clear as-deposited state. Figure 5:5 b) shows the dark state obtained after lithium intercalation in Li-PC by applying a voltage of 2.5 V. The visible transmittance in the clear state is similar to the one obtained for sample B'. The slight difference can be explained by a difference in thickness; the latter can also be observed by comparing the number of interference fringes. A thicker sample was found to yield better results in terms of electrochromism. The visible transmittance in the dark state is reduced to 13 % and presents the distinctive blue color of tungsten trioxide.
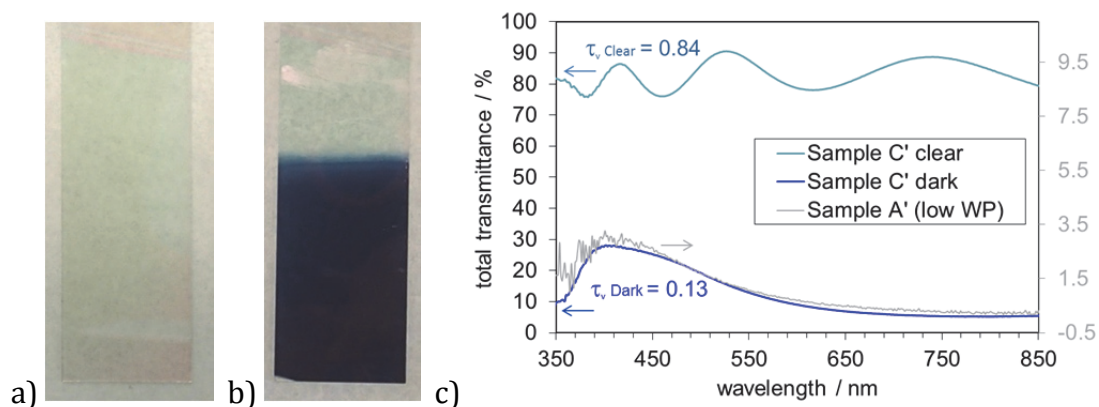
Figure 5:5   a) and b) Photograph of the sample C' in clear and dark states. c) Measured total transmittance and visible transmittance of the two states of sample C' in the visible range. For comparison, sample A' with an adapted scale is also shown. The blue tint due to lithiation and under-stoichiometry is similar.

The working pressure during deposition is known to influence the morphology of a film (Granqvist, 2014); higher working pressures are commonly used in order to get a porous film. However, the working pressure also has an impact on the stoichiometry of the film for a given O_2/Ar mass flow ratio. At higher pressure, the mean free path of sputtered tungsten atoms is shorter: the probability of collisions between tungsten and oxygen or argon atoms is higher. Therefore, a larger number of tungsten atoms are oxidized compared to the case of a deposition with a low working pressure.

Upon lithium intercalation, the clear tungsten trioxide becomes blue until reaching the dark blue final color depicted in this Figure 5:5 b). The visible transmittance coefficient is higher for the electrochromic sample in the dark state (C') comparing to the sample with low oxygen content (A'). However, their visible transmittance spectrum is similar when normalized as shown in Figure 5:5 c). This observation suggests that lithium intercalation leads to a similar effect than low oxygen content in the film and are consistent with the electronic structure observed by XPS and UPS.

5.1.3 Influence of the morphology on the switching contrast and dynamics

The modification of the working pressure during deposition can alter the stoichiometry, the optical properties and the electronic properties of tungsten trioxide if the oxygen to argon ratio is not modified. Varying the working pressure is in addition expected to influence the morphology and porosity of the film. If the working pressure is increased, the sputtered atoms undergo more collisions and therefore reach the substrate with less energy. Two samples were deposited at high and low working pressure: the main deposition parameters can be found in Table 5:3. The oxygen to argon ratio was increased in the sample deposited at low working pressure in order to obtain the appropriate stoichiometry.

	Sample A O60811	Sample B O60812
Applied power	DC-p 150 W	DC-p 150 W
Substrate	glass and Si	glass and Si
Deposition time	90 min	90 min
Ar / sccm	9.7	12.5
O_2/ sccm	9.9	8.3
Ratio O_2/Ar	1,02	0,67
Working pressure	$5,5.10^{-3}$ mbar (low working pressure)	$3,2.10^{-2}$ mbar (high working pressure)

Table 5:3 Deposition parameters

Since sub-stoichiometric tungsten oxide exhibit a blue color, the oxygen level in the plasma was increased until the obtained sample was transparent. Figure 5:6 display the spectral transmittance and reflectance of the sample A and B deposited on ITO coated glass at low and high working pressure respectively.
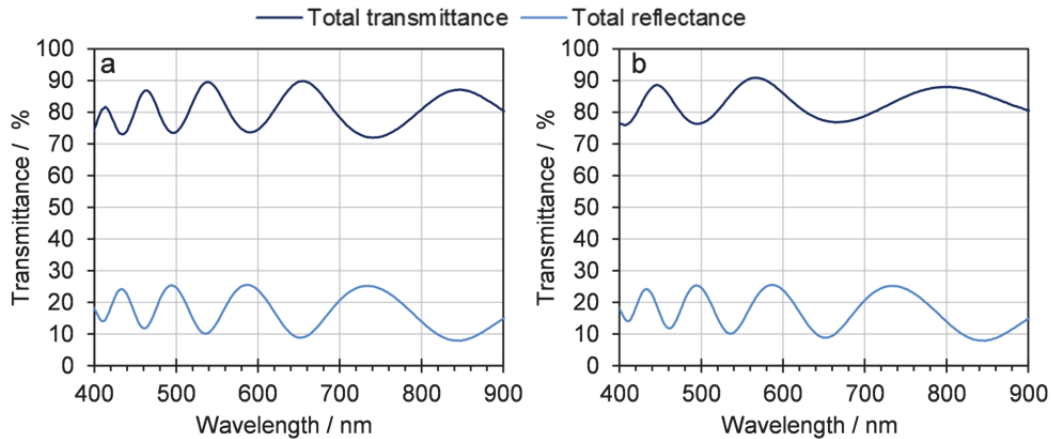
Figure 5:6   Optical transmittance and reflectance of WO_3/glass a) sample A and b) sample B. Both samples are transparent with negligible absorption.

It can be observed that both samples are transparent; therefore, they are expected to be close to stoichiometric tungsten trioxide. The deposition time was kept constant for the two samples; however, the deposition rate is faster when the working pressure is lower. The number of ripples is higher for sample A, indicating a larger thickness. Furthermore, no haze was visible indicating that the pores induced by the process parameters are small. When pores are larger than the wavelength of light, diffusion occurs and the films show a visible haze.

Sample A and B were also deposited on silicon to be studied by ellipsometry. They were measured at four angles of incidence: 60°, 65°, 70° and 75°. Since they are transparent in the visible range, a Cauchy dispersion law could be used to fit the ellipsometric data and to obtain the refractive index, as a function of wavelength. The measured data and the values generated using the refractive index and thickness determined by fitting the data on a Cauchy dispersion law are displayed in Figure 5:7. A reasonable fit could be obtained between the measured and generated values of $\tan(\Psi)$ and $\cos(\Delta)$. R^2 was above 0.97 and the root mean square error (RMSE) was below 0.03 for both samples. Profilometry was performed on the samples to have a reasonable initial guess of the thickness of the samples.
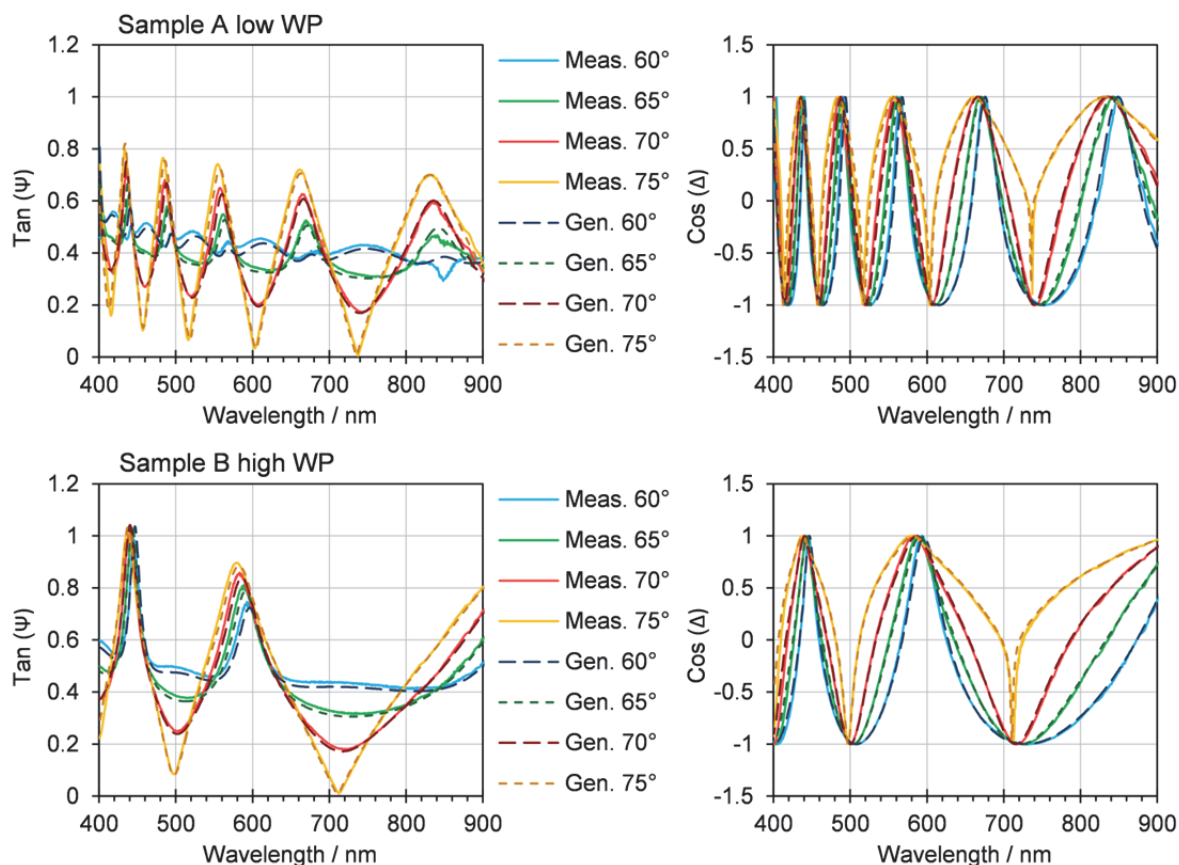
Figure 5:7   Ellipsometric data, tan(Ψ) and cos(Δ), measured in solid line and generated from the fitted thicknesses and refractive index in dashed line.

The thickness determined by ellipsometry is 744 nm for sample A and 403 nm for sample B. The refractive index determined by ellipsometry in the 400 to 900 nm region for sample A and B is shown in Figure 5:8. As expected, the refractive index decreases when the working pressure during deposition is increased.
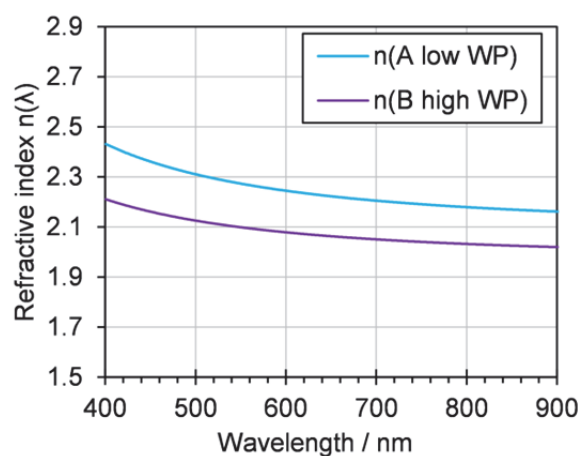
Figure 5:8   Refractive index of the samples A and B deposited at low and high working pressure (WP) determined by ellipsometry using a Cauchy dispersion law.

The Bruggeman theory (Bruggeman, 1935) can be used to model the optical properties of an inhomogeneous media consisting of two materials with known optical properties. This theory is limited to the case where the particle size is much smaller than the considered wavelength: it can be applied here for void particles in a WO_3 matrix. Since the samples exhibit no haze, the voids are smaller than the wavelength of visible light and this theory can be used. The volume fraction, f_α, can be evaluated from the Bruggeman theory using eq. (28) to compare different samples (Bruggeman, 1935; Schüler, 2000).

$$f_\alpha \cdot \frac{\varepsilon_\alpha - \varepsilon_{EFF}}{\varepsilon_\alpha + 2\varepsilon_{EFF}} + (1 - f_\alpha) \cdot \frac{\varepsilon_\beta - \varepsilon_{EFF}}{\varepsilon_\beta + 2\varepsilon_{EFF}} = 0 \qquad (28)$$

where f_α is the volume fraction of the material α (in vol.%), ε_α is the complex dielectric function of material α, ε_β is the complex dielectric function of material β and ε_{EFF} is the complex dielectric function of the effective medium.

Material α is a dense and amorphous WO_3 whose optical properties were described in detail by Deb (1973); material β is air with a refractive index of 1. Table 5:4 shows the volume fraction of WO_3 in a WO_3:air effective medium, calculated according to eq. (28). It indicates that the volume fraction f_α of sample A is 81 % and 70 % for sample B meaning there is about 19 % of nanoporosity in sample A and 30% in sample B.

Sample	n at 550 nm	Fraction of WO_3 / vol.%	Pore fraction /vol.%
WO_3 thin film (Deb,1973)	2.59	100	0
A low WP	2.28	81	19
B high WP	2.10	70	30

Table 5:4 Volume fraction calculated using the Bruggeman effective medium theory.

Sample B was produced at high working pressure in order to obtain a certain degree of porosity to facilitate the movement of lithium ions. Chronoamperometry, e.g. application of a voltage step on an electrode, was performed on sample A and B. The WO_3 deposited on ITO coated glass was place in a glass cell filled with Li-PC (propylene carbonate containing dissolved $LiClO_4$ salt); an $Ag/AgNO_3$ electrode cell was used as a reference electrode and a platinum wire as a counter electrode. The current and the transmission spectra were recorded while potential steps of +2,5 V and -2,5 V vs. $Ag/AgNO_3$ were applied successively for 300 s each. The spectral transmittance was measured in the range 350 nm–1600 nm; above 1600 nm, the absorptance of the electrolyte was too strong to measure the transmittance with sufficient accuracy. The spectral transmittance was measured every 7 s; the spectra were integrated using a Matlab routine to determine the light transmittance τ_v (see Chapter 3 and Annexe A1) in order to compare the switching behavior of the samples. The results are displayed in Figure 5:9.
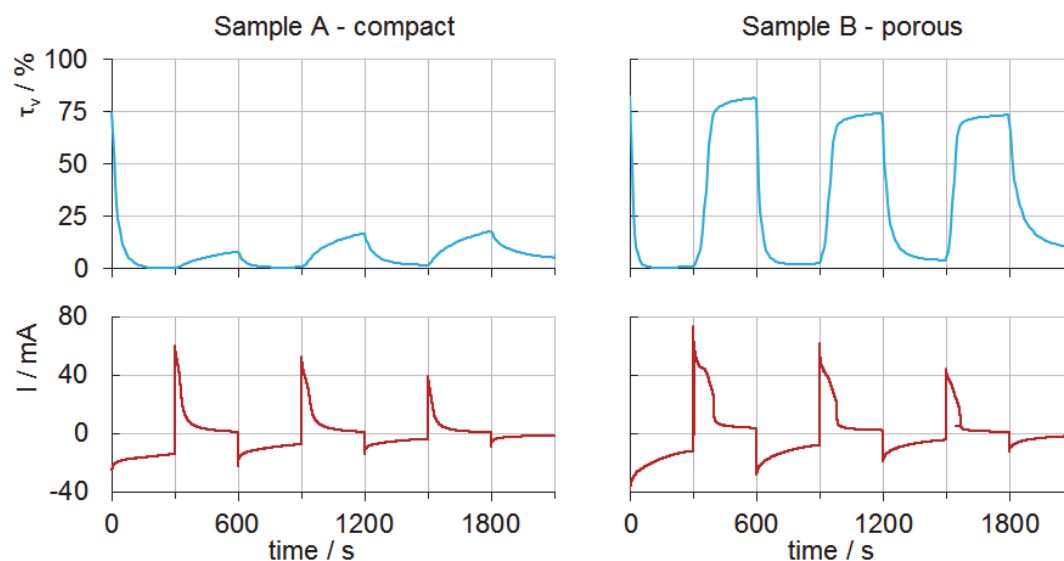
Figure 5:9   Evolution the visible transmittance (upper part) and of the current (lower part) as a function of time while the potential applied to the electrodes was stepped from 2.5 V to -2.5V vs. Ag/AgNO$_3$ every 300 seconds.

The lower part of the graph shows the current as a function of time. As soon as the potential step is applied, the current starts to increase from negative values; when the potential is reversed, the current switches to positive values and decrease rapidly accompanied with a rapid increase of the transmittance. Before the start of the cycle, both samples A and B are transparent with a visible transmittance of 75 and 82% respectively. Upon application of the potential step, the visible transmittance abruptly decreases to reach 0.3 and 0.5% for sample A and B respectively. However, when the potential is reversed, sample A, which was deposited at low working pressure and is more compact, does not discolor. Its visible transmittance reaches only 8.3% after the first cycle and 17.9% after the third cycle. Instead, the visible transmittance of sample B reaches 81.5% at the end of the first cycle. At the end of the third cycle, it is only 73.3%, which might be due to some lithium trapped in the film during the first cycles. Furthermore, the speed of coloration is different. During the third cycle, the dense sample sees its transmittance increased by only 16 percentage point in 300 seconds while the porous sample transmittance increased by 69 p. point. Nanoporosity appears to play an important role in the switching contrast and dynamics. This may due to the formation of channels which facilitate the movement of the lithium ions. It increases also the surface area between the electrolyte and the electrochromic materials: this internal interface might be favorable to the ion transport.

5.2   Anodic electrochromic oxides based on nickel oxides

Nickel oxides were investigated as a counter electrochromic material. Pure nickel is magnetic and in magnetron sputtering deposition magnetic materials modifies the field and might cause problems. Therefore, first trials were performed with a common industrial target of nickel-vanadium (93-7 wt.% e.g. 92-8 at.%) which is non-magnetic.

5.2.1 Characterization of a Nickel-Vanadium oxide

To be able to produce an electrochromic device, an ion storage layer is needed. It can be either not changing its color during intercalation and de-intercalation of lithium or changing in the opposite direction as the tungsten oxide, e.g. when the tungsten oxide darkens, the anodic electrochromic oxide darkens too. A nickel-vanadium (Ni-V 93-7 wt%) target was used to produce an electrochromic counter electrode. The set of parameters used for the deposition of this sample is indicated in Table 5:5.

O70517	Sample Ni-V-O
Applied power	DC-p 200 W
Deposition time	30 min
Ar / sccm	41.7
O_2/ sccm	1.0
Ratio O_2/Ar	2,38
Working pressure	$1,8.10^{-2}$ mbar

Table 5:5 Deposition parameters

The sample was deposited on an ITO substrate with a resistivity of 15-30 ohm/sq, it was then immersed in a solution of propylene carbonate containing 1 mol/L of $LiClO_4$ (Li-PC). The ITO substrate and a platinum wire were connected to a potentiostat: an electric potential varying between -2 V and +0.8 V was applied. The spectral transmittance of the ITO substrate, the sample as deposited and after coloring and bleaching is shown in Figure 5:10. From these spectra, the light and solar direct transmittance were determined, they are displayed in Table 5:6.
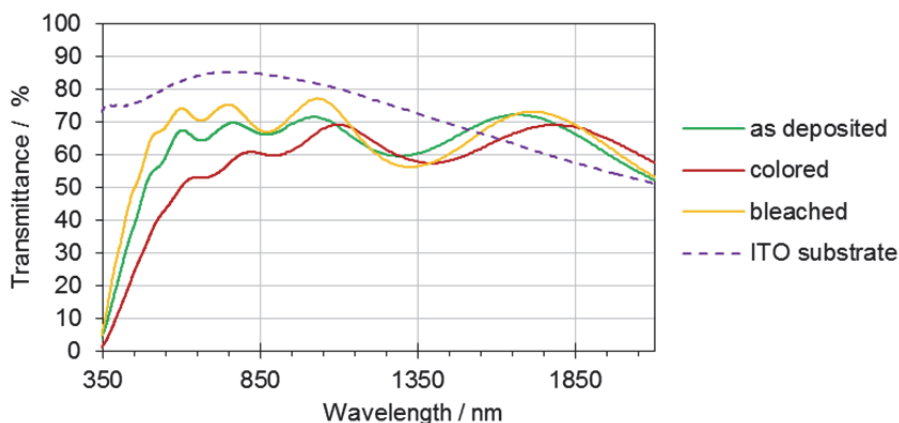
Figure 5:10   Spectral transmittance of a nickel vanadium oxide as deposited, colored and bleached along with the ITO substrate (dashed line).

	τ_e	τ_v
ITO/Glass	0.80	0.81
Ni-V-O as deposited	0.58	0.60
Ni-V-O colored	0.48	0.44
Ni-V-O bleached	0.64	0.69

Table 5:6 Solar direct transmittance and visible transmittance of the Nickel vanadium oxide

The ITO substrate displays a transmittance varying between 75 and 85 % in the visible range. It is then decreasing in the near infrared (NIR) to about 50% at 2100 nm. The nickel-vanadium-oxide as deposited, bleached and colored transmit less than ITO in the visible range. The amplitude of the modulation is of 16 % is the solar range and of 25 % in the visible range. Ripples can be observed in the three spectra and are due to differences of refractive index between ITO and nickel oxide. The samples exhibit a strong absorption in the shorter wavelengths of the visible range. It results in a brownish-yellowish color in transmission. This effect is stronger after coloration and slightly lower after bleaching. When the device is colored, the brownish color might be an advantage to create a color-neutral device; however, in the bleached state this effect should be reduced in order to obtain a window which is transparent in the visible range.

5.2.2 Effect of target composition on optical properties

In order to obtain an electrochromic device which is transparent in the bleached state, both electrochromic oxides must be transparent. Tungsten trioxide is transparent in the visible range when there are no ions intercalated, therefore, the limiting step is the counter electrochromic oxide. Nickel vanadium was first used because it is common and non-magnetic, however it revealed a strong absorption in the blue part of the spectrum leading to a brownish color in transmission of the nickel vanadium oxides.

A pure nickel target and an alloyed target of nickel and tantalum (Ni-Ta 91-9 at%) were used and compared to the sample made with the nickel vanadium target. The deposition parameters are given in Table 5:7. The name of the samples is referring to the target and does not indicate a stoichiometry. Nickel tantalum oxides were investigated because tantalum pentoxide is a promising solid state electrolyte, as will be discussed in Chapter 6.

	NiVOx	**NiOx**	**NiTaOx1**	**NiTaOx2**
	O71106-2	O80621-1	O80607	O80605-3
Target	Ni-V	Ni	Ni-Ta	Ni-Ta
Applied power	DC-p 200 W	DC-p 200 W	DC-p 200 W	DC-p 200 W
Deposition time	30 min	30 min	30 min	30 min
Ar / sccm	41.7	41.7	41.7	41.7
O_2/ sccm	1.0	1.0	1.0	1.5
Ratio O_2/Ar	2,38 %	2,38 %	2,38 %	3,57 %
Working pressure	$1,6.10^{-2}$ mbar	$1,6.10^{-2}$ mbar	$1,6.10^{-2}$ mbar	$1,6.10^{-2}$ mbar

Table 5:7 Deposition parameters.

The applied power, power source, working pressure, deposition time and oxygen to argon ratio were maintained constant and tried with the three targets: the transmittance spectra are displayed in Figure 5:11.
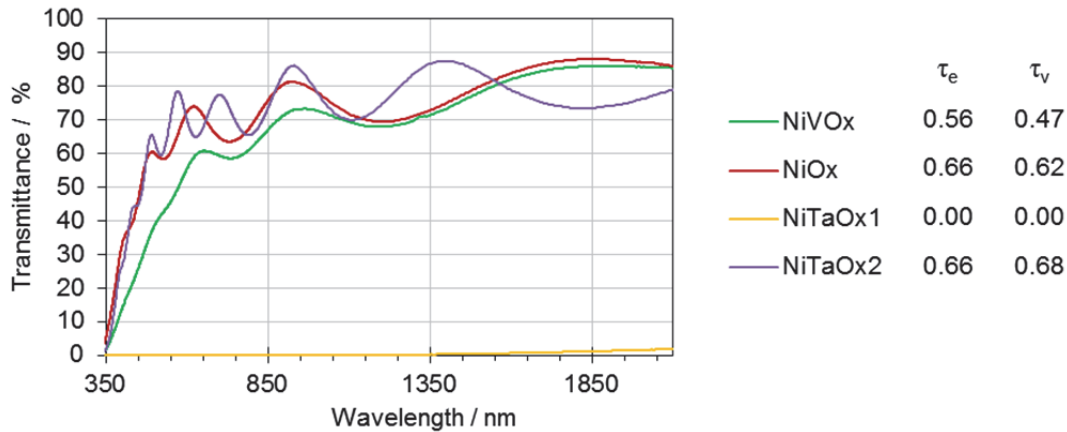
Figure 5:11   Spectral transmittance of a nickel vanadium oxide, nickel oxide and nickel tantalum oxides as deposited. The solar direct and light transmittance τ_e and τ_v are also indicated.

Samples made from the Ni-V and Ni targets at the same parameters are both oxidized. However, higher levels of oxygen were needed in order to obtain an oxidized nickel tantalum oxide. Sample NiTaOx1 had a metallic aspect and exhibit virtually no transmittance in the solar range. To be fully oxidized, a tantalum atom needs five oxygen atoms while nickel needs only one. Vanadium exists in numerous oxidized forms and VO_2 can already be somewhat transparent in the visible range. This might explain why the samples produced for the Ni-Ta target needs more oxygen to be oxidized. Furthermore, the sputter yield of the three atoms might be different, since tantalum is much heavier than nickel and vanadium (M_{Ni} = 58.7 g/mol; M_V = 50.9 g/mol; M_{Ta} = 180.9 g/mol).

It can be observed that the nickel vanadium oxide has a lower transmittance in the visible range, especially below 650 nm. It leads to a lower solar direct and light transmittance as displayed in Figure 5:11. The nickel tantalum oxide presents the same solar direct transmittance than the nickel oxide made from a pure nickel target (0.66) and its light transmittance is higher (0.68 compared to 0.62). Additionally, the Ni-Ta target with 9 at.% of tantalum has the benefit of being non-magnetic, which reduces the perturbation of the magnetic field during sputtering.

The light transmittance provides information on the quantity of visible light passing through the glazing; there is however no information on the quality, or color, of this light flux. In order to evaluate the difference, the color coordinates and the color rendering index R_a of a white illuminant (D65) after passing through the sample was determined using a Matlab routine (see Annexe A2); they are displayed in Figure 5:12. The maximum value for

R_a is 100 which means the spectral transmission is even for all visible wavelengths, indices above 90 are considered very good and good above 80.

	x	y	R_a
NiVOx	0.373	0.384	79.8
NiOx	0.341	0.362	89.4
NiTaOx2	0.341	0.371	91.8
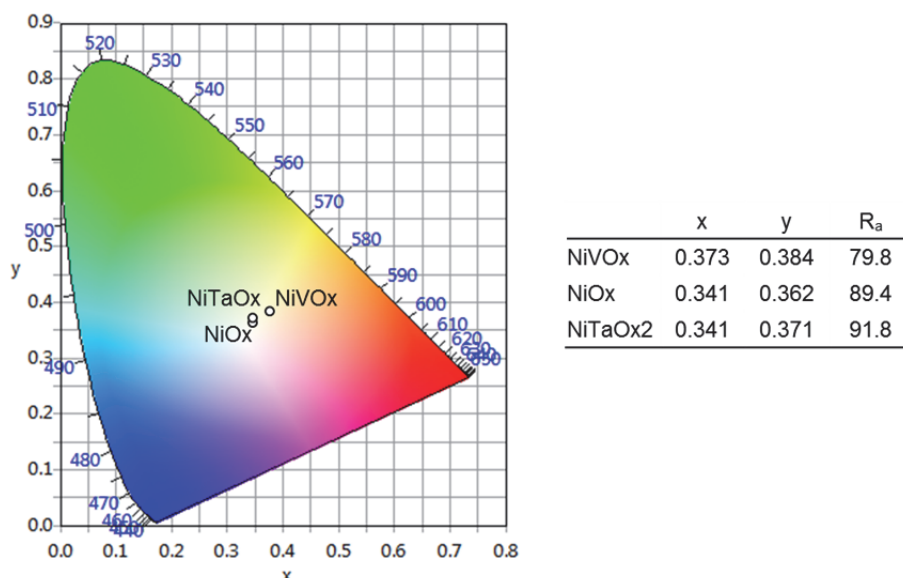
Figure 5:12   Color coordinates x,y presented in the CIE 1931 2° diagram and in a table along with the color rendering index R_a. For comparison, the color coordinates of a perfect white are x=y=0.333.

As could be perceived from the spectra, the sample NiVOx has a yellow color in transmittance. Samples NiTaOx2 and NiOx have color coordinates closer to the ideal white, with a slight yellow tint. The color rendering indices highlight this difference, sample NiVOx shows a R_a value of about 80 which is the limit for a good color rendering index. Sample NiOx reach nearly 90 and sample NiTaOx2 is slightly above which corresponds to very good values.

In the bleached state, the anodic electrochromic oxide should be as transparent and color neutral as possible. However, in the dark state, the yellow-brownish tint is advantageous: it will create a more neutral color when associated to the blue tint of the reduced tungsten trioxide as illustrated in Figure 5:13. The transmitted light through a coated glass can be considered as a light source, and when two light sources are mixed, the color of the resulting light will fall on a line between the color coordinates of the initial sources. Since WO_3 is blue upon intercalation of lithium ions, a yellow-orange counter electrode would help to reach color neutrality for the electrochromic (EC) device.
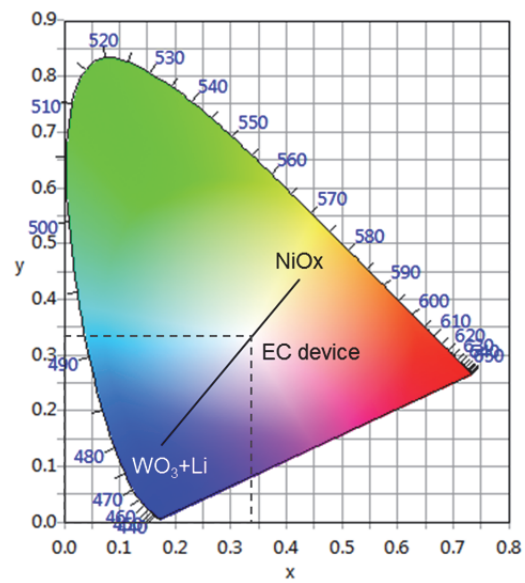
Figure 5:13   CIE 1931 2° diagram illustrating color mixing, the proper combination of a blue and a yellow transmit-ted lights can give a color neutral light. The dashed lines indicate the position of the ideal white x=0.333 and y=0.333.

5.3 Electrochromic devices with liquid electrolyte

Deposition parameters for tungsten and nickel oxides were determined in order to produce electrochromic devices. Before starting to investigate solid state devices, some electro-chromic devices with a liquid electrolyte were produced. This section describes how they were assembled and provides some experimental results obtained from these prototypes.

5.3.1 Assembly of electrochromic devices with liquid electrolyte

Tungsten oxide and nickel oxide coatings were deposited by reactive magnetron sputtering on ITO coated glass substrates (25 mm x 50 mm). To evaluate the electrochromic layers, a device with a liquid electrolyte was assembled as illustrated in Figure 5:14. For this, double-side tape was used as a spacer; a small quantity of propylene-carbonate containing 1 mol/L of $LiClO_4$ (abbreviated as Li-PC) was added between the glass slides. The sides were sealed using epoxy glue.
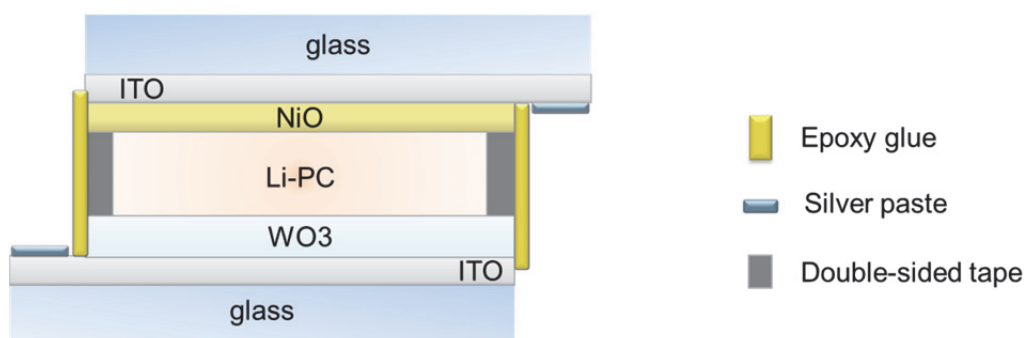
Figure 5:14   Electrochromic device with a liquid electrolyte placed between two ITO glass coated with an anodic and cathodic electrochromic oxide. The active area is 17 mm x 37 mm.

Devices with different substrates or oxide layers were prepared. Silver paste was applied on the ITO to avoid scratching of its surface when connecting the sample to the potentiostat using alligator clips. The sample was then placed in front of the collimator leading to the spectrophotometer, as illustrated in Figure 5:15. This way, the optical properties of the sample could be measured while an electrical potential was applied to the sample. A trans-mission spectrum was recorded every 0.5 seconds.
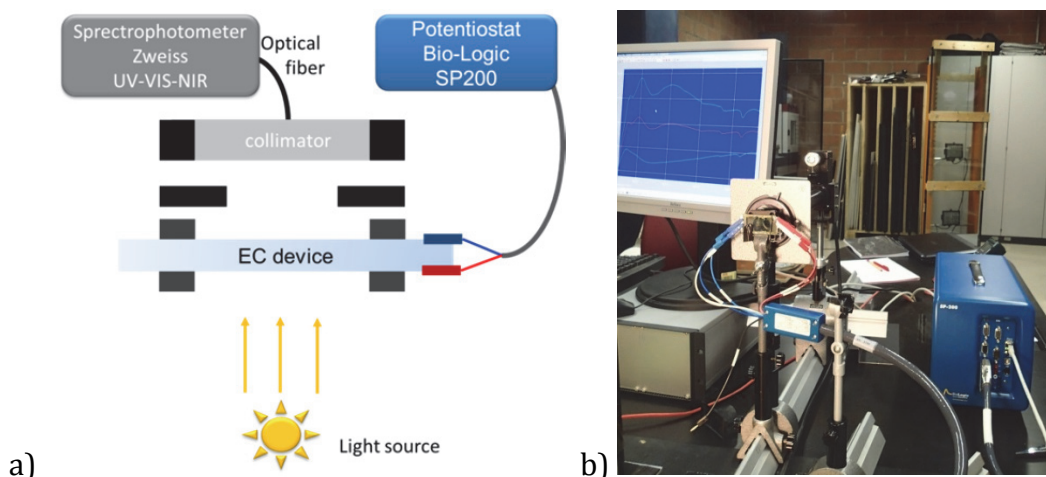
Figure 5:15   Drawing a) and photography b) of the setup used to measure the liquid electrolyte devices during switching. Unless otherwise indicated, the spectral transmittance is the specular transmittance recorded at normal incidence.

5.3.2 Cyclic voltammetry with in situ spectrophotometry

An electrochromic device with a liquid electrolyte was prepared from a tungsten oxide as well as a nickel oxide coating whose deposition parameters are described in Table 5:8. The transmittance spectrum was recorded after assembly and before any cycle was performed. At 550 nm the transmittance was 60.0 %, then, cyclic voltammetry was performed at various scan rates varying from 10 mV/s to 80 mV/s.

ECL80314	WO_3	NiVOx
Target	W	Ni-V
Applied power	DC 150 W	DC-p 200 W
Deposition time	90 min	30 min
Ar / sccm	12.5	41.7
O_2/ sccm	8.3	1.0
Ratio O_2/Ar	66.67 %	2,38 %
Working pressure	$2,4.10^{-2}$ mbar	$1,9.10^{-2}$ mbar

Table 5:8 Deposition parameters. The samples were deposited on ITO coated glass with a sheet resistivity of 15-30 ohm/sq.

The resulting voltammogram is presented in Figure 5:16 a). The experiment was performed in a two-electrode setup, a reference electrode being difficult to install in a thin film device. Therefore, the potential is applied between the two conductive surfaces and it is not possible to determine precisely the potential of the oxidation and reduction reactions at each electrode due to the ohmic drop. However, it can still provide some information on the whole electrochromic device notably on the switching kinetics and the optical response.
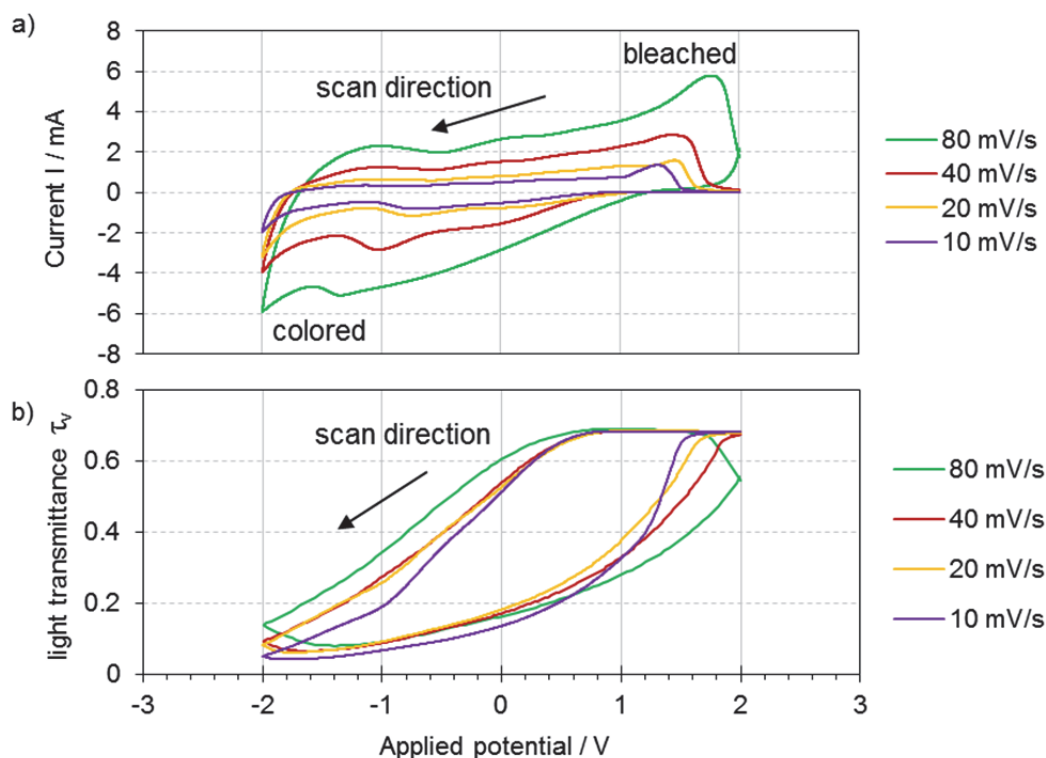
Figure 5:16   a) Cyclic voltammetry performed on a Glass/ITO/WO3-LiPC-NiVOx/ITO/Glass device from -2.0 to +2.0 V at various scan rates: 10, 20, 40 and 80 mV/s and b) light transmittance integrated from the spectral transmittance which was measured every 0.5 seconds during the cyclic voltammetry. The thickness of WO_3 is ~900 nm and of $NiVO_x$ ~500 nm.

During these experiments, oxidation and reduction reactions occur at both electrodes. When the applied potential is negative, the tungsten is reduced by lithium while the nickel is oxidized both leading to a darkening of the device. When the applied potential is positive, the tungsten is re-oxidized while the nickel is reduced by lithium, leading to a bleaching of the device. Since the experiment is in a two-electrode setup, the position of the peaks does not yield quantitative information because the distribution of the potential at each electrode is not known. Furthermore, amorphous WO_3 does not typically exhibit sharp peaks of oxidation or reduction because of the broad distribution of energetically different intercalation sites due to its amorphous and nanocrystalline composition (Bessière, 2001; Zhou, 2017a). However, the fact that the peaks are not aligned for various scan rates indicates that the kinetics of the reactions are slow and that the equilibrium is not established rapidly compared to the scan rate, this is usually the case for reactions of intercalation.

The spectral transmittance was measured every 0.5 seconds during the cyclic voltammetry; τ_e and τ_v were integrated from the measured data. The light transmittance, as a function of the applied potential, is displayed in Figure 5:16 b) and the maximum and minimum values of τ_e and τ_v are reported in Table 5:9 along with the time needed to complete one cycle for each scan rate.

	10 mV/s	20 mV/s	40 mV/s	80 mV/s
cycle duration / s	800	400	200	100
τ_e **min**	0.03	0.04	0.05	0.06
τ_e **max**	0.61	0.60	0.60	0.60
τ_v **min**	0.04	0.06	0.07	0.08
τ_v **max**	0.69	0.69	0.68	0.69

Table 5:9 Minimum and maximum solar direct transmittance and light transmittance obtained during cyclic volt-ammetry with varying scan rate.

What can be observed is the optical behavior during the potential sweep; for all scan rates, the sample start to darken when the potential is below 0.6 V and reach the darkest state just after the potential vertex, when the applied potential reaches -2 V, the potential sweep start to go towards high values. For the slowest scan rate (10 mV/s), the coloration at the potential vertex is almost similar to the minimum transmittance. Similarly, the most transparent state is reached before the 2 V potential (at around 1.6 V). This indicates that at this slow scan rate, when a full cycle needs 800 seconds, the lithium atoms have enough time to fully intercalate in the tungsten oxide. On the opposite, at faster scan rates (80 mV/s), the full coloration or bleaching is reached only after some additional time after the maximum voltage is applied. Since in cyclic voltammetry, the potential is swept on a large range, the response charge might not be all involved in the chromic process of the coatings. For a more detailed analysis, double-step chronoamperometry was performed on the same device.

5.3.3 Chronoamperometry with in situ spectrophotometry

An electrochromic device as described in section 5.3.1 and with the same deposition parameters of Table 5:8 was assembled. The spectral transmittance of the device was then measured in situ during double-step chronoamperometry (CA) experiments. A two-electrodes setup was used meaning that the applied potential is the full voltage drop by the current across the whole device, the distribution of the potential at each electrodes cannot be known precisely, the experiment reflecting the operation of the electrochromic device. Potential steps of -2.0 /+2.0 V and -2.5 /+2.5 V were applied. The duration of a step was 5 seconds. The applied potential, the response current and transmittance at 550 nm during these two experiments are plotted in Figure 5:17; a zoom on the first cycle is shown on the right side.
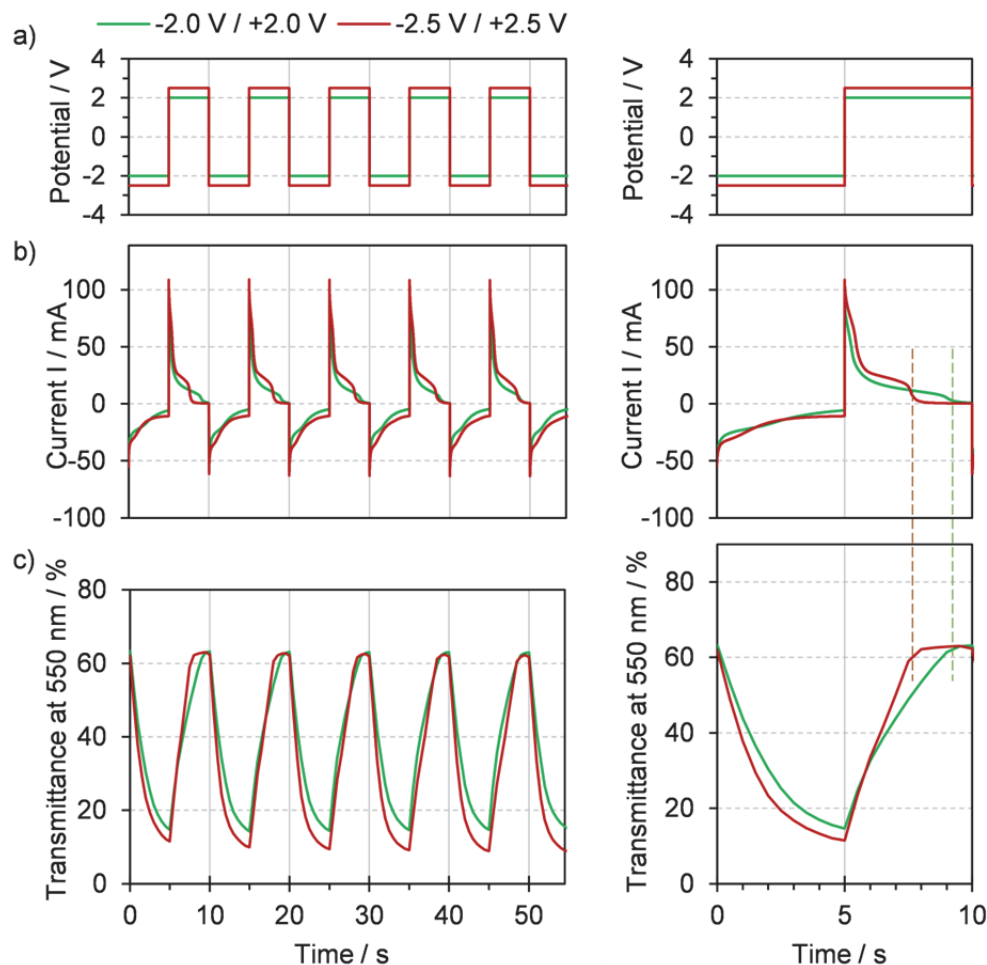
Figure 5:17   a) Potential applied during the chronoamperometry experiment to the Glass/ITO/WO3-LiPC-NiVOx/ITO/Glass device, b) current response and c) evolution of the transmittance at 550 nm during cycling. d), e) and f) zoom on the first cycle.

In a chronoamperometry experiment, the current response is recorded upon application of a constant voltage. Here, the potential was varied as a square wave from -2.0 V or -2.5 V to +2.0 V, respectively 2.5 V, to observe the coloration and discoloration of the device. According to IUPAC convention (IUPAC, 2005), the negative current correspond to the reduction and positive to the oxidation process. In this case, the negative current corresponds to the reduction of the W^{6+} to W^{5+} in Li_xWO_{3-x} leading to the coloration of the device. It starts from about -60 mA to about -5 mA for the -2.0 V / +2.0 V and to about -10 mA for the -2.5 V / +2.5 V experiment. In the meantime, the transmittance at 550 nm decreases from about 60 to 10 %. When the potential step switches to positive values, the current response is also positive with values varying from about 90 mA for the -2.0 V / +2.0 V, and 110 mA for the -2.5 V / +2.5 V experiment, to 0 mA: the transmittance at 550 nm rises from about 10 to 60 % in few seconds. This is the visible results of the reaction of Li_xWO_{3-x} to WO_3. When the Li_xWO_{3-x} is fully oxidized, the current returns to zero (see Figure 5:17 e) and f) dashed line). The inserted, and extracted, capacities (Q_i and Q_e in mC) are determined by calculating the area

above, and respectively below, the current curve and are indicated in absolute value. The transmittance at 550 nm and capacity for each cycle are given in Table 5:10 and Table 5:11.

CA -2.0 /+2.0 V	cycle 1	cycle 2	cycle 3	cycle 4	cycle 5
T_{550} min / %	14.6	14.2	14.4	14.6	14.7
T_{550} max / %	63.2	63.1	63.1	63.0	63.0
Δ T_{550} / pp	48.6	48.9	48.7	48.4	48.3
time to reach 95% of T_{550} max / s *	4.0	4.0	4.0	4.0	3.5
inserted capacity Q_i / mC	79.0	79.0	77.8	76.8	75.9
extracted capacity Q_e / mC	78.6	78.9	77.8	76.8	75.9

Table 5:10 Results obtained from the analysis of the -2.0 /+2.0 V chronoamperometry experiment displayed in Figure 5:17. *The transmittance spectra are recorded every 0.5 seconds, so the time indicated cannot be more precise than 0.5 seconds. (pp means percentage points)

CA -2.5 /+2.5 V	cycle 1	cycle 2	cycle 3	cycle 4	cycle 5
T_{550} min / %	11.5	10.0	9.5	9.1	8.9
T_{550} max / %	63.1	62.8	62.6	62.4	62.3
Δ T_{550} / pp	51.6	52.8	53.1	53.3	53.4
time to reach 95% of T_{550} max / s *	3.0	3.0	3.5	3.5	3.5
inserted capacity Q_i / mC	90.2	101.2	105.0	106.8	107.6
extracted capacity Q_e / mC	91.0	101.1	104.9	106.7	107.5

Table 5:11 Results obtained from the analysis of the -2.5 /+2.5 V chronoamperometry experiment displayed in Figure 5:17. *The transmittance spectra are recorded every 0.5 seconds, so the time indicated cannot be more precise than 0.5 seconds.

The optical contrast obtained for the +/- 2.5 V chronoamperometry (CA) experiment is slightly larger than the one obtained for the +/- 2.0 V CA experiment. It can be observed that the maximum transmittance decreases from 63.1 to 62.3 after only five cycles. This can be related to the extracted charge which is 0.1 mC lower than the inserted charge for the +/- 2.5 V CA whereas they are equal in the +/- 2.0 V CA experiment (except for the first cycle in both case which might be related to the experiment performed beforehand). The exact switching time could not be determined because the full optical contrast achievable is not known. The 0.5 seconds time interval between two spectra is limiting the accuracy of the determination of the switching speed. Nevertheless, it can be observed that the switch is faster for the +/- 2.5 V step during the first cycles. After 4 cycles, the switching speed for the two conditions is similar. As the maximum transmittance decrease, the inserted and extracted charge increase. This could be due to some degradation mechanism induced be the extra charge that would promote side reactions once the main reaction is complete.

From the charge Q (in mC/cm²) and optical density ΔOD (no unit), the coloration efficiency CE (in cm²/mC), can be calculated as described in eq. (29) and (30).

$$CE = \frac{\Delta OD}{Q/A} \qquad (29)$$

$$\text{with } \Delta OD = \log \frac{\tau_b}{\tau_c} \qquad (30)$$

where the value used for τ_b and τ_c are respectively the T_{550} max and T_{550} min indicated in Table 5:10 and Table 5:11 and A is the active area of the sample (1.7 x 3.7 cm^2).

The coloration efficiency for the coloring along with the optical density calculated for each cycle are plotted in Figure 5:18.
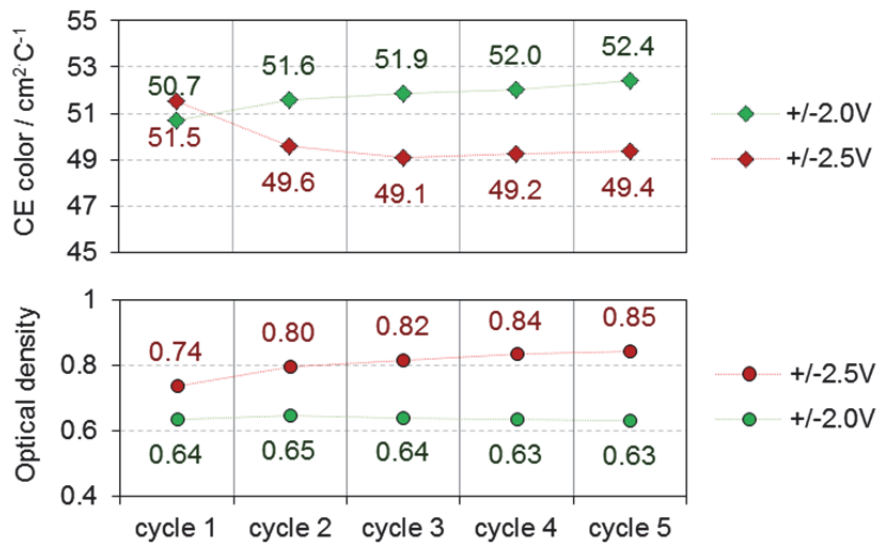
Figure 5:18   Coloration efficiency and optical density of the Glass/ITO/WO3-LiPC-NiVOx/ITO/Glass device obtained from the chronoamperometry experiments performed with -2.0 /+2.0 V steps (in green) and -2.5 /+2.5 V steps (in red).

With a larger potential window (+/- 2.5 V vs. +/-2.0 V), a larger optical density is reached; however, the coloration efficiency is slightly lower. Color efficiency of about 50 cm^2/C are considered relatively high for this type of device (Zhou, 2017a).

In further experiments, a degradation of the device was observed when a +2.5 V was applied for too long (more than 50 seconds). Bubbles started to appear and a visual inspection of the sample showed inhomogeneity in the color of the studied zone. At this voltage, side reactions may appear when the desired reaction is achieved leading to irreversible modifications of the sample.

5.3.4 Switching dynamics

Two chronoamperometry experiments were performed using the same potential step of -2.0 V and +2.0 V, with two step duration, 5 and 10 seconds, to observe the optical behavior during switching. The current response and transmittance at 550 nm as a function of time are presented in Figure 5:19.
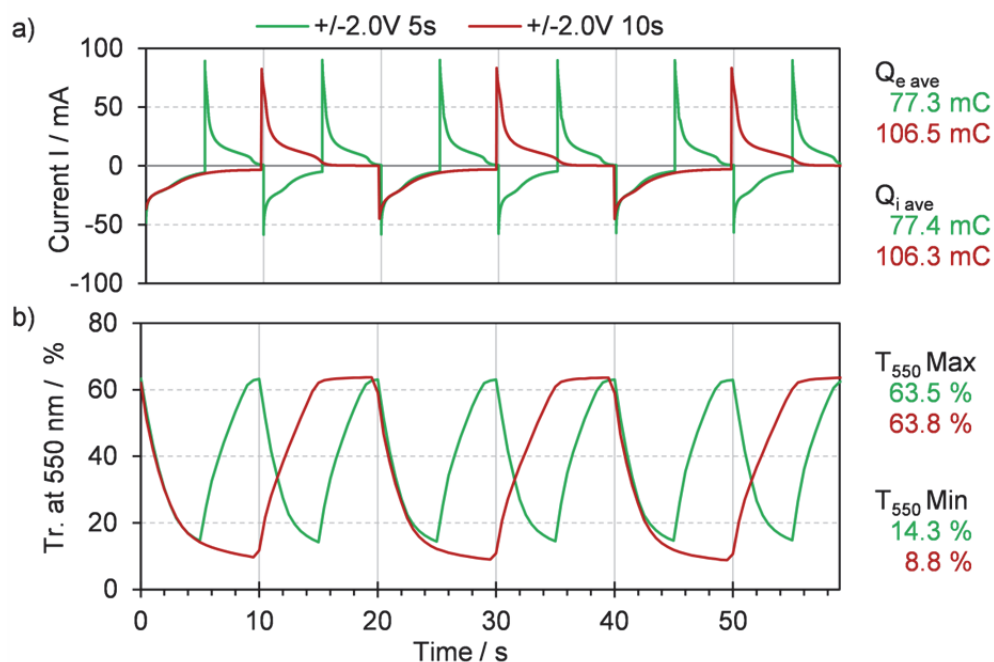
Figure 5:19   a) Current response and b) transmittance value at 550 nm to an applied potential step varying from -2.0 to +2.0 V every 5 seconds (green line) or every 10 seconds (red line) on a Glass/ITO/WO3-LiPC-NiVOx/ITO/Glass device.

The maximum transmittance is similar for both step duration (63.5 % for the 5 s step and 63.8 % for the 10 s step) but the minimum transmittance reach lower values with a longer step duration (14.3 % for the 5 s step and 8.8 % for the 10 s step). When charging time is increased from 5 to 10 seconds, the charge inserted increases by only 37 % (from 77.4 mC to 106.3 mC). The optical density obtained with a 10 s step is larger (0.86 compared to 0.64 for 5 s) but the coloration efficiency decreases slightly (50.7 compared to 52.0 cm^2/C for 5 s). A longer charging step is beneficial to have a darker device and it seems that with an even longer time, the sample could reach darker levels. However during the bleaching, a plateau is observed after 7 seconds, suggesting that the sample cannot reach higher transmittance. This transmittance is similar to the transmittance of the device "as-assembled" before any cycling. It confirms that the counter electrode has a low amplitude of optical modulation. This experiment shows that a longer time interval is needed to color the sample, e.g. to intercalate the lithium ions, than to fully bleach it. This might implies that lithium intercalation lead to a distortion of the amorphous network, creating strains in the lattice while the de-intercalation is favored by a relaxation of the crystal structure.

5.3.5 Influence of ITO sheet resistivity

WO$_3$ coatings were deposited during the same deposition run on two ITO substrates of 25 mm x 50 mm, one with a sheet resistivity of 15-30 ohm/sq and a second with a sheet resistivity of 30-60 ohm/sq (the sheet resistivity range is the one indicated by the manufacturer); the same procedure was applied for the nickel oxides. The liquid electrochromic device

were assembled, one with both oxides deposited on the 15-30 ohm/sq ITO substrate and another with both oxides on the 30-60 ohm/sq ITO substrate. Deposition parameters were identical to those presented in Table 5:8 (Section 5.3.2). The spectral transmittance of the sample was recorded during a chronoamperometry experiment; potential steps of -2.0 V and +2.0 V were applied for 5 s each. Results are displayed in Figure 5:20.
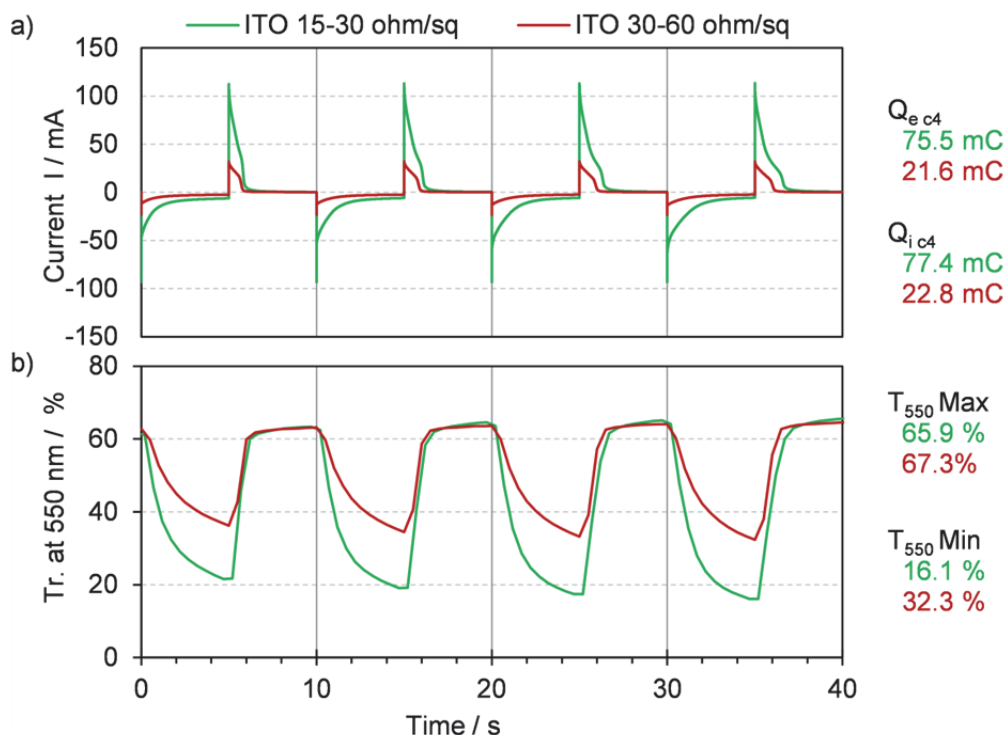
Figure 5:20   Evolution of the transmittance at 550 nm with an applied potential step varying from -2.0 to +2.0 V every 5 seconds for two ITO substrate with a sheet resistivity of 15-30 ohm/sq (green line) and 30-60 ohm/sq (red line) on a Glass/ITO/WO3-LiPC-NiVOx/ITO/Glass device. A lower sheet resistivity of the ITO substrate reduces the coloration speed but not the bleaching speed.

The device made with an ITO substrate having a sheet resistivity of 30-60 ohm/sq exhibits a smaller optical modulation (35.0 percentage point) than the one deposited on the substrate having a sheet resistivity of 15-30 ohm/sq (49.8 p.p.); the coloration is slower with the more resistive ITO. The ITO substrates have a size of 25 mm x 50 mm and the active area is 17 mm x 37 mm: even for such small samples, the influence of the resistivity of the substrate is clearly observed for the coloration step. For large electrochromic windows, the effect of the transparent conductive layer is clearly observed, the color changing as a curtain from the contacts to the center of the glazing. Even for small samples, the intercalation of lithium is not the only limiting step and therefore when comparing samples, the same type of substrate should be used and clearly specified. With both studied ITO substrates, the switching speed during bleaching appears to be similar. Both devices exhibit a steep slope and reach the clearest state in a very short time.

5.4   Discussion and perspectives

Suitable deposition parameters for the cathodic and anodic electrochromic oxides were determined. The nanoporosity produced by the use of high total pressure during the sputtering has shown to be favorable to the optical contrast and switching dynamics of WO_3. The used of pure nickel or Ni-Ta targets proved to be advantageous for the optical properties in the bleached state. There is less absorption in the short wavelength range leading to a more color neutral coating.

The electrochromic coatings were assembled to form a device with a liquid electrolyte; various tests were performed on this device. A solar transmittance of 3 % was achieved in the dark state and up to 67 % in the bleached state. The transmittance of the device could be varied from 10 to 60 % in a few seconds. The various experiments showed that the kinetics of the reaction during bleaching is much faster than to color the device. The coloration process of the device is mainly due to the intercalation of lithium ions in the tungsten oxide matrix; this reaction is triggered by the application of a voltage between two conductive surfaces. The phenomenon can be compared to a battery, where the coloration is the charging process requiring electricity and the bleaching relate to emptying the battery.

The liquid electrochromic devices studied in this chapter have color efficiency in the range of 50 cm^2/C: in the battery vocabulary and units, it means that it has a capacity of 5.5 $\mu Ah/cm^2$. The theoretical capacity of a $LiCoO_2$ film with a thickness of 1 μm is 69 $\mu Ah/cm^2$ (Matsuda, 2018); this material was especially developed for batteries and real batteries usually reach only 60 % of this capacity for films thicker than 1 μm. In the studied devices, the thickness of WO_3 was about 1 μm: considering the optical constraints which strictly limit the pore size to preserve transparency, a capacity of 5.5 $\mu Ah/cm^2$ can be considered reasonable.

In batteries, graphite is often used because its layered structure facilitates the movement of lithium atoms. In electrochromic devices, it was observed that nanoporosity improves the optical properties. This might be due to an increased number of channel paths for lithium which reduce the strains on the atom network. In addition, a porous structure can decrease the charge transfer resistance (He, 2018). Furthermore, in non-aqueous electrolytes the desolvation process of the lithium ion might reduce the kinetics of intercalation/deintercalation in the electrode (Abe, 2004) and a less ordered interface could facilitate the loss of the sheath of the solvated lithium ion (Steinrück, 2018).

Furthermore, it was also observed that the resistivity of the ITO substrate has a strong influence on the coloration speed, even on small scale samples; however, the bleaching speed did not depend on the ITO resistivity. In most electrochromic devices, the voltage is applied

to the two transparent conductors and the local distribution of the potential gradient within the depth of the film cannot be controlled. Temperature-dependent measurements could help to separate the electrical and electrochemical contributions to the coloration mechanism and get a better understanding of the rate limiting factor.

The resistance of the ITO has an influence on the lateral charge transport through the device; therefore, for larger devices this resistance will increase. For example, for a commercial ITO having a sheet resistivity of 30 ohm/sq, the resistance from the edge of a square patch (1 cm^2) at a distance of 2 cm is 60 ohm, at 10 cm it is 300 ohm and at 1 m it is 3 kohm. For small distances, the resistance through the solid electrolyte is larger or of the same order of magnitude than the resistance of the ITO layer: a solid electrolyte with an ionic conductivity σ_i = 1·10^{-6} S/cm and a thickness of 50 nm the resistance across the device would be 500 ohm. For larger devices such as electrochromic windows for building, the effect of the resistance of ITO is non negligible. A common approach to reduce the resistance of the lateral charge is to use a TCO with a higher conductivity or to increase its thickness. However, both these approaches reduce the optical transmittance of the electrochromic window in the clear state: there is a need for innovative solutions in this domain. Alternative solutions such as carbon nanotubes (Wan, 2017) or metallic grid (Han, 2014) are investigated as this type of highly transparent and highly conductive layer would not only be useful for electrochromic devices but also for various optoelectronic devices such as photovoltaic cells or organic light-emitting diodes (OLED).

In order to improve the durability of electrochromic devices, inorganic solid-state electrolytes are envisaged: some potential materials are studied in the next chapter.

Chapter 6   Inorganic electrolytes

This chapter focuses on potential candidates to be used as a solid and inorganic ion conductor. Since electrochromic devices have numerous similarities with thin film batteries, electrolytes which are of special interest in the context of batteries were studied: lithium phosphate oxy-nitride films and lithium lanthanum titanium oxide compounds. The motivation was to determine if these electrolytes would be suitable for electrochromic glazing. Furthermore, tantalum pentoxide films were studied with the aim to understand, if a porous metal oxide could be used as a solid electrolyte.

6.1   Lithium phosphate oxy-nitride coatings

Lithium phosphate oxy-nitride, often referred to as LiPON, is an amorphous solid state electrolyte, which has been largely studied for thin film lithium ion batteries since its potential as a lithium ion conductor was revealed by Bates et al. in 1992 (1992). It is advantageous for electrochromic devices because of its transparency for the solar spectrum (Su, 2016). In addition, this amorphous material can be deposited at low temperature via sputtering.

6.1.1 In situ photoelectron spectroscopy

A lithium phosphate target was used to deposit Li-P-O-N solid electrolytes by reactive sputtering in nitrogen-containing plasma. A first investigation by photoelectron spectroscopy was performed to compare the coatings deposited in pure argon flow and in pure nitrogen flow. The target does not contain nitrogen; in the following section the samples are called LiPO and LiPON though it does not indicate a stoichiometry. The deposition parameters are given in Table 6:1.

	LiPO O60209	**LiPON** O60211
Target	Li_3PO_4	Li_3PO_4
Applied power	RF 100 W	RF 100 W
Deposition time	5 h	5 h
Process gas	Ar	N_2
Working pressure	$4,2.10^{-3}$ mbar	$4,2.10^{-3}$ mbar

Table 6:1 Deposition parameters: one sample was deposited in pure argon plasma and the second in pure nitrogen plasma.

X-ray photoelectron spectroscopy was performed on the sample just after its transfer from the sputtering chamber to the analysis chamber. Figure 6:1 shows the survey spectrum and the O 1s, N1s and Li 1s core levels spectra. No smoothing was performed and the apparent difference of noise is due to the intensity of the peaks which were all measured with the same number of scans.
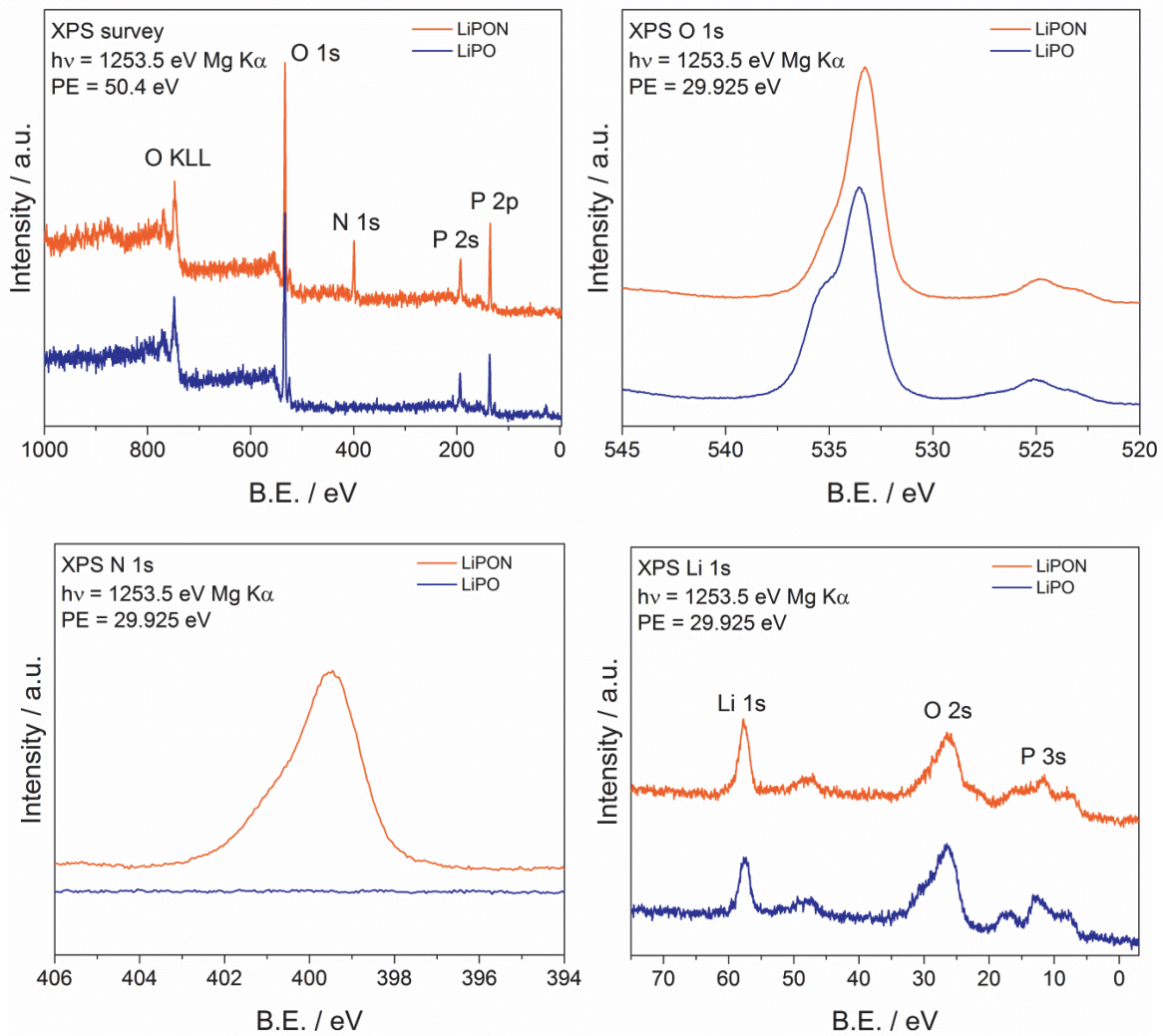
Figure 6:1   XPS of the survey spectrum and the O 1s, N 1s and Li 1s peaks. When the Li_3PO_4 target is sputtered in N_2 plasma, nitrogen is incorporated in the film as confirmed by the presence of the N1s peak.

In the survey scan, the Auger peak O_{KLL} and the core level peaks O 1s, P 2s and P 2p are observed for both spectra. When the deposition is performed in a nitrogen atmosphere (LiPON sample), nitrogen is incorporated in the coating: the N 1s core level peak appears. The spectrum of the sample deposited in a pure argon atmosphere (LiPO) does not show a nitrogen peak indicating that nitrogen is not contaminating the target. Twenty minutes of cleaning in pure argon are performed before each deposition; upon insertion of nitrogen, the shape of the O 1s peak is modified. At low binding energies, the core level peaks of Li 1s, O 2s and P 3s can be observed although their intensities are very low. The chemical composition was determined using the Scofield sensitivity factor by integrating the core-level peak area after subtraction of a Shirley background. For lithium and nitrogen, the Li1s and the N1s were the only peaks that could be used. For oxygen and nitrogen, usually O1s and P2p peaks are used; here quantification was also performed using the P2s and O2s peaks, since the results largely differ from the target composition. The obtained range is shown in Table 6:2 along with the expected ratio for Li_3PO_4 and a range of $Li_xPO_yN_z$ compounds.

	ratio Li/P	ratio O/P	ratio Li/O	ratio N/P	ratio N/O
Li_3PO_4	3	4	0.75	-	-
$Li_xPO_yN_z$	2.6 < x < 3.5	1.9 < y < 3.8	-	0.1 < z < 1.3	-
LiPO	0.9 ± 0.10	2.0 ± 0.50	0.9 ± 0.10	-	-
LiPON	1.1 ± 0.05	1.4 ± 0.25	1.15 ± 0.05	0.5 ±0.1	0.4 ±0.05

Table 6:2 Chemical composition obtained by integration of the core level peaks of the LiPO and LiPON samples. The expected ratio for Li_3PO_4 and a range of $Li_xPO_yN_z$ compounds (Fleutot, 2011) are also given.

The obtained composition of about $Li_{0.9}PO_2$ and $Li_{1.1}PO_{1.4}N_{0.5}$ diverge strongly compared to the stoichiometry of the target, which is Li_3PO_4 and compared to $Li_xPO_yN_z$ reported in the literature, which have compositions varying in ranges from 2.6 < x < 3.5, 1.9 < y < 3.8 and 0.1 < z < 1.3 (Fleutot, 2011). The determination of the Li/P ratio of a LiPON sample deposited with the same target, but with slightly different process parameters (process gas Ar+N_2 instead of pure N_2) was measured by inductively coupled plasma optical emission spectrometry (ICP OES) after acid digestion of the coating indicated a value of Li/P = 2.3. This value is also lower than expected but closer to expectations. The determination of the stoichiometry of lithium containing compounds using XPS is delicate, as the sensitivity of Li by XPS is rather low (Whitney, 2008). The XPS might underestimate the quantity of Li present in the film. Furthermore, the Scofield sensitivity factors used for the quantification were theoretically determined for isolated atoms and might not apply to all types of compounds. However, the ratio of Li/O is rather close to the expectations and since XPS is a surface sensitive technique, the LiPO or LiPON thin layer might be preferentially terminated by phosphorous atoms. More experiments would be needed to determine accurately the chemical composition of this type of samples.

To obtain a better understanding of the oxygen to phosphorous bridging, the deconvolution of the O1s spectra was performed according to model presented by Fleutot et al. (2011) and illustrated in Figure 6:2. The three components are attributed to P=O (O_1: non-bridging oxygen), $Li^{+-}O–P$ (O_2: non-bridging oxygen) and P–O–P (O_3: bridging oxygen).
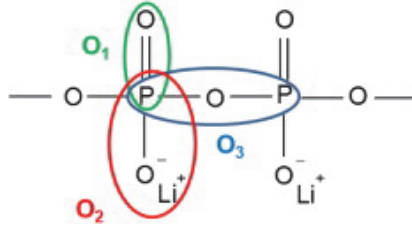
Figure 6:2   Structural model of alkali metaphosphate glasses with attribution of the O 1s components. Reproduced from (Fleutot, 2011).

The XPS experimental curves were fitted using a Gauss-Lorentz peak shape and a Shirley background. The Full Width at Half Maximum (FWHM) was maintained identical for the peaks of a same core level; the relative position of the peaks was fixed. These constraints are necessary in order to obtain a fit with a physical meaning. The results are presented in Figure 6:3 and Table 6:3.
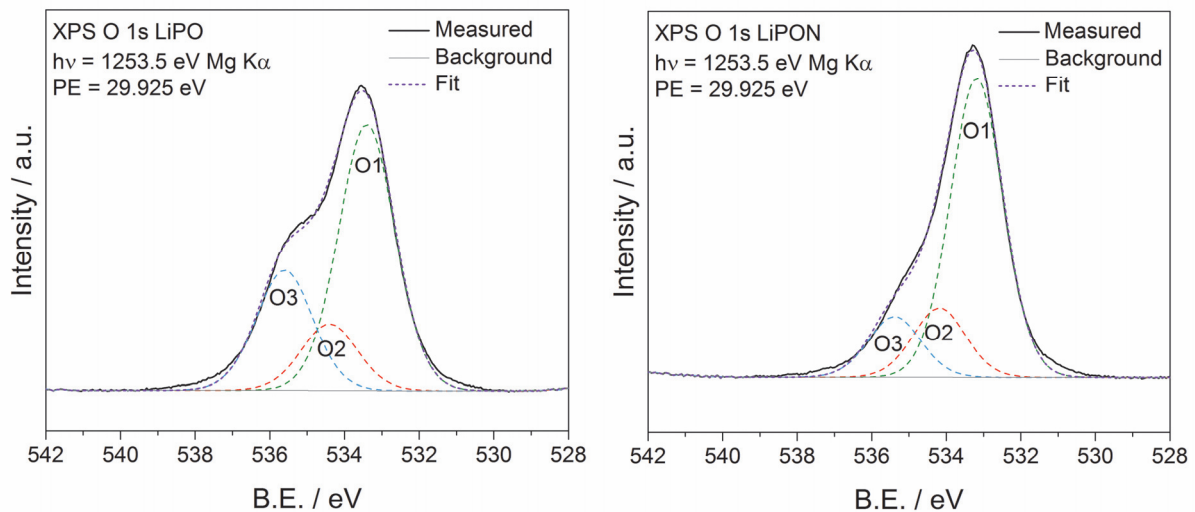
Figure 6:3   Deconvolution of the O 1s peak with the O1, O2 and O3 components described in Figure 6:2.

	LiPO			LiPON		
	position	FWHM	% area	position	FWHM	% area
O1	533.4	1.66	58.9	533.2	1.77	69.8
O2	534.4	1.66	14.6	534.2	1.77	16.1
O3	535.6	1.66	26.5	535.4	1.77	14.1

Table 6:3 Quantification of the O 1 s components.

The non-bridging oxygen (component O1) is predominant for both LiPO and LiPON samples. The introduction of nitrogen reduces the amount of bridging oxygen (O3), which can indicate a nitrogen/oxygen substitution.

The N 1s core level of the LiPON sample was fitted considering two nitrogen components (labeled N1 and N2) separated by 1.6 eV (Fleutot, 2011, Vepřek, 1981). They are attributed to a nitrogen bound to two phosphorous atoms (–N=) and to a nitrogen bound to three phosphorous atoms (-N<). The results are presented in Figure 6:4.

	LiPON		
	position	FWHM	% area
N1	399.5	1.73	78.6
N2	401.1	1.73	21.4
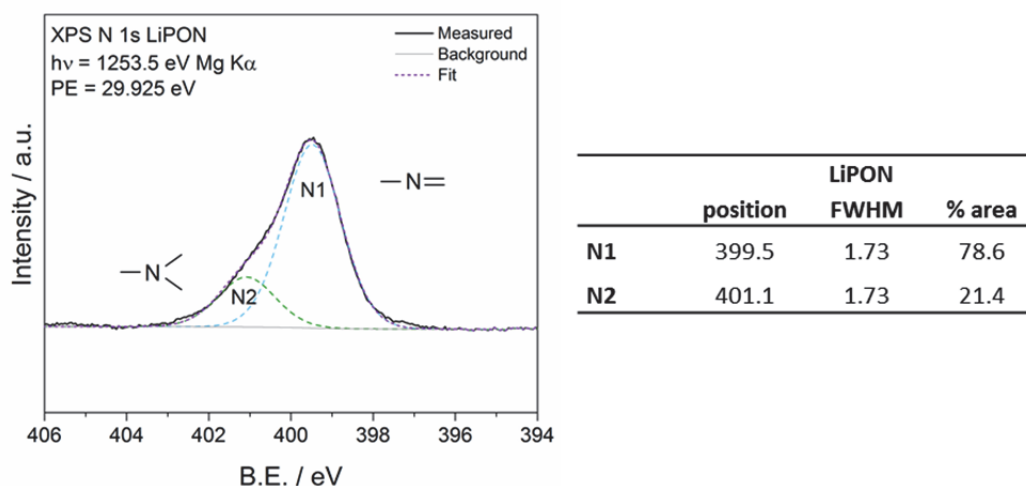
Figure 6:4   Deconvolution of the N 1s peak in two components, N1 corresponding to a nitrogen bound to two phosphorous atoms (–N=) and N2 to a nitrogen bound to three phosphorous atoms (-N<).

Fleutot et al. (2011) studied the evolution of N1/N2 ratio as a function of N/P ratio as well as the ionic conductivity as a function of the N/P ratio as illustrated in Figure 6:5. Their results suggest that a smaller N2/N1 ratio is beneficial for ionic conductivity, as depicted in Figure 6:6. The N1 component represents linear chains while the N2 component indicates cross-linking that would disrupt the linear phosphate backbone.
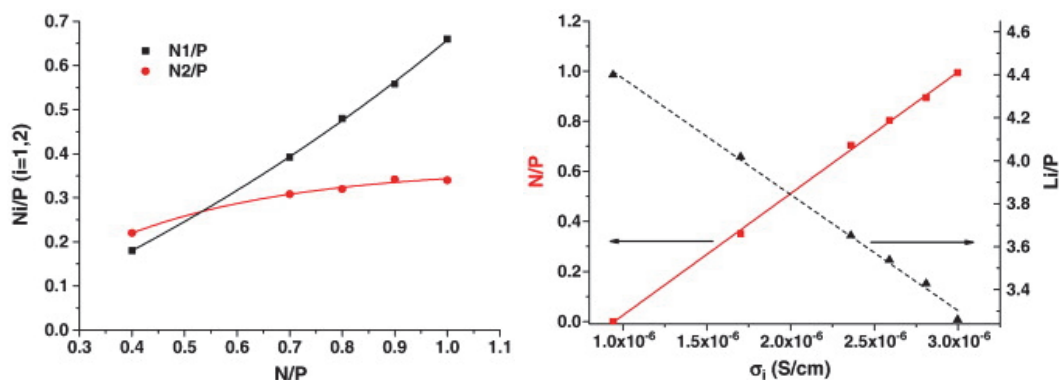
Figure 6:5   a) Evolution of N1 and N2 contents deduced from their respective areas on the N1s core peak as a function of total nitrogen amount. b) Ionic conductivity as a function of N/P ratio and Li/P ratio. Reproduced from (Fleutot, 2011).
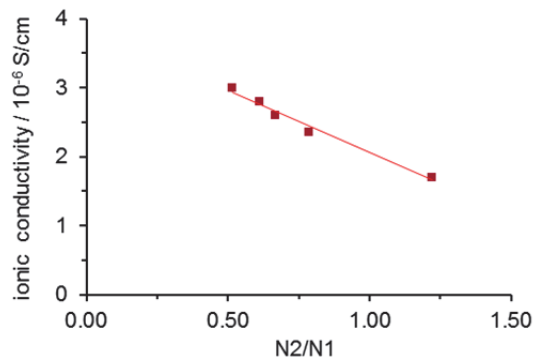
Figure 6:6 Evolution of the ionic conductivity as a function of the N2/N1 component ratio. Drawn from data presented in (Fleutot, 2011).

The LiPON sample deposited in our laboratory as a ratio of N/P = 0.5 and a ratio N2/N1 = 0.27. According to the findings of Fleutot et al., we expect to obtain LiPON samples with high ionic conductivities.

6.1.2 In situ photoelectron spectroscopy of LiPON/WO₃ interface

Some of the text and images in the following section were presented as a poster at SATF 2016, Science and Applications of Thin Films, Congress & Exhibition in Cesme, Turkey.

A step by step deposition of LiPON on WO_3 was performed by magnetron sputtering deposition. The successive layers were studied by in situ photoelectron spectroscopy (XPS and UPS): the aim of this study is to obtain information on the layer growth and on the possible interactions between the layers. The deposition parameters of the WO_3 and the LiPON layer are indicated in Table 6:4. The WO_3 layer thickness was estimated to 35 nm, according to the deposition time, the successive LiPON layers were estimated to be 0.35 nm and 1.1 nm thick.

O60902	**WO₃**	**LiPON**
Target	W	Li_3PO_4
Substrate	Si wafer	WO3/Si
	no substrate heating	no substrate heating
Applied power	DC 150 W	RF 50 W
Process and reactive gas	Ar and O_2	N_2
Gas flow / sccm	Ar : 12.5, O_2: 8.3	38.7
Ratio O₂/Ar	66.67 %	0
Working pressure	$1,6.10^{-2}$ mbar	$4 \cdot 10^{-3}$ mbar

Table 6:4 Deposition parameters.

After each deposition step, UPS and XPS measurement were performed. The experimental curves of N 1s and W 4f core level regions are displayed in Figure 6:7.
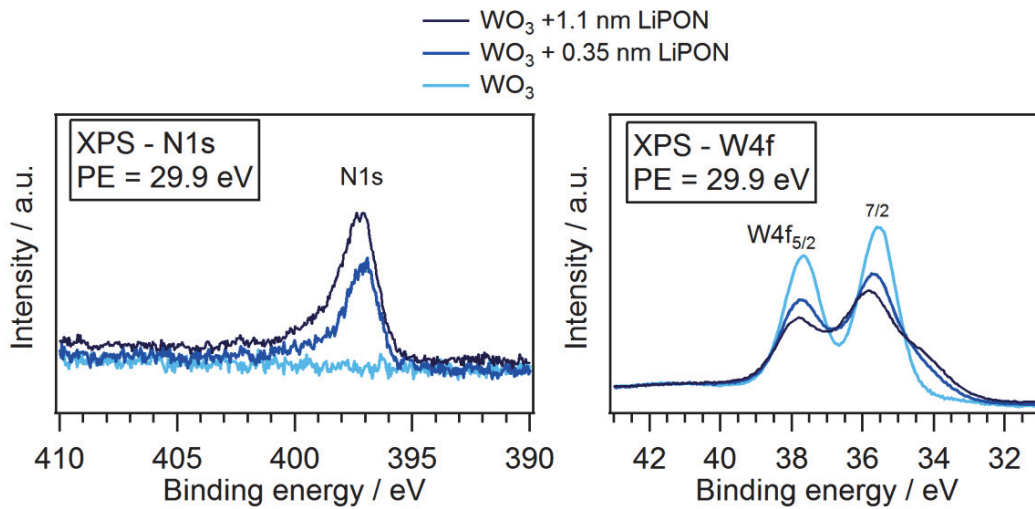
Figure 6:7   N1s core level spectrum (left) and W 4f core level spectrum (right) of the successive layers of WO_3 and LiPON/WO_3. The presence of LiPON is confirmed by the N1s peak and appear to modify the W4f peak.

The presence of LiPON on top of the WO_3 layer is confirmed by the appearance of the N 1s core level peak after deposition of thin layers of LiPON. Furthermore, a reduction of the intensity of the W4f peak can be observed; however, the Li 1s peak cannot be observed. In Figure 6:8, the decrease in intensity was compared to the attenuation estimated from the inelastic mean free path (IMFP) given by the universal curve (Seah, 1979). At a kinetic energy of 1218 eV, the IMFP, indicating the average distance travelled by an electron in a solid without loosing energy, was estimated to be λ_i = 3.35 nm, using eq. (31) from (Seah, 1979 - eq. 5) with the parameters A and B for inorganic coumponds.

$$\lambda_i = \frac{A}{E^2} + B\sqrt{E}$$

(31)
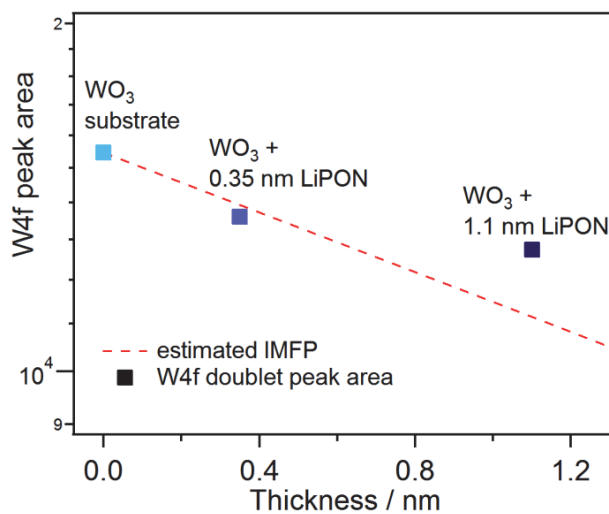
Figure 6:8   W4f peak area compared to expected attenuation from the inelastic mean free path (IMFP).

After the first step, the attenuation of the W 4f doublet is close to the estimation which would suggest a layer-by-layer growth; further depositions do not follow the same trend. There are three main types of thin film growth, the Frank-van der Merwe mode, where atoms reach the substrate and arrange layer-by-layer, the Volmer-Weber mode in which the atoms nucleate on some points and form a pile or island, and the Stranski-Krastanov which starts with a layer-by-layer growth until a critical thickness is reached, then islands are formed (Venables, 2000). The diminution of the intensity of the W4f peak suggests a Stranski-Krastanov growth mode, where layer-by-layer deposition is followed by a 3D growth. The apparently good coverage of the first layer indicates the presence of a sharp interface.

The modification of the W 4f peak shape suggests that inter-diffusion of lithium ions in tungsten oxide might occur, leading to the apparition of W^{5+} oxidation state. The full W 4f peak area was taken into account to draw Figure 6:8. After deposition of a thin layer of LiPON, the W 4f peak seems to contain more than a doublet. Deconvolution of the W 4f peak was performed using a Gaussian-Lorentzian peak shape and a Shirley background. The components determined from the deconvolution of the W 4f peak are illustrated in Figure 6:9.
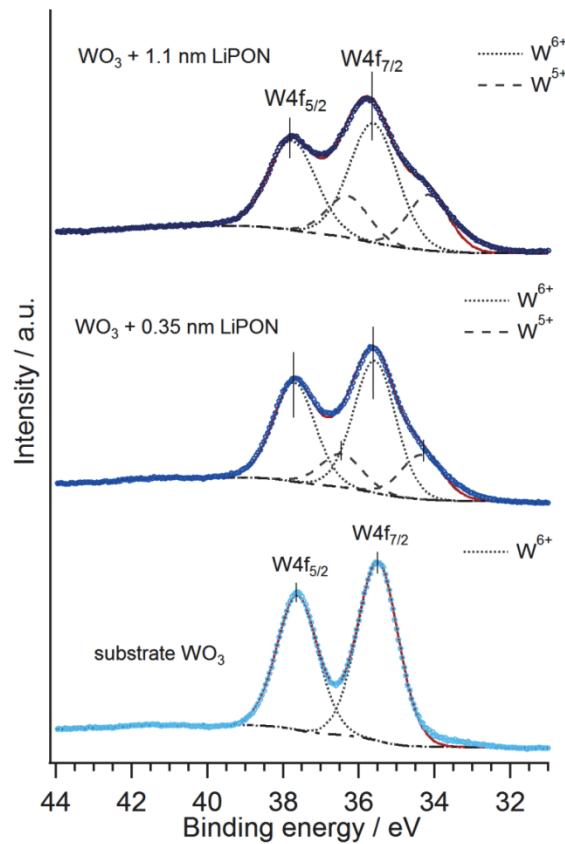
Figure 6:9   Peak fitting of W4f with a second doublet representative of the W^{5+} oxidation state. The circles represent the measured curve, the dot line the W^{6+} component, the dash line the W^{5+} component and the red solid line the sum of the fitted components. The modification of the W4f peak shape is attributed to the presence of tungsten atom with a reduced oxidation state (W^{5+}).

For the pure WO_3 sample, the W 4f doublet of W^{6+} can be observed. It can be fitted with a Gaussian-Lorentzian shape respecting the ratio of 3:4 specific to $f_{5/2}$:$f_{7/2}$ core levels. In addition to the intensity decrease, a broadening of the W 4f doublet peak can be observed. This broadening is similar to what is observed when sub-stoichiometric tungsten trioxides are deposited (Bouvard, 2016). A reasonable agreement between the sum of the components and the experimental data is obtained, when a second doublet with the same constraints is added to the deconvolution. This second doublet is attributed to the presence of W^{5+} oxidation state; this assumption is consistent with binding energies reported in the literature for reduced tungsten (Naumkin, 2012). In Chapter 7, the study of dry lithiation of WO_3 by XPS also shows a reduction of the W oxidation state, even though the O/W ratio remains constant.

The reduction of tungsten implies new states in the vicinity of the Fermi edge. The valence band region was investigated by UV-photoelectron spectroscopy, the spectra obtained using a Helium discharge lamp (He I at $h\nu$ = 21.22 eV) being presented in Figure 6:10.
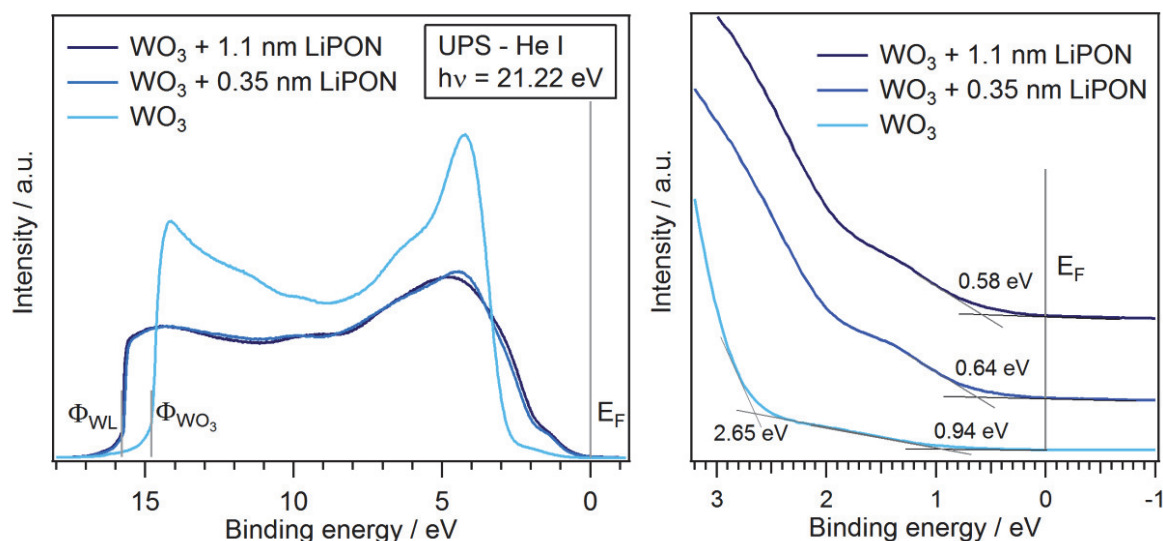
Figure 6:10   UPS spectra with a zoom on the valence band edge region. A modification of the work function and the apparition of states around 1.5 eV after deposition of LiPON can be observed.

For the WO_3 layer, a broad maximum is observed at approximately 4 eV. A slight shoulder is observed at 6 eV and a smaller broad feature around 2 eV. After LiPON deposition, there is a broadening of the 4 eV peak; a shoulder is appearing at 1.5 eV. A modification of the work function is also observed, going from Φ_{WO3} = 6.4 to Φ_{WL} = 5.4 eV KE after deposition of a LiPON layer.

The shoulder at about 6 eV is assigned to a hybridized W 5d-O 2p band. The main feature at 4 eV with the small feature at 2 eV are assigned to the O 2p derived band. The states between 2.6 eV and the Fermi edge may be an Urbach tail due to the amorphous nature of

WO_3 or to satellites peaks. In the valence band spectra of LiPON on silicon measured by UPS, no state are visible between 0 and 3 eV, therefore the occurrence of a shoulder at 1.5 eV is correlated with the partial reduction of W^{6+} and might be due to W^{5+} as observed in the under-stoichiometric tungsten oxides.

6.1.3 Influence of the nitrogen to argon ratio

While lithium phosphate is stable in air, lithium phosphate oxynitride (LiPON) is sensitive to humidity (Liu, 2006), which might limit its use in the glazing industry. Furthermore, due to the nature of the target, it has a slow deposition rate.

Two samples were deposited by varying the nitrogen to argon mass flow ratio in the plasma. Their optical properties and ionic conductivities were investigated. The deposition parameters are described in Table 6:5. The samples were deposited simultaneously on an ITO coated glass and on a piece of silicon wafer. Aluminum contacts were then deposited on the LiPON/ITO/glass sample to form electrodes and allow the electrochemical impedance spectroscopy (EIS) measurements. The LiPON deposited on silicon was measured by ellipsometry in order to determine its optical constants and thickness.

	Sample A O71102	Sample B O71129
Target	Li_3PO_4	Li_3PO_4
Substrate	ITO/glass and Si wafer	ITO/glass and Si wafer
Applied power	RF 100 W	RF 100 W
Deposition time	7 h 50	4 h 30
Process gas	$Ar + N_2$	$Ar + N_2$
Ar / sccm	13.9	13.9
N_2 / sccm	38.7	33.7
Working pressure	$3.4 \cdot 10^{-3}$ mbar	$5.4 \cdot 10^{-3}$ mbar
N_2/Ar mass flow ratio	**3.55**	**3.09**

Table 6:5   Deposition parameters. The N_2/Ar mass flow ratio is higher for sample A.

In order to determine the ionic conductivities of a sample, a precise measurement of the thickness is first needed: the samples deposited on silicon were measured by ellipsometry. They were measured at four angles of incidence: 60°, 65°, 70° and 75°. A Cauchy dispersion law was used to fit the ellipsometric data and obtain the refractive index as a function of the wavelength. The measured data and the values generated using the refractive index and thickness determined by the fit are illustrated in Figure 6:11.
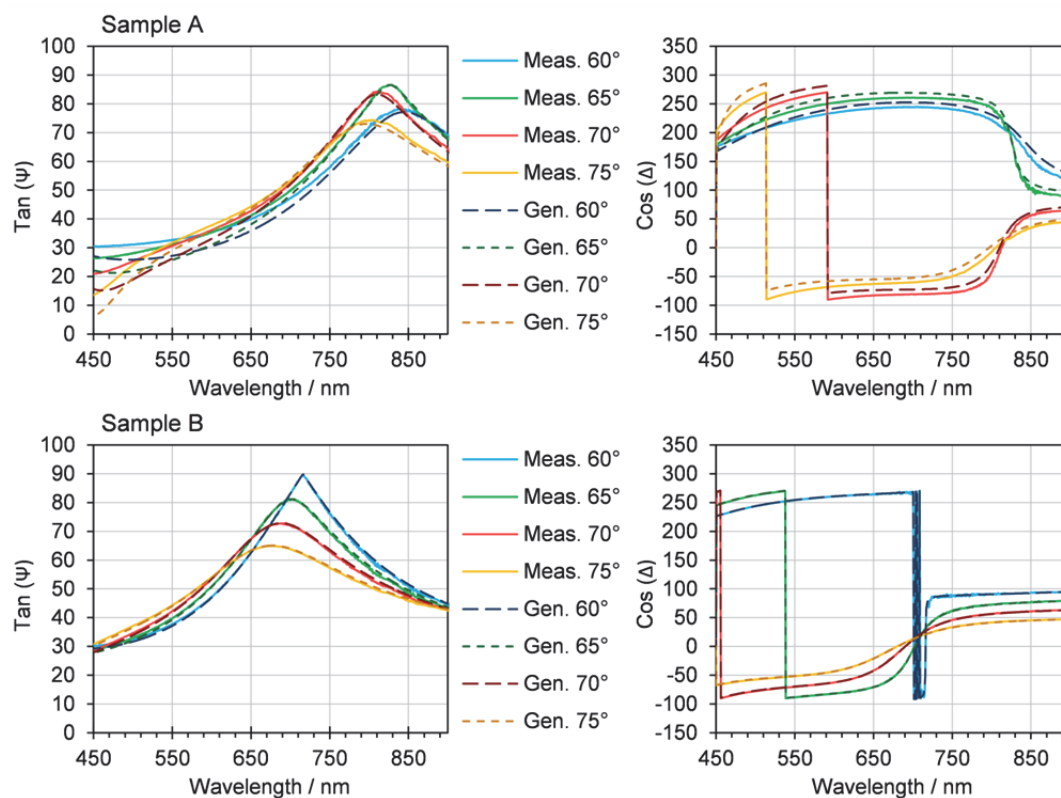
Figure 6:11   Ellipsometric data, tan(Ψ) and cos(Δ), measured in solid line and generated from the fitted thicknesses and refractive index in dashed line.

A reasonable agreement between the experimental values of tan(Ψ) and cos(Δ) and the ones obtained from the Cauchy dispersion law was achieved: R^2 was larger than 0.98 for both samples. The thickness determined by ellipsometry is 171 nm for sample A and 130 nm for sample B.

The refractive index determined by ellipsometry in the 450 to 950 nm region for sample A and B is shown in Figure 6:12. The variation in process gas ratio appears to have a strong influence on the optical properties of the samples.
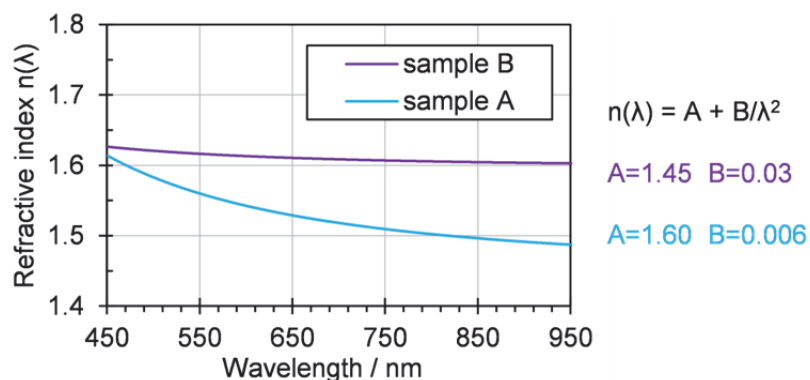
Figure 6:12   Refractive index of the samples A (O71102) and B (O71129) determined by ellipsometry, the numerical analysis is based on a Cauchy dispersion law.

The thickness of the samples being known, the Electrochemical Impedance Spectroscopy (EIS) measurements were then performed. The uncoated ITO part and the aluminum dots were connected to a potentiostat using metallic pins. A sinusoidal voltage with amplitude of 50 mV was applied and the response as a function of the frequency between 100 Hz and 2 MHz recorded. The results are presented, as the imaginary and real part of the resulting impedance, in the Nyquist representation. The measurement was repeated at various temperatures, the substrate being placed on a heating stage. The symbols in Figure 6:14 and Figure 6:15 represent the measured point at each temperature indicated in the legend for samples A and B. The EIS data was then fitted using the equivalent circuit model depicted in Figure 6:13, which is commonly used to describe a "cross plane" type of measurement of solid electrolytes (Hamon, 2006; Nisula, 2015; Li, 2017). It consists of a resistor R1 representing the wire and contact resistance, a resistor R2 in parallel with a constant phase element (CPE) Q2 representing the ionic conductivity process and a CPE Q3 representative of the capacitive behavior at low frequencies due to the conductor/insulator/conductor configuration. The resistance R2 describes the ionic conductivity of the material and is used to calculate the ionic conductivity σ_i using eq. (32). A CPE is a non-ideal capacitor, which is used to take into account the deviation to the pure capacitive behavior, generally attributed to electrode inhomogeneity or roughness (Kaplan, 1987; Rodíguez Presa, 2001). In the case of amorphous solid ion conductor, the deformation of the semi-circle, empirically modelled with a CPE, was attributed to a consequence of correlated forward-backward jumps of the ions (Shoar Abouzari, 2009), according to the concept of mismatch and relaxation in solid with disordered structures introduced by Funke et al. (2002).

$$\sigma_i = \frac{d}{R_2 \cdot A} \tag{32}$$

where d is the thickness and A the contact area.
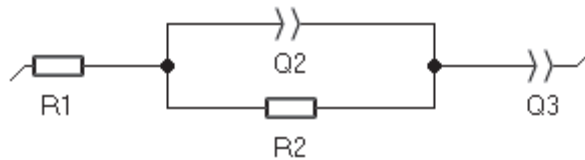
Figure 6:13   Equivalent circuit used to model the EIS data.
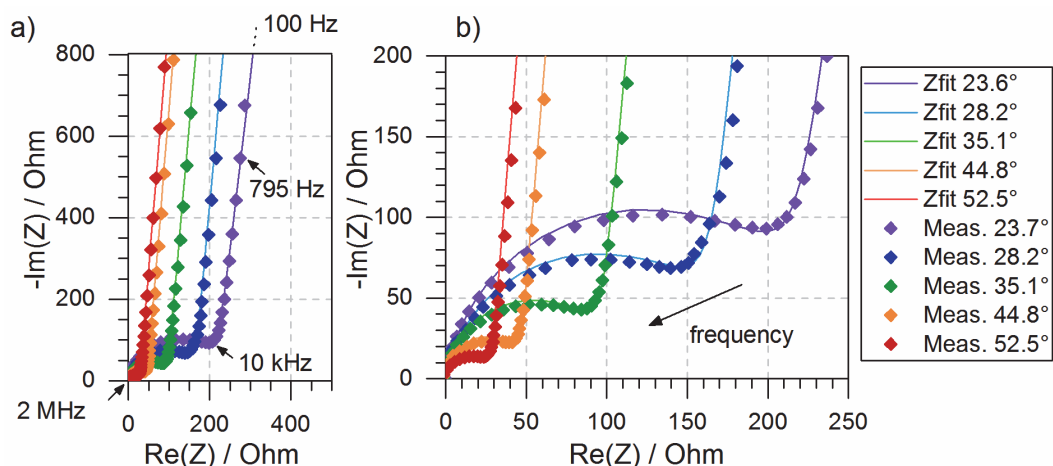
Figure 6:14   EIS measured data (symbols) fitted with the equivalent circuit described in Figure 6:13 (lines) for sample A. The response as a function of the frequency between 100 Hz and 2 MHz was recorded, the zoom show the response in the range 500Hz to 2MHz in a) and 2 kHz to 2 MHz in b).

In Figure 6:14, the EIS data present the shape of a quasi half-circle, typical of a resistance and a capacitance in parallel, followed by a straight line typical of a capacitance at low frequencies. The high frequencies are on the left-hand side of the diagram while the low frequencies are on the right-hand side. The data shown is a zoom on the half-circle part (2 kHz to 2 MHz in Figure 6:14 b)), the straight line continuing towards high values. The Nyquist diagrams obtained are fitting well with the adopted model; the resistance R2 determined from this model can be employed to determine the ionic conductivity, knowing the thickness (see eq. (32)). The "half-circle" size, decreasing with increasing temperature, reaveals that the process is thermally activated. The decrease is due to a diminution of resistance R2 (from about 200 Ω at room temperature to 30 Ω at 50°C), while Q2 remains in the range of 10^{-8} Farads. For sample B in Figure 6:15, similar features can be observed; however, the size of the "half-circle" is larger compared to sample A.
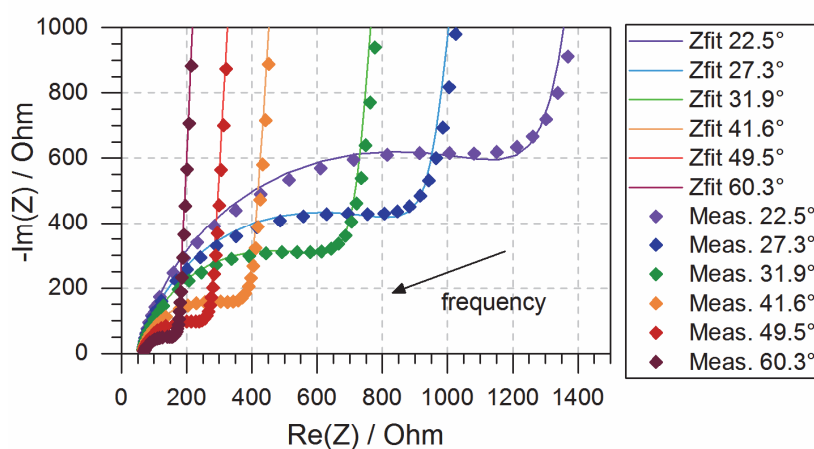
Figure 6:15   EIS measured data (symbols) fitted (with the equivalent circuit described in Figure 6:13 (lines) for sample B. The response as a function of the frequency between 100 Hz and 2 MHz was recorded, the zoom show the response in the range 1.5 kHz to 2 MHz.

It implies a larger resistance R2 in the ionic conductivity process. The ionic conductivity, as other thermally activated processes, follows an Arrhenius exponential law. It can be determined by plotting the natural logarithm of the ionic conductivity, multiplied by the temperature as a function of the inverse temperature, as in Figure 6:16.
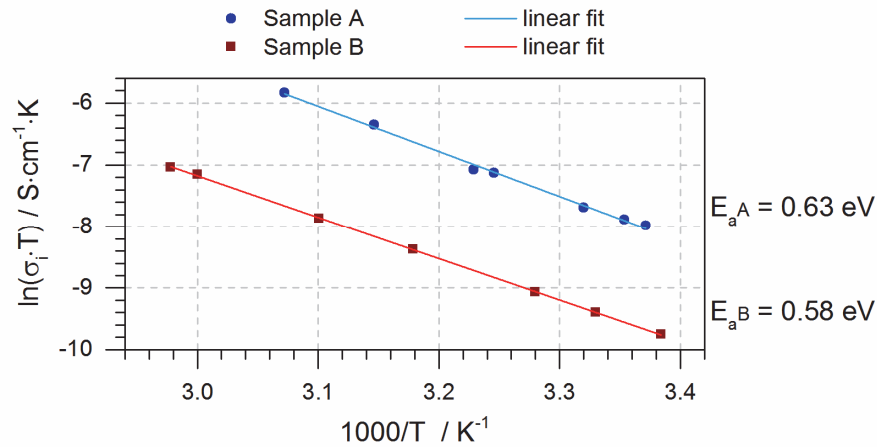
Figure 6:16   Evolution of the ionic conductivity times temperature as a function of the inverse of the temperature (dots) and linear fit of the data points (line). The slope of the trendline is used to calculate the activation energy.

A straight line is obtained, which confirm, the model for thermal activation; the slope multiplied by the Boltzmann constant is giving the activation energy. It was found to be equal to $E_a = 0.63$ eV for the sample A and $E_a = 0.58$ eV for the sample B. The ionic conductivity at 25°C was determined to be equal to $\sigma_i = 1.2 \cdot 10^{-6}$ S/cm for the sample A and $\sigma_i = 1.8 \cdot 10^{-7}$ S/cm for the sample B.

For a crystalline LiPON studied by Senevirathne et al. (2013), the minimum activation energies for Li ion vacancy and interstitial migrations were computed to be 0.4 eV and 0.8 eV, respectively, using first principles calculations. Their LiPON sample showed an activation energy of 0.6 eV; this was attributed to a migration of the Li^+ ions through vacancies in the crystal structure. The LiPON samples deposited in our laboratory are amorphous: a combination of vacancy and interstitial migrations may accordingly occur. A decrease of the activation energy can be attributed to an enhancement of the Li^+ ions mobility in the film (Rabaâ, 2001; Fleutot, 2011).

The sample B exhibits a lower ionic conductivity than sample A. However, unlike sample A, which quickly degraded in ambient air, sample B was still functional after numerous days in ambient air. EIS measurements were performed regularly for 29 days, a selection of representative results are presented in Figure 6:17.
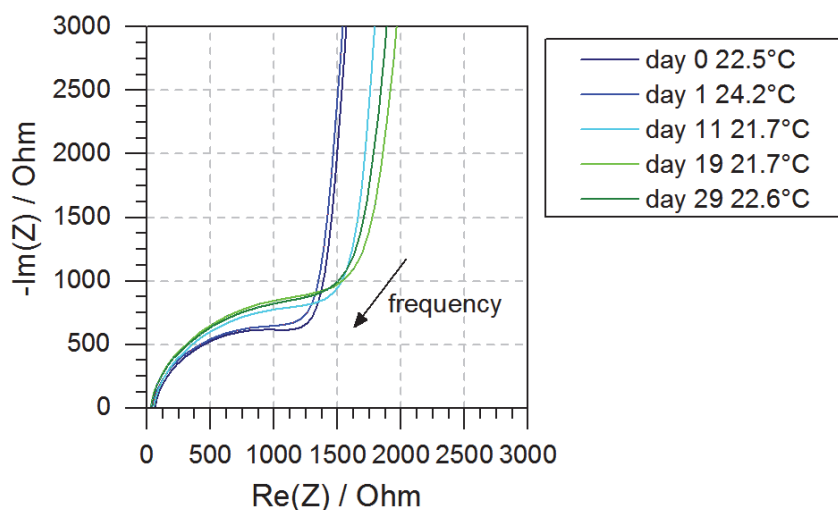
Figure 6:17   Evolution of the EIS data with time for sample B.

After the first days, a small deviation was observed. Some of this modification can be attributed to the sample temperature, which was varying a little due to room temperature variations. However, after this initial modification, stabilization was observed: the spectra looked similar. The aspect of sample B after some days also looked similar while a diffuse effect due to some particle growth could be observed on sample A, as illustrated in Figure 6:18.
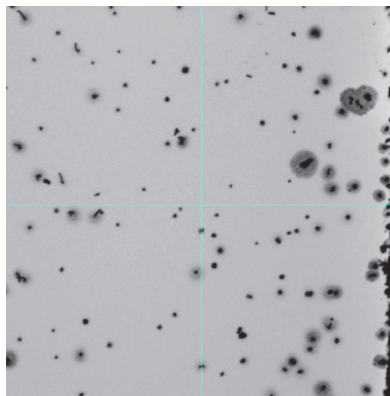
Figure 6:18 Aspect of sample A after 6 days, a diffusive aspect could be observed at the naked eye while the sample B deposited on silicon preserved a specular aspect.

Since the studied LiPON samples were transparent in the visible range, a Cauchy distribution law could be used to fit the refractive indices and thicknesses. Using an equivalent electric circuit and knowing the thickness of the sample, the ionic conductivity were inferred from the EIS measurements. They were performed over a range a temperature of 23 to 60°C to determinate the activation energy. A synthesis of the results is presented in Table 6:6.

	Sample A	Sample B
N$_2$/Ar mass flow ratio	3.55	3.09
Thickness	171 nm	130 nm
Deposition rate	21.8 nm/h	28.9 nm/h
Cauchy indices A / B	1.45 / 0.03	1.60 / 0.006
ionic conductivity at 25°C	$1.2 \cdot 10^{-6}$ S/cm	$1.8 \cdot 10^{-7}$ S/cm
Activation energy	0.63 eV	0.58 eV
Stability in air	less than a day	at least 29 days

Table 6:6 Summary of the results. The sample deposited with a lower N$_2$/Ar mass flow ratio exhibited a longer stability in ambient air.

EIS was also measured over time for sample A: after a few days, grains appeared on samples A, the measured signal being too low to provide an EIS Nyquist diagram. More experiments would be needed to understand the mechanism of degradation of LiPON in air; however, adding more argon to the plasma seems beneficial to the stability of the LiPON film in ambient air.

6.2 Lithium lanthanum titanium oxide coatings

The lithium lanthanum titanium oxides $Li_{3x}La_{2/3-x}TiO_3$ are a type of perovskite Li^+-ion conductors; they are made of a solid solution with a composition usually in the range of $0.06 < x < 0.14$ (Robertson, 1995; Fourquet, 1996) and usually referred as LLTO. These Li conductors are stable in dry and hydrated atmosphere as well as in a wide range of temperatures from 4K to 1600 K (Bohnke, 2008). Their use in thin films batteries is somewhat limited by the presence of Ti^{4+} ions, that can be reduced in contact with a lithium metal anode (Bohnke, 2008); however, they can be useful as electrolytes for electrochromic devices. LLTO films were deposited by RF magnetron sputtering. The optical properties were studied by ellipsometry and spectrophotometry; XRD and SEM were used to characterize the film morphology.

6.2.1 In situ photoelectron spectroscopy

A $Li_{0.5}La_{0.5}TiO_3$ target prepared at the Izmir Institute of Technology was used to deposit LLTO films. Details on the target preparation can be found in the paper of Ulusoy et al. (2018). A first investigation by photoelectron spectroscopy was performed to compare the coatings deposited in pure argon flow and those deposited with a small amount of oxygen. The deposition parameters are given in Table 6:7.

	LLTO-0 O70424	LLTO-1 O70425
Target	$Li_{0.5}La_{0.5}TiO_3$	$Li_{0.5}La_{0.5}TiO_3$
Applied power	RF 100 W	RF 100 W
Temperature	250°C	250°C
Deposition time	90 min	90 min
Ar / sccm	50.0	50.0
O_2 / sccm	/	0.5
O_2/Ar mass flow ratio	0	0.01
Working pressure	$4,5.10^{-3}$ mbar	$4,5.10^{-3}$ mbar

Table 6:7 Deposition parameters.

X-ray photoelectron spectroscopy was performed on the samples right after deposition without taking the samples out of the vacuum. The survey spectrum, La 3d, O 1s, and Ti 2p core levels peaks, are shown in Figure 6:19.

In the survey spectrum of the two LLTO samples, numerous peaks can be observed; they correspond to the La 3d, O 1s, Ti 2p, La 4p, La 4d, Ti 3p core levels and to the O_{KLL} and La_{MNN} Auger peaks. Smaller peaks, invisible on the scale of the survey spectrum, are also present: the Ti 3s, Ti 3p, La 5p and Ti 3d core levels. The Li 1s and O 2s core levels peaks cannot be

distinguished. The position of the core-level peaks of the La $3d_{5/2}$, O 1s and Ti 2p are in accordance with results from Pham et al. (2004) as depicted in Figure 6:19 with dashed lines.
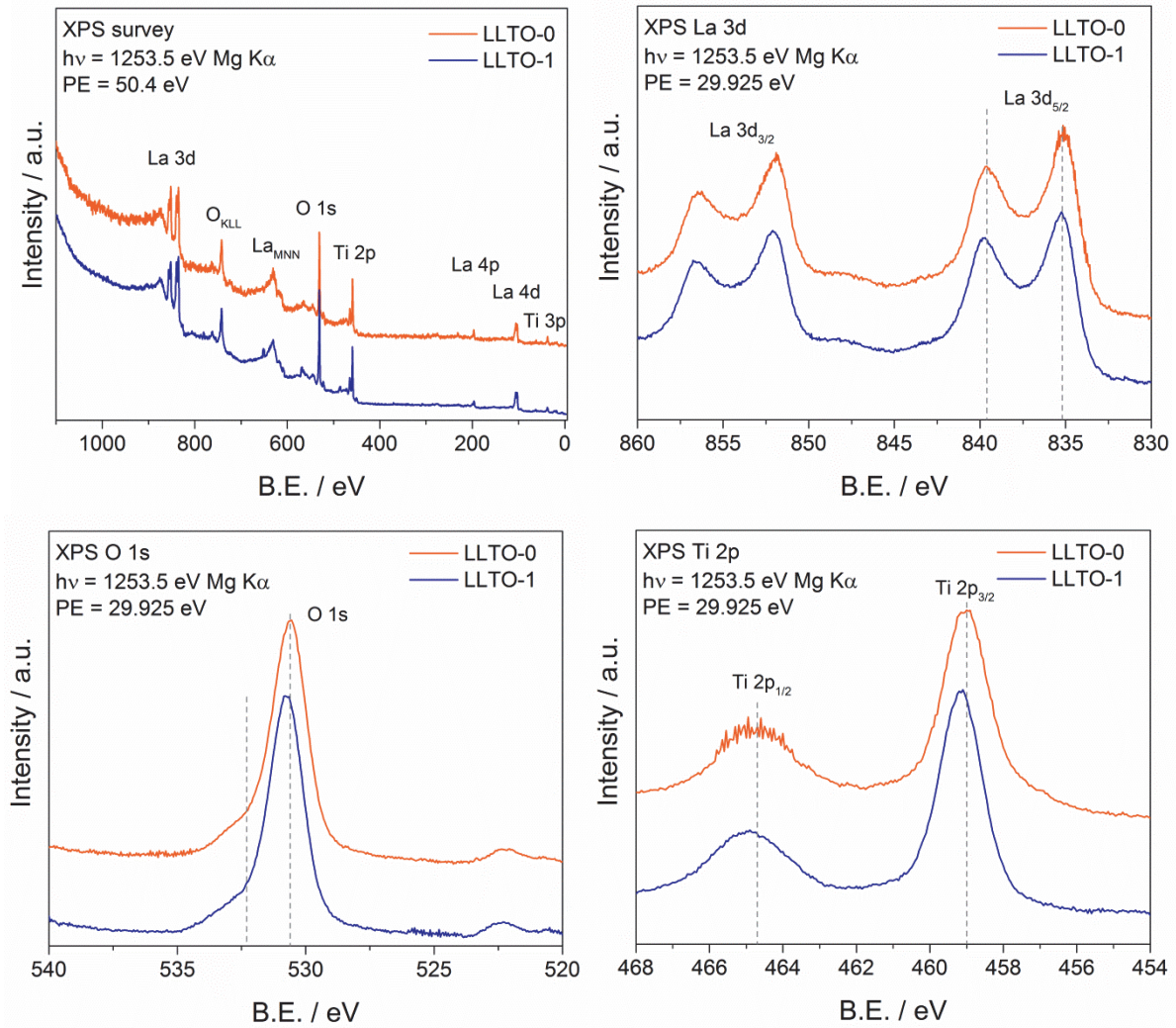
Figure 6:19   XPS of the survey spectrum, La 3d, O 1s, and Ti 2p peaks. Peak positions from (Pham, 2004).

The core level peak of La 3d exhibits a complex shape due to the well-separated spin-orbit components being further divided by multiplet splitting: the four visible peaks are due to one chemical state. The La 3d shake-up satellites, core-holes and plasmons play a role in the complex shape of the La 3d region (Sunding, 2011). The multiplet separation of the La $3d_{3/2}$ and La $3d_{5/2}$ is typical of the oxidation state of lanthanum. The typical value for La_2O_3, e.g. La having an oxidation state +III, is 4.6 eV. For both samples LLTO-0 and LLTO-1, this separation was found to be 4.5 eV, therefore suggesting a La^{3+} oxidation state.

The O 1s peak was found to be around 530.6 eV and is composed of the contributions from the three atoms it might be linked to: Li, La and Ti. Binding energy values for O 1s core level peak in mixed perovskite crystals are usually in the range 228-232 eV (Pawlak, 2002).

The Ti 2p core level peak displays two spin-orbit components Ti $2p_{1/2}$ and Ti $2p_{3/2}$, which are clearly separated. The split value is indicative of the chemical state and is 6.1 eV for Ti metal and 5.7 eV for fully oxidized Ti (Biesinger, 2010). Usually, $2p_{1/2}$ and $2p_{3/2}$ components have the same full width at half maximum; however for titanium, the Ti $2p_{1/2}$ is much broader than the Ti $2p_{3/2}$ peak due to the Coster-Kronig effect, the Ti$2p_{1/2}$ state being very short-lived compared to Ti $2p_{3/2}$ state. The measured split for both samples LLTO-0 and LLTO-1 is 5.7 eV, indicating an oxidation state Ti^{4+}.

The lithium core level peak cannot be distinguished due to its low sensitivity factor; therefore the precise chemical composition of the studied samples cannot be determined. However, to determine if some oxygen is needed in the plasma, the ratio of oxygen to titanium and lanthanum to titanium were determined by integrating the core levels of La3d, Ti 2p and O 1s after subtraction of a Shirley background. The results are presented in Table 6:8.

	Li / at.%	La / at.%	Ti / at.%	O / at.%	O/Ti	La/Ti
LLTO-0	<d.l.	9.7	18.5	71.7	3.88	0.52
LLTO-1	<d.l.	9.3	17.9	72.7	4.06	0.52

Table 6:8   Chemical composition obtained by integration of the La 3d, Ti 2p and O 1s core level peaks. The lithium peak was below the detection limit (d.l.).

The sample LLTO-0 was deposited without oxygen in the plasma: a ratio of O/Ti = 3.88 was obtained. The target from which it is sputtered has the following stoichiometry $Li_{0.5}La_{0.5}TiO_3$ and therefore a ratio of O/Ti = 4 is expected. However, it is common when sputtering from an oxide target to obtain a slightly under-stoichiometric film. During the deposition of sample LLTO-1, a small amount of oxygen was introduced in the plasma (O_2/Ar=0.01): a ratio O/Ti = 4.06 was obtained. An atomic ratio of La/Ti = 0.52 was found for both samples which is corresponding to the expected value of 0.5. The Li1s peak could not be observed and could therefore not be used for the determination of the chemical composition.

The oxidation states of the elements in $Li_{0.5}La_{0.5}TiO_3$ are Li^{1+}, La^{3+}, Ti^{4+} and O^{2-}, which is consistent with the values determined from the XPS results. The small addition of oxygen in the plasma does not seem to have a strong influence on the oxidation state of the elements. However, it is necessary, and enough, to reach the expected stoichiometry. The peak of lithium is not visible: this suggests a deficiency of lithium in the film. It might indicate a loss of lithium during the shipping of the target or during sputtering.

6.2.2 Determination of the optical properties

Since LLTO films are mostly studied in the context of thin film batteries, little is known regarding their optical properties. LLTO coatings were deposited on glass and silicon and

their optical properties determined by spectrophotometry and ellipsometry. Table 6:9 indi-cates the process parameters used for the deposition of LLTO samples, whose optical prop-erties were studied.

	LLTO O71026
Target	$Li_{0.5}La_{0.5}TiO_3$
Applied power	RF 100 W
Substrate	Si and glass
Temperature	no heating
Ar / sccm	50.0
O_2 / sccm	0.5
O_2/Ar	0.01
Working pressure	$3,9.10^{-3}$ mbar

Table 6:9 Deposition parameters.

The spectral transmittance of a sample deposited on glass, along with the one of the glass substrate is presented in Figure 6:20. The sample showed no haze and appeared highly transparent. The light transmittance and solar direct transmittance were determined: τ_v = 0.79 and τ_e = 0.81, these high values make LLTO suitable to be used in electrochromic de-vices. Ripples are visible and indicate both a significant thickness of the sample and a differ-ence of refractive index between glass and LLTO. The ripples maxima, equal to the transmit-tance value of the substrate, indicates a very low absorptance (most probably below 1%) and an extinction coefficient k close to zero. The value given for the solar direct transmit-tance and the light transmittance are determined for a film with a certain thickness and would differ for varying thicknesses due to the interference ripples.
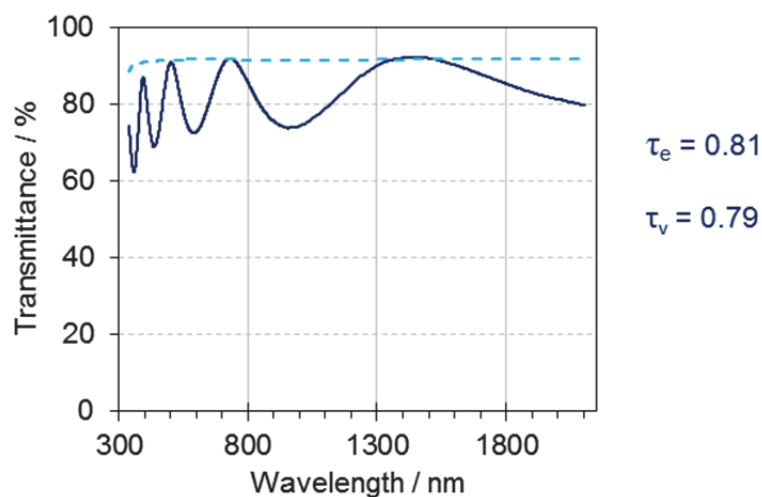
Figure 6:20   Spectral transmittance of the LLTO sample (solid line) on glass and the glass substrate alone (dashed line). The solar direct transmittance and the light transmittance of the LLTO are indicated.

In order to determine precisely the thickness and refractive index of the deposited material, an ellipsometry measurement was performed at three angles. The measured parameters of the ellipse tan (Ψ) and cos(Δ) are presented in Figure 6:21 (solid line).
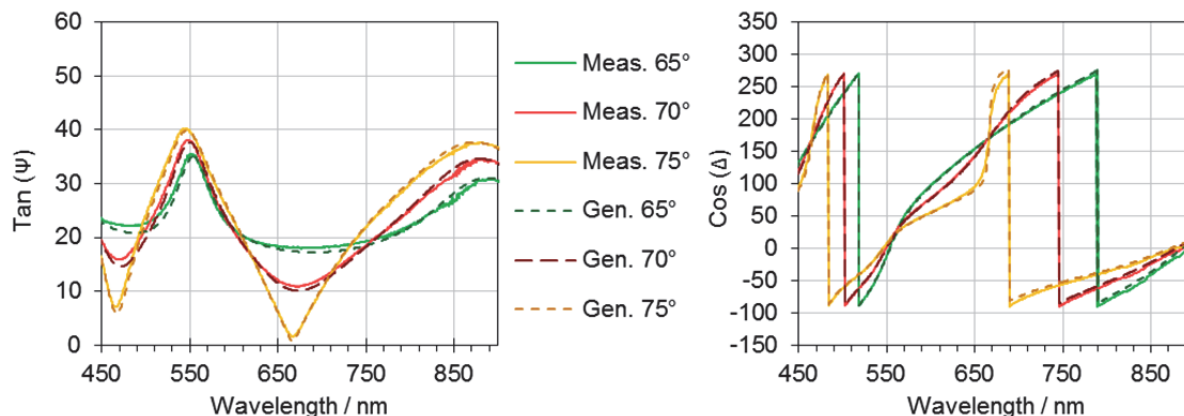
Figure 6:21   Ellipsometric data of the LLTO sample on Si substrate, tan(Ψ) and cos(Δ), measured in solid line and generated from the fitted thicknesses and refractive index in dashed line.

The deposited LLTO samples were transparent in the visible range. A Cauchy fit was performed to determine the refractive index and thickness material in the range 450 to 900 nm. Hereby, the extinction coefficient k was set to zero, considering that there is no absorption above 450 nm. Below 450 nm, some absorption is present, and therefore this part of the spectrum was not considered in the fitting procedure. The tan(Ψ) and cos(Δ) determined according to this fit are showed in dashed line in Figure 6:21; they are in good agreement with the experimental data, which confirms the assumption that absorption is nearly zero in the range 450-900 nm. The same measurement was performed on samples of various thicknesses deposited with similar parameters; the same refractive index can be used to fit the new data and therefore validate the obtained results. The refractive index and the parameters of the Cauchy distribution law are presented in Figure 6:22.

$$n(\lambda) = A + B/\lambda^2$$

A=2.05 B=0.033

k = 0
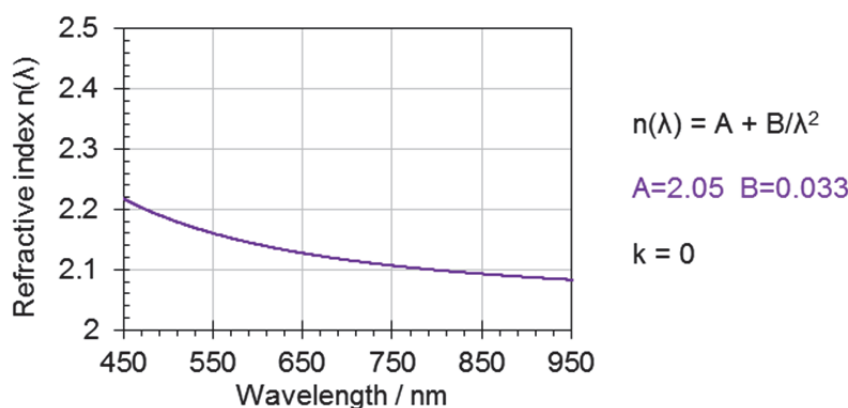
Figure 6:22   Refractive index of the LLTO samples, deposited with the parameters indicated in Table 6:9, determined by ellipsometry using a Cauchy distribution law and considering k=0.

The LLTO samples deposited were transparent and showed no haze and are therefore candidates to serve as an electrolyte in devices requiring high transparency in the solar range, such as electrochromic devices. The high refractive index, close to the one of WO_3 with about 30% of porosity (see Chapter 5), might be beneficial to reduce the reflection at interfaces in an all-solid state device.

6.2.3 Challenges for the use in electrochromic devices

Further investigations on LLTO were carried out to determine the electrochemical properties and the crystal structure. The samples were mostly deposited at room temperature for the same reason than ITO: high temperature deposition would modify the crystallinity of the underlying layers and lead to unwanted diffusion. X-ray diffraction measurements were performed in order to determine if the samples deposited at room temperature were amorphous or crystalline. The diffraction pattern measured from a sample deposited with the same parameters as indicated in Table 6:9 (section 6.2.2) is illustrated in Figure 6:23.
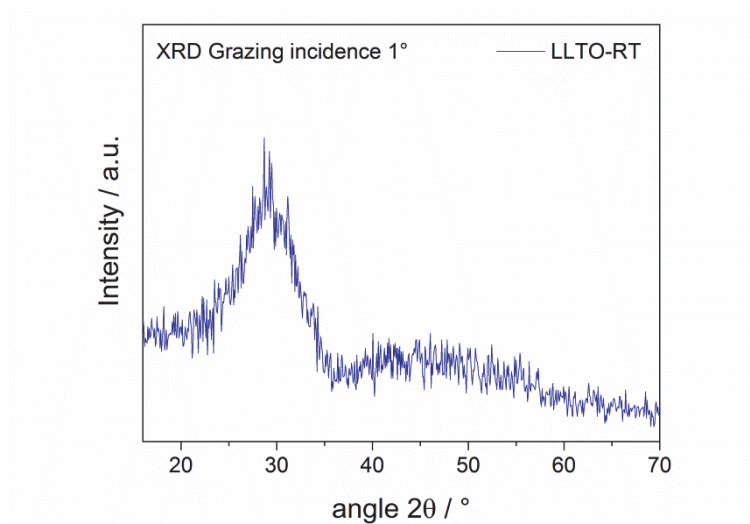
Figure 6:23   XRD pattern of a LLTO sample deposited with no substrate heating. No peak distinctive of a crystalline phase are observed.

The XRD pattern does not exhibit sharp peak typical of a crystal structure: this suggests an amorphous or nanocrystalline structure. The large bump situated around 28.9° is about 5.9° wide at half intensity. According to the Scherrer formula (see Chapter 3), it means that the majority of the crystalline grains are smaller than 1.4 nm, indicating a low long-range order in the atom network.

Electrochemical experiments were carried out in order to determine the ionic conductivity of the deposited thin films with various contact electrodes. However, the signal to noise ratio was too low and the ionic conductivity could not be determined. The setup was similar to the one use for LiPON samples. Since the setup was validated for LiPON samples, it seems

that the fact that LLTO samples could not be measured would come from the composition or structure of the LLTO films. The lithium was not visible in the XPS experiment and indicates that the amount of lithium is the film is lower than expected. Low lithium content would also be detrimental to the ionic conductivity of the film and the fact that the ionic conductivity could not be measured might originate from the low Li content. As an alternative to the ITO substrate, silver was deposited and used as an electrode: the LLTO film showed very poor adhesion to the Ag layer as illustrated in Figure 6:24 and no ionic conductivity could be extracted from the electrochemical measurements.
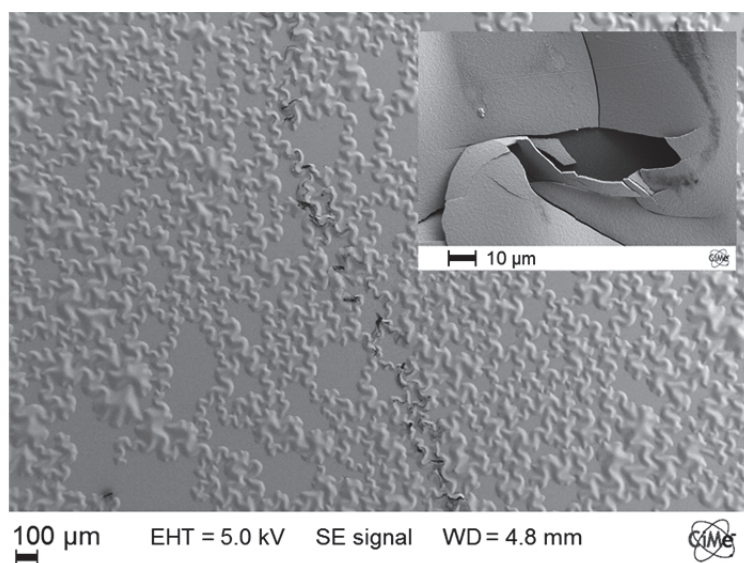
Figure 6:24   SEM image of a LLTO sample deposited on Ag/Si. The inset shows the delamination of the film.

The research on LLTO electrolytes is usually performed on samples deposited at elevated temperatures or subjected to a thermal treatment after deposition. In the large scale glazing industry, it is preferable to avoid substrate heating during deposition of coatings, since it requires relatively large effort to obtain homogeneous temperature on large surfaces. Therefore, in this study, room temperature deposition of LLTO was considered. However, a deficiency of lithium in the deposited films is suspected and might originate from a loss of lithium in the target, or during the deposition, which might explain the poor electrochemical results. Post-lithiation for the LLTO films was attempted but a segregation of lithium on the surface of the film could be observed and the ionic conductivity of these samples could not be determined either. Furthermore, LLTO coatings similarly to LiPON coatings require relatively slow deposition rate due to the nature of the target; therefore, another approach was envisaged using a porous metal oxide, Ta_2O_5, which can be deposited from a metal target.

6.3 Tantalum pentoxide as a lithium electrolyte

Tantalum pentoxide, noted Ta_2O_5, is a high band gap insulator material with a high refractive index and low absorption: it is widely used for capacitors and optical coatings. It was identified long ago, as a proton conducting material that could be used in electrochromic devices (Ozer, 1997); however, the use of tantalum pentoxide (Ta_2O_5) to operate as a Li^+ ion conductor in an all-solid-state device was not as widespread (Frenning, 2001; Dong, 2018). Using a metal oxide electrolyte is advantageous because of the low cost and higher deposition rate of metal targets compared to lithium containing targets.

6.3.1 Optimization of the deposition parameters

When depositing ceramic coatings via reactive magnetron sputtering, the oxygen partial pressure to obtain a fully oxidized sample must be determined. In DC or bipolar-pulse DC sputtering, a convenient way to do so is to monitor the discharge voltage, for a constant power, as a function of the increase of the oxygen level. Figure 6:25 shows the evolution of the discharge voltage of the Ta target with a constant applied power of 100 W, an argon level set to 17 and a working pressure of $2,5.10^{-2}$ mbar (12 ¾ turns).
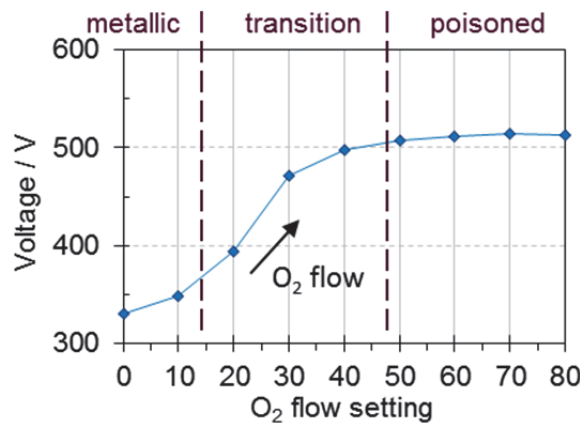
Figure 6:25   Discharge voltage on the Ta target as a function of the oxygen level. The process parameters are chosen at the end of the transition zone.

Three zones can be observed corresponding to three targets modes: metallic, transition and poisoned. For a fully oxidized coating, the process parameters should be chosen at the end of the transition zone: here, a working point of O_2 at 40.0 was chosen. The obtained sample was highly transparent, as can be seen in Figure 6:26.
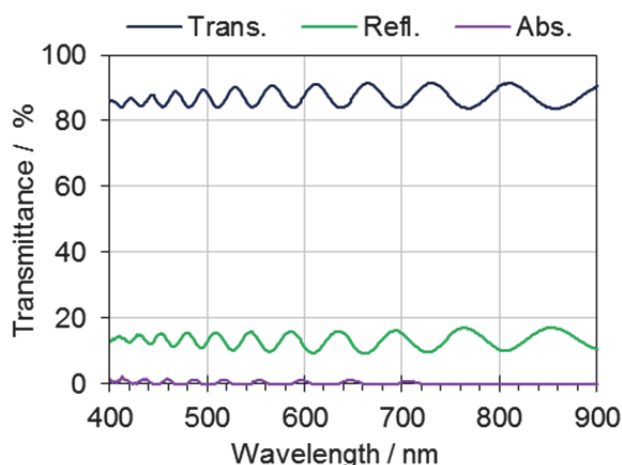
Figure 6:26   Spectral transmittance, reflectance and absorptance of the sample deposited with the parameters chosen. The absorptance is below 1 % in most of the visible range.

Furthermore, the sample, deposited at a high working pressure, did not exhibit haze, indicating that the porosity induced by the process is smaller than the wavelength of light. Further characterization was performed by ellipsometry in order to evaluate the degree of porosity.

6.3.2 Characterization of the porosity

Nanoporosity was shown to be beneficial to the insertion of Li^+ ions in WO_3; therefore, a similar approach was chosen for Ta_2O_5 and samples were deposited at various working pressure as indicated in Table 6:10. Samples 3, 4 and 5 were expected to have high porosity. The oxygen to argon mass flow ratio was adapted to the other process parameters in order to obtain only fully oxidized samples.

	1 A80318	**2** O80213	**3** O80215	**4** O80305	**5** O80319-2
Target	Ta	Ta	Ta	Ta	Ta
Applied power	DC-p 150 W	DC-p 50 W	DC-p 50 W	DC-p 100 W	DC-p 100 W
Deposition time	70 min	17 min	30 min	30 min	30 min
Working pressure	$2,2.10^{-3}$ mbar	$2,3.10^{-3}$ mbar	$2,5.10^{-2}$ mbar	$2,5.10^{-2}$ mbar	$2,6.10^{-2}$ mbar

Table 6:10 Deposition parameters: the working pressure is in the 10^{-3} mbar range for samples 1 and 2 and 10^{-2} mbar for samples 3, 4 and 5.

The films were deposited on silicon substrate to be studied by ellipsometry. All the considered samples were transparent and could be fitted using a Cauchy distribution law; the obtained results for one of the Ta_2O_5 coating (sample 4) are displayed in Figure 6:27.
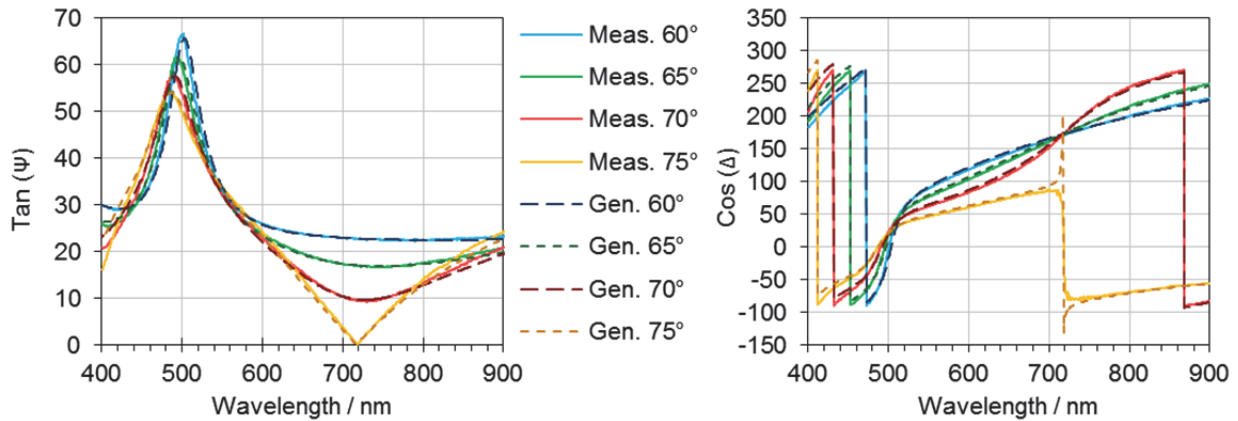
Figure 6:27   Ellipsometric data of a Ta_2O_5 coating (sample 4) on Si substrate, tan(Ψ) and cos(Δ), measured in solid line and generated from the fitted thicknesses and refractive index in dashed line.

The data generated from the fitting procedure using a Cauchy distribution law is in good agreement with the measured data. The refractive indices determined in this manner are shown in Figure 6:28.
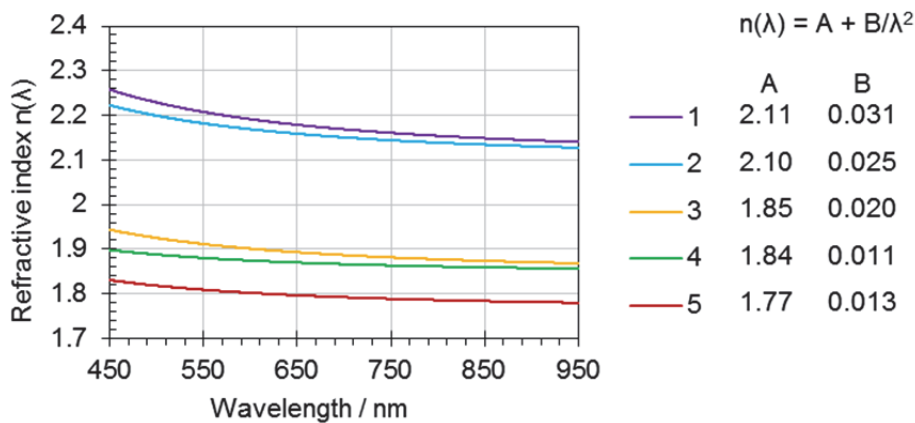
Figure 6:28   Refractive index of the Ta_2O_5 samples deposited at with working pressure is in the 10^{-3} mbar range for samples 1 and 2 and 10^{-2} mbar for samples 3, 4 and 5. Precise working pressures are indicated in Table 6:10.

Depending on the deposition conditions, refractive indices in the range 1.8 to 2.2 at 550 nm were obtained. Sample 1 was deposited at a low working pressure and high power density in order to obtain a compact sample. Since air has a refractive index of 1, nanoporosity is expected to decrease the value of the refractive index. Sample 2 deposited at a similar low working pressure but with a lower power density shows also a high refractive index indicating a low porosity level. The Bruggeman effective medium theory (Bruggeman, 1935) was used to estimate the porosity level in the samples, as performed on WO_3 samples (see Chapter 5). The volume fraction of Ta_2O_5 in a Ta_2O_5:air matrix was determined and is shown in Table 6:11 along with the thickness and refractive index at 550 nm determined from the ellipsometry measurements.

Sample	Working pressure	thickness / nm	n at 550 nm	Volume fraction of Ta_2O_5	Pore volume fraction
1	$2,2.10^{-3}$ mbar	749.2	2.21	1.00	0
2	$2,3.10^{-3}$ mbar	65.3	2.18	0.98	0.02
3	$2,5.10^{-2}$ mbar	857.8	1.91	0.76	0.24
4	$2,5.10^{-2}$ mbar	222.8	1.88	0.74	0.26
5	$2,6.10^{-2}$ mbar	193.3	1.81	0.68	0.32

Table 6:11 Thickness and refractive index at 550 nm determined by ellipsometry, volume fraction calculated using the Bruggeman effective medium theory. Sample 1 was considered fully compact. Sample 3, 4 and 5 deposited at high working pressure (10^{-2} mbar range) exhibit porosity up to 32 %.

Sample 1 deposited at low working pressure and high power density was considered to be fully compact: the other samples are compared to this sample. These results show that increasing the working pressure effectively increased the nanoporosity level. Sample 5 deposited at $2,6.10^{-2}$ mbar shows about 30 % of voids according to this calculation: sample 3 and 4 display around 25 % of porosity. Deposition parameters can thus be chosen to tune the optical and morphological properties of a film to reach the desired properties.
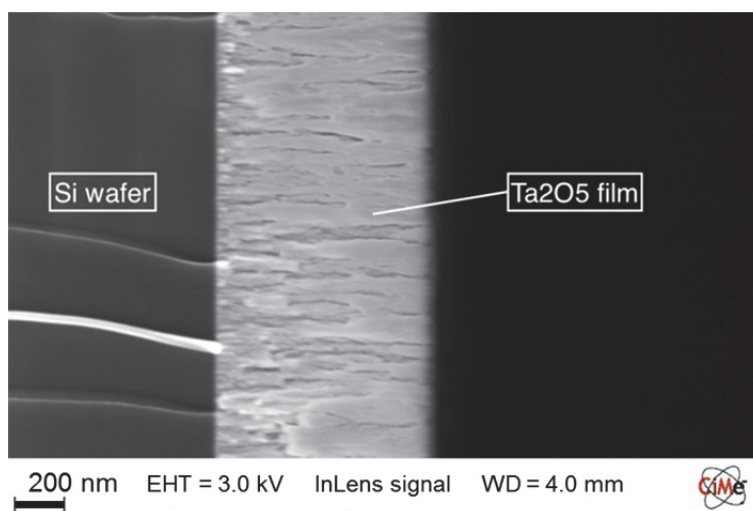
Figure 6:29   SEM image of a Ta_2O_5 coating (sample 3) showing the porous nature of the film.

Scanning electron microscopy was performed to observe the morphology of the film. An image of sample 3 is shown in Figure 6:29. The in-lens detector (also called Through The Lens detector) was used: it collects the secondary electron in a symmetrical manner allowing for a shadow free image with high topographic resolution. A columnar and loose packing morphology can be observed confirming the porous nature of the film.

6.3.3 Ionic and DC conductivity

The measurement of the Li ion transport in Ta_2O_5 coatings requires the presence of lithium and the Ta_2O_5 films, as deposited, did not contain any lithium. Dry lithiation of the film in order to be able to perform the measurement was attempted: but it created leakage currents between the electrodes and no results could be obtained from the measurements.

Another characteristic needed to be used as an electrolyte is to have a low electrical conductivity. An estimation of the electronic leakage was determined by applying successive potentials steps for long period of times on a Al/Ta$_2$O$_5$/ITO sample. DC current decay curves were measured for 24h applying a voltage drop of 1, 2 and 3 V as shown in Figure 6:30.
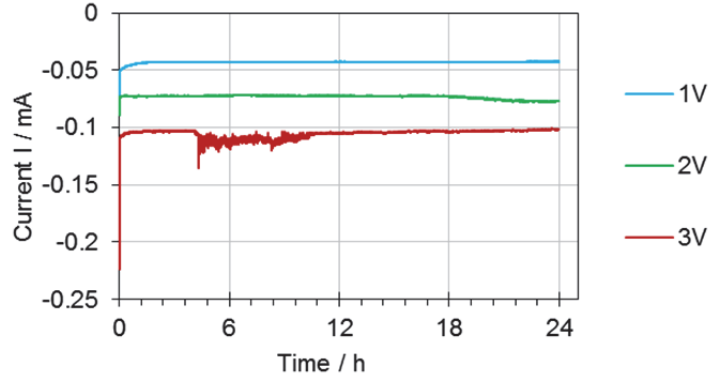
Figure 6:30   Current response measured to applied potential steps of 1, 2 and 3V.

The current decreases and reaches a steady state due to the electronic leakage current. The electronic resistance R can be obtained from the slope of voltage-current curve presented in Figure 6:31, the electronic conductivity σ is then determined using eq. (33).

$$\sigma = \frac{t}{R \cdot A}$$

(33)

where t is the thickness and A the contact area.
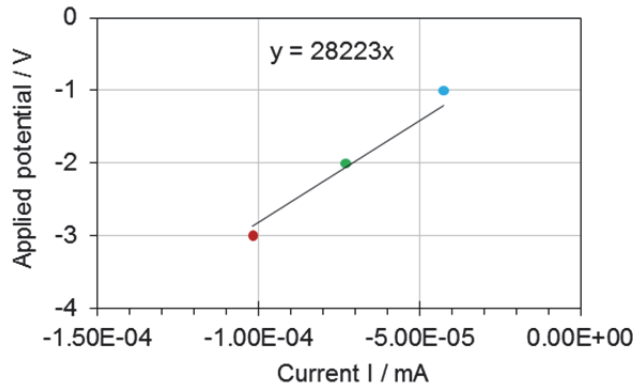
Figure 6:31   Potential-current curve.

In this experiment t = 200 nm and A = 3.14 mm^2, the resistance defined by the slope of the voltage-current curve was found to be 28.22 kΩ, giving an electronic conductivity σ = 2.3·10^{-8} S/cm. The electronic conductivity should be more than ten orders of magnitude lower than the ionic conductivity; usually, electronic conductivities in the range of 10^{-12} S/cm are expected for electrolytes. During the experiment, it was observed that the film is sensitive to scratches and it might be possible that the installation of electric contacts would

deteriorate the film locally; therefore, it might also modify its thickness locally. Furthermore, the electronic conductivity was measured perpendicularly to the substrate plane and could have been influenced by small pin-holes. This kind of measurement provides only an upper limit value of the electronic partial conductivity (Su, 2015) and not a single value of the electronic conductivity. Furthermore, the noise observed in Figure 6:30 after few hours of applications of the 3 V potential might indicate other degradations in the film.

6.3.4 Influence of Ta_2O_5 in a liquid electrolyte device

In order to assess if Ta_2O_5 coatings could be used as solid electrolytes, it was decided to deposit a layer of Ta_2O_5 on a WO_3/ITO/glass and to assemble it with a NiO/ITO/glass to form a liquid state electrochromic device. The aim is to determine if the Li^+ ions can travel through the Ta_2O_5 coating to intercalate in the WO_3 layer. The NiO_x counter electrode was deposited on an ITO substrate deposited at room temperature as the ITO layer to be used in all-solid-state devices. The process parameters used for the deposition of the WO_3, Ta_2O_5, NiO_x and ITO layers are indicated in Table 6:12; the setup are illustrated in Figure 6:32.

	WO_3 O80304	Ta_2O_5 O80319-2	$NiVO_x$ O80319-3	ITO O80326-2
Target	W	Ta	Ni-V	ITO
Substrate	ITO X190/glass	WO_3/ITO/glass	RT-ITO/glass	Glass
Applied power	DC 150 W	DC-p 100 W	DC-p 200 W	DC-p 65 W (50 kHz)
Deposition time	30 min	30 min	30 min	20 min
Ar / sccm	12.5	23.6	41.7	25.0
O_2 / sccm	8.3	4.0	1.0	1.6
Ratio O_2/Ar	66.67 %	16.81 %	2,38 %	6.35 %
Working pressure	$2,0.10^{-2}$ mbar	$2,6.10^{-2}$ mbar	$1,6.10^{-2}$ mbar	$2,6.10^{-3}$ mbar

Table 6:12 Deposition parameters; the samples WO_3 was deposited on ITO coated glass with a sheet resistivity of 15-30 ohm/sq (ITO X190 from Delta Technologies). The NiOx coatings were deposited on an ITO coating deposited at room temperature (RT ITO).
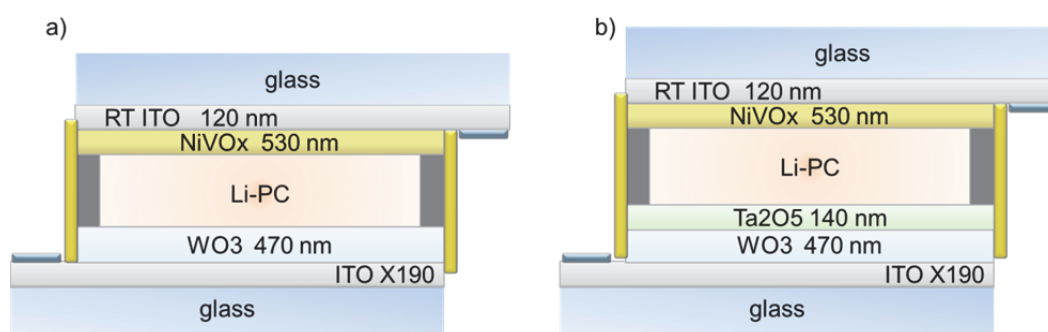
Figure 6:32 Illustration of the devices used to study the influence of the Ta_2O_5 layer (not to scale).

The two devices were connected to the potentiostat and chronoamperometry experiments were performed. The applied voltage, the current response and the light transmittance, determined from the spectral transmittance measured every 0.5 seconds, are displayed in Figure 6:33Figure 5:17 a), b) and c) respectively.
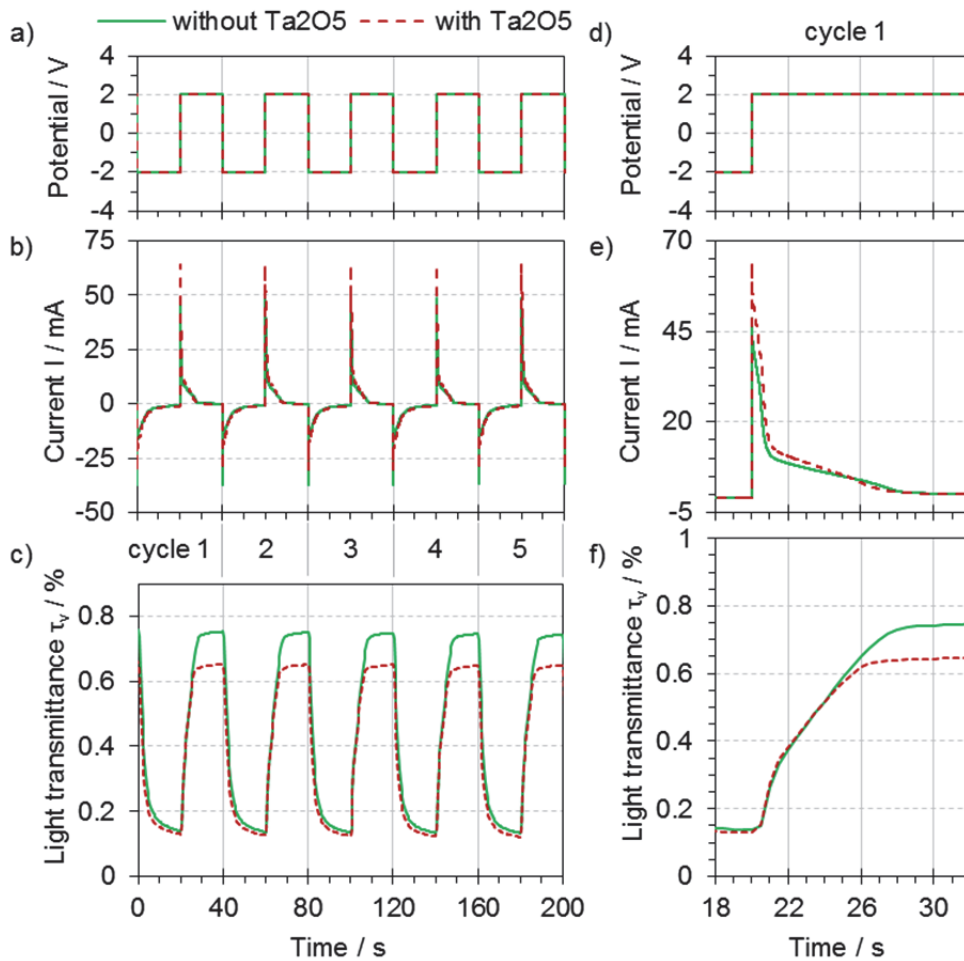
Figure 6:33 Chronoamperometry experiment on the Glass/ITO/WO3-LiPC-NiO/ITO/Glass device and the Glass/ITO/WO3/Ta2O5-LiPC-NiO/ITO/Glass device: a) Potential applied, b) current response and c) evolution of the transmittance at 550 nm during cycling. d), e) and f) zoom on the first cycle.

The applied voltage was successively -2 V and +2 V, each step lasting 20 seconds; five cycles of coloring/bleaching are shown in Figure 6:33. The Ta_2O_5 layer does not seem to prevent the movement of Li^+ ions in the device, this result being promising for the use of Ta_2O_5 as solid state electrolyte. The current response shape looks similar for both samples; however, the amount of charge passing in the sample with the Ta_2O_5 layer is higher: 81.9 mC versus 68.0 mC without (for cycle 5). The difference can be observed in the zoomed Figure 6:33 e) were a higher current for the device with a Ta_2O_5 layer is clearly seen.

The variation of the light transmittance during switching is similar in terms of speed and minimum value reached (13.8 and 13.0 %); however, in the clear state, the sample without Ta_2O_5 reaches higher values (75.7 versus 65.8 % for the sample with Ta_2O_5). The values of light transmittance τ_v and capacity Q determined for cycle 5 are indicated in Table 6:13; they were used to calculate the optical density (OD) and the color efficiency (CE).

	without Ta$_2$O$_5$	with Ta$_2$O$_5$
τ_v min / %	13.3	12.1
τ_v max / %	74.3	64.9
$\Delta \tau_v$	61.0	52.8
inserted capacity Q$_i$ / mC	68.0	81.9
extracted capacity Q$_e$ / mC	66.7	81.4
OD(550) = log (τ_v max/τ_v min)	0.75	0.73
CE (coloring) = OD*A/Q$_i$	69.1	56.0
CE (discoloring) = OD*A/Q$_e$	70.4	56.4

Table 6:13 Comparison of the liquid devices with and without a Ta$_2$O$_5$ layer. OD is the optical density, CE the coloration efficiency and A the area of the device.

The switching contrast $\Delta\tau_v$ is lower for the Ta$_2$O$_5$ sample while the inserted charge is higher; therefore, the color efficiency is lower for this sample. The extra-charge does not lead to an extra coloration; it is possible that the Li$^+$ ions are inserted in the Ta$_2$O$_5$ layer. Tantalum oxides were reported to have a cathodic electrochromic behavior (Granqvist, 1995).

Since Ta$_2$O$_5$ is highly transparent in the visible range, this lower light transmittance cannot originate from absorption; it may be due to an additional reflection at the WO$_3$/Ta$_2$O$_5$ interface, at the Ta$_2$O$_5$/electrolyte interface or to some bubbles in the liquid electrolyte. The Figure 6:33 shows the spectral transmittance of both devices, as described in Figure 6:32, after connection to the potentiostat but before any cycling test. A lower light and solar direct transmittance is already observed.
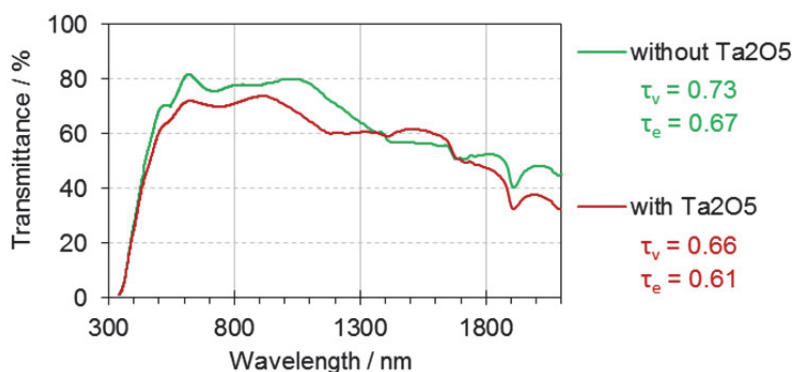
Figure 6:34   Spectral transmittance of the Glass/ITO/WO3-LiPC-NiO/ITO/Glass device and the Glass/ITO/WO3/Ta2O5-LiPC-NiO/ITO/Glass device after connection to the potentiostat but before any cycling.

The tantalum pentoxide layer was shown to allow lithium ions to move from the liquid electrolyte to the tungsten trioxide layer; this result suggests that a Ta$_2$O$_5$ film can be used as a solid electrolyte in an all-solid-state device. Furthermore, the ITO substrate used for the counter electrode was deposited at room temperature, as it would be in an all-solid-state device; and the device is moreover well colored after 20 seconds and can discolor in about 5 seconds.

6.4   Discussion and perspectives

The aim of this chapter was to study potential solid ion conductor for an all-solid-state electrochromic device. Two promising electrolytes from the field of thin film batteries were investigated. LiPON were deposited successfully at room temperature with ionic conductivities in the range usually obtained for sputtered LiPON films (Hamon, 2006). An activation energy of 0.6 eV was obtained suggesting a migration of the Li ions through vacancies in the LiPON atom network. Furthermore, it was found that increasing the argon content in the argon-nitrogen plasma can enhance the stability of a LiPON film to ambient air. LLTO which has theoretically higher ionic conductivity than LiPON was also considered. This material is not widely studied in the context of electrochromic devices and therefore, the optical properties are not easily available. It was found than amorphous LLTO films exhibit a high transparency in the solar range with solar direct transmittance and light transmittance of 80%. The refractive index could be determined using a Cauchy distribution law and was found to be relatively similar to that of a tungsten oxide with about 30% porosity. However, the ionic conductivity of the deposited LLTO films could not be assessed, most probably due to insufficient lithium content in the films. The LLTO target was prepared in the framework of collaboration with Izmir institute of technology and is not a commercial product. Loss of lithium may have occurred during the shipping of the target or due to the preparation or deposition conditions. Lithium could not be observed by XPS for the LLTO films, while a Li 1s core level peak was clearly visible for LiPON films. Besides, LiPON and LLTO film require slow deposition rate to avoid a damage of the lithium-containing ceramic target.

Tantalum pentoxide was investigated, as a lithium-free electrolyte alternative. This material is widely used in the industry, especially for capacitors and also for optical coatings. The process parameters for the depositions can be adjusted to tailor the refractive index, the porosity and the deposition rate to specific needs. It was not possible to measure the ionic conductivity of the Ta_2O_5 in the solid state, since it does not contain lithium as-deposited. In order to evaluate if it could be used as an electrolyte for an all-solid-state electrochromic device, a Ta_2O_5 film was deposited on top of a WO_3 coating and assembled with a counter electrode in a liquid device. The light transmittance of the device could still be varied and the switching speed did not seem to be reduced. Therefore, the use of nanoporous Ta_2O_5 films for all-solid-state devices will be considered in Chapter 7. In a liquid device, the lithium is initially contained in the liquid electrolyte; therefore, a way to introduce the lithium in vacuum is needed to produce a solid and inorganic device without the need to charge the electrochromic layer in a liquid bath.

Chapter 7   All-solid-state devices

This chapter describes the manufacturing and the study of all-solid state electro-chromic devices. First, a method to supply lithium to the electrochromic layers is presented; its impacts on the optical and electronic properties of the films are characterized. Using the results obtained in the previous chapters and the method to lithiate the films under vacu-um, all-solid-state devices are produced and electrochemical experiments are performed to study their switching behavior. The uses of tantalum pentoxide, as a solid ion conductor, and of nickel-tantalum nanocomposite oxide, as a counter electrode, are investigated.

The goal is to determine if a dry lithiation of the sample is possible without requir-ing lithium compound targets, which are sensitive to humidity, to evaluate if tantalum pent-oxide can be used as a solid electrolyte and to assess the electrochromic behavior of an all-solid-state device comprising such an electrolyte.

7.1   Dry lithiation

In an electrochromic glazing using a liquid, gel or polymer electrolyte, the lithium is often initially contained in the electrolyte. In order to develop an all-solid-state device fully de-posited under vacuum, a dry lithiation method was developed. It is called dry lithiation in opposition to a wet lithiation, where the electrochromic layer is immersed in a bath con-taining Li$^+$ ions and a voltage applied to drive the Li$^+$ ions from the electrolyte to the elec-trochromic film.

7.1.1 Installation of the dry lithiation setup

Alkali metal dispensers are used in industrial sectors such as the manufacture of displays, sensors and electronic devices: they allow the deposition of ultrapure alkali metals, such as lithium, cesium, potassium and sodium. The alkali metal to be deposited is embedded in a stable salt (mostly lithium chromate) and released upon heating. In this work, the transfer chamber of the deposition machine was adapted in order to lithiate the electrochromic lay-ers without taking the samples out of vacuum. An electrical feedthrough was installed in the chamber along with a tunnel equipped with a shutter. On the vacuum side, lithium dispens-ers are hold and connected to the copper wires by copper blocks with screws and on the

side of the ambient air, the cable is connected to a DC power supply. The lithium dispenser can thus be heated via resistive heating, letting the lithium evaporate onto the sample placed above, as illustrated in Figure 7:1. A shutter is used to protect the sample during the conditioning step.
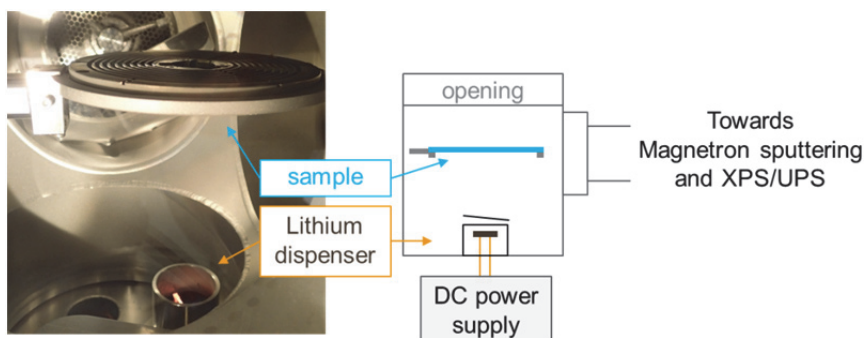
Figure 7:1   Photography and illustration of the lithiation chamber connected to the deposition chamber.

An electrochromic oxide can be deposited in the magnetron sputtering chamber, then conveyed to the transfer chamber to be lithiated and moved back to the sputtering chamber to deposit a second layer, such as a solid ion conductor, remaining in vacuum during the process.

7.1.2 Homogeneity of dry lithiation

The distance from the sample to the dispenser was chosen to cover the full diameter of the substrate holder (100 mm). In order to estimate the zone which could be lithiated, WO_3 was deposited on three glass slide to form a square of 75 mm x 75 mm on the substrate holder and was transferred in the lithiation chamber. Lithium was evaporated: it was observed that the WO_3 coatings, which were initially transparent, became blue as illustrated in Figure 7:2, and that the coloration was homogenous.
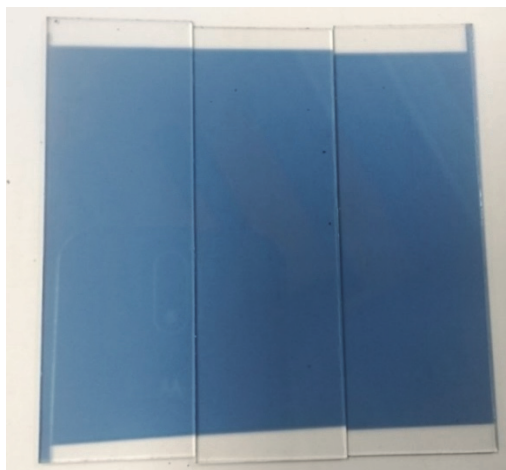
Figure 7:2   Visual aspect of three glass slides (A, B and C, 25 mm x 75 mm) coated with WO_3 and lithiated in situ. Initially transparent, the WO_3 coatings appear homogeneously blue after lithiation.

The spectral transmittance at the center of the three samples was measured and is shown in Figure 7:3. The transmittance of a WO_3 coating deposited with the same process parameters (except for the duration) is also shown for comparison.
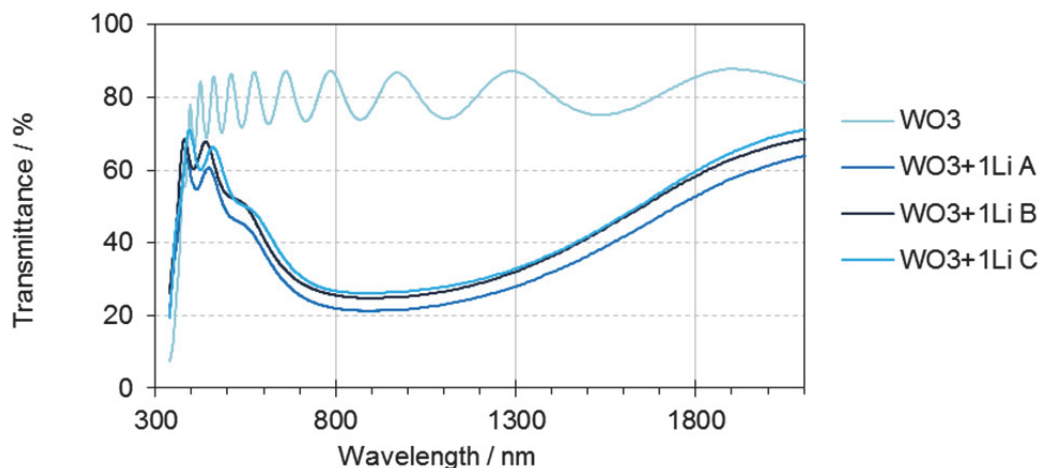
Figure 7:3   Spectral transmittance of the three lithiated WO_3 samples. The transmittance of a non-lithiated WO_3 sample deposited with the same process parameters but for a longer deposition time is also shown.

A slight deviation is observed, especially with sample A, which has an average transmittance difference of 5 % compared to sample B and C. This could be due either to a partial shading of the Li dispenser by the protection tunnel or to the position of the sample above maybe not perfectly centered. This experiment demonstrates that a relatively uniform coloration can be obtained using lithium evaporation in vacuum.

7.1.3 Spectral transmittance of WO_3 as a function of Li insertion

In the previous section, only one dispenser, containing 1.7 mg of Li, was used. The transmittance is reduced but the sample is not dark enough to represent the colored state of the electrochromic layer. Successive lithiation steps were applied and the decrease in transmittance measured. The sample was brought to the air to be measured and placed back in vacuum to undergo the next lithiation step. The WO_3 sample was deposited on an ITO/glass substrate according to the parameters indicated in Table 7:1 (sample A).

	Sample A O71219	Sample B O80219
Applied power	DC-p 150 W	DC-p 150 W
Substrate	ITO coated glass and Si (for ellipsometry)	glass
Deposition time	90 min	10 min
Ar / sccm	12.5	12.5
O_2 / sccm	8.3	8.3
Ratio O_2/Ar	66.67 %	66.67 %
Working pressure	$2{,}5.10^{-2}$ mbar	$2{,}0.10^{-2}$ mbar

Table 7:1 Deposition parameters.

The thickness of the WO_3 layer of sample A was estimated by ellipsometry to be about 1290 nm. Six successive lithiation steps were performed and the spectral transmittance measured after each of them is shown in Figure 7:4. The solar direct transmittance and the light transmittance were determined for each spectrum and are indicated in Table 7:2.
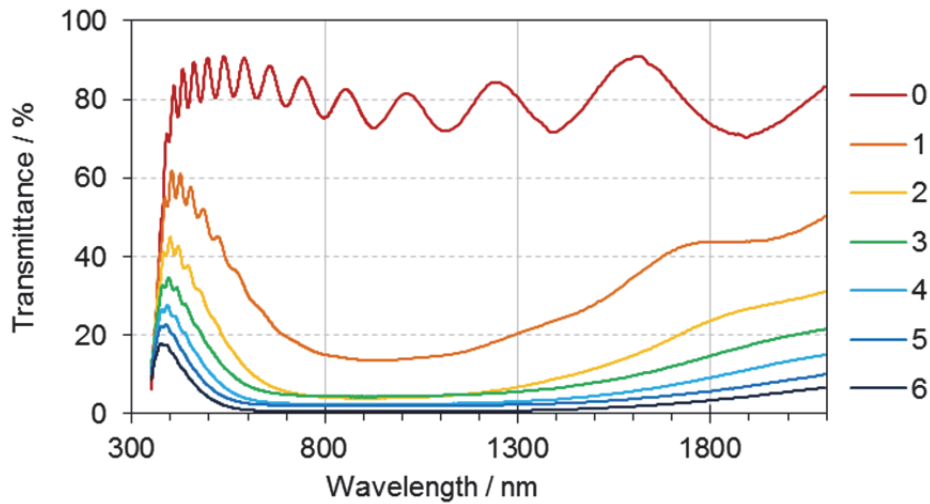
Figure 7:4 Spectral transmittance of sample A after successive lithiations, the legend indicates the number of lithiation steps.

lithiation steps	τ_e	τ_v
0	79.6%	85.3%
1	29.0%	37.7%
2	14.0%	17.1%
3	10.6%	10.8%
4	6.9%	6.3%
5	5.2%	4.1%
6	3.1%	2.0%

Table 7:2 Evolution of solar direct transmittance τ_e and light transmittance τ_v of WO_3/glass as a function of the number of lithiation steps.

The spectral transmittance of the WO_3 sample decreases as the amount of lithium in the film is increased. As deposited, the solar direct transmittance is close to 80 % and the light transmittance above 85 %, which is common for stoichiometric WO_3. Upon dry lithiation, the sample can reach remarkably low transmittance value, the solar direct transmittance being close to 3 % and the light transmittance to 2 % after six successive lithiation.

Ashrit et al. (1993) also presented a method of dry lithiation were a lithium niobate powder is heat-treated under vacuum to release lithium atoms. They studied the optical properties of dry lithiated tungsten oxide; the minimum light transmittance reached was about 20 % with an effect of saturation after a few numbers of lithiations. Using the same method, Ashrit (2001) and Beydaghyan et al. (2008) studied the influence of the crystalline structure and morphology, respectively, of tungsten trioxide under dry lithiation; a reduction of the transmittance to about 50 % in the solar range was reported.

The decrease observed for sample A is especially large in the range 600 – 1300 nm causing a modification of the color perceived through the sample. The color coordinates were determined for each spectra and the x, y coordinates plotted in the CIE 1931 2° diagram in Figure 7:5 a) highlighting the variation of the hue. The light transmittance reported in Table 7:2 was plotted in Figure 7:5 b) to illustrate how the sample is darkening.
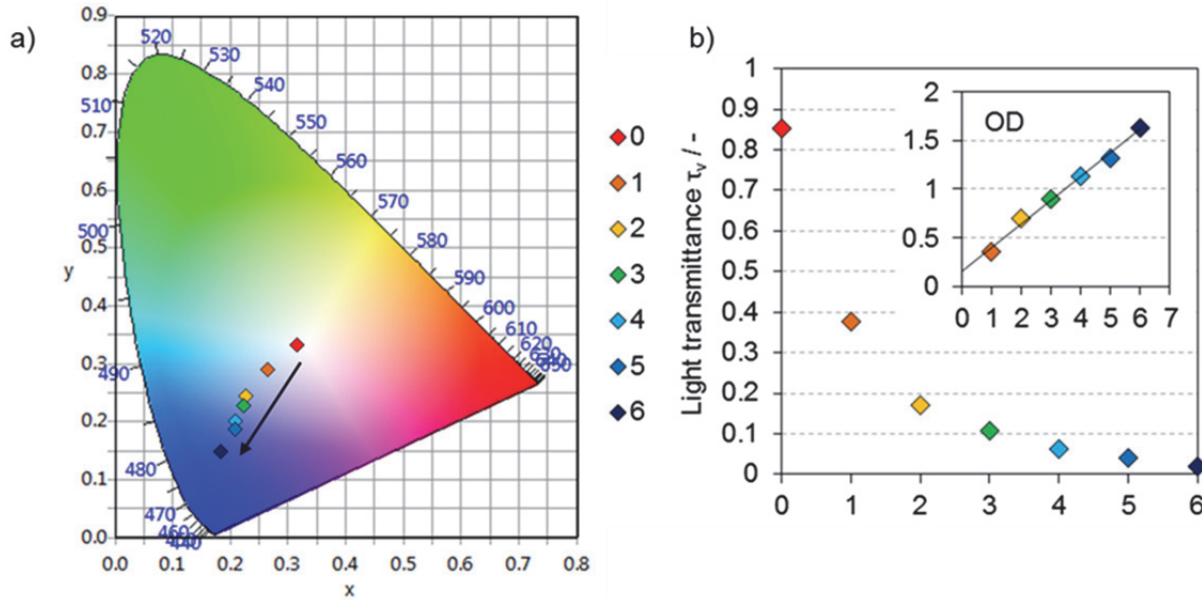
Figure 7:5   a) x, y color coordinates and b) light transmittance τ_v of the sample A before (0) after successive (1 to 6) lithiations. The arrow indicates the direction of the hue modification with successive lithiations steps i. An exponential decay of the light transmittance is observed. The optical density OD representing $\log(\tau_{v0}/\tau_{vi})$, is plotted in inset.

The transmitted color is modified from transparent to blue. In the meantime, the sample also becomes darker. The light transmittance is decreased by a factor 40 between the 'as-deposited' sample and the one subjected to six lithiation steps. This coloration phenomenon is due to the reduction of tungsten oxidation state, as explained in Chapter 2 and observed by XPS in the next section. Since the evaporation of lithium causes the coloration of tungsten, it suggests that Li atoms effectively enter the WO_3 layer and do not remain on the surface. Furthermore, the exponential decay of the light transmittance suggests a Beer-Lambert relationship between the number of atoms intercalated in the sample and the optical transmittance, see eq. (4) (Scarminio, 1999).

$$-\log \frac{I(\lambda)}{I_0(\lambda)} = -\log T(\lambda) = -\log \tau_v \equiv OD_{\tau_v} \qquad (34)$$

where I_0 and I are, respectively, the intensity of the incident and transmitted intensities at the wavelength λ, $T(\lambda)$ is the spectral transmittance and OD is the optical density being equal to the logarithm of the initial transmittance over the transmittance of the colored sample.

Thus, the optical density OD and the coloration efficiency CE can be defined as a function of the number of lithiation steps as shown in Table 7:3.

lithiation steps i	OD = log(τ_{v0}/τ_{vi})	CE / Li step
0	-	-
1	0.35	0.35
2	0.70	0.34
3	0.90	0.20
4	1.13	0.23
5	1.32	0.19
6	1.63	0.31

Table 7:3 Evolution of the optical density OD and the coloration efficiency CE of WO_3/glass as a function of the number of lithiation steps.

The optical density is plotted in inset in Figure 7:5 b) and shows a linear trend confirming the applicability of the Beer-Lambert relationship. The coloration efficiency per lithiation steps is rather similar for the six lithiation steps with values of 0.27±0.08 per lithiation step. However, a decreasing trend is observed suggesting an easier intercalation at the beginning of the lithiation procedure when all intercalation sites are free.

A similar experiment was performed with a thin WO_3 layer (~140 nm), whose deposition parameters are described in Table 7:1 (sample B). The spectral transmittance before and after two lithiations is shown in Figure 7:6.
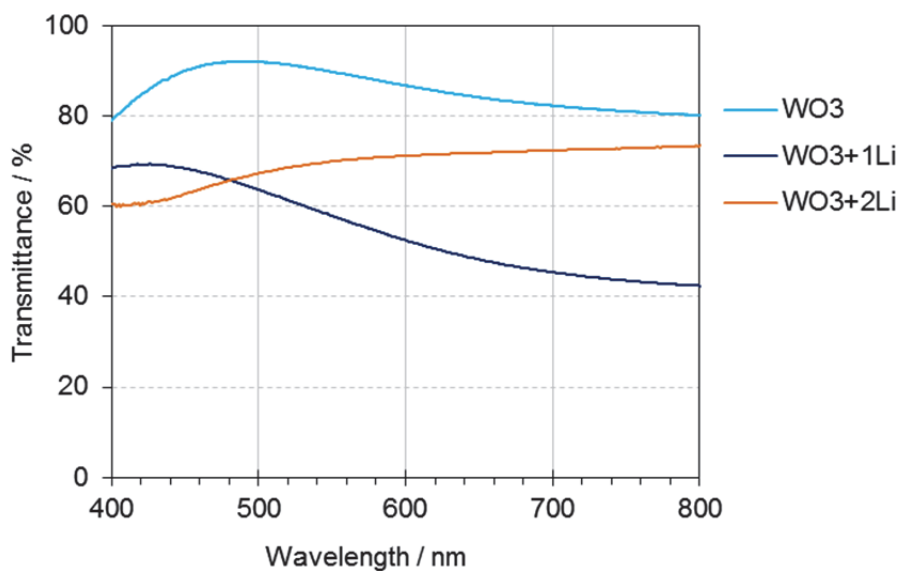
Figure 7:6   Spectral transmittance of the thin WO_3 sample B before and after 1 and 2 lithiations. After the second lithiation, a brownish tint is observed.

Sample B being almost ten times thinner than sample A, lithiation saturation of the layer appears much quicker. Excessive lithiation of a thin WO_3 layer lead to a brownish color of the sample. The spectra in Figure 7:6 show a decrease in transmittance in the short wavelengths (400-450 nm). WO_2 crystal is known to present a bronze color (Wells, 1984) and

addition of lithium could further reduce tungsten: this effect is attributed to the formation of W^{4+} oxidation state. This oxidation state does not present a reversible electrochromism and is therefore not desirable. Excessive lithiation should be avoided and is also related to the fact that in thin film batteries based on lithium, overcharging should be strictly avoided.

7.1.4 Electronic structure of WO_3 with Li insertion

The effect of lithium insertion on the electronic properties of tungsten trioxide was studied by photoelectron spectroscopy. A WO_3 coating (~140 nm) was deposited on silicon and on glass according to the parameters described in Table 7:1 (sample B). The silicon substrate coated with WO_3 was transferred to the XPS/UPS measurement chamber and the WO_3 coated glass was brought to the air to be measured. After lithiation (Sample B WO3+1Li), a decrease in transmittance and a blue color are observed, similarly to previous experiments. Lithium is expected to have entered the WO_3 film. The film was studied by photoelectron spectroscopy to understand the influence of lithium on its electronic and optical properties. X-ray photoelectron spectroscopy was used and the spectra of the W4f and O1s core levels are shown in Figure 7:7.
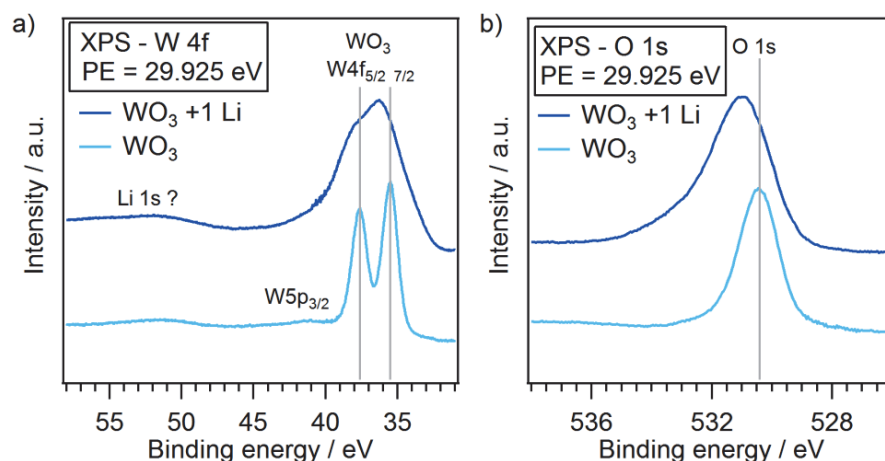
Figure 7:7   W4f and O1s core level spectra. The binding energy of Li 1s is usually about 54 eV, no corresponding peak is observed. However, the shape of the W4f peak is strongly modified after lithiation.

The W4f core level of the sample before lithiation is typical of a $4f_{5/2}$ and $_{7/2}$ doublet, corresponding to the W^{6+} oxidation state with a doublet separation of 2.1 eV. The core level of the lithiated sample exhibits a broad peak, with a maximum at 36.4 eV and a complex shape indicating the superposition of various doublets. The Li1s core level is usually found between 50 and 56 eV depending on its chemical state, Ozer and Lampert (1999) determined a position of 53.6 eV for Li 1s in lithiated WO_3-V_2O_5 films after cycling. A peak corresponding to Li1s, in Figure 7:7 a), could not be observed which indicates that the quantity of lithium present at the surface of the film is below the detection limit of XPS. The O1s core level spectra of the sample before lithiation exhibits a peak at 530.4 eV, which is close to values

found in the literature (Naumkin, 2012). After lithiation, a broadening of the peak and a shift toward higher binding energies (maximum at 531 eV) is observed. For comparison, in WO_2, O1s peak values from 530.4 to 531 eV were reported (Naumkin, 2012) and in $Li_2W_2O_7$ a value of 531 eV was reported by Chowdari et al. (1992). Therefore this shift could be attributed to the influence of lithium or the reduction of the tungsten oxidation state. The integration of the core level spectra of W4f and O1s peak area after subtraction of a Shirley background was performed to determine the oxygen to tungsten ratio of the samples; it was found to be O:W = 3.0 for both samples suggesting that the lithium insertion does not induce a formation of oxygen vacancies.

For a better understanding of the shape of the W4f peaks, a deconvolution, using Gaussian-Lorentzian contributions after subtraction of a Shirley background, was performed as shown in Figure 7:8.
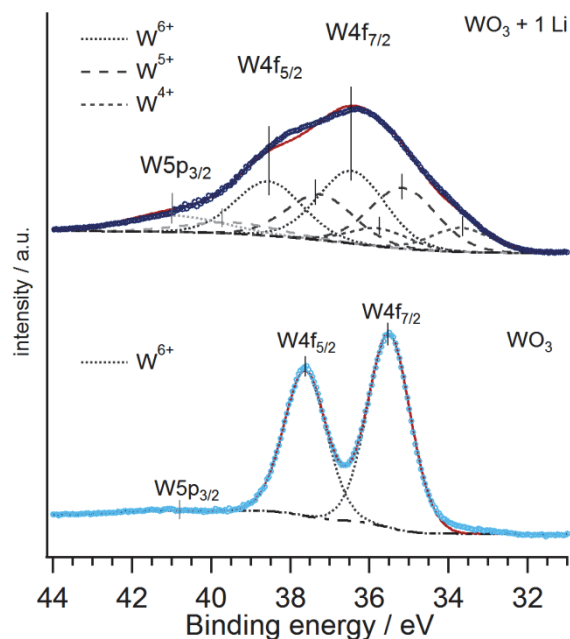
Figure 7:8   Deconvolution of the W4f core level spectra before and after lithiation. The complex shape of the W4f peak after lithiation is attributed to the presence of three oxidation states of tungsten.

Before lithiation, the theoretical curve corresponding to a single doublet respecting the ratio of 3:4 for $4f_{5/2}$ and $_{7/2}$ components could fit the experimental data. After lithiation, the broad shape was fitted considering the presence of three oxidation states W^{6+}, W^{5+} and W^{4+}, taking into account the contribution of the $W5p_{3/2}$ peak around 41 eV. The contribution of each oxidation state was determined by comparing the relative area of the three doublets, the results being indicated in Table 7:4.

oxidation state	before lithiation	after lithiation
W^{6+}	100 %	46.8 %
W^{5+}	-	39.2 %
W^{4+}	-	14.0 %

Table 7:4 Relative contribution of the three oxidation states of tungsten on the shape of the W4f peak calculated from the area under each doublet.

Before lithiation, the sample appears to be stoichiometric, showing only one W4f doublet. After lithiation, the O:W atomic ratio is still 3.0 but the W4f core level indicates a reduction of the oxidation state of tungsten, about 40 % being attributed to W^{5+} and 14% to W^{4+}. The presence of W^{5+} is commonly linked to the blue color of lithiated tungsten oxide, as is the case for under-stoichiometric tungsten trioxide. The presence of W^{4+} oxidation state is generally not desirable for electrochromic applications, it might occur due to the thin layer used for this experiment. Only 140 nm of WO_3 was deposited similarly to sample B, and in contrast with sample A studied in Figure 7:4 (~1290 nm). A second lithiation was shown to strongly modify the transmittance of sample B suggesting an irreversible reduction to W^{4+}. Sufficient thickness of WO_3 was found to be necessary in order to obtain a sufficiently dark blue-coloration.

The oxygen to tungsten ratio remained unchanged after lithiation, while the W4f peaks clearly indicates a reduction of the oxidation state of the tungsten. This confirms a reduction of tungsten by lithium as suggested by the blue color of the sample after lithiation. The modification of the electronic structure of tungsten can also be observed in the valence band region using UV-photoelectron spectroscopy (UPS) as shown in Figure 7:9.
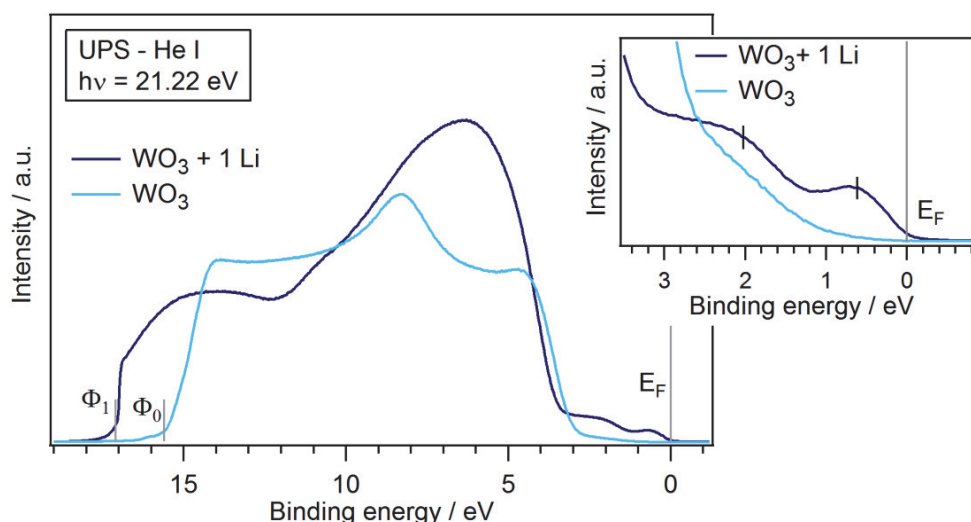
Figure 7:9 He I valence-band spectra obtained by UPS from the WO_3 sample before and after lithiation. Inset, zoom into the region of the Fermi level when new states can be observed. These states can be related to the charge distribution illustrated in Chapter 1 Figure 1:15 (Bondarenko, 2015).

Before lithiation, a maximum can be observed at approximately 8 eV; in addition, a feature can be observed around 5 eV. The region at approximately 6 eV is generally assigned to a hybridized W 5d-O 2p band (Höchst, 1982; Du, 2014) and the one at 4 eV is assigned to the O 2p derived band (Höchst, 1982; Du, 2014). After lithiation, the observed shape of the valence band is strongly modified with a broad maximum around 6.5 eV, states appearing in the vicinity of the fermi level with small features around 2 and 0.5 eV. These features are indicative of new occupied states forming inside the band gap (Vasilopoulou, 2014). The onset edge of the valence band spectra is shifting towards higher binding energies, indicating a modification of the work function from Φ_0= 5.8 eV KE to Φ_1= 4.2 eV KE.

In Chapter 5, the valence band of under-stoichiometric tungsten trioxide was observed by UPS. The spectra obtained for the lithiated WO_3 and the under-stoichiometric $WO_{2.7}$ sample are shown in Figure 7:10; comparable features are observed in the vicinity of the Fermi level and suggest similarities between the reduction of tungsten by lithium or by oxygen vacancies. However, the work function of the under-stoichiometric oxide determined to be Φ_x= 6.0 eV KE is close to the one determined for stoichiometric WO_3 (Φ_0= 5.8 eV KE), while it is strongly reduced by the addition of lithium (Φ_1= 4.2 eV KE).
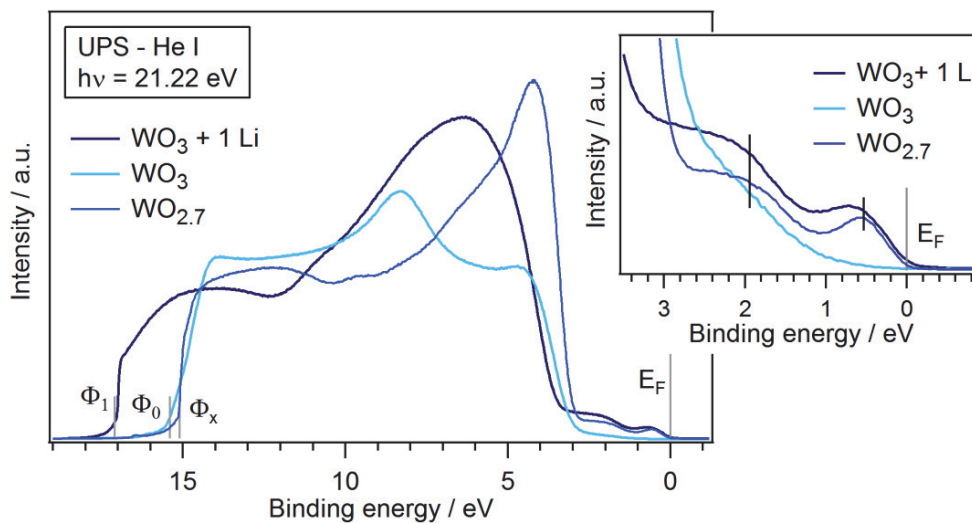
Figure 7:10   He I valence-band spectra obtained by UPS from the WO_3 sample before and after lithiation compared to the under-stoichiometric $WO_{2.7}$ studied in Chapter 5. Inset, zoom into the region of the Fermi level. These states can be related to the charge distribution illustrated in Chapter 1 Figure 1:15. Similar features are observed in the vicinity of the Fermi level in the lithiated and under-stoichiometric tungsten trioxide.

According to the first principle calculations of Mahmoudi et al. (2016), the introduction of a lithium ion in a cubic WO_3 structure would lead to the formation of states near the Fermi level. They attribute it to the displacement of the "d" states of the W atoms to the conduction band. In the same publication, the "s" states of Li were found to have a very low occupation, indicating that Li remains ionized in the tungsten oxide (Mahmoudi, 2016). Bondarenko et al. (2015) calculated the energy barriers for polaron propagation and suggest that

W^{5+}-W^{5+} bipolarons situated along the [001] plane are the most favorable electronic configuration both in the presence of oxygen vacancy or intercalated Li ions (Bondarenko, 2015).

The low occupation states due to Li might be followed by a minimum in the unoccupied states around 2.5 eV allowing the blue (~3.1 eV) to be transmitted while the red (~1.9 eV) is absorbed. This would explain the typical blue color in transmission of electrochromic tungsten oxide.

7.2   Inorganic electrochromic devices

7.2.1 Preparation of the samples

All-solid-state electrochromic devices were prepared on ITO coated glass substrate. A part of the ITO was masked to leave space for contacts, then the tungsten oxide layer was deposited and lithiated followed by the deposition of a thin layer of solid ion conductor. A second mask, illustrated in Figure 7:2 a), was used to delimitate a second layer of solid ion conductor, the counter electrode (nickel oxides) and the top ITO coating. The device architecture is depicted in Figure 7:2 b).
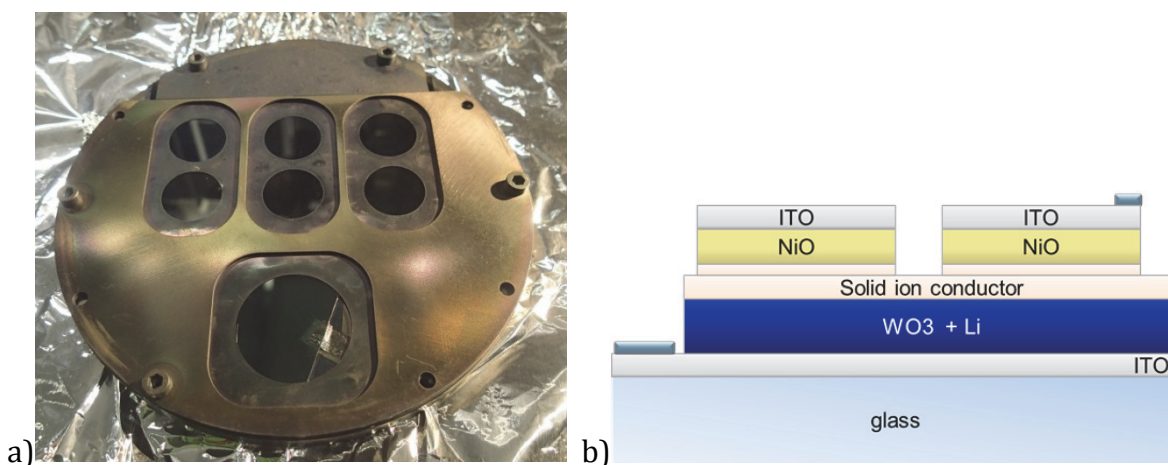
Figure 7:11   a) Mask used to produce the all-solid-state devices. b) Architecture of the all-solid-state devices. An ITO/coated glass is used as a substrate, a part of the ITO is masked. After deposition and lithiation of the WO3 layer and of the solid ion conductor, the mask depicted in Figure 7:11 a) is applied. Then a second layer of solid ion conductor is deposited, followed by a nickel oxide and a top ITO layer.

The mask is made of two layers of stainless steel, a thin one (0.05 mm) flexible, allowing a good contact and a thicker one (1 mm) to keep the first mask in place: they hold onto the substrate holder thanks to vented screws. From this setup, up to seven identical devices could be produced in the same deposition run. In the photography of Figure 7:2 a), a piece of silicon was placed in one of the circles delimited by the mask in order to be able to measure thickness by profilometry and observe the morphology by SEM more easily. A $NiVO_x/LiPON/WO_3$ stack deposited on silicon is shown in Figure 7:12; the columnar and loose-packing structure of the tungsten and nickel oxides can be observed. Electrochemical measurements on this sample were not possible due to the presence of leakage currents between the bottom and top conductive layers causing the discoloring of the sample after few hours.
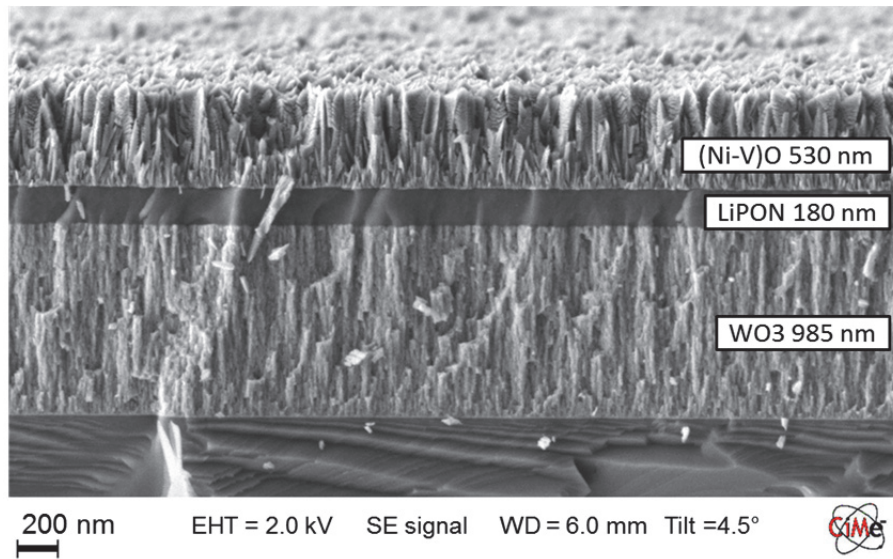
Figure 7:12   SEM cross-section image of a NiVOx/LiPON/WO$_3$ stack deposited on silicon and cleaved.

Using the described mask, a clear separation of the bottom and top ITO is obtained: no short circuit coming from the sides could be observed. However, some devices appeared to have some shunts between the top and bottom ITO electrodes. A full device is about one micron thick and many dust particles larger than a micron are present in ambient air as indicated in Table 7:5. These particles might create pinholes in the layer, which can then be filled by the conductive layer and induce leakage currents.

In order to avoid short circuits in the devices, a vertical laminar air flow hood was installed above the transfer chamber as shown in Figure 7:13.

Figure 7:13   Installation of a laminar flow hood above the transfer chamber to reduce dust contamination.

particle max. size	Measured number of particles/m^3			Max. number of particles/m^3	
	ambient air	Hood on, no curtain	Hood on, shielding screen	ISO 5 Class 100	ISO 6 Class 1000
0.3 μm	2 866 667	30 000	3 667	10 200	102 000
1.1 μm	173 333	2 333	400	832	8 320
5 μm	10 000	200	0	29	293

Table 7:5 Number of particles according to their maximum size measured at the level of the entrance of the transfer chamber. For comparison, the admissible values ISO 14644-1 Cleanroom Standards and its FED STD 209E equivalent are also indicated. Using the laminar air flow hood with the shielding screen, levels equivalent to a cleanroom ISO 5 are achieved at the entrance of the transfer chamber.

The hood filters the ambient air and pushes it in a laminar flow above the machine. The number of particles is drastically reduced upon installation of a laminar flow hood and the installation of shielding screen as indicated in Table 7:5. This setting made it possible to produce functional electrochromic stacks.

7.2.2 Solid state device using tantalum pentoxide as an electrolyte

A Glass/ITO/WO_3/Ta_2O_5/Ni-V-O/ITO device was deposited according to the parameters given in Table 7:6 and using the masks described in section 7.2.1. An all-solid-state device, using Ta_2O_5 as an electrolyte, was thus obtained. An image of the cross-section was made using a scanning electron microscope and is displayed in Figure 7:14: the columnar and porous morphology of the layers can be observed. The image was obtained using the InLens detector which detects secondary electrons through the lens; a high topography contrast with little shadow can be acquired. All layers were deposited without heating the substrate; XRD analysis revealed that only the nickel oxide layer exhibits X-ray crystallinity, the other ones being amorphous or nano-crystalline.

ECS80330-1h	WO_3	Lithiation	Ta_2O_5	$NiVO_x$	ITO
Target	W	Li dispenser x 7	Ta	Ni-V	ITO
Applied power	DC 150 W	7,3 A	DC-p 100 W	DC-p 200 W	DC-p 65 W (50 kHz, τ_{OFF} = 2016 ns)
Deposition time	90 min	7 x 60 min	2 x 15 min	30 min	45 min
Ar / sccm	12.5	-	23.6	41.7	25.0
O_2 / sccm	8.3	-	4.0	1.0	1.6
Ratio O_2/Ar	66.67 %	0 / no process gas	16.8 %	2,38 %	6.35 %
Working pressure	$2,4.10^{-2}$ mbar	10^{-6} - 10^{-7} mbar (transfer chamber)	$2,5.10^{-2}$ mbar	$1,6.10^{-2}$ mbar	$2,6.10^{-3}$ mbar

Table 7:6 Deposition parameters; the WO_3 layer was deposited on ITO coated glass with a sheet resistivity of 15-30 ohm/sq (ITO X190 from Delta Technologies) and on silicon. The sample was taken to air after the WO_3 deposition and between the two Ta_2O_5 layers to apply the mask.
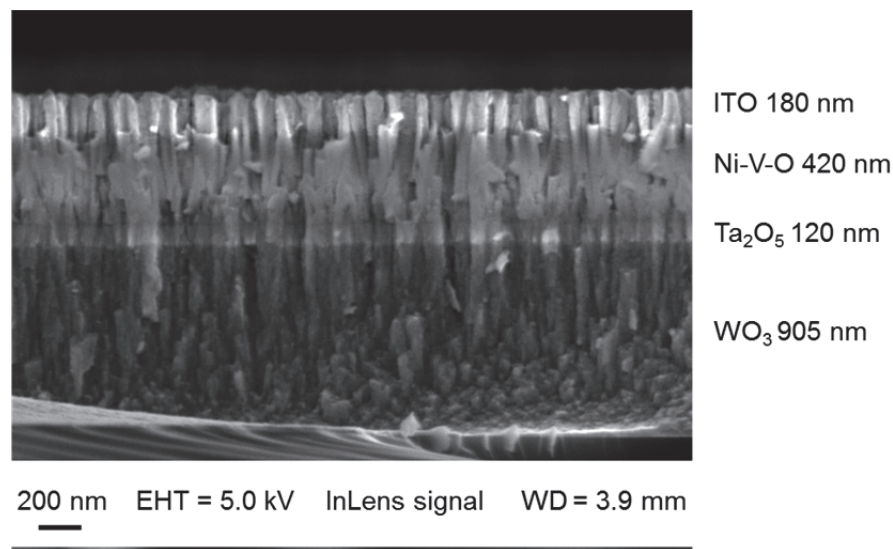
Figure 7:14   Secondary electrons image of the cross-section of the cleaved Si/WO$_3$/Ta$_2$O$_5$/Ni-V-O/ITO sample. The columnar and loose packing structure of the layers can be observed.

The transmittance spectra of the device as deposited, after connection to the potentiostat and after bleaching, are shown in Figure 7:15, their color coordinates are indicated in Figure 7:16.
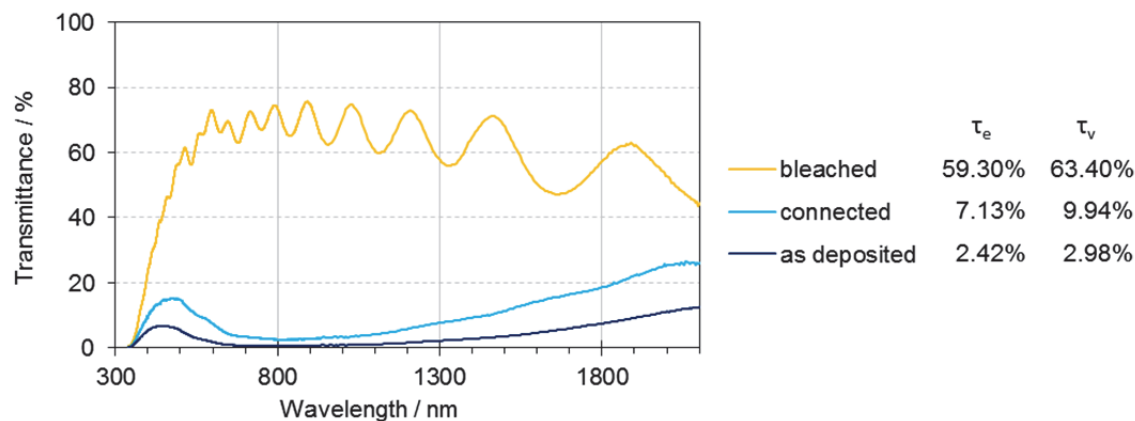
Figure 7:15   Spectral transmittance of the Glass/ITO/WO$_3$/Ta$_2$O$_5$/NiVOx/ITO device as-deposited, after connection of the device to the potentiostat and after bleaching. As-deposited, the solar direct transmittance is only 2.4%. After connection to the potentiostat, the device started to discolor slightly.
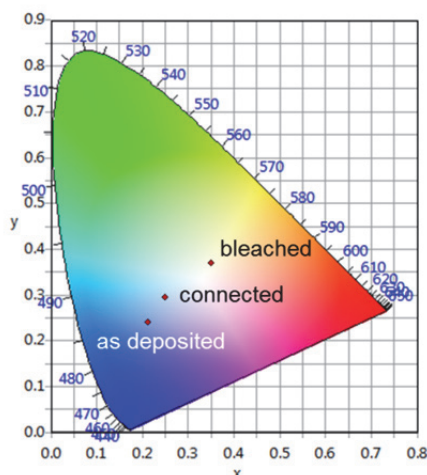
Figure 7:16   x, y color coordinates of the sample Glass/ITO/WO3/Ta2O5/NiO/ITO device as deposited, after con-
nection of the device to the potentiostat and after bleaching.

Due to the in-situ lithiation, the 'as-deposited' sample is dark blue with a solar direct trans-
mittance as low as 2.4 %. Silver paint was applied on the top and bottom ITO and the device
connected to a potentiostat to be cycled. Before starting the chronoamperometry experi-
ment, the sample begun to discolor, as can be seen from the transmittance spectrum. Upon
application of a voltage, the device could be discolored reaching a light transmittance larger
than 60% with a slight yellow tint.

The fact that the sample started to discolor when connected to the potentiostat might indi-
cate an external current leading the "battery" made from the electrochromic device to "dis-
charge" in the potentiostat, whose impedance is not seen as infinite by the device. The sam-
ple was cycled but could not reach again the dark level of the 'as-deposited' state; this could
be due to some lithium trapped in the other layers or to a discharge of the device during the
charging step. It might also indicate that the counter electrode is not thick enough to ac-
commodate all the lithium ions inserted in the device, leading to lithium ions reaching the
ITO layer in an irreversible process. Nonetheless, this experiment confirms that Ta_2O_5 can
act as an ion conductor and is not blocking the way of Li^+ ions.

7.2.3 Chronoamperometry with in situ spectrophotometry

Another Glass/ITO/WO$_3$/Ta$_2$O$_5$/Ni-V-O/ITO device was deposited using the process pa-
rameters indicated in Table 7:7. After deposition, silver paste was applied on the ITO elec-
trodes. The resistance of the device was tested using a multimeter and a diode behavior was
observed, as illustrated in Figure 7:17. No current can be detected using a multimeter from
the top ITO electrode to the bottom one, but current can flow in the reverse direction with a
resistance of about 4 MΩ.

ECS80418B	WO₃	Lithiation	Ta₂O₅	NiOₓ	RT-ITO
Target	W	Li dispenser x 7	Ta	Ni-V	ITO
Applied power	DC 150 W	7,3 A	DC-p 100 W	DC-p 200 W	RF 75 W
Deposition time	45 min	7 x 60 min	2 x 15 min	60 min	45 min
Ar / sccm	12.5	-	23.6	41.7	25.0
O₂ / sccm	8.3	-	4.0	1.0	0.4
Ratio O₂/Ar	66.67 %	0, no gas	16.8 %	2,38 %	1.6 %
Working pressure	$2,4.10^{-2}$ mbar	10^{-6} - 10^{-7} mbar (transfer chamber)	3.10^{-2} mbar	$1,6.10^{-2}$ mbar	$3,6.10^{-3}$ mbar

Table 7:7   Deposition parameters; the WO₃ layer was deposited on ITO coated glass with a sheet resistivity of 15-30 ohm/sq (ITO X190 from Delta Technologies). The sample was taken to air between the two Ta₂O₅ layers to apply the mask.
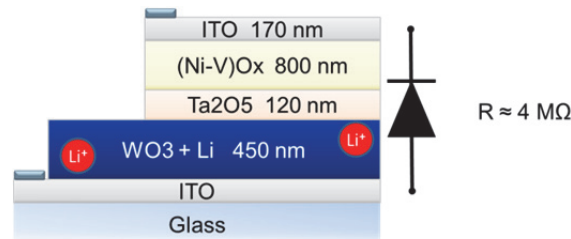
Figure 7:17   Direction of the diode behavior observed. The current can flow from the bottom ITO electrode to the top one with a resistance of about 4 MΩ but cannot be detected by a multimeter in the reverse direction.

While stoichiometric NiO and Ta₂O₅ are insulators at room temperature, doped or non-stoichiometric nickel oxides are usually p-type semiconductor (Grilli, 2016); however, ITO is a well-known n-type semiconductor (Kim, 1999). Therefore, a PN junction might be formed at the Ni-V-O/ITO interface and causes the diode behavior.

Various chronoamperometry experiments (CA) with in situ spectrophotometry were performed on the sample; some are shown in Figure 7:18. The transmittance spectra were recorded every 0.5 second and were integrated to obtain the solar direct transmittance τ_e and the light transmittance τ_v. A first experiment with long time step (in CA1 the applied voltage is -2.5 V and + 2.5V for 120s and 40s respectively) were applied to determine the minimum and maximum solar transmittance; then a voltage of -2.0 V and +2.0V is used and various time steps were applied as indicated in Figure 7:18. The solar transmittance varied between 6 % and 51 % during CA1, CA2 and CA3 (these values are represented by the dashed lines). In CA4, the solar transmittance varied between 10 and 50 %, indicating that in 10s the device is almost fully bleached and colored at 90%. The switching speed t_s can be defined as the speed needed to reach 95 % of the full coloration, for this sample t_s = 17 s for coloration and t_s = 13 s for bleaching. As observed in the liquid electrochromic devices, the coloration needs more time than the bleaching: this may be due to the diode behavior since the bleaching occurs when the applied potential is positive (i.e. the direction of the current being from the bottom to the top electrode). In Figure 7:19, selected cycles from CA3 and CA4 are shown with the associated current response.
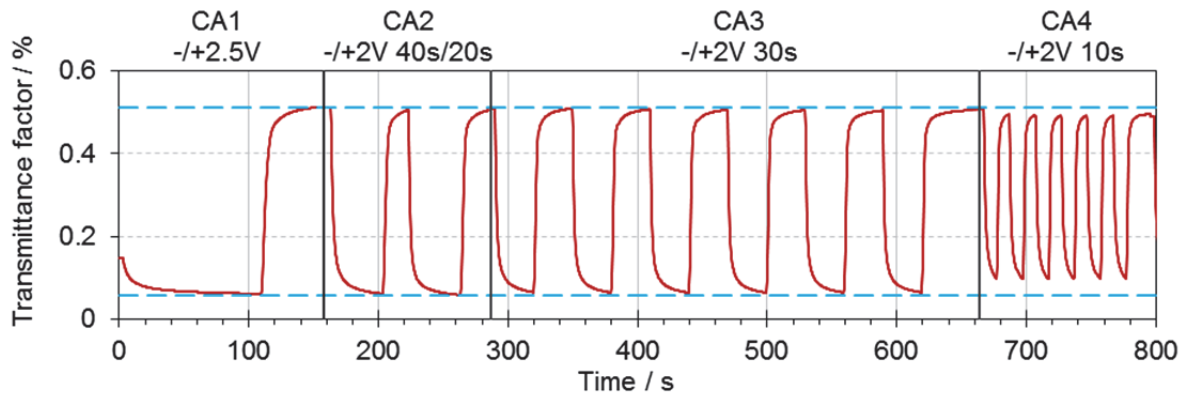
Figure 7:18 Chronoamperometry experiment on the Glass/ITO/WO$_3$/Ta$_2$O$_5$/Ni-V-O/ITO device: evolution of the solar direct transmittance τ$_e$ (in red) during 4 chronoamperometry (CA) experiments. The dashed lines represent the minimum and maximum solar direct transmittance reached.
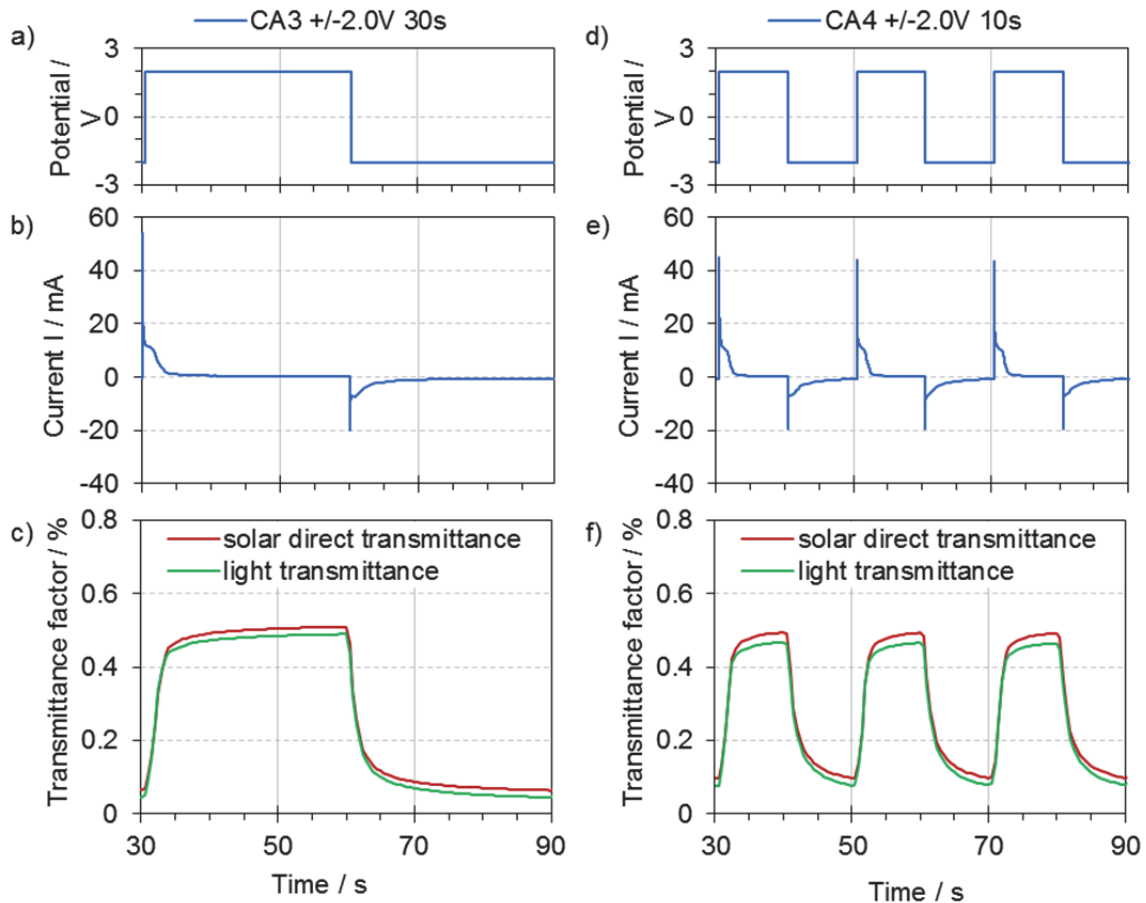
Figure 7:19 Chronoamperometry experiment on the Glass/ITO/WO$_3$/Ta$_2$O$_5$/Ni-V-O/ITO device: a) Potential applied, b) current response and c) evolution of the solar direct transmittance τ$_e$ (in red) and light transmittance τ$_v$ (in green) during CA3 and CA4.

The light transmittance and capacity observed for CA3 and CA4 are indicated in Table 7:8; they were used to assess the optical density OD and the coloration efficiency CE of the device. It can be observed that, despite a yellow tint, the coloration efficiency of the device

reach 63 cm^2.C^{-1} for CA4 which is larger than what was obtained for the liquid electro-chromic device and a rather good performance compared to the values found in literature (Dong, 2018; Zhou, 2017b). For CA3, where the charging step is 30s, the coloration efficiency is only 43.7 cm^2.C^{-1}, indicating that when the device is fully coloured, some charges are lost for non-colouring processes.

	CA3 +/-2.0V 30s	CA4 +/-2.0V 10s
τ_v min / %	4.5	7.8
τ_v max / %	48.9	46.6
$\Delta \tau_v$	44.4	38.8
inserted capacity Q_i / mC	38.2	21.8
OD(vis) = log (τ_v max/τ_v min)	1.04	0.78
CE (coloring) / cm^2.C^{-1}	43.7	63.0

Table 7:8 Properties of the all-solid-state device with an active electrode area of 1.77 cm^2.

The color coordinates were determined for each measured transmittance spectrum during the CA4 experiment and are plotted in Figure 7:20. It can be observed that the device shows a yellow hue during the full experiment: it does not reach the dark blue tint of lithiated tungsten oxide alone.
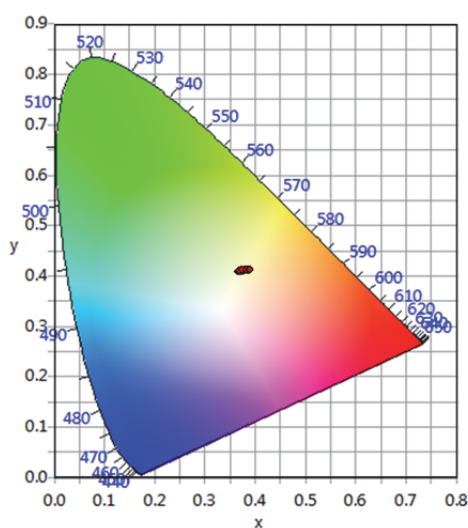
Figure 7:20   x, y color coordinates of the Glass/ITO/WO$_3$/Ta$_2$O$_5$/Ni-V-O/ITO sample during the chronoamperometry experiment.

The thickness of the WO$_3$ layer in this device is thinner (~650 nm) than the one of the sample described in section 7.1.3 (~1290 nm), while the thickness of the nickel oxide is larger (~800 nm). The yellow tint is due to the nickel vanadium oxide layer and impacts also the dark state, because the WO$_3$ layer is too thin to reach a strong dark blue.

7.3   Towards devices based on nanocomposites

In an electrochromic device using a liquid electrolyte, the electrochromic layers are porous in order to facilitate the movement of ions. In a solid state device, interfaces are usually sharper; in order to mimic this porosity at a smaller scale nanocomposite layers are envisioned. An electrode/electrolyte nanocomposite is expected to create new migration path for the ions through the solid layer. Since tantalum pentoxide was used as a solid electrolyte, nickel-tantalum oxides are studied for the counter electrode.

7.3.1 Electronic structure of a nickel tantalum oxide

A nickel tantalum oxide was studied by photoelectron spectroscopy as deposited and after dry lithiation. It was deposited on a silicon substrate with the deposition parameters given in Table 7:10 for the Ni-Ta-Ox sample, whose optical properties have been studied in the next section. After the UPS and XPS analysis, the sample was transferred under vacuum to the lithiation chamber and two lithium dispensers were evaporated on the sample. UPS and XPS analysis were performed on the same sample after lithiation; the spectra obtained by XPS are shown in Figure 7:21. In the survey spectrum of the 'as-deposited' Ni-Ta-O film, before lithiation, the core-level peaks of Ni2s, Ni2p, Ta4s, O1s Ta4p, Ni3s, Ta5s, Ni3p, Ta4f, Ni3d and Ta5d and the Auger peaks of O_{KLL} and Ni_{LMM} can be observed. However, after lithiation, only the O1s, OKLL, Li1s peaks and a small contribution from the Ta4f peak are visible. The intensity of the Li1s core-level peak is very small compared to that of the O1s due to the small atomic number of Li.
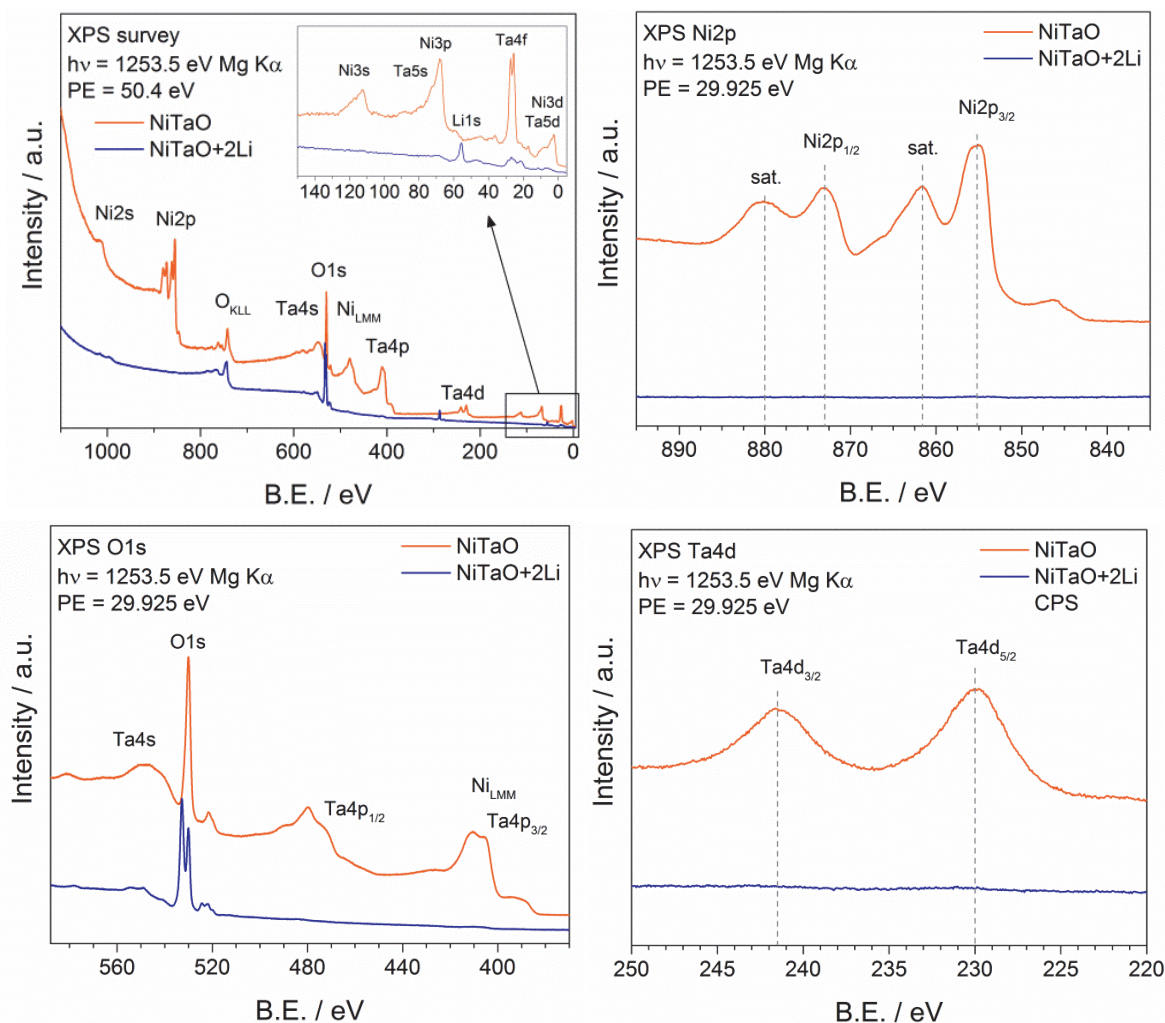
Figure 7:21   XPS from the Ni-Ta-O sample before and after lithiation. The Ni and Ta core level peaks cannot be detected after lithiation.

The analysis of the Ni2p core-level peak shape in a nickel oxide is challenging due to the multiplet splitting and the shake-up and plasmon loss satellite peaks (Besinger, 2009). The main peak of Ni2p$_{3/2}$ appears to be around 855 eV on the 'as-deposited' sample, which suggests a Ni^{2+} oxidation state (NiO compound), while after lithiation, the Ni2p peak is not visible. In the 580-390 eV binding energy region, only the O1s peak is still visible after lithiation and exhibits two distinct peaks while only one could be seen in the 'as-deposited' sample. The Ta4d$_{5/2}$ and $_{3/2}$ peaks, occuring around 230 and 241 eV respectively, suggest an oxidation state of tantalum of Ta^{5+} as it would be in the Ta$_2$O$_5$ compound. The chemical composition was determined by integration of the Ni 2p, Ta4d, O1s and Li1s core level peaks after subtraction of a Shirley background and using Scofield sensitivity factors; results are indicated in Table 7:9.

	Ni / %	Ta / %	O / %	Li / %	ratio Ta/Ni	ratio O/(Ni+Ta)	ratio Li/O
Ni-Ta-O	40.1	4.6	55.3	0	0.115	1.24	-
Ni-Ta-O + 2Li	~0.1	~0.1	33.8	66.0	-	-	1.96

Table 7:9 Chemical composition and atomic ratio obtained by integration of the Ni 2p, Ta4d, O1s and Li1s core level peaks. After lithiation, the peaks of Ni and Ta are not strong enough to perform accurate quantification. Therefore, the ratio Ta/Ni and O/(Ni+Ta) were not calculated.

The Ta/Ni atomic ratio was determined to be 11.5%, which is slightly higher than the target stoichiometry having an atomic ratio of Ta/Ni of 9%. This deviation is slightly larger than the expected error of this method and might indicate a preferential sputtering of tantalum or a segregation of Ta at the surface.

After lithiation, the peaks of Ni and Ta are hardly distinguished, contrary to the Li1s and O1s peaks giving a Li/O atomic ratio of 1.96. This ratio is close to Li_2O and can indicate an oxidation of the lithium. Hoenigman et al. (1984) calculated that 50 seconds in a vacuum at $6.7.10^{-7}$ mbar would be enough to oxidize lithium. In this study, lithium is deposited on an oxidized surface and under a vacuum in the range of 10^{-7} mbar, it is then transferred to the measurement chamber and this operation takes about 5-10 minutes. Furthermore, during the XPS analysis the vacuum remains about $1-2. 10^{-8}$ mbar for more than ten hours. Therefore, lithium oxides are expected to be present at the surface of the sample. The formation of Li_2O and Li_2O_2 are possible as observed by Wu et al. (2005). Residual water in the vacuum can also dissociate and form LiOH at the surface, the O1s component associated with LiOH being usually found at about 533 eV (Hoenigman, 1984).

A zoom on the O1s peak of the 'as-deposited' and lithiated samples is shown on Figure 7:22 a): before lithiation, one main peak is visible. The O1s position for Ta_2O_5 and NiO are very similar and two indiscernible components might compose this apparently single peak centered at 530.0 eV. In the NIST database (Naumkin, 2012), the O1s peak in NiO is reported in a range of binding energy values from 528.9 to 531.0 eV while the O1s peak in Ta_2O_5 is reported in the range 529.8-530.8 eV. It can be seen that a single Gaussian-Lorentzian peak shape (GL30) does not correspond precisely to the peak, using two peaks for the deconvolution, many combinations can give a reasonable agreement with the experimental measurement but it is not possible to decide which one would have a physical meaning. Furthermore, an asymmetry can be observed towards higher binding energies and might be due to a partial screening of electrons which could be fitted using a Doniach-Sunjic line shape, or to defects. After lithiation, the O1s core-level clearly shows two components: one centered at 530.1 eV and the other at 532.8 eV. The first peak has a similar position to the O1s peak before lithiation; considering that Ta and Ni peaks are not visible, it seems that it would mainly be due to Li_2O. The second peak could be due to LiOH, since Li is highly reactive and that the measurement duration is long enough for contamination by residual water vapor in the

vacuum (Tanaka, 2000). This second peak was also attributed to Li_2O_2 in other studies (Wu, 2005).
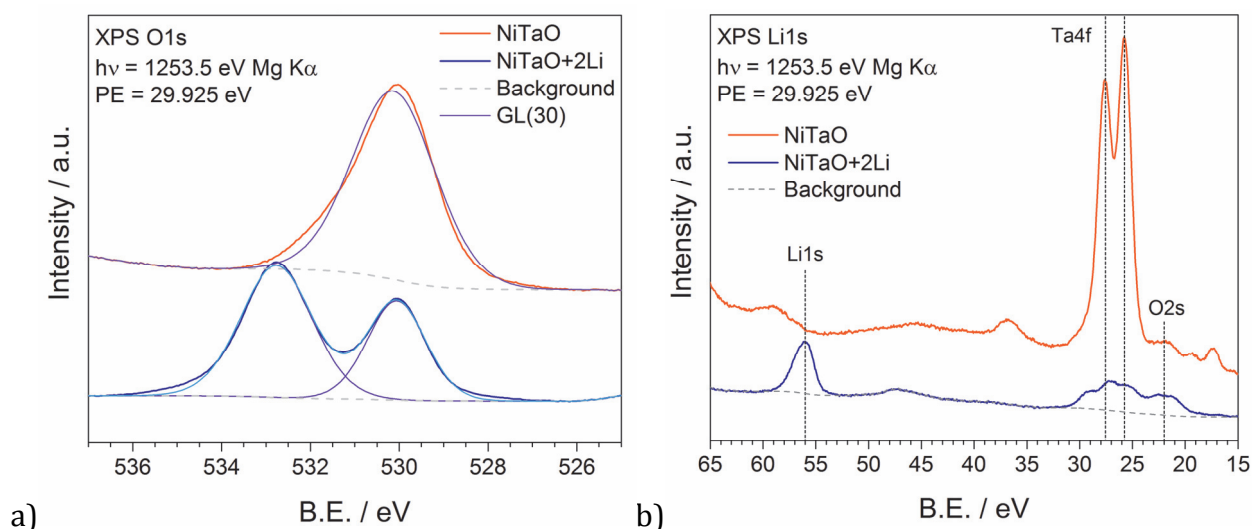
Figure 7:22 a) O1s core-level spectra from the Ni-Ta-O sample before and after lithiation. The dashed lines repre-sent the Shirley background and the purple lines were drawn using a symmetric Gaussian-Lorentzian peak shape. After lithiation a second O1s peak appears. b) Li1s and Ta4f core-level spectra from the Ni-Ta-O sample before and after lithiation.

A zoom on the Li1s and Ta4f peaks is shown in Figure 7:22 b). After lithiation only the Li1s peak is clearly visible and the features towards the low binding energies (20-30 eV) are at-tributed to the Ta4f and O2s core-level peaks. The Li1s peak of metallic Li is usually found at 55.0±0.3 eV (Naumkin, 2012), its value increases towards higher binding energies upon exposure to residual water vapour or oxygen (Hoenigman, 1984). In this study, the Li1s was determined to be at 56 eV, which is consistent with oxidized lithium. The Ta4f peak is a clear doublet with the $Ta4f_{5/2}$ at 27.55 eV and the $Ta4f_{7/2}$ at 25.75 eV before lithiation, which seems to indicate a single oxidation state. After lithiation, the Ta4f peak has a com-plex and attenuated broad shape. The small feature towards the low binding energies at around 22 eV is attributed to O2s. In transition metal oxides, a peak of the O2s core level can usually be observed around 22±1.8 eV (Naumkin, 2012); the peak is still visible after lithiation, which might indicate that it is indeed related to oxygen. The feature at about 37 eV is attributed to Ta_2O_5 plasmon loss and the one at about 17 eV to Ta_2O_5 satellite peaks.

From the universal curve (Seah, 1979), the inelastic mean free path for an inorganic com-pound at a kinetic energy of 1227 eV (corresponding to the binding energy of the $Ta4f_{7/2}$ peak) is 3.36 nm, while at a kinetic energy of 398 eV (corresponding to the binding energy of the $Ni2p_{3/2}$ peak) it is only 1.92 nm. Since the Ni2p peaks are not visible but the Ta4f ap-pears slightly, it is believed that a layer of lithium oxides is covering the Ni-Ta-O layer with a thickness of about 2 to 3 nm.

The shape of the valence band was studied by UV photoelectron spectroscopy: the spectra obtained from the Helium I and Helium II sources are shown in Figure 7:23. The spectra are given in binding energy (B.E.), calibrated to the Fermi level of a sputter cleaned Au reference sample.

As-deposited, the shape is analogous to what was observed for NiO with features around 2.2 and 3.6 eV attributed to the Ni d bands and a feature at 4.8 eV originating from the O2p bands (Kuhlenbeck, 1991). In Ta_2O_5, the valence band is usually dominated by the p-orbitals of oxygen, while the d-orbitals of Ta are in the conduction band (Shvets, 2008). The valence band edge is found at 0.9 eV with a tail towards the Fermi level.

After lithiation, the feature around 5 eV cannot be attributed to the O2p in NiO or Ta_2O_5 since UPS is more surface sensitive than XPS and that the Ni and Ta peaks are not visible in the XPS spectrum. However, the oxygen would still be in the same oxidation state in Li_2O and can be attributed to O2p in Li_2O (Thorpe, 2013) in accordance with theoretical density of state of Li_2O (Liu, 1996) or possibly from O2p in LiOH (Tanaka, 2000). A valence band edge is observed at 4.3 eV.
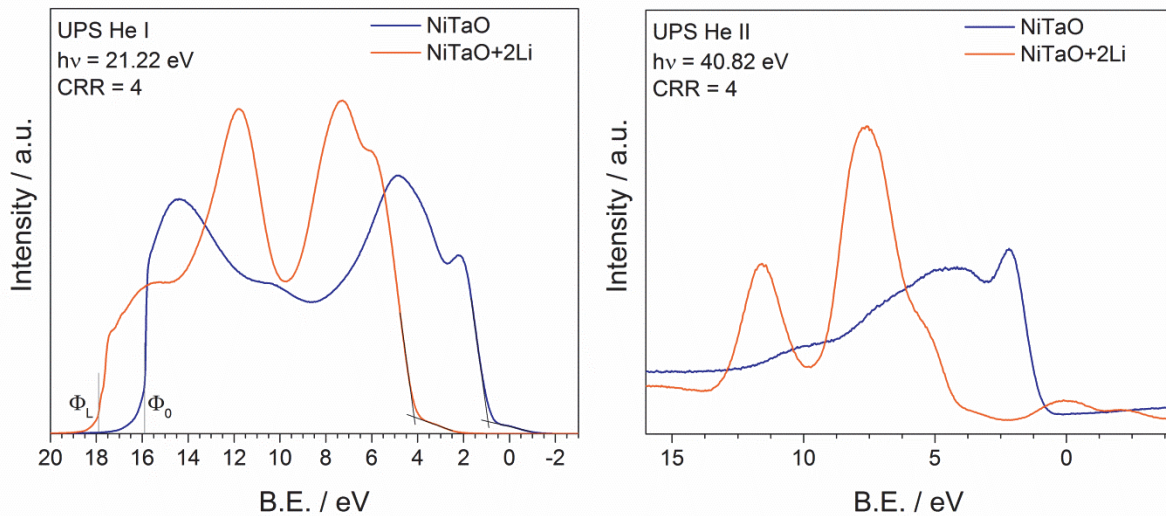
Figure 7:23   He I and He II valence-band spectra obtained by UPS from the Ni-Ta-O sample before and after lithiation. The black lines on the He I indicate the position of a valence band edge at 0.9 eV for the sample NiTaO and at 4.3 eV for the sample NiTaO+2Li.

From calculations based on density functional theory by Duan and Sorescu (2009), in Li_2O, a band with a width of 2.6 eV is present just below the valence band maximum and is mainly due to the interaction of the p orbital of O with the s and p orbitals of Li. Theoretical calculations of the partial density of states of Li_2O_2, by Garcia-Lastra et al. (2011), shows that the valence band of Li_2O_2 is dominated by the O 2p bonding and antibonding orbitals (σ_g, π_u and π^*_g) forming narrow bands centered at -5.6, -4.1, and -0.8 eV relative to the top of the valence band, respectively.

The two prominent features around 7 and 11 eV are assigned to O 2p orbitals in Li_2O_2 which was found to be present at the top-most surface of over-lithiated oxides (Wu, 2005; Thorpe, 2013). Furthermore, it can be seen that the work function of the sample is strongly modified by the lithiation step (Φ_0= 5.3 eV KE before and Φ_L= 3.3 eV KE after lithiation).

The results from this photoelectron study suggest the formation of an oxidized lithium layer on the surface of the deposited Ni-Ta oxide. The thin film and lithium were deposited simultaneously on a silicon substrate for UPS and XPS analysis as well as on a glass substrate; it was observed that after lithiation the sample appearance is modified as shown in Figure 7:24, confirming that some of the lithium intercalate in the film even if a part of it remains at the surface. The optical properties of the coating deposited on glass were measured and are presented in the next section.
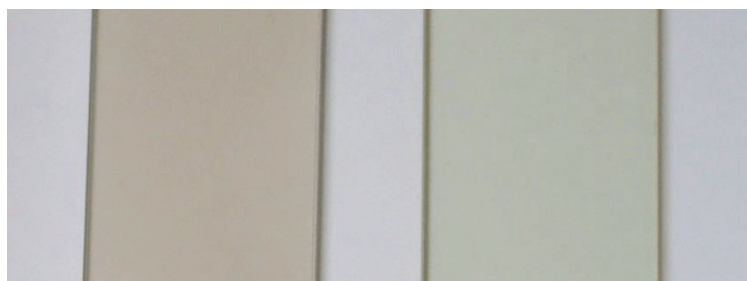
Figure 7:24   Photography of the Ni-Ta-O sample before (left) and after lithiation (right). A better transparency is observed for the lithiated sample.

7.3.2 Optical properties of nanocomposite nickel oxides

Dry lithiation was performed on nickels oxides in order to observe if it would also lead to modifications of their optical properties. Nickel oxides from the Ni-V and Ni-Ta targets were deposited on a glass substrate according to the parameters indicated in Table 7:10. They are named hereafter Ni-V-Ox and Ni-Ta-Ox, which does not indicate a stoichiometry.

	Ni-V-Ox	Ni-Ta-Ox
	O70807-2	O80625
Target	Ni-V (92-8 at. %)	Ni-Ta (91-9 at. %)
Applied power	DC-p 200 W	DC-p 100 W
Substrate	glass	glass
Deposition time	30 min	30 min
Ar / sccm	41.7	62.6
O_2 / sccm	1.0	1.5
Ratio O_2/Ar	2.38 %	2.38 %
Working pressure	$1,8.10^{-2}$ mbar	$1,9.10^{-2}$ mbar

Table 7:10 Deposition parameters.

The spectral transmittance was recorded after deposition of the nickel oxide layer; the samples were placed back in vacuum to undergo three lithiation steps. After each one, their transmittance was measured; the results are displayed in Figure 7:25.
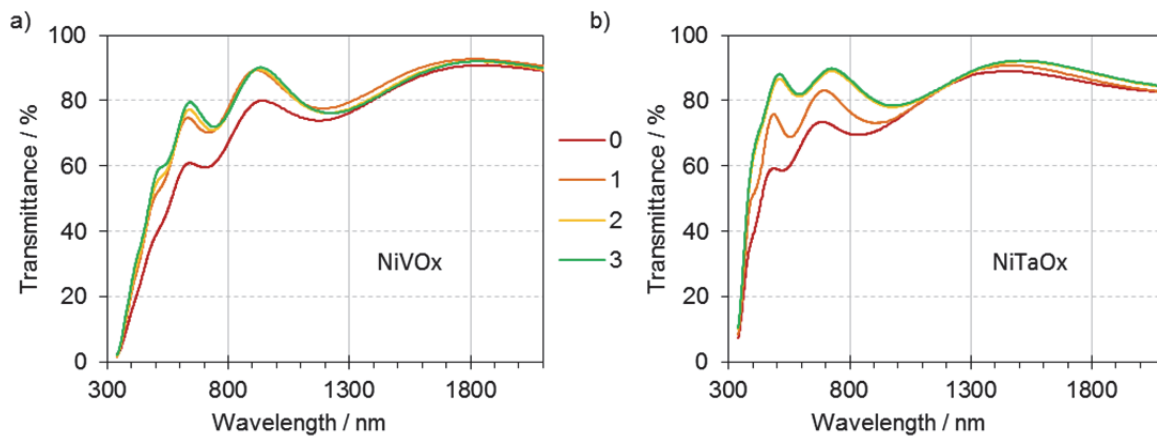
Figure 7:25   Spectral transmittance after successive lithiations, the legend indicates the number of lithiation steps applied on the a) Ni-V-Ox sample (thickness ~420 nm) and b) Ni-Ta-Ox sample (thickness ~330 nm).

As deposited, the Ni-V-Ox sample exhibits a strong brownish color: one lithiation make it brighter and the second and third lithiation have only a little effect of the optical properties. The Ni-Ta-Ox sample has, as deposited, a very slight brown tint. The successive lithiations increase the transmittance especially around 500 nm. The solar direct transmittance and light transmittance of both samples are indicated in Table 7:11.

	Ni-V-Ox		Ni-Ta-Ox	
lithiation steps	τ_e	τ_v	τ_e	τ_v
0	56.8%	48.5%	66.8%	62.1%
1	65.7%	60.8%	73.8%	71.5%
2	66.3%	62.3%	80.6%	83.3%
3	67.5%	64.3%	81.4%	84.3%

Table 7:11 Evolution of solar direct transmittance τ_e and light transmittance τ_v as a function of the number of lithium dispenser used. The lithiated Ni-Ta-O sample reaches τ_v = 84 %.

As already showed in Chapter 5, the samples produced from the Ni-Ta target exhibit higher transmittances, especially in the short wavelengths. It has a large influence on the solar direct transmittance which goes from 67 % for the Ni-V-Ox sample to 81 % for the Ni-Ta-Ox sample after three lithiations. Furthermore, it seems that the transmittance increase of the sample Ni-V-Ox is not very strong after the first lithiation and might imply saturation. This low transmittance has also an impact on the hue and the light transmittance, as depicted in Figure 7:26.
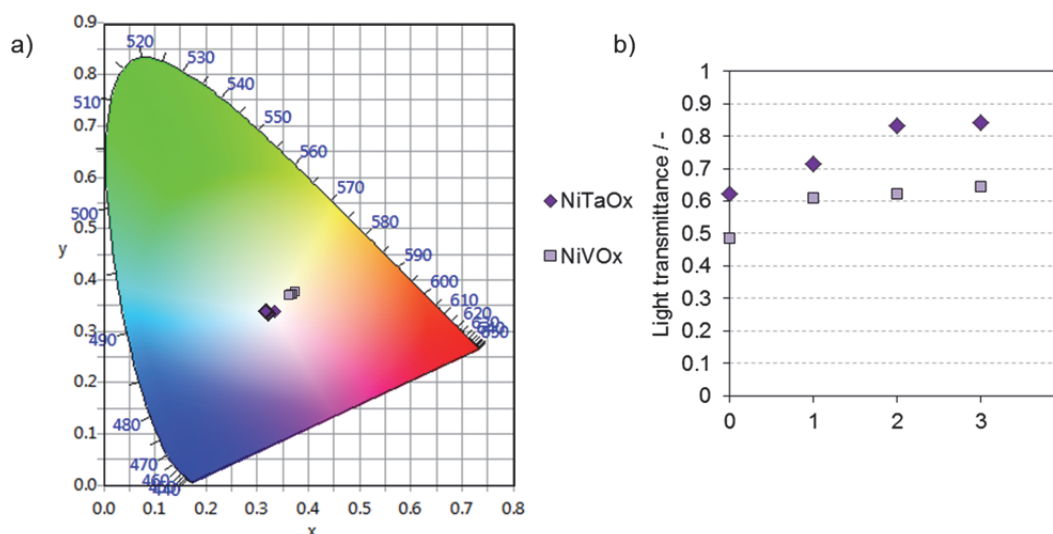
Figure 7:26   a) x, y color coordinates and b) light transmittance before after successive lithiations of the Ni-V-Ox sample (light squares) and the Ni-Ta-Ox sample (dark diamonds). The Ni-Ta-O sample is color neutral.

The light transmittance of the Ni-Ta-O sample reached higher levels and this sample shows better color neutrality compared to the Ni-V-O sample. The color rendering index varies from 91.4 to 97.6 % for the Ni-Ta-O sample while it ranges from 80.3 to 83.7 % for the Ni-V-O sample. Ni-Ta-O is therefore a promising candidate towards electrochromic device with high color neutrality in the bleach state. Dong et al. (2018) also investigated ways to increase the transmittance of electrochromic devices in the short wavelengths by adding Mg and Li to the nickel oxide; the transmittance reached at 400 nm is 62 % for their Ni-Mg-Li-O sample which is similar to the one achieved with our lithiated Ni-Ta-O sample. However, the transmittance at 600 nm of their Ni-Mg-Li-O sample is 66 % while it is above 80 % for our sample.

The study of the electronic properties of a Ni-Ta-O sample deposited with similar process parameters and on which two lithium dispensers were evaporated revealed the formation of a lithium layer at the surface. The optical properties indicate an increase in transmittance after lithiation, therefore it is believed that a fraction of the lithium intercalates in the Ni-Ta oxide until saturation is reached, the rest of lithium remaining on the surface and quickly oxidizing.

7.3.3 Crystal structure of a lithiated nickel tantalum oxide

The crystal structure of a nickel tantalum oxide sample deposited on glass was studied using X-ray diffraction (XRD). The sample was cut in two parts: one part was lithiated and the two parts were then measured by XRD, the resulting diffractograms being shown in Figure 7:27. The angles corresponding to diffraction peaks cubic NiO are indicated with dashed lines.
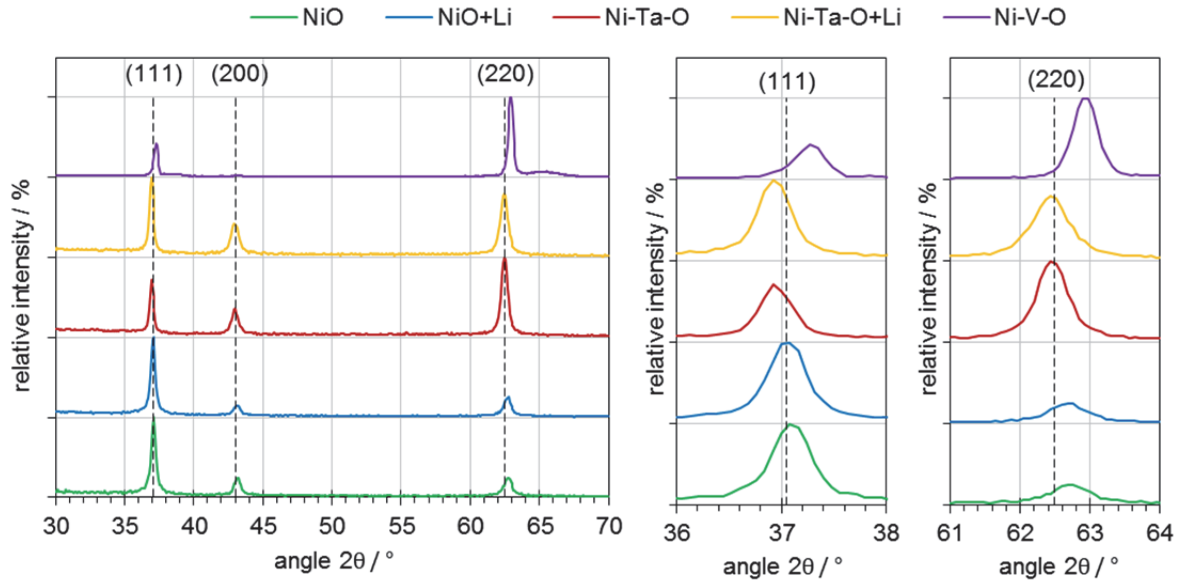
Figure 7:27   Diffraction pattern of a Ni-Ta and Ni oxide before and after lithiation obtained by XRD. Ni-V-O is also shown. The vertical dashed lines indicate the (111), (200) and (220) diffraction planes of cubic NiO (reference pattern ICDD:04-005-9695). The intensity was weighted relative to the most intense peak for each diffractograms.

	(111)			(200)			(220)		
	2θ / °	B / °	L / nm	2θ / °	B / °	L / nm	2θ / °	B / °	L / nm
NiO	36.90	0.567	14.8	43	0.761	11.2	62.41	0.952	9.8
NiO+Li	36.97	0.423	19.8	43.04	0.577	14.8	62.59	0.62	15.0
Ni-Ta-O	36.95	0.361	23.2	42.98	0.526	16.2	62.46	0.526	17.7
Ni-Ta-O+Li	36.93	0.368	22.8	42.98	0.641	13.3	62.43	0.612	15.2
Ni-V-O	37.26	0.341	24.6	43.15	0.576	14.8	62.93	0.423	22.0

Table 7:12 Peak position (2θ), full-width at half maximum (determined by fitting the data with a Voigt profile) which accounts for the grain size broadening (B) and crystallite size (L) determined according to Scherrer Formula from the XRD spectra presented in Figure 7:27.

The studied Ni-Ta oxide exhibits the typical diffraction peaks of crystalline NiO (with a cubic structure, *bunsenite*) located at 37.044, 43.038 and 62.497 ° for the (111), (200) and (220) diffraction planes respectively. In the reference pattern (ICDD:04-005-9695), the strongest peak originate from the (200) orientation followed by the (111) and the (220) ones. In the diffractograms shown in Figure 7:27, the main orientation is (111) for the Ni-Ta and Ni oxides while for the Ni-V oxide it is (220). This indicates a preferential orientation of the grains in the coatings. The crystallite size was determined from the peak position and the FWHM using the Scherrer formula, values being reported in Table 7:12. Upon insertion of lithium and/or tantalum, the peak position does not vary significantly indicating that Li and Ta are not distorting the NiO cubic structure. Furthermore, no amorphization can be observed which confirm that the NiO structure is not altered. On the contrary, the diffraction peaks of the Ni-V oxide are shifted towards high angles compared to the NiO sample and reference pattern, this might indicates that vanadium atoms enters the crystal lattice

and decreases the lattice parameters of NiO. It can also be observed that the crystallite size is larger for the (111) peak and smaller for the peaks (200) and (220) at higher angles suggesting vertical columns, in agreement with the SEM images.

The crystalline phase of β-Ta_2O_5 is usually observed when temperatures during deposition or calcination above 400°C are used. Here, the sample was deposited without substrate heating and this phase is not observed. The NiO cubic structure appears to be the only crystalline phase present in the sample and does not seem to be distorted by the tantalum: the NiO peaks are not shifted and the full-width at half-maximum is not broadened. Therefore, tantalum may be present as amorphous tantalum pentoxide suggesting a $NiO:Ta_2O_5$ nanocomposite layer.

Tungsten and tantalum oxides, when deposited at room temperature, are amorphous whereas all the nickel, nickel vanadium and nickel tantalum oxides studied were crystalline.

7.3.4 Electrochromic device containing nickel tantalum oxide

Tantalum was shown to improve the optical properties of nickel oxide. Since the crystalline structure of NiO is not altered and no amorphization is observed, it is believed that a $NiO:Ta_2O_5$ nanocomposite layer is formed. Ta_2O_5 is used as a solid ion conductor, therefore a $NiO:Ta_2O_5$ nanocomposite is expected to facilitate the migration path for lithium ions and improves the electrochromic properties. A device containing tungsten oxide, tantalum pentoxide and a nickel tantalum oxide nanocomposite was deposited layer-by-layer by magnetron sputtering on ITO coated glass. The lithium was inserted in the tungsten oxide and Ni-Ta oxide layers using the dry lithiation method described in the section 7.1. The details of the parameters used for deposition of this Glass/ITO/WO_3/Ta_2O_5/ $NiO:Ta_2O_5$/ITO device are described in Table 7:13.

ECS80703	WO₃	Lithiation	Ta₂O₅	Ni-Ta-Oₓ	RT-ITO
Target	W	Li dispenser x (4+2)	Ta	Ni-Ta	ITO
Applied power	DC 150 W	7,3 A	DC-p 100 W	DC-p 100 W	RF 75 W
Deposition time	90 min	6 x 60 min	2 x 15 min	2 x 30 min	45 min
Ar / sccm	12.5	-	23.6	62.6	25.0
O₂ / sccm	8.3	-	4.0	1.5	0.4
Ratio O₂/Ar	66.67 %	0 / no process gas	16.8 %	2,38 %	1.6 %
Working pressure	$2,5.10^{-2}$ mbar	10^{-6} - 10^{-7} mbar (transfer chamber)	$2,7.10^{-2}$ mbar	$1,9.10^{-2}$ mbar	$4,0.10^{-3}$ mbar

Table 7:13 Deposition parameters; the WO_3 layer was deposited on ITO coated glass with a sheet resistivity of 15-30 ohm/sq (ITO X190 from Delta Technologies). The sample was taken to air between the two Ta_2O_5 layers to apply the mask. 4 lithiation steps were performed after the deposition of the WO_3 layer and 2 were performed in-between two Ni-Ta-Ox layers. The resulting thicknesses are shown in Figure 7:29.

The optical properties of the device were investigated as-deposited and during chrono-amperometry experiments. The transmittance was measured in the darkest and clearest state obtained and compared to the 'as-deposited' one; results are shown in Figure 7:28.
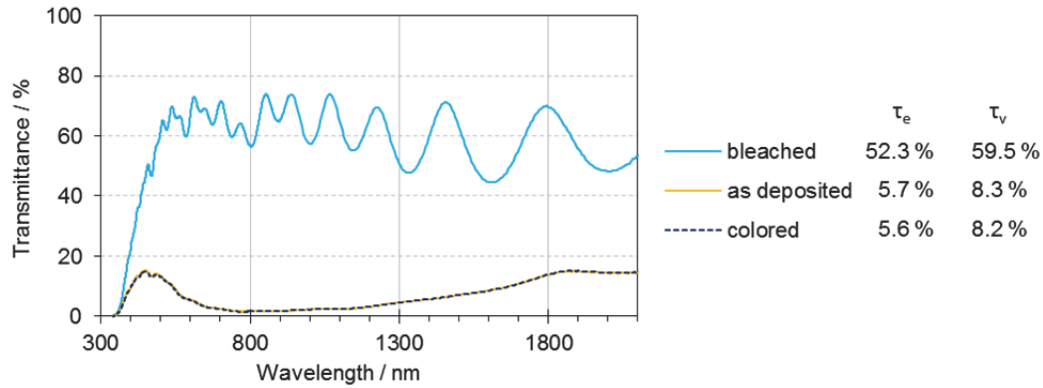
Figure 7:28   Spectral transmittance of the Glass/ITO/WO3/Ta2O5/NiO:Ta_2O_5/ITO device as-deposited, bleached and colored. The corresponding solar direct transmittance and light transmittance are indicated.

Due to the in-situ lithiation, the sample was relatively dark as-deposited with a solar direct transmittance of 5.7% and a light transmittance of 8.3%. Upon cycling, no further darkening was obtained despite the fact that some of the lithium was evaporated in the Ni-Ta-O layer. A slow bleaching occurred and a maximum light transmittance of 59.5% was obtained. During the chrono-amperometry experiments, the sample could not return to a dark state.

The sample was deposited simultaneously on a silicon substrate, which was cleaved in order to observe the cross section by scanning electron microscopy, as shown in Figure 7:29. In order to see the different elements, a back-scattered electron detector was used. Using this detector, the gray scale of the image gives an indication on the atomic mass; heavy elements are in bright shades and lighter ones in darker shades.
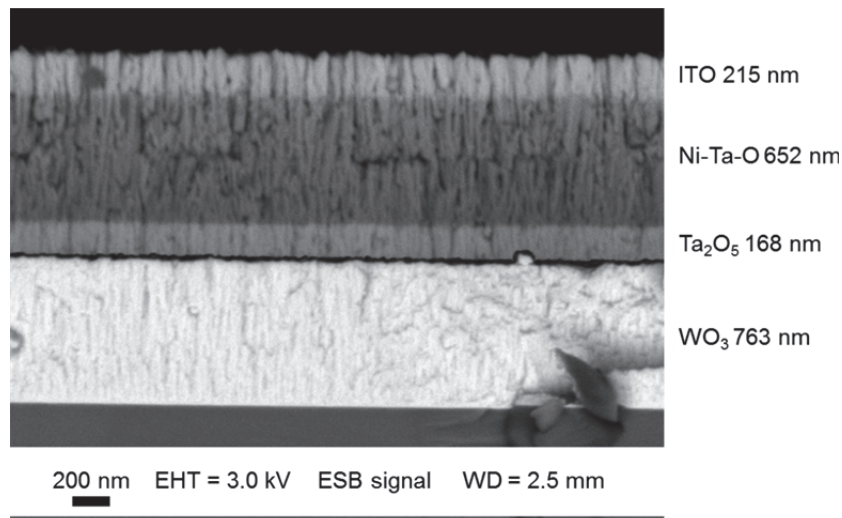
Figure 7:29   Backscattered electrons image (ESB) of the cross-section of the cleaved Si/WO_3/Ta_2O_5/ NiO:Ta_2O_5/RT-ITO sample. The gray shades are indicative of the atomic mass, the brighter being the heavier.

The four layers of the electrochromic device can clearly be distinguished due to the large difference of atomic mass of the various elements; the expected loose-packing and columnar structure is present. However, a strong delamination can be observed between the WO_3 and Ta_2O_5 layers: this delamination may have occurred during the cleavage of the silicon substrate. Nevertheless, it is not visible between the other layers. A good adhesion between the interfaces is crucial for the electrochromic properties; a weak bond between the WO_3 and Ta_2O_5 layers could be the reason of the poor cycling abilities of this device. In the previous device made with nickel vanadium oxide, this delamination was not observed even though the electrolyte was also Ta_2O_5. The deposition of a Ni-Ta oxide on Ta_2O_5 may have generated stresses on the Ta_2O_5 layer and weaken its interface to WO_3.

7.4 Discussion and perspectives

The aim of this chapter was to investigate novel all-solid-state devices. A method of dry lithiation to insert lithium ions in a solid-state device, without using sensitive lithium containing sputtering targets or taking the sample to air, was presented. It was successfully used to lithiate tungsten trioxide and decreases its light transmittance from 83 to 2%. It was observed that dry lithiation on ex-situ samples is also possible. The water and hydrocarbon that might deposit on the surface of the sample during exposure to air do not prevent the lithiation process under vacuum. Furthermore, dry lithiation was found to be a convenient method to study the electronic properties of metal oxide, since the sample can be treated in vacuum and transferred to the UPS/XPS analysis chamber. It was shown that to obtain a dark tungsten trioxide, a sufficient thickness of tungsten oxide is needed, otherwise the lithium can further reduce some of the tungsten atoms to a non-electrochromic compound. In nickel tantalum oxide, it was observed that a fraction of the lithium is not intercalated in the film and remains at the surface forming lithium oxides.

Using this lithiation method and a tantalum pentoxide electrolyte, all-solid-state devices could be produced successfully. The solar direct transmittance could be varied between 6 % and 51 % in less than 20 seconds; however, this device exhibited a yellowish tint. Nickel-tantalum mixed oxides were investigated in order to improve the color neutrality of the device, especially in the bleached state. It was found that tantalum can effectively improve the optical properties of nickel oxides in the short wavelengths. Furthermore, since tantalum pentoxide is used as an ion conductor, tantalum is expected to provide additional channels to lithium migration in the nickel oxide and further work on nanocomposites is intended.

All-solid-state device contains many semiconductor hetero-structures and studies of the interfaces by photoelectron spectroscopy can yield to a better understanding of their diode or rectifier behaviors. It was observed that coloring the device takes longer than bleaching it; studying the interfaces could help to understand the rate limiting factor in the coloration speed and efficiency. It was also observed that, if short-circuits are present in the device or if a resistance is connected to the two electrodes, it will discolor in a few minutes. An all-solid-state electrochromic device is similar to a thin-film battery and can be discharged or discolored by connecting a load to the circuit: this similarity to batteries could be used to optimize the charging strategies. In this study and in the literature, chrono-amperometry or the simple application of a voltage step is often used to color and discolor a sample. However, to limit the degradation of the lithium batteries, a current limit is generally used and should be applied to further studies on electrochromic devices.

Chapter 8   Conclusion

8.1   Achievements

In this doctoral thesis, the relation between the electronic and optical properties of coatings for architectural glazing was studied. Two applications were considered: coatings with a high transparency in the visible range, reflecting the infrared radiation and transparent to the microwaves as well as on electrochromic coatings to modulate the solar heat gains in a building.

The possibility to use a laser patterning process on conventional low infrared emissivity coatings to create a double effect of spectral selectivity (Vis/NIR/MW) was demonstrated experimentally. **A transmission of microwave close to the one of uncoated glass substrate was achieved with negligible impact on the thermal and optical properties of the glazing.** The effect of this patterning on the attenuation was measured for double glazing, thus taking into account both glass panes and the air gap. Furthermore, the pattern is not distinguishable in most common lighting situations, thus it does not disturb the view through the window. These new patterned coatings were manufactured on full scale glazing thanks to a fruitful collaboration with industrial partners (AGC Verres Industriels Moutiers and Class4Laser) and these windows are already installed on 10 regional trains from the BLS company as of November 2017.

Given the fact that the glazing fraction is increasing in trains and in buildings, solutions to mitigate the excessive solar heat gains in summertime are now required. Novel materials and methods for electrochromic windows were investigated. In electrochromic glazing, an electrochromic device containing two transparent conductive electrodes, two electrochromic materials (cathodic and anodic) and an ion conductor are present. In order to study electrochromic devices, the understanding, the optimization and the deposition of these four different layers is required.

Indium-tin oxide (ITO) was chosen for the bottom and top transparent electrodes. The use of substrate heating during deposition was not adequate for the top electrode because ITO films are to be deposited on top of four other layers: excessive heating could damage and/or modify the crystallinity of the underlying layers. ITO coatings with a resistivity $5.1 \cdot 10^{-4}$

Ω.cm and a solar direct transmittance of 81% were obtained, which is comparable to state-of-the-art ZnO films and not far from the performances of commercial ITO films (Ellmer, 2012). For the thickness used in this study, it represents a sheet resistivity of 32 Ω/sq, which is comparable to the commercial ITO coatings used as substrates. These experiments showed that it was possible to obtain **ITO coatings with satisfactory electrical and optical properties without heating** the substrate or proceeding to a thermal annealing.

Many oxides of transition metals exhibit an electrochromic behavior. Tungsten trioxide is according to the current state of the art, the one showing the strongest optical contrast possible is the visible range. The impact of the deposition parameters on the electronic, optical and morphological properties of tungsten trioxide was investigated. It revealed that the **nanoporosity** produced by the use of high total pressure during the sputtering **is favorable to the optical contrast and switching dynamics of WO₃**. For the counter electrochromic layer, nickel oxides were investigated. The used of pure nickel or **Ni-Ta** targets proved to be **advantageous for the optical properties in the bleached state,** because of their lower absorption in the short wavelength range compared the commonly used nickel vanadium oxides.

Various inorganic electrolytes were investigated: LiPON and LLTO considered in the field of thin film batteries and tantalum pentoxide. LiPON could be deposited successfully at room temperature with ionic conductivities in the range of the one usually obtained for sputtered LiPON films (Hamon, 2006). An activation energy of 0.6 eV was observed and suggests a migration of the Li ions through vacancies in the LiPON atom network. Furthermore, it was found that increasing the argon content in the **argon-nitrogen plasma enhances the chemical stability of a LiPON film to ambient air**. LLTO is not widely studied in the context of electrochromic devices and therefore, the optical properties were not easily available. It was found that amorphous **LLTO films exhibit a high transparency** in the solar range with solar direct transmittance and light transmittance about 80%. Nanoporous tantalum pentoxide was deposited and used in an electrochromic device with a liquid electrolyte; it was shown that it does not reduce the switching speed of the device compared to a device without a tantalum pentoxide layer. Tantalum pentoxide can be deposited from a metallic Ta target allowing faster deposition rate and easier implementation on a larger scale.

When a liquid electrolyte is used, it is usually the source of lithium ions. In order to study all-solid-state electrochromic devices, a method to insert lithium in vacuum was developed. This method of **dry lithiation** does not require the use of sensitive lithium containing compounds, which avoid the need for a dry and controlled atmosphere during use and handling. It was **successfully used to lithiate tungsten trioxide** and decreases its light transmit-

tance from 83 to 2%. It was observed that dry lithiation on ex-situ samples is also possible. The water and hydrocarbon that might deposit on the surface of the sample during exposure to air does not prevent the lithiation process under vacuum. Furthermore, dry lithiation was found to be a convenient method to study the electronic properties of metal oxide, since the sample can be treated in vacuum and transferred to the UPS/XPS analysis chamber. It was shown that to obtain a dark tungsten trioxide, a sufficient thickness of tungsten oxide is required, otherwise the lithium can further reduce some of the tungsten atoms to a non-electrochromic compound. In nickel tantalum oxide, it was observed that a fraction of the lithium is not intercalated in the film and remains at the surface forming lithium oxides.

Using the dry lithiation method and a tantalum pentoxide electrolyte, a functional all-solid-state device was produced. The solar direct transmittance could be varied between 6 % and 51 % in less than 20 seconds; however, this device exhibited a yellowish tint.

8.2   Outlook

Commercial electrochromic glazing is reaching the market but some challenges are still present. The color neutrality in the transmittance in the bleached state should be improved and the durability of the materials must correspond with the lifetime of a building; furthermore, their cost is still prohibitive for many market segments. Indium-tin oxide is generally used because it is today the best material available in terms of transparency and electrical conductivity; however, indium is produced mainly as a byproduct of zinc from mineral ores containing less than 100 parts per million (Lokanc, 2015); its supply is limited and its price volatile. Research on transparent conductors is an active field and many indium-free alternatives are investigated. Indium-free electrochromic devices were produced, e.g. by Li et al. and Koubli et al. (Li, 2015; Koubli, 2015) using $WO_3/Ag/WO_3$ stacks where the WO_3 layers serve both as an electrochromic material and electrode. One could imagine using pyrolytic fluorine-doped tin oxide coated glass, as a substrate, and a dielectric/Ag/dielectric stack, as a top electrode, to use materials which are well known in the glass industry. Being able to deposit all the required layers in vacuum might help to reduce the price even though vacuum equipment is in itself expensive, because it allows for a precise control of the deposited thicknesses and thus optimization of the processes. In addition to this, minimizing the substrate heating or avoiding the need for a step where heat is needed over large surfaces can reduce the energy cost.

In batteries, graphite is often used because its layered structure facilitates the movement of lithium atoms. In electrochromic devices, it was observed that nanoporosity improves the optical properties. This might be due to an increased number of channel paths for lithium,

which reduce the strains on the atom network. In addition, a porous structure can decrease the charge transfer resistance (He, 2018). Furthermore, in non-aqueous electrolytes the desolvation process of the lithium ion might reduce the kinetics of intercalation/deintercalation in the electrode (Abe, 2004). A less ordered interface could also facilitate the loss of the sheath of the solvated lithium ion (Steinrück, 2018). Furthermore, it was also observed that the resistivity of the ITO substrate has a strong influence on the coloration speed even on small scale samples; however, the bleaching speed did not depend on the ITO resistivity at those scales. In most electrochromic devices, the voltage is applied to the two transparent conductors and the local distribution of the potential within the depth of the multilayer sample cannot be controlled. Temperature-dependent measurements could help to separate the electrical and electrochemical contributions to the coloration mechanism and get a better understanding of the rate limiting factors. Furthermore, nano-composite layers containing nickel oxide and tantalum pentoxide in combination with a tantalum pentoxide electrolyte is expected to provide additional channels to lithium migration and further work on nanocomposites is intended.

All-solid-state device contain many semiconductor hetero-structures and studies of the interfaces by photoelectron spectroscopy can yield to a better understanding of their diode or rectifier behaviors. It was observed that coloring the device takes more time than bleaching it and studying the interfaces could help to understand the rate limiting factor in the coloration speed and efficiency. It was also observed that if short-circuits are present in the device or if a resistance is connected to the two electrodes, it will discolor in a few minutes. An all-solid-state electrochromic device is similar to a thin-film battery and can be discharged or discolored by connecting a load to the circuit: this similarity to batteries could be used to optimize the charging strategies. In this study and in the literature, chrono-amperometry or the simple application of a voltage step is often used to color and discolor a sample. However, to limit the degradation of the lithium batteries, a current limit is generally employed and should be applied to further studies on electrochromic devices.

Annexes

A1. Matlab routine for the determination of solar direct transmittance and light transmittance from multiple transmittance spectra

The files necessary to run the Matlab routine are available on the "groupe nano" folder:

\GENERAL\strategies\display_window_test_bench_data\time cyclic Te-Tv-CRI\ CalculationTR_EC_cyclic.m

- Copy the folder "time cyclic Te-Tv-CRI" on your local drive, open matlab, make this folder your working folder, add access to subfolders. The measurement files should be pasted in "workfiles"
- Open Calculation_TR_EC_cyclic.m
- change directory name, file names (fichTR), product name (prodn), cycle description (time cyclic Te-Tv-CRI) and time interval between two spectra (ts)
- Run the program, it should display the graph and export them in the "Results" subfolder
- results_TR.xls contains τ_e and τ_v and spectral_data_visible_1nm.csv can then be used to calculate color coordinates using Calculation_CRI_EC_cyclic.m

```
% prog
close all
clear all
clc

% Programm to calcultate optical factor according to EN 410 : solar direct transmittance TauE and light transmittance TauV

% Measured data
fichTR = 'workfiles\measured cyclic transmittance.csv';  % measured transmittance:
%first column wavelength in nm, following colums spectral transmittance in %

% product name
prodn = 'type here the reference or product name';  % IMPORTANT CHANGE PRODUCT NAME and CYCLE DESCRIPTION
cycledescr = 'type here cycle description'; % and CYCLE DESCRIPTION
ts = 0.5; % IMPORTANT CHECK TIME BETWEEN TWO SPECTRA in seconds is ok !!!!!

%common variables and file
load('g173cut.mat'); % spectre solaire G 173 Global tilt
load('D65V.mat') % spectre de sensibilité de l'oeil * illuminant D65

% To set default colors in 12 rainbow colors
C = [0.729412 0.333333 0.827451
   0.541176 0.168627 0.886275
   0.294118 0 0.509804
   0 0 1
   0.117647 0.564706 1
   0.133333 0.545098 0.133333
   0.196078 0.803922 0.196078
   1 0.843137 0
   1 0.54902 0
   1 0 0
   0.8 .07 0.1
   0.545098 0 0
   0.3 0 0];
set(0,'DefaultAxesColorOrder', C);

%Importation data
dataaTR = [0,0];
dataaTR = importdata (fichTR);
dataaTR = dataaTR(2:end,:); % enlève la première ligne qui contient des zeros
```

197

```matlab
datat = dataaTR;
sd = size(datat); % size of the data matrix
s_sp = sd(1,2)-1;

% declaration des variables
TauE = zeros(s_sp,2); % Facteur de transmission énergétique totale. pour créer une matrice vide de la bonne taille,
TauV = zeros(s_sp,2); % Facteur de transmission visible . pour créer une matrice vide de la bonne taille,
tss = zeros(s_sp,1); % time interval between two measurements

% time spectro
for i = [1:s_sp]
tss(i,1) = 0+(i-1)*ts ; % time spectro define above
TauE(:,1) = tss;
end

% TauE
%Spectre solaire
datatpg = interp1(datat(:,1),datat(:,2:end),g173cut(:,1)); % interpolate data to have same x values than solar spectrum
g173cutn = g173cut(:,2)./sum(g173cut(:,2)); % normalise
fs = sum(g173cutn); % Pour vérification : vu que c'est normalisé, ça doit être égal à 1

%Measured transmittance weighted by solar spectrum
SpecTRA = zeros(size(datatpg,1),s_sp);

for i = [1:s_sp]
SpecTRA(:,i) = datatpg(:,i).*g173cutn(:,1); % multiplication membre à membre
TauE(i,2) = sum(SpecTRA(:,i)); % energetic transmittance factor
T_E(:,2) = TauE(:,2)./100;
end

% TauV
TauV(:,1)= TauE(:,1);

%D65Vp = interp1(D65V(:,1),D65V(:,2),datat(:,1)); % fait une interpolation linéaire
datatp = interp1(datat(:,1),datat(:,2:end),D65V(:,1));
D65Vn = D65V(:,2)./sum(D65V(:,2));

SpecTV = zeros(size(D65V,1),s_sp); % spectre mesuré * snetibilité oeil * D65
for i = [1:s_sp]
SpecTV(:,i) = datatp(:,i).*D65Vn; % multiplication membre à membre
TauV(i,2) = sum(SpecTV(:,i)); % visible transmittance factor
T_V(:,2) = TauV(:,2)./100;
end

%résumé des resultats
tss_TauE_TauV_TauEsurTauV = [TauE(:,1),T_E(:,2),T_V(:,2)];

%AffichageTR
figure(1)
plot(datat(:,1),datat(:,2:end),'linewidth',1); grid on
title(prodn);
xlabel('wavelength / nm');
ylabel('Measured transmittance %');
legend(cycledescr);

figure(2) % plot solar direct transmittance and visible light transmittance
plot(TauE(:,1),T_E(:,2),'r-', TauV(:,1),T_V(:,2),'b-','linewidth',2); grid on
title(prodn);
xlabel('time / seconds');
ylabel('Intensity %');
%xlim([0 80])
ylim([0 1])
legend('Solar direct transmittance','Visible light transmittance', 0)


% EXPORT
saveas(figure(1),[pwd '\Results\measured_transmittance.tiff'], 'tiffn'); % to export the first graph
saveas(figure(2),[pwd '\Results\TauE_TauV.tiff'], 'tiffn');  % to export the 2nd graph
T = {prodn,'Tau E','Tau V'}; % headers for results
N = num2cell (tss_TauE_TauV_TauEsurTauV); % Convert numeric data, N, to a cell array of doubles
outCell = [T;N];% Concatenate dataCell and Tinto one cell array
xlswrite('Results\results_TR.xls',outCell) % to export the concatenated matrix

% interpolated spectrum by 1 nm step for visible range (380-780nm)
% to be used in Calculation_CRI_EC_cyclic
```

```
data_1nm = zeros(401,sd(1,2));
data_1nm(:,1) = D65V(:,1);
data_1nm(:,2:sd(1,2)) = datatp(:,1:s_sp);
csvwrite('Results\spectral_data_visible_1nm.csv',data_1nm) % to export the spectral data
ok = 'done'        %OB2016 %thks ncl  %platypus
```

A2.   Matlab routine for the determination of color coordinates and color rendering index from multiple transmittance spectra

The files necessary to run the Matlab routine are available on the "groupe nano" folder:

\GENERAL\strategies\display_window_test_bench_data\time cyclic Te-Tv-CRI\ CalculationCRI_EC_cyclic.m

- Copy the folder "time cyclic Te-Tv-CRI" on your local drive, open matlab, make this folder your working folder, add access to subfolders. The measurement files should be pasted in "workfiles"
- Open Calculation_CRI_EC_cyclic.m right after having run Calculation_TR_EC_cyclic.m (or copy the desired spectral_data_visible_1nm.csv in the "Results" folder.
- change the product name (prodn) and Run the program
- an excel file containing the color coordinates index will appear in the "Results" folder (color1.xls)

```
% prog
close all
clear all
clc

% Programm to calcultate color rendering index and color coordinates according to EN 410 :

%transmittance spectrum of the glass to analyze
load('results\spectral_data_visible_1nm.csv')  ;
fich1 = 'results\spectral_data_visible_1nm.csv';  % measured transmittance from TR_EC_cyclic
% product name
prodn = 'type here the reference or product name';
 % time between two spectra
ts = 0.5; % IMPORTANT CHECK TIME BETWEEN TWO SPECTRA in seconds is ok !!!!!

%data needed as defined in EN 410
load('D65V.mat') % spectre de sensibilité de l'oeil * illuminant D65
load('CIE1931.mat') % Observateur colorimétrique standard CIE 1931 (2°).
load('CIE1964.mat') % CIE 1964 suppl. standard colorimetric observer (10°)
load('testcolor.mat') % testcolor numbers beta i d'après le tableau de la CIE : 380 à 780 nm avec pas de 10
load('D65.mat') % spectre de l'illuminant D65
load('UVW.mat') % Valeurs de U * r,i , V* r,i , W * r,i pour les couleurs-test éclairées par l'illuminant normalisé D 65

%Importation
dataCRI = [0,0];
dataCRI = importdata (fich1);
sd = size(dataCRI);
sd1 = sd(1,2);
s_sp = sd(1,2)-1; % size of data to adapt all cycles
dataCRI2 = dataCRI(:,2:sd1)/100;

% mise aux memes dimensions
CIE1931p = CIE1931;
CIE1931p = interp1(CIE1931(:,1),CIE1931(:,2:end),D65V(:,1)); % interpolate data to have same x values than D65V, 1 by 1 nm
D65p = D65;
D65p = interp1(D65(:,1),D65(:,2:end),D65V(:,1)); % interpolate data to have same x values than D65V, 1 by 1 nm
D65pn = D65p(:,1)./sum(D65p(:,1));
testcolorp = testcolor;
testcolorp = interp1(testcolor(:,1),testcolor(:,2:end),D65V(:,1)); % interpolate data to have same x values than D65V, 1 by 1 nm

for j = [1:s_sp] % loop to calculate color coordinates for each spectrum of the cycle

dataCRIp = dataCRI2(:,j);

% Color coordinates X Y Z
```

```matlab
% X
specx = [0,0];
specx = dataCRIp(:,1).*CIE1931p(:,1).*D65p(:,1); % multiplie la transmittance par x-barre et l'illuminant D65
X_t(1,j) = sum(specx)/10;
% /10 car on est passé de 2 intervalle de 5 à 2 intervalles de 1, donc c'est 2 fois 5 fois trop
% Y
specy = [0,0];
specy = dataCRIp(:,1).*CIE1931p(:,2).*(D65p(:,1)); % multiplie la transmittance par y-barre et l'illuminant D65
Y_t(1,j) = sum(specy)/10;
% Z
specz = [0,0];
specz = dataCRIp(:,1).*CIE1931p(:,3).*(D65p(:,1)); % multiplie la transmittance par z-barre et l'illuminant D65
Z_t(1,j) = sum(specz)/10;


% Color coordinates Xi Yi Zi (* beta i - testcolor)
% X
X_t_i = zeros(2,8);
SpecX = zeros(size(D65p,1),8); % spectre mesuré * x-barre * D65
for i = [1:8]
SpecX(:,i) = specx.*testcolorp(:,i); % multiplication membre à membre
X_t_i(2,i) = sum(SpecX(:,i))/10; % coordonnées de couleur pour couleur ref i
X_t_i(1,i) = i;
end
% Y
Y_t_i = zeros(2,8);
SpecY = zeros(size(D65p,1),8); % spectre mesuré * x-barre * D65
for i = [1:8]
SpecY(:,i) = specy.*testcolorp(:,i); % multiplication membre à membre
Y_t_i(2,i) = sum(SpecY(:,i))/10; % coordonnées de couleur pour couleur ref i
Y_t_i(1,i) = i;
end
% Z
Z_t_i = zeros(2,8);
SpecZ = zeros(size(D65p,1),8); % spectre mesuré * x-barre * D65
for i = [1:8]
SpecZ(:,i) = specz.*testcolorp(:,i); % multiplication membre à membre
Z_t_i(2,i) = sum(SpecZ(:,i))/10; % coordonnées de couleur pour couleur ref i
Z_t_i(1,i) = i;
end

% Color coordinates X Y Z en u v
u(1,j)=(4*X_t(1,j))/(X_t(1,j)+15*Y_t(1,j)+3*Z_t(1,j));
v(1,j)=(6*Y_t(1,j))/(X_t(1,j)+15*Y_t(1,j)+3*Z_t(1,j));

% Color coordinates Xi Yi Zi (* beta i - testcolor) en u v
% u_i
u_i = zeros(2,8);
for i = [1:8]
u_i(2,i) = (4*X_t_i(2,i))/(X_t_i(2,i)+15*Y_t_i(2,i)+3*Z_t_i(2,i)); % coordonnées de couleur pour couleur ref i en u v
u_i(1,i) = i;
end
%v_i
v_i = zeros(2,8);
for i = [1:8]
v_i(2,i) = (6*Y_t_i(2,i))/(X_t_i(2,i)+15*Y_t_i(2,i)+3*Z_t_i(2,i)); % coordonnées de couleur pour couleur ref i en u v
v_i(1,i) = i;
end

% ct et dt
c = (1/v(1,j))*(4-u(1,j)-10*v(1,j));
d = (1/v(1,j))*(1.708*v(1,j)+0.404-1.481*u(1,j));

% cti et dti
%c_t_i
c_i = zeros(2,8);
for i = [1:8]
c_i(2,i) = (1/v_i(2,i))*(4-u_i(2,i)-10*v_i(2,i));
c_i(1,i) = i;
end
%d_t_i
d_i = zeros(2,8);
for i = [1:8]
d_i(2,i) = (1/v_i(2,i))*(1.708*v_i(2,i)+0.404-1.481*u_i(2,i));
d_i(1,i) = i;
```

```
end

% coordonnées trichromatiques corrigées en fonction de la distorsion par adaptation chromatique, pour les huit échantillons éclairés
par la lumière transmise
% u prime t i
up_i = zeros(2,8);
for i = [1:8]
up_i(2,i) = (10.872+(0.8802*(c_i(2,i)/c))-(8.2544*(d_i(2,i)/d)))/(16.518+(3.2267*(c_i(2,i)/c))-2.0636*(d_i(2,i)/d));
up_i(1,i) = i;
end
% v prime t i
vp_i = zeros(2,8);
for i = [1:8]
vp_i(2,i) = (5.520)/(16.518+(3.2267*(c_i(2,i)/c))-2.0636*(d_i(2,i)/d));
vp_i(1,i) = i;
end

%Conversion au système d'espace chromatique uniforme CIE 1964 : on utilise les formules suivantes pour la conversion relative à
chaque couleur-test
%W* t, i
W_i = zeros(2,8);
for i = [1:8]
W_i(2,i) = 25*(((100*Y_t_i(2,i))/Y_t(1,j))^(1/3))-17;
W_i(1,i) = i;
end
%U* t, i
U_i = zeros(2,8);
for i = [1:8]
U_i(2,i) = 13*W_i(2,i)*(up_i(2,i)-0.1978);
U_i(1,i) = i;
end
%V* t, i
V_i = zeros(2,8);
for i = [1:8]
V_i(2,i) = 13*W_i(2,i)*(vp_i(2,i)-0.3122);
V_i(1,i) = i;
end
%Valeurs de U * r,i , V* r,i , W * r,i pour les couleurs-test éclairées par l'illuminant normalisé D 65
Ur(1,:) = UVW(1,:);
Vr(1,:) = UVW(2,:);
Wr(1,:) = UVW(3,:);

%Détermination de la distorsion totale de la couleur i. Pour chaque échantillon de couleur-test i :
%Ecart des couleurs
dE = zeros(2,8);
for i = [1:8]
dE(2,i) = (((U_i(2,i)-Ur(1,i))^2)+((V_i(2,i)-Vr(1,i))^2)+((W_i(2,i)-Wr(1,i))^2))^(1/2);
dE(1,i) = i;
end
Ri = zeros(2,8);
for i = [1:8]
Ri(2,i) = 100-4.6*dE(2,i);
Ri(1,i) = i;
end

%Ra Color rendering index
Ra(1,j) = (1/8)*(sum(Ri(2,:)));

% color coordinates small x, small z
petit_x(1,j) = X_t(1,j)/(X_t(1,j)+Y_t(1,j)+Z_t(1,j));
petit_y(1,j)= Y_t(1,j)/(X_t(1,j)+Y_t(1,j)+Z_t(1,j));
end

% time spectro
tss = zeros(s_sp,1); %to have the color coordinate according to the time of measurement
for i = [1:s_sp]
tss(i,1) = 0+(i-1)*ts ; % time spectro defined above
Result(1,1:s_sp) = tss;
end

%Results
Result(2,1:s_sp) = X_t;
Result(3,1:s_sp) = Y_t;
Result(4,1:s_sp) = Z_t;
```

```
Result(5,1:s_sp) = petit_x;
Result(6,1:s_sp) = petit_y;
Result(7,1:s_sp) = u;
Result(8,1:s_sp) = v;
Result(9,1:s_sp) = Ra;
T1 = {prodn,'X_t','Y_t','Z_t','petit_x','petit_y','u','v','Ra'}; % headers for column 1
T2 = transpose (T1);
N2 = num2cell (Result);
N1 = transpose (N2);
outCell1 = [T1; N1];% Concatenate dataCell and T into one cell array
xlswrite('Results\color1.xls',outCell1) % to export the concatenated matrix transposed so it can fit in excel
ok ='ça marche' % :)    %OB2016-2018   %thks ncl
```

A3. Experimental Determination of Optical and Thermal Properties of Semi-transparent Photovoltaic Modules Based on Dye-sensitized Solar Cells

Abstract

The demand for energy efficiency of buildings and on-site electricity production is rising. Building integrated photovoltaic can provide a part of the electricity demand. Many studies are related to the module efficiency. However, architectural integration, optical and thermal properties also require attention. Semi-transparent modules are especially interesting for architectural integration in the glazed part of the façade. Dye sensitized solar cells, offering color and semi-transparency, are in the process of market introduction. However, dye-sensitized solar cells are fragile and there are not many examples of architectural integration due to the technical challenge of introducing these cells in a glazing. A glazing containing colored photovoltaic modules could be used to design an active façade.

In order to determine the thermal behaviour of the building, the precise optical and thermal properties of the used materials need to be known. Performances of semi-transparent photovoltaic modules based on dye-sensitized solar cells were investigated. These modules come from the same manufacturer, using the same technology. However, they differ in terms of shades and nuances. Common practice is to indicate optical properties at normal angle of incidence. Yet, for most latitudes, the properties for a large range of angles of incidence are more relevant. Therefore, the spectral transmittance and the reflectance were measured at 12 angles of incidence ranging from 0° to 75°. From these data, the solar direct transmittance τ_e, the solar direct reflectance ρ_e and the visible transmittance τ_v and selectivity were calculated.

The solar gain factor was determined on a prototype double glazing under illumination with a solar simulator by measuring the temperatures of the external and inner surface of the product. Combined with the values of absorptance obtained from the transmittance and reflectance values, this measurement allows us to determine the internal heat transfer coefficient q_i and thus the solar gain factor of the double glazing (also called total energetic transmittance or g-value).

Final performance of a façade containing these modules will depend on the composition of the double glazing in which they will be laminated. The performance of the module itself will help to determine the best composition for each climate. For instance, a solar protection coating may be needed. The modules can be laminated to a glass pane and then be assembled in a double glazing. Therefore the architectural integration is facilitated and compatible with existing façade systems. In highly glazed building, a part of the façade could then be a photovoltaic façade and deliver a fraction of the energy demand while providing colourful options to enhance the aesthetic of the building.

1. Introduction

Dye-sensitized solar cells (DSSC) have been studied for a long time as a new generation of photovoltaic cells [1]. Commercial photovoltaic modules based on this technology are starting to be introduced in the market. The use of semi-transparent photovoltaic modules could increase the part of renewable energy produced on-site. Effectively, being embedded in a classical double glazing, they could find more easily their place on the façade. In addition, such modules provide colors and new possibilities for aesthetics [2]. In order to facilitate the building integration of such modules, thermal behavior and detailed optical properties should be known [3]. Comparison of optical properties with photovoltaic efficiencies was done by Yoon et al. [4].

In this paper, optical and thermal properties of prototype photovoltaic modules based on DSSC were studied. The solar direct transmittance and the light transmittance were determined as a function of the angle of incidence. In addition, the solar gain (g-value) of a double glazing comprising such modules was calculated based on the results of experiments. Results will help to choose the combination of glazing to provide the desired values.

2. Experimental

2.1. Samples

Five photovoltaic modules based on dye-sensitized solar cells were analyzed. These modules were produced by Glass2Energy, a Swiss company which is developing semi-transparent photovoltaic modules to facilitate architectural integration of renewable energy in the buildings. These products are particularly promising because they can be laminated to the glass pane of a classical double (or triple) glazing and be installed as a regular window. Table 1 lists the products which were measured.

Table 1. List of studied products

Ref.	Denomination	Dye	Carrier layer	Frame
G1	Opaque green	Green, type 1	TiO_2, type 1	Single glazing
G2	Transparent green	Green, type 1	TiO_2, type 2	" "
R1	Opaque red	Red, type 1	TiO_2, type 1	" "
R2	Transparent red	Red, type 1	TiO_2, type 2	" "
R3	Double glazing red	Red, type 2	TiO_2, type 3	Double glazing

As noted in Table 1, the two green samples (G1 and G2) are made with the same dye. In a similar manner, the two red modules (R1 and R2) are also made of the same dye. Only the nanostructure of the TiO_2 carrier layer changes. Fig. 1 shows photographs of the studied modules. Rothenberger et al. studied the difference between a strongly scattering TiO_2 and a transparent one [5].
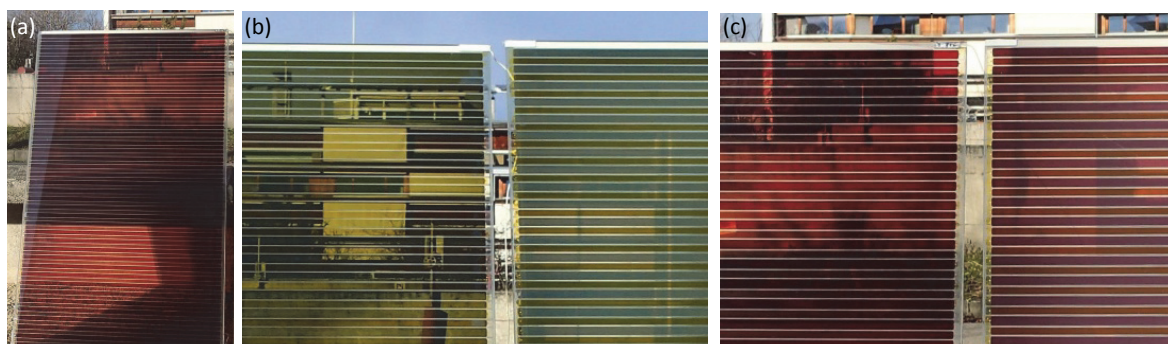
Fig. 1. Photographs of (a) full size R2 module 60 cm x 100 cm; (b) transparent (left) and opaque (right) green samples; (c) transparent (left) and opaque (right) red samples. (color online)

Fig. 1 (a) shows the whole R2 module which dimensions are 60 cm x 100 cm. The change of appearance due to the different TiO_2 carrier layer used is particularly observable in Fig. 1 (b): on the left, the module G2 provide clear, yet colored, view to the surroundings; on the right, only some contours can be seen through the G1 module. Fig 1 (c) depicts the R2 and R1 modules.

2.2. Angular-dependent optical properties

Physical properties of façade elements play an important role in energy management. Precise data allows a better prediction of overheating risks and thermal losses. For new products such as dye-sensitized solar modules, it is important to determine the obtained properties. Values commonly given by manufacturers are valid at normal incidence of light. However, sun rays rarely strikes the façade at normal incidence. To overcome this, a window test bench capable of measuring transmittance and reflectance for angles between 0° and 75° was developed originally at the University of Basel [6] and now installed at EPFL/LESO-PB in Lausanne. This experimental set-up is composed of a light source, a support able to carry and rotate a real-size glazing, a receiver collimator and a Zeiss diode array spectrometer. For transmittance, the collimator is placed in line with the light source. For reflectance measurements, the collimator can be moved to have the same light path length for each angle. Spectral intensities are displayed in the software AspectPlus for wavelength ranging from 350 nm to 2100 nm (UV-Vis-NIR).

These values are used to determine the coefficient of solar direct energy transmission τ_e, the light transmission τ_v, the solar direct reflectance ρ_e and the light reflectance ρ_v according to the EN 410 standard [7]. The light transmittance τ_v of the glazing is calculated from the spectral transmittance of the glazing for the visible range and considering to the sensitivity of the human eye for a white illuminant. The light reflectance ρ_v is calculated by replacing the spectral transmittance with the spectral reflectance.

The solar direct transmittance τ_e of the glazing represents the fraction of solar energy transmitted through the glazing. The solar direct reflectance ρ_e is determined in a similar manner, by replacing the spectral transmittance by the spectral reflectance. The solar direct absorptance α_e can be found using the relation (1).

$$\tau_e + \rho_e + \alpha_e = 1 \tag{1}$$

These factors are commonly used to characterize window with low emissivity coatings or tinted glass.

2.3. Angular-dependent solar gain factor

In order to calculate the solar gains of a building, one must know the solar gain factor of the components of the transparent part of the façade. The solar gain factor (or total energy transmittance) is the amount of energy passing though the building element, either transmitted or absorbed and radiated inside. It is defined by equation (2):

$$g = \tau_e + q_i \tag{2}$$

Where τ_e is the coefficient of solar direct energy transmission and q_i is the secondary internal heat transfer factor. q_i represents the part of energy absorbed by the glass and reemitted as heat in the interior side. For accurate evaluation, the solar gain factor should be known as a function of the angle of incidence. The angular dependent solar gain was determined using the method developed by Reber et al. [8]. This method is based on the measurement of the external and internal surface temperature of the double glazing under illumination with a solar simulator. The light source of the solar simulator is a water-cooled xenon arc lamp (1000 W). A spectral distribution similar to the solar radiation is achieved using specific filters. Using these temperatures and the previously calculated solar transmittance factor τ_e, it is possible to determine the solar gain factor.

3. Results

3.1. Angular-dependent transmittance, reflectance and optical performances

The five photovoltaic modules were installed on the pivoting window holder. The spectral transmittance and reflectance were measured at different angles ranging between 0° and 75°. Results obtained for the red opaque module (R2) are displayed in Fig. 2 (a). The maximum transmittance is obtained at all angles for a wavelength of about 1030 nm. At normal incidence, the transmittance reaches 41.6%, while when the light hits the module with an angle of 75° to the normal, the maximum transmittance is dived by two (20.8%). At oblique incidences, more light is reflected.

Fig. 2 (b) shows the spectrum of transmittance at normal incidence of the four single modules. In the visible range, the transmittance of each sample is very low which is due to the dye absorption. Samples G1 and R1, so called opaque in this study, presents a similar optical response in the range 600-2100 nm. The maximum transmittance is for both spectrums around 1000 nm, slightly above 40 % and a decrease is observed in the near-infrared from 1000 nm to almost zero transmittance after 2100 nm. This behavior indicates usually the presence of a conductive coating. In this case, it is certainly due to the presence of the transparent conductive oxide necessary to conduct electricity. Samples G2 and R2, so called transparent in this paper, display higher transmittance values. G2 sample has a maximum transmittance of 56.6% at 873 nm. R2 sample present the highest transmittance with a peak of 62.5 % at 786 nm.

As presented in Table 1, two types of titanium dioxide carrier layer are used. They differ in terms of nanostructure. If we except the visible part, which is representative of the dye used, we can see that the carrier layer plays an important role in terms of optical properties. Using the same dye, the transmittance of a module can go from 62 % (for R2) to only 41 % (R1).
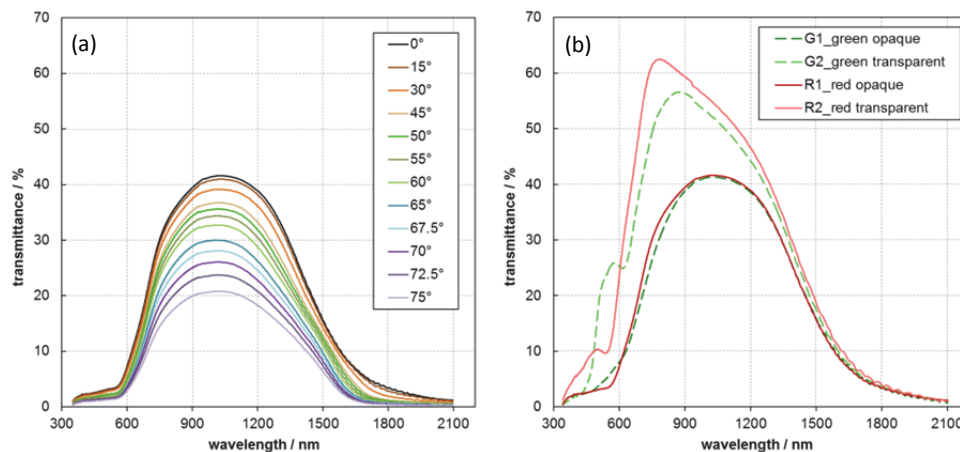
Fig. 2. (a) angular dependent transmittance spectrum of R1 sample; (b) transmittance spectrum at normal incidence of the four different samples.

Using the spectrum of transmittance and reflectance, the coefficient of solar direct energy transmission τ_e, light transmission τ_v, solar direct reflectance ρ_e and light reflectance ρ_v, can be calculated according to the method described in section 2.2.

In Table 2, results are presented for normal incidence.

Table 2. Solar direct energy transmission τ_e, light transmission τ_v, solar direct reflectance ρ_e, light reflectance ρ_v, and solar direct energy absorptance α_e at normal incidence

	τ_e	τ_v	ρ_e	α_e	τ_e/τ_v
G1 opaque green	0.19	0.06	0.07	0.74	3.17
G2 transparent green	0.31	0.23	0.08	0.61	1.35
R1 opaque red	0.19	0.05	0.07	0.73	3.80
R2 transparent red	0.33	0.15	0.08	0.59	2.20
R3 double glazing red	0.14	0.06	0.10	0.76	2.33

From Table 2, it can be noted that visible transmittance are very small, especially for the opaque and double glazing modules. It is not surprising as the dye-sensitized solar cells function by using the visible light and are therefore absorptive in this range. The solar direct energy transmission is higher because the modules are more transparent in the infrared part of the solar spectrum. This leads to a ratio τ_e/τ_v greater than one for all modules. It means that the modules are providing more heat than light in the building. This ratio is commonly used by architects to define different class of glazing. The reflectance does not really changes being quite close to the reflectance of a single glass of pane, which is approximately four percent per interface.

3.2. Thermal performances : determination of the total energy transmittance

Using the experiment detailed in section 2.3, the temperatures of the exterior and interior glass panes were measured (respectively, position 1 and 4 according to Fig. 3 (a)). Temperatures obtained are displayed in Fig. 3 (b), ambient temperature is recorded to identify possible general rise of temperatures. At the beginning, every element has the same temperature, and then the light source is turned on facing the exterior glass pane. After approximately three hours, a stabilisation of the temperature is observed. The temperatures of the exterior glass pane and the interior glass pane at stabilisation are used to determine the internal coefficient of heat transfer q_i. This coefficient is determined considering an emissivity of the glass of 0.837, a U-value of 3 W/(m^2.K) for the double glazing.
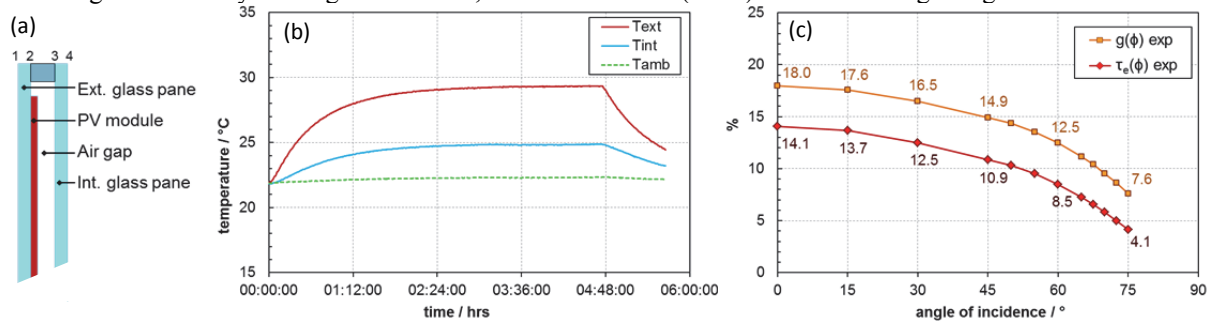
Fig. 3. (a) Double glazing configuration. The photovoltaic module is laminated on the exterior glass pane position 2; (b) Temperature measured on the exterior side (facing the light source) T_{ext} and the interior side T_{int} of the double glazing module, ambient temperature T_{amb} is shown as an explanation of the slight global increase of temperatures; (c) Obtained solar gain factor (g-value) and τ_e as a function of the angle of incidence.

Once q_i is known, it is possible to calculate the total energy transmittance $g(\varphi)$ as a function of the angle of incidence by using the solar direct energy transmission τ_e previously found. Results are presented in Fig. 3 (c). At normal incidence, the total energy transmittance is $g(0)$=18% while the direct energy transmission is τ_e =14%. A high proportion of the solar energy is absorbed in the glass and in the PV module, 4% are then re-emitted inside the building. The PV module being laminated on the exterior glass pane, a large part of the absorbed energy is emitted towards the exterior.

4. Discussion

Precise data on optical and thermal performances of new products are essential to use them as a façade element. Data on single elements can be used to define the best configuration of glazing, for example, on which position to laminate the PV module and if selective coatings are necessary. Depending on the climate, it can be interesting to take benefits of the passive solar gains from the near infrared part of the spectrum. On the contrary, in combination with a solar protection coating, these modules could be used as a shading element is warm climates. Due to their very limited visible light transmittance, these modules cannot be used as a proper window. However, they can be used in combination with windows having high visible transmittance. In addition, the view through these modules is clear but colored. Therefore, attention is needed to preserve good inside lighting conditions for places where people stay a long time such as office rooms. On the other hand, where decorative color is desired, light effects similar to stained glass can be obtained such as in the new Swiss Tech Conference Center in Lausanne [9].

These colored photovoltaic modules are promising because their architectural integration is compatible with existing façade systems. The next step would be to calculate the color rendering index of each module. In addition, it would be interesting to determine the U-value of these modules as a function of the configuration of glazing used.

5. Conclusions

Measurements on these modules indicate a low visible transmittance and therefore they could not be used for a whole façade, however, they can be combined with clear glass for visibility where it is needed and modules laminated in the same shape of double glazing. The modules can be used as any double glazing. In highly glazed building, a part of the façade could become a photovoltaic façade and provide a fraction of the energy demand while providing colorful options to enhance the aesthetic of the building.

Acknowledgements

References

[1] O'Regan B, Grätzel M. A low-cost, high-efficiency solar cell based on dye-sensitized colloidal TiO2 films. Nature. 24 oct 1991;353(6346):737‑40.

[2] Hinsch A, Brandt H, Veurman W, Hemming S, Nittel M, Würfel U, et al. Dye solar modules for facade applications: Recent results from project ColorSol. Solar Energy Materials and Solar Cells. juin 2009;93(6-7):820‑4.

[3] Chen F, Wittkopf SK, Khai Ng P, Du H. Solar heat gain coefficient measurement of semi-transparent photovoltaic modules with indoor calorimetric hot box and solar simulator. Energy and Buildings. oct 2012;53:74‑84.

[4] Yoon S, Tak S, Kim J, Jun Y, Kang K, Park J. Application of transparent dye-sensitized solar cells to building integrated photovoltaic systems. Building and Environment. oct 2011;46(10):1899‑904.

[5] Rothenberger G, Comte P, Grätzel M. A contribution to the optical design of dye-sensitized nanocrystalline solar cells. Solar Energy Materials and Solar Cells. juill 1999;58(3):321‑36.

[6] Steiner R., Oelhafen P., Reber G., Romanyuk A. Experimental determination of spectral and angular dependent optical properties of insulating glasses. CISBAT 2005 Proceedings.

[7] NF EN 410, Glass in building, Determination of luminous and solar characteristics of glazing. 2011. AFNOR

[8] Reber G., Steiner R., Oelhafen P., Romanyuk A. Angular dependent solar gain for insulating glasses from optical and thermal data. CISBAT 2005 Proceedings.

[9] Barraud E. Stained Glass Solar Windows for the Swiss Tech Convention Center. CHIMIA International Journal for Chemistry. 27 mars 2013;67(3):181-2.

References

« La fonction essentielle d'une bibliothèque est de favoriser la découverte de livres dont le lecteur ne soupçonnait pas l'existence et qui s'avèrent d'une importance capitale pour lui. »

Kant et l'Ornithorynque, Umberto Eco

Abe, T., Fukuda, H., Iriyama, Y., Ogumi, Z., 2004. Solvated Li-Ion Transfer at Interface Between Graphite and Electrolyte. Journal of The Electrochemical Society 151, A1120. https://doi.org/10.1149/1.1763141

Agilent "Time Domain Analysis Using a Network Analyzer", Application Note 1287-12, 2007, Literature Number 5989-5723EN

Agrawal, R.C., Pandey, G.P., 2008. Solid polymer electrolytes: materials designing and all-solid-state battery applications: an overview. Journal of Physics D: Applied Physics 41, 223001. https://doi.org/10.1088/0022-3727/41/22/223001

Anders, A., 2010. A structure zone diagram including plasma-based deposition and ion etching. Thin Solid Films 518, 4087–4090. https://doi.org/10.1016/j.tsf.2009.10.145

Arbab, M., 1997. Sputter-Deposited Low-Emissivity Coatings on Glass. MRS Bulletin 22, 27–35. https://doi.org/10.1557/S0883769400033972

Arrhenius, S., 1889. Über die Dissociationswärme und den Einfluss der Temperatur auf den Dissociationsgrad der Elektrolyte. Zeitschrift für Physikalische Chemie 4U. https://doi.org/10.1515/zpch-1889-0408

Ashrit, P., 2001. Dry lithiation study of nanocrystalline, polycrystalline and amorphous tungsten trioxide thin-films. Thin Solid Films 385, 81–88. https://doi.org/10.1016/S0040-6090(00)01895-2

Ashrit, P., Benaissa, K., Bader, G., Girouard, F., Truong, V., 1993. Lithiation studies on some transition metal oxides for an all-solid thin film electrochromic system. Solid State Ionics 59, 47–57. https://doi.org/10.1016/0167-2738(93)90230-Z

Asp, A., Sydorov, Y., Valkama, M., Niemela, J., 2012. Radio signal propagation and attenuation measurements for modern residential buildings. IEEE, pp. 580–584. https://doi.org/10.1109/GLOCOMW.2012.6477638

Augustin Louis Cauchy, 1836 « Sur la dispersion de la lumière », Bulletin des sciences mathématiques, vol. 14, no 9.

Aukkaravittayapun, S., Wongtida, N., Kasecwatin, T., Charojrochkul, S., Unnanon, K., Chindaudom, P., 2006. Large scale F-doped SnO2 coating on glass by spray pyrolysis. Thin Solid Films 496, 117–120. https://doi.org/10.1016/j.tsf.2005.08.259

Avendeño, E. D., 2004. Electrochromism in Nickel-based Oxides - Coloration mechanisms and optimization of sputter-deposited thin films. Uppsala Universitet. https://uu.diva-portal.org/smash/get/diva2:164817/FULLTEXT01

Bard A., Faulkner L., 2001. Electrochemical methods : fundamentals and applications, 2nd ed. Wiley, New York.

Barnes, T.M., Reese, M.O., Bergeson, J.D., Larsen, B.A., Blackburn, J.L., Beard, M.C., Bult, J., van de Lagemaat, J., 2012. Comparing the Fundamental Physics and Device Performance of Transparent, Conductive Nanostructured Networks with Conventional Transparent Conducting Oxides. Advanced Energy Materials 2, 353–360. https://doi.org/10.1002/aenm.201100608

Bates, J., 1992. Electrical properties of amorphous lithium electrolyte thin films. Solid State Ionics 53–56, 647–654. https://doi.org/10.1016/0167-2738(92)90442-R

Belkind A. and Scholl R., "Single-Magnetron Approach Reactive Sputtering of Dielectrics",

Berggren, L., Jonsson, J.C., Niklasson, G.A., 2007. Optical absorption in lithiated tungsten oxide thin films: Experiment and theory. Journal of Applied Physics 102, 083538. https://doi.org/10.1063/1.2800838

Berning, P.H., Turner, A.F., 1957. Induced Transmission in Absorbing Films Applied to Band Pass Filter Design. Journal of the Optical Society of America 47, 230. https://doi.org/10.1364/JOSA.47.000230

Bessière, A., Badot, J.-C., Certiat, M.-C., Livage, J., Lucas, V., Baffier, N., 2001. Sol–gel deposition of electrochromic WO3 thin film on flexible ITO/PET substrate. Electrochimica Acta 46, 2251–2256. https://doi.org/10.1016/S0013-4686(01)00383-8

Beydaghyan, G., Bader, G., Ashrit, P.V., 2008. Electrochromic and morphological investigation of dry-lithiated nanostructured tungsten trioxide thin films. Thin Solid Films 516, 1646–1650. https://doi.org/10.1016/j.tsf.2007.05.006

Biesinger, M.C., Lau, L.W.M., Gerson, A.R., Smart, R.S.C., 2010. Resolving surface chemical states in XPS analysis of first row transition metals, oxides and hydroxides: Sc, Ti, V, Cu and Zn. Applied Surface Science 257, 887–898. https://doi.org/10.1016/j.apsusc.2010.07.086

Biesinger, M.C., Payne, B.P., Lau, L.W.M., Gerson, A., Smart, R.S.C., 2009. X-ray photoelectron spectroscopic chemical state quantification of mixed nickel metal, oxide and hydroxide systems. Surface and Interface Analysis 41, 324–332. https://doi.org/10.1002/sia.3026

Bohnke, O., 2008. The fast lithium-ion conducting oxides Li3xLa2/3−xTiO3 from fundamentals to application. Solid State Ionics 179, 9–15. https://doi.org/10.1016/j.ssi.2007.12.022

Bonaccorso, F., Sun, Z., Hasan, T., Ferrari, A.C., 2010. Graphene photonics and optoelectronics. Nature Photonics 4, 611–622. https://doi.org/10.1038/nphoton.2010.186

Bondarenko, N., Eriksson, O., Skorodumova, N.V., 2015. Polaron mobility in oxygen-deficient and lithium-doped tungsten trioxide. Physical Review B 92. https://doi.org/10.1103/PhysRevB.92.165119

Bouvard O., Lanini M., Burnier L., Witte R., Cuttat B., Salvadè A., Schüler A. 2017a. Structured transparent low emissivity coatings with high microwave transmission. Applied Physics A. 2017 Jan;123(1). Available from: http://link.springer.com/10.1007/s00339-016-0701-8

Bouvard, O., Burnier, L., Oelhafen, P., Tonin, A., Wüst, P., Sidler, F., Zweifel, G., Schüler, A., 2018. Solar heat gains through train windows: a non-negligible contribution to the energy balance. Energy Efficiency. https://doi.org/10.1007/s12053-018-9643-7

Bouvard, O., Krammer, A. & Schüler, A. In situ core-level and valence-band photoelectron spectroscopy of reactively sputtered tungsten oxide films. Surface and Interface Analysis (2016). https://doi.org/10.1002/sia.5927

Bouvard, O., Krammer, A., Schüler, A., 2016. In situ core-level and valence-band photoelectron spectroscopy of reactively sputtered tungsten oxide films: In situ XPS and UPS study of reactively sputtered tungsten oxide films. Surface and Interface Analysis. https://doi.org/10.1002/sia.5927

Bouvard, O., Lanini, M., Burnier, L., Witte, R., Cuttat, B., Salvadè, A., Schüler, A., 2017a. Structured transparent low emissivity coatings with high microwave transmission. Applied Physics A 123. https://doi.org/10.1007/s00339-016-0701-8

Bouvard, O., Lanini, M., Burnier, L., Witte, R., Cuttat, B., Salvadè, A., Schüler, A., 2017b. Mobile communication through insulating windows: a new type of low emissivity coating. Energy Procedia 122, 781–786. https://doi.org/10.1016/j.egypro.2017.07.396

Bouvard, O.; González Lazo, M. A.; Krammer, A.; Schüler, A. 2015. In situ photoelectron spectroscopy: a powerful tool to develop electrochromic materials. CISBAT 2015 Proceedings, EPFL 2015

Bouvard, O.; Krammer, A.; Schüler, A. 2015. In situ core-level and valence-band photoelectron spectroscopy of reactively sputtered tungsten oxide films. ECASIA 2015 Proceedings.

Brewer, S.H., Franzen, S., 2002. Optical properties of indium tin oxide and fluorine-doped tin oxide surfaces: correlation of reflectivity, skin depth, and plasmon frequency with conductivity. Journal of Alloys and Compounds 338, 73–79. https://doi.org/10.1016/S0925-8388(02)00217-7

Bringans, R.D., Höchst, H., Shanks, H.R., 1981. Defect states in W O 3 studied with photoelectron spectroscopy. Physical Review B 24, 3481–3489. https://doi.org/10.1103/PhysRevB.24.3481

Broclawik, E., Góra, A., Liguzinski, P., Petelenz, P., Slawik, M., 2005. Quantum chemical modelling of the process of lithium insertion into WO3 films. Catalysis Today 101, 155–162. https://doi.org/10.1016/j.cattod.2005.01.013

Broclawik, E., Góra, A., Liguzinski, P., Petelenz, P., Witek, H.A., 2006. Quantum chemical modeling of electrochromism of tungsten oxide films. The Journal of Chemical Physics 124, 054709. https://doi.org/10.1063/1.2150824

Bruggeman, D.A.G., 1935. Berechnung verschiedener physikalischer Konstanten von heterogenen Substanzen. I. Dielektrizitätskonstanten und Leitfähigkeiten der Mischkörper aus isotropen Substanzen. Annalen der Physik 416, 636–664. https://doi.org/10.1002/andp.19354160705

Burnier, L., Lanini, M., Bouvard, O., Scanferla, D., Varathan, A., Genoud, C., Marguerit, A., Cuttat, B., Dury, N., Witte, R., Salvadè, A., Schüler, A., 2017. Energy saving glazing with a wide band-pass FSS allowing mobile communication: Upscaling and characterization. IET Microwaves, Antennas & Propagation. https://doi.org/10.1049/iet-map.2016.0685

Bussolotti, F., Lozzi, L., Passacantando, M., La Rosa, S., Santucci, S., Ottaviano, L., 2003. Surface electronic properties of polycrystalline WO3 thin films: a study by core level and valence band photoemission. Surface Science 538, 113–123. https://doi.org/10.1016/S0039-6028(03)00696-4

Byker, H.J., 2015. Solution-Phase Electrochromic Devices and Systems, in: Mortimer, R.J., Rosseinsky, D.R., Monk, P.M.S. (Eds.), Electrochromic Materials and Devices. Wiley-VCH Verlag GmbH & Co. KGaA, Weinheim, Germany, pp. 399–418. https://doi.org/10.1002/9783527679850.ch14

Cao, W., Li, J., Chen, H., Xue, J., 2014. Transparent electrodes for organic optoelectronic devices: a review. Journal of Photonics for Energy 4, 040990. https://doi.org/10.1117/1.JPE.4.040990

Casini, M., 2018. Active dynamic windows for buildings: A review. Renewable Energy 119, 923–934. https://doi.org/10.1016/j.renene.2017.12.049

CasaXPS, 2011. Uncertainty Estimates in XPS. accessible from: www.casaxps.com/ help_manual/manual_updates/Basics_Quantification_of_XPS_Spectra.pdf

Chowdari, B.V.R., Tan, K.L., Chia, W.T., 1992. Raman and X-ray photoelectron spectroscopic studies of lithium phosphotungstate glasses. Solid State Ionics 53–56, 1172–1178. https://doi.org/10.1016/0167-2738(92)90308-C

Cohen, M.L., 2012. Electronic structure and optical properties of semiconductors. Springer, ISBN-13: 978-3-642-97082-5.

Corà, F., Stachiotti, M.G., Catlow, C.R.A., Rodriguez, C.O., 1997. Transition Metal Oxide Chemistry: Electronic Structure Study of WO 3 , ReO 3 , and NaWO 3. The Journal of Physical Chemistry B 101, 3945–3952. https://doi.org/10.1021/jp963724z

Costa, F.; Monorchio, A.; Manara, "An Overview of Equivalent Circuit Modeling Techniques of Frequency Selective Surfaces and Metasurfaces", ACES JOURNAL, Vol. 29, No. 12, Dec. 2014

Costa, F.; Monorchio, A.; Manara, G.; "Analysis and Design of Ultra Thin Electromagnetic Absorbers Comprising Resistively Loaded High Impedance Surfaces," IEEE Transactions on Antennas and Propagation, vol.58, no.5, pp.1551-1558, May 2010.

David, C., Tinkham, B.P., Prunici, P., Panckow, A., 2017. Highly conductive and transparent ITO films deposited at low temperatures by pulsed DC magnetron sputtering from ceramic and metallic rotary targets. Surface and Coatings Technology 314, 113–117. https://doi.org/10.1016/j.surfcoat.2016.09.022

de Wijs, G.A., de Groot, R.A., 1999. Structure and electronic properties of amorphous WO3. Physical Review B 60, 16463–16474. https://doi.org/10.1103/PhysRevB.60.16463

Deb, S.K., 1973. Optical and photoelectric properties and colour centres in thin films of tungsten oxide. Philosophical Magazine 27, 801–822. https://doi.org/10.1080/14786437308227562

Devreese, J.T., 1996. Polarons, in: WILEY-VCH Verlag GmbH & Co KGaA (Ed.), Digital Encyclopedia of Applied Physics. WILEY-VCH Verlag GmbH & Co KGaA, Weinheim, Germany. Vol. 14, pp. 383 – 409.

Dong, D., Wang, W., Barnabé, A., Presmanes, L., Rougier, A., Dong, G., Zhang, F., Yu, H., He, Y., Diao, X., 2018. Enhanced electrochromism in short wavelengths for NiO:(Li, Mg) films in full inorganic device ITO/NiO:(Li, Mg)/Ta2O5/WO3/ITO. Electrochimica Acta 263, 277–285. https://doi.org/10.1016/j.electacta.2018.01.049

Dowell, D.H., Schmerge, J.F., 2009. Quantum efficiency and thermal emittance of metal photocathodes. Physical Review Special Topics - Accelerators and Beams 12. https://doi.org/10.1103/PhysRevSTAB.12.074201

Du, Y., Zhang, K. H. L., Varga, T. & Chambers, S. A. 2014. Appl Phys Lett. 105, 051606.

Du, Y.A., Holzwarth, N.A.W., 2010. First-principles study of LiPON and related solid electrolytes. Physical Review B 81. https://doi.org/10.1103/PhysRevB.81.184106

Duan, Y., Sorescu, D.C., 2009. Density functional theory studies of the structural, electronic, and phonon properties of Li2O and Li2CO3 : Application to CO2 capture reaction. Physical Review B 79. https://doi.org/10.1103/PhysRevB.79.014301

EC-Lab® software, 2016. Bio-Logic - Science Instruments, Seyssinet-Pariset, France.

Elliott S. R., 1990. Physics of Amorphous Materials, 2nd ed., Longman, Harlow, UK.

Ellmer, K., 2012. Past achievements and future challenges in the development of optically transparent electrodes. Nature Photonics 6, 809–817. https://doi.org/10.1038/nphoton.2012.282

EN 410:2011. Glass in building, Determination of luminous and solar characteristics of glazing. 2011. ISSN 0335-3931, AFNOR.

Fan, J.C.C., Bachner, F.J., Foley, G.H., Zavracky, P.M., 1974. Transparent heat-mirror films of TiO 2 /Ag/TiO 2 for solar energy collection and radiation insulation. Applied Physics Letters 25, 693–695. https://doi.org/10.1063/1.1655364

Fergus, J.W., 2010. Ceramic and polymeric solid electrolytes for lithium-ion batteries. Journal of Power Sources 195, 4554–4569. https://doi.org/10.1016/j.jpowsour.2010.01.076

Fisher, A. C. 2010 "Electrochemistry Teaching Notes" in the website of the Department of Chemical Engineering and Biotechnology, University of Cambridge. http://www.ceb.cam.ac.uk/research/groups/rg-eme/teaching-notes

Fleutot, B., Pecquenard, B., Martinez, H., Letellier, M., Levasseur, A., 2011. Investigation of the local structure of LiPON thin films to better understand the role of nitrogen on their performance. Solid State Ionics 186, 29–36. https://doi.org/10.1016/j.ssi.2011.01.006

Fourquet, J.L., Duroy, H., Crosnier-Lopez, M.P., 1996. Structural and Microstructural Studies of the Series La2/3−xLi3x□1/3−2xTiO3. Journal of Solid State Chemistry 127, 283–294. https://doi.org/10.1006/jssc.1996.0385

Fraser, D.B., Cook, H.D., 1972. Highly Conductive, Transparent Films of Sputtered In2−xSnxO3−y. Journal of The Electrochemical Society 119, 1368. https://doi.org/10.1149/1.2403999

Frenning, G., Nilsson, M., Westlinder, J., Niklasson, G.., Mattsson, M.S., 2001. Dielectric and Li transport properties of electron conducting and non-conducting sputtered amorphous Ta2O5 films. Electrochimica Acta 46, 2041–2046. https://doi.org/10.1016/S0013-4686(01)00412-1

Friedrich W.; Knipping P.; von Laue.,1912. "Interferenz-Erscheinungen bei Röntgenstrahlen". Sitzungsberichte der Mathematisch-Physikalischen Classe der Königlich-Bayerischen Akademie der Wissenschaften zu München. 1912: 303.

Funke, K., Banhatti, R.D., Brückner, S., Cramer, C., Krieger, C., Mandanici, A., Martiny, C., Ross, I., 2002. Ionic motion in materials with disordered structures: conductivity spectra and the concept of mismatch and relaxation. Physical Chemistry Chemical Physics 4, 3155–3167. https://doi.org/10.1039/b200122p

Garcia-Lastra, J.M., Bass, J.D., Thygesen, K.S., 2011. Communication: Strong excitonic and vibronic effects determine the optical properties of Li 2 O 2. The Journal of Chemical Physics 135, 121101. https://doi.org/10.1063/1.3645544

Ghaffarzadeh, K., Das, R., 2018. Transparent Conductive Films and Materials 2018-2028: Forecasts, Technologies, Players. IDTechEx.

Gibson, Walton C. , 2008, The Method of Moments in Electromagnetics, Boca Raton, FL: Chapman & Hall/CRC Press, pp. xv+272, ISBN 978-1-4200-6145-1, MR 2503144, Zbl 1175.78002.

Gillaspie, D., Norman, A., Tracy, C.E., Pitts, J.R., Lee, S.-H., Dillon, A., 2010. Nanocomposite Counter Electrode Materials for Electrochromic Windows. Journal of The Electrochemical Society 157, H328. https://doi.org/10.1149/1.3276779

Gillham, E.J., Preston, J.S., Williams, B.E., 1955. CXIX. A study of transparent, highly conducting gold films. The London, Edinburgh, and Dublin Philosophical Magazine and Journal of Science 46, 1051–1068. https://doi.org/10.1080/14786441008521119

Ginley, D.S., Hosono, H., Paine, D.C. (Eds.), 2010. Handbook of transparent conductors. Springer, New York.

Gläser, H.J., 2000. Large area glass coating, 1. ed. Von Ardenne Anlagentechnik, Dresden.

Gläser, H.J., 2008. History of the development and industrial production of low thermal emissivity coatings for high heat insulating glass units. Applied Optics 47, C193. https://doi.org/10.1364/AO.47.00C193

Goodenough, J.B., 1960. Direct Cation- -Cation Interactions in Several Oxides. Physical Review 117, 1442–1451. https://doi.org/10.1103/PhysRev.117.1442

Goodenough, J.B., 1971. The two components of the crystallographic transition in VO2. Journal of Solid State Chemistry 3, 490–500. https://doi.org/10.1016/0022-4596(71)90091-0

Granqvist, C. G. 2002. Handbook of inorganic electrochromic materials. Elsevier.

Granqvist, C.G., 1995. Introduction, in: Handbook of Inorganic Electrochromic Materials. Elsevier, pp. 1–15. https://doi.org/10.1016/B978-044489930-9/50001-5

Granqvist, C.-G., 2006. Electrochromic materials: Out of a niche. Nature Materials 5, 89–90. https://doi.org/10.1038/nmat1577

Granqvist, C.G., 2007. Transparent conductors as solar energy materials: A panoramic review. Solar Energy Materials and Solar Cells 91, 1529–1598. https://doi.org/10.1016/j.solmat.2007.04.031

Granqvist, C.G., 2012. Preparation of thin films and nanostructured coatings for clean tech applications: A primer. Solar Energy Materials and Solar Cells 99, 166–175. https://doi.org/10.1016/j.solmat.2011.11.048

Granqvist, C.G., 2014. Electrochromics for smart windows: Oxide-based thin films and devices. Thin Solid Films 564, 1–38. https://doi.org/10.1016/j.tsf.2014.02.002

Granqvist, C.-G., 2015. Electrochromic Metal Oxides: An Introduction to Materials and Devices, in: Mortimer, R.J., Rosseinsky, D.R., Monk, P.M.S. (Eds.), Electrochromic Materials and Devices. Wiley-VCH Verlag GmbH & Co. KGaA, Weinheim, Germany, pp. 1–40. https://doi.org/10.1002/9783527679850.ch1

Green, et al. Structure and optical properties of electrochromic tungsten-containing nickel oxide films. Solar Energy Materials and Solar Cells 126, 2014.

Grilli, M.L., Menchini, F., Dikonimos, T., Nunziante, P., Pilloni, L., Yilmaz, M., Piegari, A., Mittiga, A., 2016. Effect of growth parameters on the properties of RF-sputtered highly conductive and transparent p-type NiO x films. Semiconductor Science and Technology 31, 055016. https://doi.org/10.1088/0268-1242/31/5/055016

Grosse, P., Hertling, R., Müggenburg, T., 1997. Design of low emissivity systems based on a three-layer coating. Journal of Non-Crystalline Solids 218, 38–43. https://doi.org/10.1016/S0022-3093(97)00130-0

Grosvenor, C.A.; Novotny, D.; Johnk, R.; Canales, N.; Veneman, J., 2002 "Shielding effectiveness measurements using the direct illumination technique," in Electromagnetic Compatibility. IEEE International Symposium on , vol.1, no., pp.389-394 vol.1, 19-23. doi: 10.1109/ISEMC.2002.1032510

Habasaki J., León C., Ngai K.L., 2016. Dynamics of glassy, crystalline and liquid ionic conductors. Springer Science+Business Media, New York, NY.

Hales, T.C., 2001. The Honeycomb Conjecture. Discrete & Computational Geometry 25, 1–22. https://doi.org/10.1007/s004540010071

Hamon, Y., Douard, A., Sabary, F., Marcel, C., Vinatier, P., Pecquenard, B., Levasseur, A., 2006. Influence of sputtering conditions on ionic conductivity of LiPON thin films. Solid State Ionics 177, 257–261. https://doi.org/10.1016/j.ssi.2005.10.021

Han, B., Pei, K., Huang, Y., Zhang, X., Rong, Q., Lin, Q., Guo, Y., Sun, T., Guo, C., Carnahan, D., Giersig, M., Wang, Y., Gao, J., Ren, Z., Kempa, K., 2014. Uniform Self-Forming Metallic Network as a High-Performance Transparent Conductive Electrode. Advanced Materials 26, 873–877. https://doi.org/10.1002/adma.201302950

Hashimoto, S., 1991. Lifetime of Electrochromism of Amorphous WO[sub 3]-TiO[sub 2] Thin Films. Journal of The Electrochemical Society 138, 2403. https://doi.org/10.1149/1.2085985

He, Y., Zhang, F., Zhang, Q., Dong, G., Zhong, X., Diao, X., 2018. High capacity and performance lithium based electrochromic device via amorphous tantalum oxide protective layer. Electrochimica Acta 280, 163–170. https://doi.org/10.1016/j.electacta.2018.05.123

Ho, S.F., Contarini, S., Rabalais, J.W., 1987. Ion-beam-induced chemical changes in the oxyanions (Moyn-) and oxides (Mox) where M = chromium, molybdenum, tungsten, vanadium, niobium and tantalum. The Journal of Physical Chemistry 91, 4779–4788. https://doi.org/10.1021/j100302a027

Höchst, H., Bringans, R.D., 1982. Electronic structure of evaporated and annealed tungsten oxide films studied with UPS. Applications of Surface Science 11–12, 768–773. https://doi.org/10.1016/0378-5963(82)90119-2

Hoenigman, J.R., Keil, R.G., 1984. An XPS study of the adsorption of oxygen and water vapor on clean lithium films. Applications of Surface Science 18, 207–222. https://doi.org/10.1016/0378-5963(84)90045-X

Holland, L., Siddall, G., 1953. the properties of some reactively sputtered metal oxide films. Vacuum 3, 375–391. https://doi.org/10.1016/0042-207X(53)90411-4

Holland, L., Siddall, G., 1958. Heat-reflecting windows using gold and bismuth oxide films. British Journal of Applied Physics 9, 359–361. https://doi.org/10.1088/0508-3443/9/9/304

Huizenga C., Arasteh D., Curcija C., Klems J., Kohler C., Mitchell R., Yu T., Zhu L., Czarnecki S., Vidanovic S., Zelenay K., 2015. Berkeley Lab Window software v7.4.6.0. University of California.

Hwang, M.-S., Lee, H.J., Jeong, H.S., Seo, Y.W., Kwon, S.J., 2003. The effect of pulsed magnetron sputtering on the properties of indium tin oxide thin films. Surface and Coatings Technology 171, 29–33. https://doi.org/10.1016/S0257-8972(03)00231-7

IEA, 2013. International Energy Agency, Transition to Sustainable Buildings Accessed from: https://webstore.iea.org/transition-to-sustainable-buildings

IEA, 2017. International Energy Agency, Energy technology perspectives. Accessed from: https://www.iea.org/buildings/.

IEEE Recommended Practice for Measurement of Shielding Effectiveness of High-Performance Shielding Enclosures," in IEEE Std 299-1969 , vol., no., pp.0_1-, 1969. doi: 10.1109/IEEESTD.1969.120578

International Union of Pure and Applied Chemistry (2005). Nomenclature of Inorganic Chemistry (IUPAC Recommendations 2005). Cambridge (UK): RSC–IUPAC. ISBN 0-85404-438-8.

Ishikawa, R., Higashia T., Fisher C., Sasano S., Kimura T., Ikuhara Y. H., Shibata N., Ikuhara Y., 2018. Grain Boundary Resistance at (La,Li)TiO3 Grain Boundary. Presented at the 19th International Meeting on Lithium Batteries, Kyoto. www.imlb2018.org/pdf/a11_2552727.pdf

ITU-RM Report 2376-0. 2015. 'Technical feasibility of IMT in bands above 6 GHz'.

Jelle, B. P. et al. Fenestration of today and tomorrow: A state-of-the-art review and future research opportunities. Solar Energy Materials and Solar Cells 96, 1–28, 2012.

Kamaya, et al. A lithium superionic conductor. Nature Materials 10, 2011.

Kang, M.-G., Guo, L.J., 2007. Nanoimprinted Semitransparent Metal Electrodes and Their Application in Organic Light-Emitting Diodes. Advanced Materials 19, 1391–1396. https://doi.org/10.1002/adma.200700134

Kaplan, T., Gray, L.J., Liu, S.H., 1987. Self-affine fractal model for a metal-electrolyte interface. Physical Review B 35, 5379–5381. https://doi.org/10.1103/PhysRevB.35.5379

Katayama, M., 1999. TFT-LCD technology. Thin Solid Films 341, 140–147. https://doi.org/10.1016/S0040-6090(98)01519-3

Kelly P., Arnell R. Magnetron sputtering: a review of recent developments and applications. Vacuum. 2000 Mar;56(3):159–72. https://doi.org/10.1016/S0042-207X(99)00189-X

Kiani G. I., Karlsson A., Olsson L.. Glass characterization for designing frequency selective surfaces to improve transmission through energy saving glass windows. CODEN: LUTEDX/(TEAT-7170)/1-7/(2008)

Kiani, G. I., 2009. Passive, active and absorbing frequency selective surfaces for wireless communication applications. PhD Thesis, Macquarie University.

Kiani, G.I., Olsson, L.G., Karlsson, A., Esselle, K.P., 2010. Transmission of infrared and visible wavelengths through energy-saving glass due to etching of frequency-selective surfaces. IET Microwaves, Antennas & Propagation 4, 955. https://doi.org/10.1049/iet-map.2009.0439

Kiani, G.I., Olsson, L.G., Karlsson, A., Esselle, K.P., Nilsson, M., 2011. Cross-Dipole Bandpass Frequency Selective Surface for Energy-Saving Glass Used in Buildings. IEEE Transactions on Antennas and Propagation 59, 520–525.

Kim, H., Gilmore, C.M., Piqué, A., Horwitz, J.S., Mattoussi, H., Murata, H., Kafafi, Z.H., Chrisey, D.B., 1999. Electrical, optical, and structural properties of indium–tin–oxide thin films for organic light-emitting devices. Journal of Applied Physics 86, 6451–6461. https://doi.org/10.1063/1.371708

Kim, Y.H., Sachse, C., Machala, M.L., May, C., Müller-Meskamp, L., Leo, K., 2011. Highly Conductive PEDOT:PSS Electrode with Optimized Solvent and Thermal Post-Treatment for ITO-Free Organic Solar Cells. Advanced Functional Materials 21, 1076–1081. https://doi.org/10.1002/adfm.201002290

Kirchhoff, G., 1860. Ueber das Verhältniss zwischen dem Emissionsvermögen und dem Absorptionsvermögen der Körper für Wärme und Licht. Annalen der Physik und Chemie 185, 275–301. https://doi.org/10.1002/andp.18601850205

Kitao, M., Akram, H., Urabe, K., Yamada, S., 1992. Properties of solid-state electrochromic cells using Ta2O5 as electrolyte. Journal of Electronic Materials 21, 419–422. https://doi.org/10.1007/BF02660405

Knauth, 2009. Inorganic solid Li ion conductors: An overview. Solid State Ionics 180. The author thanks Prof. Alain Levasseur and Dr. Brigitte Pecquenard for their kind permission to use the unpublished figure 1.

Köstlin, H., Jost, R., Lems, W., 1975. Optical and electrical properties of doped In2O3 films. Physica Status Solidi (a) 29, 87–93. https://doi.org/10.1002/pssa.2210290110

Kostro, A.G., 2015. Microstructured glazing for daylighting, glare protection, seasonal thermal control and clear view. EPFL, Lausanne.

Koubli, E., Tsakanikas, S., Leftheriotis, G., Syrrokostas, G., Yianoulis, P., 2015. Optical properties and stability of near-optimum WO3/Ag/WO3 multilayers for electrochromic applications. Solid State Ionics 272, 30–38. https://doi.org/10.1016/j.ssi.2014.12.015

Kovalenko et al, Effect of Deposition Conditions On Microstructure of LIPON Films Obtained by RF Magnetron Sputtering, IEEE XXXIV International Scientific Conference Electronics and Nanotechnology (ELNANO). 2014

Kugler M., 2015. Historic trajectories for building related energy technologies - Lessons for business and policy makers (Master thesis). ETH Zürich.

Kuhlenbeck, H., Odörfer, G., Jaeger, R., Illing, G., Menges, M., Mull, T., Freund, H.-J., Pöhlchen, M., Staemmler, V., Witzel, S., Scharfschwerdt, C., Wennemann, K., Liedtke, T., Neumann, M., 1991. Molecular adsorption on oxide surfaces: Electronic structure and orientation of NiO on NiO(100)/Ni(100) and on NiO(100) as determined from electron spectroscopies and ab initio cluster calculations. Physical Review B 43, 1969–1986. https://doi.org/10.1103/PhysRevB.43.1969

Lampert, C.M., 2004. Chromogenic smart materials. Materials Today 7, 28–35. https://doi.org/10.1016/S1369-7021(04)00123-3

Landau, L.D., 1933. Über die bewegung der elektronen in kristalgitter. Phys. Z. Sowjetunion, 3, pp.644-645.

Lanini, M., 2015. Shielding effectiveness of engraved low-e coated glasses - Measurement and simulation. Final report (Confidential report). SUPSI - TTHF Lab, Manno.

Lasia A., Electrochemical Impedance Spectroscopy and Its Applications, Modern Aspects of Electrochemistry, B. E. Conway, J. Bockris, and R.E. White, Edts., Kluwer Academic/Plenum Publishers, New York, 1999, Vol. 32, p. 143-248.

Laubach, Sonja, Laubach, Stefan, Schmidt, P.C., Ensling, D., Schmid, S., Jaegermann, W., Thißen, A., Nikolowski, K., Ehrenberg, H., 2009. Changes in the crystal and electronic structure of LiCoO2 and LiNiO2 upon Li intercalation and de-intercalation. Physical Chemistry Chemical Physics 11, 3278. https://doi.org/10.1039/b901200a

Layani, M., Kamyshny, A., Magdassi, S., 2014. Transparent conductors composed of nanomaterials. Nanoscale 6, 5581–5591. https://doi.org/10.1039/C4NR00102H

Leftheriotis, G. & Yianoulis, P. in Comprehensive Renewable Energy 313–355. Elsevier, 2012.

Lemarchand, P, 2018. Key enabling technologies for smart and adaptive windows. LESO Lunchtime seminars.

Li, H., Lv, Y., Zhang, X., Wang, X., Liu, X., 2015. High-performance ITO-free electrochromic films based on bifunctional

Li, L., Xue, X., Liu, S., Zhou, H., 2017. Thermally activated ionic conduction and local structure in solid LiPON thin films. Ionics 23, 1451–1459. https://doi.org/10.1007/s11581-016-1963-z

Liikenne-ja viestintäministeriö, 2013. Mobile network reception problems in low energy buildings. Working group report.

Lin, F., Nordlund, D., Weng, T.-C., Sokaras, D., Jones, K.M., Reed, R.B., Gillaspie, D.T., Weir, D.G.J., Moore, R.G., Dillon, A.C., Richards, R.M., Engtrakul, C., 2013. Origin of Electrochromism in High-Performing Nanocomposite Nickel Oxide. ACS Applied Materials & Interfaces 5, 3643–3649. https://doi.org/10.1021/am400105y

Lippens, P., Muehlfeld, U., 2012. Indium Tin Oxide (ITO): Sputter Deposition Processes, in: Chen, J., Cranton, W., Fihn, M. (Eds.), Handbook of Visual Display Technology. Springer Berlin Heidelberg, Berlin, Heidelberg, pp. 779–794. https://doi.org/10.1007/978-3-540-79567-4_54

Liu, L., Henrich, V.E., Ellis, W.P., Shindo, I., 1996. Bulk and surface electronic structure of Li 2 O. Physical Review B 54, 2236–2239. https://doi.org/10.1103/PhysRevB.54.2236

Liu W.-Y., Li C.-L. & Fu Z.-W. Stability of Lithium Phosphorous Oxynitride Thin Films in Humid Air. Acta Phys. -Chim. Sin., 2006, 22(11): 1413-1418. http://www.whxb.pku.edu.cn/10.3866/PKU.WHXB20061121

Lokanc, M., Eggert, R., Redlinger, M., 2015. The Availability of Indium: The Present, Medium Term, and Long Term (Report No. NREL/SR-6A20-62409), NREL.

Mahmoudi, A., Faraoun, H.I., Benabadji, M.K., Abdellaoui, I., Dergal, M., 2016. Structural, electronic and optical properties of Li intercalated on MO3 (M: Mo, W): A first principle investigation. Solid State Communications 229, 37–42. https://doi.org/10.1016/j.ssc.2016.01.001

Maier J., 2004. Physical Chemistry of Ionic Materials, John Wiley and Sons, Ltd, Chichester.

Mansour, D., Bouvard, O., Schüler, A., 2017. Development and characterization of electrochromic oxide and ion conductor deposited by reactive magnetron sputtering. Energy Procedia 122, 787–792. https://doi.org/10.1016/j.egypro.2017.07.397

Manthiram, A., Yu, X., Wang, S., 2017. Lithium battery chemistries enabled by solid-state electrolytes. Nature Reviews Materials 2. https://doi.org/10.1038/natrevmats.2016.103

Matsuda, Y., Kuwata, N., Kawamura, J., 2018. Thin-film lithium batteries with 0.3–30 µm thick LiCoO 2 films fabricated by high-rate pulsed laser deposition. Solid State Ionics 320, 38–44. https://doi.org/10.1016/j.ssi.2018.02.024

Michalski, K.A.; Mosig, J.R., "Multilayered media Green's functions in integral equation formulations," in Antennas and Propagation, IEEE Transactions on , vol.45, no.3, pp.508-519, Mar 1997. doi: 10.1109/8.558666

Mittra, R., Chan C.-H., Cwik T., Techniques for analyzing frequency selective surfaces - A review, IEEE Proceedings, vol. 76, pp. 1593-1615, Dec 1988.

Monk, P., Mortimer, R., Rosseinsky, D., 2007. Electrochromism and Electrochromic Devices. Cambridge University Press, Cambridge. https://doi.org/10.1017/CBO9780511550959

Movchan B.A., Demchishin A.V. 1969. Fiz. Met. Metalloved. (USSR), (Phys. Met. Metallogr.), vol. 28, p. 653

Munk, B. 2003. Finite antenna arrays and FSS. (IEEE Press ; Wiley-Interscience).

Munk, B., 2000. Frequency selective surfaces: theory and design. John Wiley, New York.

Nakamura, T., 2017. Nonstoichiometry and the Origin of Electrochemical Properties of Functional Oxides for Energy Conversion and Storage Technologies. Electrochemistry 85, 552–558. https://doi.org/10.5796/electrochemistry.85.552

Naumkin, A. V., Kraut-Vass A., Gaarenstroom S. W., and Powell C. J., 2012. NIST X-ray Photoelectron Spectroscopy Database, NIST Standard Reference Database 20, Version 4.1. Available from: http://srdata.nist.gov/xps/

NF EN 673. Glass in building, Determination of thermal transmittance (U value) Calculation method, eq. 1-5. 2011. ISSN 0335-39. AFNOR.

Nguyen, C.A., Xiong, S., Ma, J., Lu, X., Lee, P.S., 2011. High ionic conductivity P(VDF-TrFE)/PEO blended polymer electrolytes for solid electrochromic devices. Physical Chemistry Chemical Physics 13, 13319. https://doi.org/10.1039/c0cp01505a

Niklasson, G.A., Berggren, L., Larsson, A.-L., 2004. Electrochromic tungsten oxide: the role of defects. Solar Energy Materials and Solar Cells 84, 315–328. https://doi.org/10.1016/j.solmat.2004.01.045

Niklasson, G.A., Granqvist, C.G., 2007. Electrochromics for smart windows: thin films of tungsten oxide and nickel oxide, and devices based on these. J. Mater. Chem. 17, 127–156. https://doi.org/10.1039/B612174H

Nisula, M., Shindo, Y., Koga, H., Karppinen, M., 2015. Atomic Layer Deposition of Lithium Phosphorus Oxynitride. Chemistry of Materials 27, 6987–6993. https://doi.org/10.1021/acs.chemmater.5b02199

OpenStax, Chemistry. OpenStax CNX. Jun 20, 2016 https://opentextbc.ca/chemistry/wp-content/uploads/sites/150/2016/05/CNX_Chem_06_01_emspectrum.jpg

Oukassi, S., Giroud-Garampon, C., Dubarry, C., Ducros, C., Salot, R., 2016. All inorganic thin film electrochromic device using LiPON as the ion conductor. Solar Energy Materials and Solar Cells 145, 2–7. https://doi.org/10.1016/j.solmat.2015.06.052

Ozer, N., Lampert, C.., 1999. Electrochromic performance of sol-gel deposited WO 3 –V 2 O 5 films. Thin Solid Films 349, 205–211. https://doi.org/10.1016/S0040-6090(99)00144-3

Ozer, N., Lampert, C.M., 1997. Structural and optical properties of sol-gel deposited proton conducting Ta2O5 films. Journal of Sol-Gel Science and Technology 8, 703–709. https://doi.org/10.1007/BF02436926

Pankove, J. I. Optical Processes in Semiconductors Ch 1 (Dover, 1971).

Paolo, D.P., Mario, Z., Carlo, E., 1972. Generation of Alkali Metal Vapors. US3667513 (A).

Pawlak, D.A., Ito, M., Oku, M., Shimamura, K., Fukuda, T., 2002. Interpretation of XPS O (1s) in Mixed Oxides Proved on Mixed Perovskite Crystals. The Journal of Physical Chemistry B 106, 504–507. https://doi.org/10.1021/jp012040a

Pehlivan, İ.B., Marsal, R., Pehlivan, E., Runnerstrom, E.L., Milliron, D.J., Granqvist, C.G., Niklasson, G.A., 2014. Electrochromic devices with polymer electrolytes functionalized by SiO2 and In2O3:Sn nanoparticles: Rapid coloring/bleaching dynamics and strong near-infrared absorption. Solar Energy Materials and Solar Cells 126, 241–247. https://doi.org/10.1016/j.solmat.2013.06.010

Perumal, A., 2016. Web course: Characterization of Materials, National Programme on Technology Enhanced Learning (NPTEL). http://nptel.ac.in/courses/115103030/40

Pham, Q.N., Bohnke, C., Bohnke, O., 2004. Effect of surface treatments on Li0.30Ln0.57TiO3 (Ln=La, Nd) perovskite ceramics: an X-ray photoelectron spectroscopy study. Surface Science 572, 375–384. https://doi.org/10.1016/j.susc.2004.09.012

Philippakis, M., Martel, C., Kemp, D., Clift, M., Massey, S., Appleton, S., Damerell, W., Burton, C., 2004. Application of FSS Structures to Selectively Control the Propagation of signals into and out of buildings (ERA report 2004-0072), Antenna systems. Era technology Ltd, UK.

Rabaâ, H., Hoffmann, R., Cruz Hernández, N., Fernandez Sanz, J., 2001. Theoretical Approach to Ionic Conductivity in PhosphorusOxynitride Compounds. Journal of Solid State Chemistry 161, 73–79. https://doi.org/10.1006/jssc.2001.9269

Rahman, H.; Saha, P.K.; Dowling, J.; Curran, T., 1992 "Shielding effectiveness measurement techniques for various materials used for EMI shielding," in Screening of Connectors, Cables and Enclosures, IEE Colloquium on , vol., no., pp.9/1-9/6,

Ramana, C.V., Baghmar, G., Rubio, E.J., Hernandez, M.J., 2013. Optical Constants of Amorphous, Transparent Titanium-Doped Tungsten Oxide Thin Films. ACS Applied Materials & Interfaces 5, 4659–4666. https://doi.org/10.1021/am4006258

Reber G. , Oelhafen P., Burnier, L., Schüler A., 2005. Angular Dependent Solar Gain for Insulating Glasses from Experimental Optical and Thermal Data. Proc. of CISBAT, EPFL. www.glassdbase.ch/glassdocs/2211-CISBAT2013_Reber.pdf

Robertson, A.D., Martin, S.G., Coats, A., West, A.R., 1995. Phase diagrams and crystal chemistry in the Li + ion conducting perovskites, Li 0.5 − 3x RE 0.5 +x TiO 3 : Re La, Nd. J. Mater. Chem. 5, 1405–1412. https://doi.org/10.1039/JM9950501405

Rodíguez Presa, M.J., Tucceri, R.I., Florit, M.I., Posadas, D., 2001. Constant phase element behavior in the poly(o-toluidine) impedance response. Journal of Electroanalytical Chemistry 502, 82–90. https://doi.org/10.1016/S0022-0728(00)00512-X

Romanyuk, A., Oelhafen, P., 2006. Evidence of different oxygen states during thermal coloration of tungsten oxide. Solar Energy Materials and Solar Cells 90, 1945–1950. https://doi.org/10.1016/j.solmat.2006.01.001

Rossnagel S. M. Sputter Deposition. In: Sproul WD, Legg KO, editors. Opportunities for Innovation: Advanced Surface Engineering. Switzerland: Technomic Publishing Co., 1995.

SAES Getters S.p.A, Italy. https://www.saesgetters.com/products-functions/products/dispensers/alkali-metals-dispensers

Scarminio, J., Urbano, A., Gardes, B., 1999. The Beer-Lambert law for electrochromic tungsten oxide thin films. Materials Chemistry and Physics 61, 143–146. https://doi.org/10.1016/S0254-0584(99)00132-7

SCCER FEEB&D Innovation Roadmap, March 2015. Accessed from http://www.sccer-feebd.ch/wp-content/uploads/SCCER-FEEBD-Innovation-Roadmap-March-20152.pdf

Schaefer, C., Bräuer, G., Szczyrbowski, J., 1997. Low emissivity coatings on architectural glass. Surface and Coatings Technology 93, 37–45. https://doi.org/10.1016/S0257-8972(97)00034-0

Schirmer, O.F., 1977. Dependence of WO3 Electrochromic Absorption on Crystallinity. Journal of The Electrochemical Society. 124, 749. https://doi.org/10.1149/1.2133399

Schüler, A., Ellenberger, C., Oelhafen, P., Haug, C., Brenn, R., 2000. Optical properties of titanium containing amorphous hydrogenated carbon films (a-C:H/Ti). Journal of Applied Physics 87, 4285–4292. https://doi.org/10.1063/1.373067

Schwöbel, A., Jaegermann, W., Hausbrand, R., 2016. Interfacial energy level alignment and energy level diagrams for all-solid Li-ion cells: Impact of Li-ion transfer and double layer formation. Solid State Ionics. https://doi.org/10.1016/j.ssi.2015.12.029

Scofield, J.H., 1976. Hartree-Slater subshell photoionization cross-sections at 1254 and 1487 eV. Journal of Electron Spectroscopy and Related Phenomena 8, 129–137. https://doi.org/10.1016/0368-2048(76)80015-1

Seah, M.P., Dench, W.A., 1979. Quantitative electron spectroscopy of surfaces: A standard data base for electron inelastic mean free paths in solids. Surface and Interface Analysis 1, 2–11. https://doi.org/10.1002/sia.740010103

Seeger, K. 1991. Semiconductor Physics Ch 4. Springer.

Senevirathne, K., Day, C.S., Gross, M.D., Lachgar, A., Holzwarth, N.A.W., 2013. A new crystalline LiPON electrolyte: Synthesis, properties, and electronic structure. Solid State Ionics 233, 95–101. https://doi.org/10.1016/j.ssi.2012.12.013

Shim, H.-S., Ahn, H.-J., Kim, Y.-S., Sung, Y.-E., Kim, W.B., 2006. Ta2O5-Incorporated WO3 Nanocomposite Film for Improved Electrochromic Performance in an Acidic Condition. Journal of Nanoscience and Nanotechnology 6, 3572–3576. https://doi.org/10.1166/jnn.2006.059

Shirley, D.A., 1972. High-Resolution X-Ray Photoemission Spectrum of the Valence Bands of Gold. Physical Review B 5, 4709–4714. https://doi.org/10.1103/PhysRevB.5.4709

Shoar Abouzari, M.R., Berkemeier, F., Schmitz, G., Wilmer, D., 2009. On the physical interpretation of constant phase elements. Solid State Ionics 180, 922–927. https://doi.org/10.1016/j.ssi.2009.04.002

Shvets, V.A., Aliev, V.S., Gritsenko, D.V., Shaimeev, S.S., Fedosenko, E.V., Rykhlitski, S.V., Atuchin, V.V., Gritsenko, V.A., Tapilin, V.M., Wong, H., 2008. Electronic structure and charge transport properties of amorphous Ta2O5 films. Journal of Non-Crystalline Solids 354, 3025–3033. https://doi.org/10.1016/j.jnoncrysol.2007.12.013

Smart R., McIntyre S., Bancroft M., Bello I., 2004. X-ray photoelectron spectroscopy. Available from: http://mmrc.caltech.edu/SS_XPS/XPS_PPT/XPS_Slides.pdf

Song, J., Jacke, S., Cherkashinin, G., Schmid, S., Dong, Q., Hausbrand, R., Jaegermann, W., 2011. Valence Band Off-sets of LiPON∕LiCoO2 Hetero-Interfaces Determined by X-ray Photoelectron Spectroscopy. Electrochemical and Solid-State Letters 14, A189. https://doi.org/10.1149/2.006112esl

Song, J.Y., Wang, Y.Y., Wan, C.C., 2000. Conductivity Study of Porous Plasticized Polymer Electrolytes Based on Poly(vinylidene fluoride) A Comparison with Polypropylene Separators. Journal of The Electrochemical Society 147, 3219. https://doi.org/10.1149/1.1393886

Sorar, I., Pehlivan, E., Niklasson, G.A., Granqvist, C.G., 2013. Electrochromism of DC magnetron sputtered TiO2 thin films: Role of deposition parameters. Solar Energy Materials and Solar Cells 115, 172–180. https://doi.org/10.1016/j.solmat.2013.03.035

Springer, S., 2004. Free carriers in nanocrystalline titanium dioxide thin films. EPFL Thesis - Infoscience. Available from: https://infoscience.epfl.ch/record/33409/files/EPFL_TH2934.pdf

stacked WO3/Ag/WO3 structures. Solar Energy Materials and Solar Cells 136, 86–91. https://doi.org/10.1016/j.solmat.2015.01.002

Steiner R., P. Oelhafen, G. Reber, A. Romanyuk, 2005. Experimental determination of spectral and angular dependent optical properties of insulating glasses. Proc. of CISBAT, EPFL. www.glassdbase.ch/glassdocs/2121-CISBAT2005_Oelhafen1Logo.pdf

Steinrück, H.-G., Cao, C., Tsao, Y., Takacs, C.J., Konovalov, O., Vatamanu, J., Borodin, O., Toney, M.F., 2018. The nanoscale structure of the electrolyte–metal oxide interface. Energy & Environmental Science 11, 594–602. https://doi.org/10.1039/C7EE02724A

Stolze, M., Camin, B., Galbert, F., Reinholz, U., Thomas, L.., 2002. Nature of substoichiometry in reactively DC-sputtered tungsten oxide thin films and its effect on the maximum obtainable colouration by gases. Thin Solid Films 409, 254–264. https://doi.org/10.1016/S0040-6090(02)00058-5

Stone W., 1997. NIST Construction Automation Program Report No. 3 Electromagnetic Signal Attenuation in Construction Materials (No. NISTIR 6055). NIST.

Su, Y., Falgenhauer, J., Polity, A., Leichtweiß, T., Kronenberger, A., Obel, J., Zhou, S., Schlettwein, D., Janek, J., Meyer, B.K., 2015. LiPON thin films with high nitrogen content for application in lithium batteries and electrochromic devices prepared by RF magnetron sputtering. Solid State Ionics 282, 63–69. https://doi.org/10.1016/j.ssi.2015.09.022

Su, Y., Zhang, J., Shokhovets, S., Polity, A., Meyer, B.K., 2017. Spectroscopic ellipsometry and optical transmission study of LiPON thin films prepared by RF sputtering: Spectroscopic ellipsometry and optical transmission study of LiPON thin films. physica status solidi (b) 254, 1600424. https://doi.org/10.1002/pssb.201600424

Sun, X., Liu, Z., Cao, H., 2010. Effects of film density on electrochromic tungsten oxide thin films deposited by reactive dc-pulsed magnetron sputtering. Journal of Alloys and Compounds 504, S418–S421. https://doi.org/10.1016/j.jallcom.2010.03.155

Sunding, M.F., Hadidi, K., Diplas, S., Løvvik, O.M., Norby, T.E., Gunnæs, A.E., 2011. XPS characterisation of in situ treated lanthanum oxide and hydroxide using tailored charge referencing and peak fitting procedures. Jour-

nal of Electron Spectroscopy and Related Phenomena 184, 399–409. https://doi.org/10.1016/j.elspec.2011.04.002

Szczyrbowski, J., Dietrich, A., Hartig, K., 1989. Bendable silver-based low emissivity coating on glass. Solar Energy Materials 19, 43–53. https://doi.org/10.1016/0165-1633(89)90022-1

Sze S. M., 1981. Physics of Semiconductor Devices, John Wiley and Sons, Inc., Singapore ().

Tanaka, S., Taniguchi, M., Tanigawa, H., 2000. XPS and UPS studies on electronic structure of Li2O. Journal of Nuclear Materials 283–287, 1405–1408. https://doi.org/10.1016/S0022-3115(00)00251-8

Thornton, J.A., 1974. Influence of apparatus geometry and deposition conditions on the structure and topography of thick sputtered coatings. Journal of Vacuum Science and Technology 11, 666–670. https://doi.org/10.1116/1.1312732

Thorpe, R., Rangan, S., Sina, M., Cosandey, F., Bartynski, R.A., 2013. Conversion Reaction of CoO Polycrystalline Thin Films Exposed to Atomic Lithium. The Journal of Physical Chemistry C 117, 14518–14525. https://doi.org/10.1021/jp404875g

Tougaard, S., 2010. Energy loss in XPS: Fundamental processes and applications for quantification, non-destructive depth profiling and 3D imaging. Journal of Electron Spectroscopy and Related Phenomena 178–179, 128–153. https://doi.org/10.1016/j.elspec.2009.08.005

Uitz, M., Epp, V., Bottke, P., Wilkening, M., 2017. Ion dynamics in solid electrolytes for lithium batteries: Probing jump rates and activation energies through time-domain Li NMR. Journal of Electroceramics 38, 142–156. https://doi.org/10.1007/s10832-017-0071-4

Ullah, I., Habibi, D., Xiaoli Zhao, Kiani, G., 2011a. Design of RF/Microwave efficient buildings using frequency selective surface. IEEE, pp. 2070–2074.

Ullah, I., Zhao, X., Habibi, D., Kiani, G., 2011b. Transmission improvement of UMTS and Wi-Fi signals through energy saving glass using FSS. IEEE, pp. 1–5.

Ulrich, S., Szyszko, C., Jung, S., Vergöhl, M., 2017. Electrochromic properties of mixed oxides based on titanium and niobium for smart window applications. Surface and Coatings Technology 314, 41–44. https://doi.org/10.1016/j.surfcoat.2016.11.078

Ulusoy, S., Gulen, S., Aygun, G., Ozyuzer, L., Ozdemir, M., 2018. Characterization of thin film Li 0.5 La 0.5 Ti 1−x Al x O 3 electrolyte for all-solid-state Li-ion batteries. Solid State Ionics 324, 226–232. https://doi.org/10.1016/j.ssi.2018.07.005

Unser, M.; Blu, T., 2005. "Generalized smoothing splines and the optimal discretization of the Wiener filter," in Signal Processing, IEEE Transactions on , vol.53, no.6, pp.2146-2159. doi: 10.1109/TSP.2005.847821

Valyukh, et al. 2012. Ellipsometrically determined optical properties of nickel-containing tungsten oxide thin films: Nanostructure inferred from effective medium theory. Journal of Applied Physics 112.

van Boort, H. J. J. & Groth, 1968. R. Low-pressure sodium lamps with indium oxide filters. Phil. Tech. Rev. 29, 47–48.

Van Der Pauw, L.J., 1958. A method of measuring specific resistivity and hall effect of disks of arbitrary shape. Philips research reports 13, 1–9.

Vasilopoulou, M., Soultati, A., Georgiadou, D.G., Stergiopoulos, T., Palilis, L.C., Kennou, S., Stathopoulos, N.A., Davazoglou, D., Argitis, P., 2014. Hydrogenated under-stoichiometric tungsten oxide anode interlayers for efficient and stable organic photovoltaics. J. Mater. Chem. A 2, 1738–1749. https://doi.org/10.1039/C3TA13975A

Venables, J., 2000. Introduction to surface and thin film processes. Cambridge University Press, Cambrige, UK ; New York.

Venkataraj, S., Kappertz, O., Weis, H., Drese, R., Jayavel, R., Wuttig, M., 2002. Structural and optical properties of thin zirconium oxide films prepared by reactive direct current magnetron sputtering. Journal of Applied Physics 92, 3599–3607. https://doi.org/10.1063/1.1503858

Vepřek, S., Iqbal, Z., Brunner, J., Schärli, M., 1981. Preparation and properties of amorphous phosphorus nitride prepared in a low-pressure plasma. Philosophical Magazine B 43, 527–547. https://doi.org/10.1080/01418638108222114

Vijitha V., 2014. Ellipsometry- non destructive measuring method. National Institute for Interdisciplinary Science & Technology.

Vossen, J.L., Poliniak, E.S., 1972. The properties of very thin R.F. sputtered transparent conducting films of SnO2:Sb and In2O3:Sn. Thin Solid Films 13, 281–284. https://doi.org/10.1016/0040-6090(72)90296-9

Wan, J., Xu, Y., Ozdemir, B., Xu, L., Sushkov, A.B., Yang, Z., Yang, B., Drew, D., Barone, V., Hu, L., 2017. Tunable Broadband Nanocarbon Transparent Conductor by Electrochemical Intercalation. ACS Nano 11, 788–796. https://doi.org/10.1021/acsnano.6b07191

Wells, A.F., 1984. Structural inorganic chemistry, 5th ed. ed. Clarendon Press, Oxford. ISBN 0-19-855370-6

Weppner W., 1999, in Materials for Lithium-Ion Batteries, Julien Z. C. a. S., Ed. p. 401, Kluwer Academic Publishers, Dordrecht.

Werner, W.S.M., 1992. Towards a universal curve for electron attenuation: Elastic scattering data for 45 elements. Surface and Interface Analysis 18, 217–228. https://doi.org/10.1002/sia.740180307

Whitney, S.M., The University of Texas at Austin. Mechanical Engineering, 2008. Neutron Depth Profiling Benchmarking and Analysis of Applications to Lithium Ion Cell Electrode and Interfacial Studies Research. University of Texas at Austin.

Widenberg, Björn and Rodriguez, José Victor (2002) In Technical Report LUTEDX/(TEAT-7110/1-14/(2002). Accessible at http://lup.lub.lu.se/record/530536

Wilson, P.F.; Ma, M.T.; Adams, J.W., 1988 "Techniques for measuring the electromagnetic shielding effectiveness of materials. I. Far-field source simulation," in Electromagnetic Compatibility, IEEE Transactions on , vol.30, no.3, pp.239-250. doi: 10.1109/15.3302

Witte, R., Frei, B., Schneeberger, S., Bücheler, S., Nishiwaki, S., Burn, A., Muralt, M., Romano, V., Krainer, L., Investigation of a reliable all-laser scribing process in thin film Cu(In,Ga)(S,Se) 2 manufacturing. Proc. SPIE 8607, Laser Applications in Microelectronic and Optoelectronic Manufacturing (LAMOM) XVIII, 86071B (March 13, 2013). doi:10.1117/12.2003872

Wu, Q.-H., Thissen, A., Jaegermann, W., 2005. Photoelectron spectroscopic study of Li oxides on Li over-deposited V 2 O 5 thin film surfaces. Applied Surface Science 250, 57–62. https://doi.org/10.1016/j.apsusc.2004.12.023

Xie, F.Y., Gong, L., Liu, X., Tao, Y.T., Zhang, W.H., Chen, S.H., Meng, H., Chen, J., 2012. XPS studies on surface reduction of tungsten oxide nanowire film by Ar+ bombardment. Journal of Electron Spectroscopy and Related Phenomena 185, 112–118. https://doi.org/10.1016/j.elspec.2012.01.004

Xiong, S., Lee, P.S., Lu, X., 2015. Nanostructures in Electrochromic Materials, in: Mortimer, R.J., Rosseinsky, D.R., Monk, P.M.S. (Eds.), Electrochromic Materials and Devices. Wiley-VCH Verlag GmbH & Co. KGaA, Weinheim, Germany, pp. 249–288. https://doi.org/10.1002/9783527679850.ch9

Young, W.C., Budynas, R.G., Sadegh, A.M., Roark, R.J., 2012. Roark's formulas for stress and strain, 8th ed. ed. McGraw-Hill, New York.

Zhang, L., Zhou, Y., Guo, L., Zhao, W., Barnes, A., Zhang, H.-T., Eaton, C., Zheng, Y., Brahlek, M., Haneef, H.F., Podraza, N.J., Chan, M.H.W., Gopalan, V., Rabe, K.M., Engel-Herbert, R., 2016. Correlated metals as transparent conductors. Nature Materials 15, 204–210. https://doi.org/10.1038/nmat4493

Zhou, K., Wang, H., Zhang, Y., Liu, J., Yan, H., 2017a. Understand the Degradation Mechanism of Electrochromic WO 3 Films by Double-step Chronoamperometry and Chronocoulometry Techniques Combined with in situ Spectroelectrochemical Study. Electroanalysis 29, 1573–1585. https://doi.org/10.1002/elan.201700049

Zhou, D., Xie, D., Xia, X., Wang, X., Gu, C., Tu, J., 2017b. All-solid-state electrochromic devices based on WO3||NiO films: material developments and future applications. Science China Chemistry 60, 3–12. https://doi.org/10.1007/s11426-016-0279-3

List of Figures

List of Tables

Acknowledgements

I would like to thank Andreas Schüler for giving me the opportunity to work in his group, first for a short bachelor thesis, then for a short project and now for this PhD thesis. I would like to acknowledge his enthusiasm and passion for science, and his excellent ideas and scientific intuition. I also would like to thank Jean-Louis Scartezzini for his support and for welcoming me in his laboratory.

Furthermore, I would like to thank Dr P. Lemarchand, Dr. S. Oukassi, Prof. F. Sorin, and Prof. S. Haussener for accepting to be members of the Jury of my doctoral exam.

I would like to thank the academic partners for the interesting exchanges and discussions especially Matteo Lanini from Supsi, Mehtap Özdemir, Gülnur Aygün and Lutfi Ozyuzer from Izmir institute of technology as well as Peter Oealhafen and Andreas Tonin from the University of Basel.

I also thank the industrial partners for allowing lab research to become a product, especially Luc Houlmann, Nicolas Noirjean, Arnaud Marguerit and Bernard Cuttat from AGC Verres Industriels Moutiers, Reiner Witte from Class4Laser and Christoph Isenschmid from BLS.

I am grateful I could use the facilities of CIME for SEM characterization -and benefit from the help of Grégoire Barroz to obtain nice images-, of CMi for to have access to a profilometer and of the Material Characterization Platform IPHYS for XRD with the help of Wen Hua David Bi and Arnaud Magrez.

I would like to acknowledge the Swiss competence center for energy research on Future Energy Efficient Buildings & Districts and Innosuisse for financing most of this work in the context of the Swiss energy strategy 2050 but also the Swiss Federal Office for Transportation for supporting research on energy efficiency of public transport.

I also want to thank the following for permission to reproduce the figures (in alphabetical order):

- Dr. N. Bondarenko, Uppsala University
- Dr. A C Fisher, Department of Chemical Engineering and Biotechnology, University of Cambridge
- R. Steiner, University of Basel
- AIP Publishing
- American Physical Society
- Elsevier
- Springer Nature
- Wiley
- Wiley book

Finally, special thanks to Anna Krammer for forming a nice "équipe de choc" in the Lab Life, the office and outside, and to all the "nano team": Luc, Jérémy, André, Jing, Antonio, Martin, Marina, Miguel, Antoine, Alexandre, Djamel, Raman... I also thank the students in semester project who participated in the electrochromic project at some point: Tom, Delphine, Joanne and Adrien.

I am grateful to Laurent, Michel and especially Pierre for helping me to obtain all the pieces and components I needed to build new experimental setups or repair the old ones.

I would like to thank all the "Lezards", past and present, for the nice atmosphere and time shared: Ali, Silvia, Apiparn, Chantal, Diane, Govinda, Nikos, Lenka, Pietro, Dan, Dasun, Marta, Dasaraden, Roberto, Yujie, Alina, Kilian, Jérôme, Adil, Fred, Mario, Natalya... but also: Suzanne, Barbara, Marlène and the IT team for their support.

And also the one who make my everyday life easier and nicer: Nicolas as well as my friends, from Lausanne and around the world, and all my family (and also the sun, who dares to bake chocolate cakes !).

Merci ☺

Curriculum Vitae

Olivia Bouvard
Chemin des Cottages 6
1007 Lausanne, Switzerland

olivia.bouvard@gmail.com
Tel : +4178 924 41 01/+336 68 76 03 61

RESEARCH AND TEACHING ACTIVITIES

· Main focus of research on all-solid state electrochromic devices (electrochromic materials and solid ions conductors) for advanced windows.

Deposition of thin films by reactive magnetron sputtering. Characterisation of electronic properties and chemical environment by photoelectron spectroscopies (UPS, XPS), optical and electrochromic properties by UV-Vis-NIR spectrophotometry and electrochemistry (CA, EIS…) and morphology by SEM, XRD and profilometry.

· Teaching assistant for the course "Physique du Bâtiment I & II" taught by Prof. J.-L. Scartezzini and Dr. A. Schüler at EPFL to 1st year Architecture students.

Organization of the exercise class (selection of assistant-students, preparation of the print outs…), assistance to students for the exercises and problems resolution.

· Supervision of bachelor/master students in materials science projects in the laboratory

EDUCATION

2014-2018	**PhD student in Nanotechnologies for solar energy group,**
	Solar Energy and Building Physics Laboratory (LESO-PB),
	EPFL, Lausanne, Switzerland
	Optical and electronic properties of coatings for advanced windows, development of electrochromic materials by magnetron sputtering deposition.
2009-2011	**Diplôme d'ingénieur Grenoble INP – PHELMA (Master)**
	Electrochimie et Procédés pour l'Energie et l'Environnement
	Institut National Polytechnique de Grenoble, France
	Electrochemistry, process, physics, chemistry, material science, thin films, surface treatment, design of experiment, intellectual property, innovation management…
2006-2007	**BEng Energy and Environmental Engineering (Bachelor)**
	Napier University, Edinburgh, United Kingdom.
	Renewable energies: principle and design, wind power, thermal solar energy, photovoltaic, building physics, economy, material engineering…
2004-2006	**Diplôme Universitaire Technologique en Science et Génie des Matériaux,**
	Institut Universitaire Technologique de Nîmes, France
	Two-year degree in material science and engineering.
2004	**Baccalauréat Scientifique spécialité Physique-Chimie mention Bien**
	Lycée Joliot Curie, Sète, France
	Scientific high school certificate with major in physics/chemistry obtained with distinction.

WORK EXPERIENCE

2013-2014 **Project engineer, EPFL**
Solar Energy and Building Physics Laboratory (LESO-PB),
EPFL, Lausanne, Switzerland
Project on energy efficiency of public transportation, development of innovative coatings for train windows, optical and thermal characterisations.

2012 **Technological watch manager, CEA Grenoble (temp. contract, 6 months)**
Cellule d'intelligence économique et scientifique, France
· Realisation of strategic studies and technological watch for CEA laboratories.

2011 **Research engineer, CEA Grenoble – Liten (internship, 6 months)**
Laboratoire des Composants pour la Récupération de l'Energie, France
· Evaluation and development of characterisation methods for printed thin film photovoltaic solar cells (CIGS). Collaboration with the Screen Solar start-up.

2010 **Assistant engineer, Solar energy institute INES (internship, 4 months)**
CEA, Laboratoire du Stockage Electrique, Le Bourget du Lac, France
· Study of the impact of different additives and internal components over the life time of lead acid batteries for stand-alone PV.

2007-2009 **Technician (full time, 2 years)**
Saint-Gobain Isover research center
Service Matériaux, Métrologie et Systèmes, Rantigny, France
· Mechanical and optical characterisations of insulation materials, development of new characterisation methods, infrared thermography of refurbished buildings.

2006 **Research assistant (internship, 2 months)**
Solar Energy and Building Physics Laboratory (LESO-PB),
EPFL, Lausanne, Switzerland
· Feasibility study of the deposition of selective black coatings for solar thermal collector via sol-gel process.

CONTINUING TRAINING

· MOOC Rénovation performante (Online course ASDER-ARCANNE, Autumn semester 2017)
· Presenting and explaining in class (EPFL Teaching Support Center, December 2016)
· Material Science for Energy Conversion (International Summer School, Bucharest, July 2015)
· Développement durable, critique de(s) principe(s) (EPFL master course, Spring semester 2015)
· New Materials from Physics to Applications (EPFL-ETHZ Winter school MSE-647, March 2015)
· IMX Seminar Series (EPFL Institute of Material Science, various invited speakers)
· Scanning electron microscopy techniques (EPFL course MSE-636, December 2014)

MISCELLANEOUS

Languages

French: mother tongue
English: fluent + technical
Spanish: intermediate

IT skills

Windows, Pack Office (Word, Excel, PowerPoint…), Matlab, Scilab, EC-Lab, Origin, Inventor …

Driving license + car

PUBLICATIONS & CONFERENCES

O. Bouvard, M. Lanini, L. Burnier, R. Witte, B. Cuttat, A. Salvadè, A. Schüler; Structured transparent low emissivity coatings with high microwave transmission. *Applied Physics A* 123:66, (2017).

O. Bouvard, L. Burnier, P. Oelhafen, A. Tonin, P. Wüst, F. Sidler, G. Zweifel, A. Schüler; Solar heat gains through train windows: a non-negligible contribution to the energy balance. *Energy Efficiency (2018).*

L. Burnier, M. Lanini, O. Bouvard, D. Scanferla, A. Varathan, C. Genoud, A. Marguerit, B. Cuttat, Noémie Dury, R. Witte, A. Salvadè, A. Schüler; Novel energy saving glazing with a wide band-pass FSS allowing mobile communication: Upscaling and characterization. *IET Microwaves, Antennas & Propagation*, 31 pp (2017).

O. Bouvard, M. Lanini, L. Burnier, R. Witte, B. Cuttat, A. Salvadè, A. Schüler;Mobile communication through insulating windows : a new type of low emissivity coating, oral presentation at CISBAT 2017, Future Buildings & Districts – Energy efficiency from Nano to Urban Scale and published in Energy Procedia (2017) pp. 781-786.

D. Mansour, O. Bouvard & A. Schüler; Development and characterization of electrochromic oxide and ion conductor deposited by reactive magnetron sputtering, oral presentation at CISBAT 2017, Future Buildings & Districts – Energy efficiency from Nano to Urban Scale and published in Energy Procedia (2017); 122:787–92.

O. Bouvard, A. Schüler. « Vitrages innovants pour la façade du futur/Innovatives Glas für die Fassade der Zukunft" Invited talk presented at Windays 2017, 24/03/2017 Bienne.

O. Bouvard, A. Schüler. « Nouvelles technologies pour les énergies solaires, couches minces et nanotechnologie » Invited talk presented at Ambition Négawatt, journée thématique Le Photon. Programme ECO21 SIG, 15/03/2016 Geneva.

O. Bouvard, A. Krammer, A. Schüler; In situ photoelectron spectroscopy of LiPON/WO3 interface for electrochromic devices, a preliminary study. Poster presented at SATF 2016, Science and Applications of Thin Films, Congress & Exhibition. 2nd best poster award of poster session A.

O. Bouvard, A. Krammer & A. Schüler; *In situ* core-level and valence-band photoelectron spectroscopy of reactively sputtered tungsten oxide films: *In situ* XPS and UPS study of reactively sputtered tungsten oxide films. Poster presented at ECASIA'15, 16th European Conference on Applications of Surface and Interface Analysis and paper published in *Surface and Interface Analysis* (2016).

O. Bouvard, M. A. González Lazo, A. Krammer, A. Schüler. In situ photoelectron spectroscopy: a powerful tool to develop electrochromic materials. Poster presented at CISBAT 2015, Future Buildings & Districts - Sustainability from Nano to Urban Scale.

M. Joly, O. Bouvard, T. Gascou, Y. Antonetti, M. Python, M.A. González Lazo, P. Loesch, A. Hessler-Wyser, A. Schüler; Optical and structural analysis of sol–gel derived Cu–Co–Mn–Si oxides for black selective solar nanocomposite multilayered coatings. *Solar Energy Materials and Solar Cells* 143, 573–580 (2015).

O. Bouvard, S. Vanzo, & A. Schüler; Experimental Determination of Optical and Thermal Properties of Semi-transparent Photovoltaic Modules Based on Dye-sensitized Solar Cells. Poster presented at IBPC 2015, 6th International Building Physics Conference and paper published in *Energy Procedia 78, 453–458* (2015)*. Best poster award.